L aboratório
N acional de
C omputação
C ientífica

Post-graduate program in Computational Modeling

Computational models for the geometric and functional assessment of the coronary circulation

By

Carlos Alberto Bulant

PETRÓPOLIS, RJ - BRASIL

MARCH, 2017

MODELOS COMPUTACIONAIS PARA A ANÁLISE GEOMÉTRICA E FUNCIONAL DA CIRCULAÇÃO CORONÁRIA

Carlos Alberto Bulant

TESE SUBMETIDA AO CORPO DOCENTE DA COORDENAÇÃO DE FORMAÇÃO DE RECURSOS HUMANOS DO LABORATÓRIO NACIONAL DE COMPUTAÇÃO CIENTÍFICA COMO PARTE DOS REQUISITOS NECESSÁRIOS PARA A OBTENÇÃO DO GRAU DE DOUTOR EM MODELAGEM COMPUTACIONAL.

DOUTOR EM CIÊNCIAS

Aprovado por:

_____

Prof. Pablo Javier Blanco, Sc.D. (PRESIDENTE)

_____

Abimael Fernando Dourado Loula, D.Sc.

_____

Gilson Antônio Giraldi, D.Sc.

_____

Pedro Alves Lemos Neto, D.Sc.

_____

Rodrigo Weber dos Santos, D.Sc.

_____

Gustavo Carlos Buscaglia, D.Sc.

PETRÓPOLIS, RJ - BRASIL

MARÇO, 2017

MODELOS COMPUTACIONAIS PARA A ANÁLISE GEOMÉTRICA E FUNCIONAL DA CIRCULAÇÃO CORONÁRIA

Carlos Alberto Bulant

Março/2017

Orientadores: Pablo Javier Blanco, Diretor de Tese
Raúl Antonino Feijóo, Co-Diretor de Tese

A doença coronáriana é uma das principais causas de morte em todo o mundo. Embora vários fatores de risco sejam bem conhecidos; muitas lesões não podem ser explicadas apenas por esses fatores.

A hipótese das artérias desenvolverem lesões devido à sua morfologia, conhecida como fatores de risco geométricos e/ou devido a forças hemodinâmicas, foi levantada há mais de trinta anos. Embora tenha sido encontrada uma conexão entre variáveis geométricas/hemodinâmicas e lesões, não existe um índice quantificável que ajude os médicos a prever os riscos reais.

Mesmo quando uma lesão grave está presente, estudos recentes descobriram que alguns pacientes podem desenvolver circulação colateral para fornecer fluxo sanguíneo suficiente para o miocárdio, evitando assim a isquemia. Por sua vez, o padrão ouro para avaliar a funcionalidade de uma lesão é o exame médico invasivo chamado Reserva de Fluxo Fracionada (FFR por suas siglas em inglês). Além disso, esses estudos são caros, exigem profissionais altamente qualificados e envolvem riscos para o paciente durante a intervenção. Nesse contexto, os objetivos desta tese são (i) caracterizar completamente as artérias coronárias de uma perspectiva geométrica, buscar características geométricas hereditárias e correlações entre morfologia e doença; (ii) construir uma metodologia de modelagem para a estimativa do FFR, utilizando modelos da dinâmica dos fluidos computacional (CFD por suas siglas em inglês) construídos a partir de imagens médicas de artérias coronárias de pacientes específicos.

Resultados para meta (i) incluem a caracterização geométrica de uma amostra de pacientes constituída por pares de irmãos. Vários estudos são realizados envolvendo índices padronizados e não tradicionais baseados na geometria, nos quais foram encontradas associações entre geometria e presença de lesão, bem como indicações de herdabilidade de geometria arterial entre irmãos. Em relação às simulações hemodinâmicas no contexto de FFR, isto é, meta (ii), é apresentada e testada uma nova técnica para definir condições de contorno específicas para cada paciente em modelos 3D; ainda, foi avaliado pela primeira vez o impacto da modalidade de imagem, em particular, tomografia computadorizada coronária (CCTA) e ultrassom intravascular (IVUS), sobre variáveis hemodinâmicas, o que ajuda a avaliar melhor os resultados obtidos pela combinação de simulações numéricas e imagens médicas. Também é apresentada uma comparação de simulações de CFD empregando modelos 3D e 1D do fluxo sanguíneo coronário focado puramente na estimação do FFR. Vários cenários são comparados com medidas invasivas com resultados similares aos encontrados no estado de arte da técnica.

COMPUTATIONAL MODELS FOR THE GEOMETRIC AND FUNCTIONAL ASSESSMENT OF THE CORONARY CIRCULATION

Carlos Alberto Bulant

March/2017

Advisors: Pablo Javier Blanco, Thesis Advisor
            Raúl Antonino Feijóo, Thesis Co-Advisor

Coronary heart disease is one of the leading causes of death worldwide. Although several risk factors are well known; many lesions cannot be explained by these factors alone.

The hypothesis of arteries developing lesions due to its morphology, known as geometric risk factors and/or due to hemodynamic forces, has been raised more than thirty years ago. Although investigators have found connection between geometric/hemodynamic variables and lesions, there exists no quantifiable index that helps physicians to predict actual risks. Even when a severe lesion is present, recent studies have found that some patients can develop collateral circulation to provide sufficient blood flow to the myocardium, thus avoiding ischemia. In turn, the gold standard for functional stenosis assessment is an invasive medical exam called Fractional Flow Reserve (FFR). Moreover, these studies are expensive, require highly qualify professionals and involve risks to the patient during intervention.

In this context, the goals of the proposed thesis are (i) to fully characterize coronary arterial trees from a geometrical perspective, search for hereditary geometric features and correlations between morphology and disease; (ii) to construct a modeling methodology for the estimation of FFR making use of computational fluid dynamic models built on top of patient-specific medical images of coronary arterial networks.

Results for goal (i) include the geometric characterization of a patient sample consisting of siblings. Several studies involving standard and non-traditional geometry-based indexes, in which associations between geometry and lesion presence was found, as well as indications of arterial geometry heritability between siblings. Regarding hemodynamic simulations in the context of FFR, i.e. goal (ii), a novel technique to define patient-specific boundary conditions in 3D models was presented and tested; the impact of image modality, i.e. coronary computed tomography (CCTA) and intravascular ultrasound (IVUS), on hemodynamics variables was assessed for the first time, which helps to better assess the results obtained from the combination of numerical simulations and medical images. A comparison of 3D and 1D CFD simulations for coronary blood flow based purely on FFR is presented. Several computational settings are compared to invasive measurements with results comparable to the state of the art.

Preface

This Doctoral Thesis represents, for me, the culmination of a very important chapter in my life. I like to think of it as an adventure, a glance of the academic world and the beginning of, what I expect to be, a life-time journey into it. As many adventures, it started with a trip, six years ago when Lis, my better half and I moved to Petrópolis, RJ, Brazil, to start my Masters studies at the *Laboratório Nacional de Computação Científica* (LNCC). Through those two years of Master studies, I learned a lot, but also Lis and I got to know some wonderful people. When the Master was completed, four years ago, we decided to stay and start the doctorate studies. This Thesis is the result of four years of hard work and synergistic interaction at HeMoLab research group, at the LNCC, and an strong collaboration with a team of cardiologist at the Instituto do Coração (InCor), SP, Brazil.

Fortunately, this was not a lonely journey, through all these years I counted with the company and support of my family and friends. I would like to acknowledge and register here my deepest gratitude to everyone that, in someway, influenced this work.

First of all, I would like to thank my mentors, Pablo J. Blanco and Raúl A. Feijóo, for their guidance, confidence, patience and friendship. Through uncountable discussions, they won my most sincere admiration and respect, I am really thankful for the chance to know them and the opportunity to work with them.

I said before that my journey began with a trip, and for that I need to thank my graduate professor, Alejandro Clausse. He encouraged me to start my post-graduate studies, with all his confidence on me. He also collaborated directly in some topics studied in the first Part of this Thesis.

I was lucky to meet professors Santiago Urquiza, Pablo Sanchez and Enzo Dari, they visited regularly the HeMoLab group, and every time was a chance to learn something and unpurposedly they were an inspiration to perusing an academic career back in Argentina.

I want to thank my friend Lucas, for his tremendous help with 1D models and several discussions regarding the second part of this work. I would like to thank to the development group of the HeMoLab project for their support and many technical advices, specially my friend Paulo. I also want to mention my brilliants colleagues, former and current students in the group: Sansuke, Paulo, Rafael, Felipe, Alonso, Goga and Goncholas. They were always predisposed to help, and thanks to them I got the big picture of several aspects regarding the modeling of the cardiovascular system. I hope to continue working with them in the future.

I would like to thank my long-time friends Paul, Paez, Leo, Mati, Lucho, Lomu and Marco, they are always there. During the time in Petrópolis, we get to know new friends: Goncholas, Carla, Pablo, Maru, Lucas, Wenddi and Camilla. They helped making Petrópolis feel like home, we shared a lot of weekends, birthdays, *asados* and afternoon *mates* together. I hope that, wherever we are in the future we can keep in touch, and I wish all of them the best in life. I would like to thank Goga for his friendship, we finished

our undergraduate studies together, and came to Petrópolis with the same goal, now that we are done we are taking different paths, but I know we will keep working together and continue our friendship from a distance.

I want to thank the family of Lis, which I feel mine, Raúl, Mirta, Fernando, Vanina and Sven, for their affection.

There are no words to describe my gratitude to my mother Dora, my father Miguel, and my brother Marcelo, for their unconditional love, affection and support every day of my life.

At last, and more importantly, I would like to thank Lis, my love, my partner, my best friend. She was always there when I need her the most, encouraging and cheering with a smile.

Carlos Alberto Bulant
March 2017, Petrópolis - RJ

To my family and friends

I learned the value of hard work by working hard.

— Margaret Mead

Contents

List of symbols and abbreviations

Chapter 1

CVD	Cardiovascular disease	FFR	Fractional Flow Reserve
CAD	Coronary artery disease	P_d	Post-stenotic pressure
AX	Angiography	P_a	Aortic pressure
OCT	Optical coherent tomography	CFD	Computational fluid dynamics
CCTA	Coronary computed tomography angiography	FFR_{CT}	A technique to estimate FFR from CCTA data, trademark of HeartFlow Inc.
MRI	Magnetic resonance imaging		
WSS	Wall shear stress		
OSI	Oscillatory share index	FFR_{CE}	Computational estimation of FFR, as proposed in this work

Chapter 2

C	Myocardial convex hull	w_p	Weight factor for propagation term in the Level-Set method
$S(t)$	Implicit surface of the Level-Set segmentation algorithm	w_k	Weight factor for smoothing term in the Level-Set method
$\phi(\mathbf{x}, t)$	Scalar function describing the iso surface S	w_a	Weight factor for advection term in the Level-Set method
$\mathbf{x}$	Pixel coordinate	I_f	Featured image of the Level-Set method
$P(\mathbf{x})$	Propagation scaling function of the Level-Set method	ROI	Region of interest
$K(\mathbf{x})$	Curvature scaling function of the Level-Set method	$\mathcal{S}_{\text{myo}}$	Myocardial surface
$A(\mathbf{x})$	Advection scaling function of the Level-Set method	sf_{myo}	Scale factor for myocardial surface
$\kappa(\mathbf{x})$	Mean curvature of the zero-level surface		

Chapter 3

LAD	Left anterior descendant artery	A	A given artery
LCx	Left circumflex artery	LDDMCM	Large deformation diffeomorphic metric curve mapping
LM	Left main artery		
RCA	Right coronary artery	ℓ	The length of an arterial segment
Ao	Aorta		

s	Arc length coordinate of an arterial centerline	H	Entropy
χ	Tortuosity	T	Temperature
$\kappa(s)$	Point-wise curvature	P	Pressure
$\tau(s)$	Point-wise torsion	$\mathcal{L}$	Lagrangian of the Thermodynamic's problem
$\zeta(s)$	Point-wise combined curvature	λ, ϕ	Lagrangian multipliers of $\mathcal{L}$
$r(s)$	Point-wise lumen radius	γ	Ratio of specific heats
Λ_r	Aspect ratio	H_n	Intersection-counting-based Entropy
Λ_κ	Curvature ratio	T_n	Intersection-counting-based Temperature
Λ_τ	Torsion ratio		
ξ_κ	Bending energy	P_n	Intersection-counting-based Pressure
ξ_τ	Twisting energy		
ϱ	Fractal dimension	H_κ	Curvature-based entropy
α	The angle between a given artery and it parent	T_κ	Curvature-based temperature
		P_κ	Curvature-based pressure
β	The mean of α over the offspring of a given artery	X	Random variable
		$\mathcal{G}$	Set of energy levels of a curve
Υ	The number of branches arising from a given artery	p	Probability distribution
		$\mathcal{F}(\mathbf{m})$	A parametric function defining a curve, $\mathbf{m}$ is the vector of parameters
η	The number of lesion of a given artery		
$\bar{\kappa}_d$	Average distal curvature	$\mathscr{F}^N$	Space of parametric functions with N parameters
s_d	Arc length value defining the distal region for $\bar{\kappa}_d$ computation	$\mathcal{O}(\Gamma, \mathcal{F})$	Functional operator
		S	The exploration set of parameters, with cardinality J
Γ	A given planar curve	M	Number of buckets in a spatial partition of a centerline
C	The perimeter of the convex hull of Γ		
$\bar{n}$	Expected number of intersection points between Γ and a random hyperplane	f	A point-wise distributed feature
		F	The cumulative value of f in a given bucket
p_n	Probability distribution of n		

Chapter 4

$\mathscr{F}$	Euclidean space for the geometric features	$\mathscr{P}$	Cardinality of the patient sample
$\mathcal{G}_{\mathscr{D}}^{\mathscr{A}}$	A subset of features for an artery $\mathscr{A}$, with $\mathscr{D}$ the features identifiers	SRI	Sibling ranking index
		rSRI	Relative sibling ranking index
$\hat{\mathbf{p}}$	Representation of a patient as a vector of features	χ^2	Statistical test for independence
$\mathbf{p}$	Normalized representation of a patient in $\mathscr{F}$	r	Pearson's correlation coefficient
$d(\mathbf{a}, \mathbf{b})$	Distance between two patients $\mathbf{a}, \mathbf{b} \in \mathscr{F}$	ρ	Spearman's correlation coefficient
$r(\mathbf{a}, \mathbf{b})$	Ranking of distances of patient $\mathbf{b}$ to $\mathbf{a}$ relative to the rest of the patient sample	SD	Standard deviation
		PBWR	ProbandWise ratio
		B	Number of sibling pairs where both patient tested positive

O	Number of sibling pairs where only on patient tested positive	KDE	Kernel density estimation
E	Number of sibling pairs where neither patient tested positive	KDC	Kernel density classification
SimI	Similarity index, Probability that both siblings have the same test results	f_X	Probability density function
		ϕ_λ	Gaussian kernel with zero mean and SD= λ
CI	Confidence interval	J	The number of classes in the classification problem
U-Test	Mann-Whitney or Wilcoxon statistical test	π_j	Proportion of class j in the entire sample
ICC	Interclass correlation coefficient	$\hat{P}_j$	Posterior probability in the KDC problem
RR	Risk ratio	LOOCV	Leave-one-out cross validation
OR	Odds ratio	TP, FP	True positive, false positive
PHI	Association parameter	TN, FN	True negative, false negative
COR	Critical odds ratio	Sen, Spe	Sensitivity, Specificity
Pw	Power, the probability of rejecting the null hypothesis when it is in fact false	PPV, NPV	Positive and negative predictive value
$\mathbf{w}$	Weighting vector of the linear classifier	Acc, Prev	Accuracy and prevalence
c	Linear classifier variable	ROC	Receiver operating characteristic curve
t	Linear classifier threshold	AUC	Area under the ROC
$\mathbf{f}$	Features vector for the linear classifier		

Chapter 5

BMI	Body mass index	AOCAOS	Anomalous, origin of coronary artery from opposite sinus
LDL	Low-density lipoprotein		
HDL	High-density lipoprotein	RPD	Right posterior descendant artery
MI	Miocardial infarction		
PCI	Percutaneous coronary intervention	RPLSA, LPLSA	Right/Left posterolateral segment artery
CABG	Coronary artery bypass graft	AB	Atrial branch artery
LVEF	Left ventricle ejection fraction	$A(t)$	Andrerw's transformation
$\mathbf{H}$, $\mathbf{D}$	Healthy and disease classes	$\mathbf{M}$	Ranking matrix
$\bar{F}$	Frequency of appearance of a given arterial label in the patient sample	RDI	Ranking dispersion index
		ℓ_T	Total length
		C	Area of the centerline's convex hull

Chapter 7

ECG	Electrocardiogram	CFI	Collateral flow index
QCA	Quantitative coronary angiography	BC	Boundary condition

ICA$_{\text{VD}}$	Intra-coronary administration of vaso-dilator	PP	Pressure pulse
IVA$_{\text{VD}}$	Intra-venous administration of vaso-dilator	PP*	Adjusted pressure pulse
HR	Heart rate	Q	Coronary blood flow
MSBP	Mean systemic blood pressure	LV, RV	Left/Right ventricle
SBP	Systolic blood pressure	LVMM	Left ventricle myocardial mass
DBP	Diastolic blood pressure	m	Myocardial mass
A, W, H	Age, weight and height	MBF	Myocardial blood flow
CO	Cardiac output	CBF	Coronary blood flow
SV	Stroke volume	CFR	Coronary flow reserve

Chapter 8

P_a	Aortic pressure	ROC	Rotational coronary angiography
P_d	Post-stenotic pressure		
P_w	Wedge pressure	TAG	Trans-luminal attenuation gradient
Q_a	Coronary inflow		
Q_b	Healthy coronary flow	FFR$_{\text{CT}}$	A technique to estimate FFR from CCTA data, trademark of HeartFlow Inc.
Q_s	Stenotic artery flow		
R_{m1}, R_{m2}	Myocardial resistances		
R_s	Stenotic resistance	cFFR,	Techniques to estimate FFR from CCTA and AX data, from Siemens
P_v	Venous pressure	FFR$_{\text{angio}}$	
R_c	Collateral resistance		
Q_c	Collateral flow	CT-FFR	Technique to estimate FFR from CCTA data, from Toshiba
FFR$_{\text{cor}}$	Coronary flow reserve		
FFR$_{\text{myo}}$	Myocardium fractional flow reserve, or simply FFR		
		vFFR	Technique to estimate FFR from AX images
FFR$_{\text{col}}$	Collateral flow reserve, also called collateral flow index (CFI)	FFR$_{\text{QCA}}$	Technique to estimate FFR from AX images
Ω	Three dimensional arterial domain	vFAI	CFD-based method to detect functional stenoses
Γ	Domain boundary	FFR$_{\text{OCT}}$	Technique to estimate FFR from OCT images
N_o	The number of outlet in an arterial model	FFR$_{\text{SS}}$	A technique to estimate FFR from CCTA data
$\mathbf{x}$	Spatial position in the domain		
$\mathbf{v}, p$	Flow velocity and pressure	FFR$_{\text{AM}}$	A technique to estimate FFR from CCTA data
μ, ρ	Blood viscosity and density		

Chapter 9

	Section 9.1.3	r_a	The radii of the circle which area is equal to the cross-section area at each centerline point
r_s	The radii of the maximum circumscribed sphere at each centerline point		

$\hat{r}$	The radii of the healthy artery	**Section 9.2.2**	
N	Gaussian kernel for the stenoses detection algorithm	L_k	Length of segment k
M	Modified kernel for the stenoses detection algorithm	N_j, B	Number of junctions and junction points
w	Weighting function for the stenoses detection algorithm	U	Mean velocity
		Q	Blood flow variable
$\sigma_i, \sigma_r,$	Parameters for the stenoses detection algorithm	A, A_0	Lumen cross-sectional area variable, and the reference area parameter
σ_{MAX}, a			
Θ	Percentage area of stenosis	P_{tot}	Total pressure
Θ_1, Θ_2	Threshold parameters for the stenoses detection algorithm	Q_{out}^i	Flow boundary condition curve
Δx	Spacing of the 1D Model	P_p	Pressure at inlet
	Section 9.2.1	β	Effective arterial stiffness
$\mathbf{x}$	Spatial position in the domain	ϖ	Velocity profile parameter
$\mathbf{n}$	Normal vector to domain boundary	D	Lumen cross sectional diameter
$\mathbf{v}, p$	Flow velocity and pressure	A_s	Minimum area of stenosis
$\hat{\mathbf{v}}, \hat{p}$	Variations of velocity and pressure	L_s	Stenosis length
$\mathcal{V}, \mathcal{P}$	Function spaces of $\mathbf{v}$ and p	K_v, K_t, K_u	Viscous, turbulent and inertial parameters from the Young stenosis model
μ, ρ	Blood viscosity and density		
Ω	Three dimensional arterial domain		
Γ	Domain boundary	$P_{\mathrm{loss}}, K_{1,k}$	Pressure loss coefficients from the Mynard junction model
N_o	The number of outlet in an arterial model		
$\mathcal{R}$	Resistance boundary condition	ROUKF	Reduce order unscented Kalman filter
$\bar{Q}_T$	Total mean inflow	X, θ	State variables and parameter representations in the Kalman filter formulation
P_p	Inlet pressure		
P_{ref}	Reference pressure at outlets, e.g. venous pressure		
		Y, ε^X	Initial condition and errors in the Kalman filter formulation
γ	Murray's exponent	$\mathcal{F}$	Forward problem in the Kalman filter formulation
β	Murray's coefficient		
$\bar{Q}_i^*$	Murray's flow at outlet i	Z	Measurement vector
$\bar{R}_i^*$	Murray's resistance at outlet i	ε^Z	Intrinsec error of the measurement
r_i	Lumen radius at outlet i		
PI	Pulsatility index	M	Number of stenosis
$Q_{\mathrm{MAX}},$	The max, min and mean values of the flow curve signature	ΔP	Pressure drop across stenosis
$Q_{\mathrm{MIN}}, \bar{Q}$		$\mathcal{H}$	Observation operator
α	Variable for the BC coupling outlet resistances and inflow	K_X, K_θ	Kalman matrices
		Section 9.3	
Δt	Computational time step	DMD	Distal Murray flow distribution criterion
$\bar{\Omega}$	One dimensional domain		
x	One dimensional spatial coordinate	PMD	Proximal Murray flow distribution criterion
I, O_i	Inlet and outlet boundaries of $\bar{\Omega}$	CSRD	CCTA - Simulation result flow distribution criterion
N_v	Number of 1D segments	PD	Physiological flow distribution criterion
		PDC, PDB	Two variants of PD criterion

X, Y, Z, W	Patient specific functions for determination of CFR	AWSS	Average wall shear stress
τ	Wall shear vector	T	Cardiac period
$\mathbf{v}_t$	Tangential flow velocity	Ω_{FFR}	Region where the FFR is estimated for diagnosis purposes
OSI	Oscillatory shear index		

Chapter 10

ID	The identification number of patients in the sample	ν	The `edgelengthfactor` parameter of the mesh generation algorithm
RT	Total wall clock runtime of a simulation	$\varepsilon_{(\cdot)}$	Error between two meshes in an specific variable, e.g. p or $\mathbf{v}$
NRT	The normalized total wall clock of a simulation		
#Tasks	The number of computational tasks used in a simulation	dof	Number of degrees of freedom
CD	Coronary circulation dominance	RES	Reference element size
		Γ_s	Cross sectional slice
G	Patient gender	$\partial\Gamma_s$	Contour of the cross sectional slice
AA	Adenosine administration technique	Re	Reynolds number
		s	Arc length of the centerline
IM	Number of IVUS models associated to the patient	K_v^f	Factor estimated by the Kalman filter
		SC	Study case

Chapter 1

Introduction

"It ought to be remembered that there is nothing more difficult to take in hand, more perilous to conduct, or more uncertain in its success, than to take the lead in the introduction of a new order of things. Because the innovator has for enemies all those who have done well under the old conditions, and lukewarm defenders in those who may do well under the new. This coolness arises partly from fear of the opponents, who have the laws on their side, and partly from the incredulity of men, who do not readily believe in new things until they have had a long experience of them."

Niccolò Machiavelli, *The Prince*

Cardiovascular diseases (CVD) are the main cause of death worldwide, and among them, coronary artery disease (CAD) is the leading one [281]. Although usually affecting the elderly, the antecedents of CVD, notably atherosclerosis, begin in early life, making primary prevention efforts necessary even from childhood [217]. Therefore, the scientific community has witnessed increasing emphasis on preventing atherosclerosis by tackling risk factors. Even if the medical community agrees that the most important (modifiable) risk factors are cigarette smoking, diabetes mellitus, hypertension, and hypercholesterolemia, the amount of CVD explained by these factors is center of debate [143, 206, 60, 217]. This has encouraged research on novel markers and other non-traditional risk factors to assess CVD risks [139]. For example, it is widely accepted that familial history of CAD increases risk [314, 167, 148], indicating a genetic contribution to susceptibility for this condition [253, 132, 104, 287, 221].

Regardless of the percentage of CAD explained by any of the previous risk factors, it is noteworthy that all these markers are systemic in the sense that they do not explain the localization and non-uniformity of the disease distribution, i.e. why the left coronary tree is more susceptible to atherosclerosis than the right side [69]. This gap has been addressed by the hypothesis that hemodynamically-induced mechanical forces play a fundamental role on localization, initiation and progression of atherosclerosis [120]. This hypothesis has been supported by evidence gathered from laboratory investigations that include in vivo measurements, in vitro experiments, cell culture studies and gene expression profiling [189, 365, 123, 71, 82]. As a complementary tool, accurate characterization of patient-specific hemodynamic forces acting over the endothelium is possible thanks to the combination of image processing tools and computational fluid dynamics [122, 329, 66, 65, 79, 369]. The correlation between atherosclerosis and hemodynamic variables can be taken as a second type of risk factor, which acts at the arterial level instead of the systemic one.

Following the rationale behind the influence of hemodynamic variables on the rate and site of the atherosclerotic process, the hypothesis of geometric risk factors [113] suggests that the geometric variability of the human vasculature contributes to the development of atherosclerosis. Specifically, it states that geometric features of a susceptible arterial

segment can enhance an atherogenic hemodynamic stress. However, this reasoning relies on fluid mechanics as the ultimate atherosclerosis mediator, which is also consistent with wall shear stress hypothesis [331]. Remarkably, a significantly amount of clinical observations backs up the geometric risk factors hypothesis [153, 114, 371, 101, 89, 23].

Despite the considerable inter-individual variation in arterial geometry, the idea that specific geometric descriptors might be heritable, as other morphological characteristics are, was reported elsewhere [153, 114]. Although the heritability of stenosis characteristics such us localization, extent and morphology, as well as risk of coronary events in siblings has been studied before [106, 107], there is no precedent work in the literature addressing the hypothesis of arterial geometry heritability.

Coronary artery narrowing, induced by atherosclerosis, compromises the blood supply to the heart. Lesions can be asymptomatic at first, but as the lesion severity increases, symptoms can be detected, e.g. chest pain (angina), shortness of breath, abnormal heart rhythm (arrhythmia) and ultimately a heart attack. The study of risk factors for the development of CAD can ultimately help to reduce the incidence of the disease, but determining the functional[1] severity of an existing lesion, poses other challenges and represents a research area by its own.

Nowadays, there are several clinical tests designed to detect the presence of CAD and to quantify the functional significance of a stenosis. Such procedures can be roughly divided into three categories[2]: (i) exercise test with monitoring of CAD symptoms or direct observation of coronary flow, i.e. stress test, stress echocardiography and exercise test with thallium scanning; (ii) invasive and noninvasive medical images, i.e. coronary angiography (AX), optical coherence tomography (OCT), intra-vascular ultrasound (IVUS) and coronary computed tomography angiography (CCTA); and (iii) functional assessment of lesion through physiologic response, i.e. absolute/relative coronary flow reserve.

Finally, a type (iii) test known as Fractional Flow Reserve (FFR) turned into the gold standard to detect risk of myocardial ischemia [35, 269, 332, 333, 341]. The FFR, was introduced in the early 90's by Pijls et al. [266]. It is defined as the maximally achievable flow rate in the presence of a stenosis divided by the maximum flow rate expected in the absence of the lesion, during maximal hyperemic conditions. Although the FFR conceptually represents a relationship between blood flow rates, it can be, and in practice it is, estimated from invasive pressure measurements during catheterization. Then, FFR $= P_d/P_a$, is the ratio between distal (post-stenosis) and aortic pressures, and so FFR $\in [0, 1]$, for which the cut-off value of FFR < 0.8 is used to detect functionally significant lesions.

Coronary blood flow simulations have played a major role in the understanding of hemodynamic mechanisms involved in the onset and progression of atherosclerotic disease [69, 70, 79, 187, 320], characterization of plaque location [278], plaque erosion [59] and plaque rupture [73]. Moreover, there has been an increasing interest from the medical community in the use of such computational tools to aid decision making process due to feasible estimation of FFR noninvasively [152, 328, 275, 184, 337].

Patient-specific hemodynamic simulations rely on two fundamental issues: (i) computational domains and (ii) boundary conditions. Vascular geometries are obtained using imaging methods: CCTA [73, 278, 328, 275, 184] or AX, which can be utilized alone [59, 236], or in combination with either IVUS [70, 187, 320, 313] or OCT [103]. In turn, definition of boundary condition requires knowledge of global and local hemodynamic information, i.e. systemic pressure, heart rate and blood flow distribution.

Most of computational hemodynamic studies are performed using CCTA and IVUS[3].

---

[1]An stenosis is called functional, when it represents risk of myocardial ischemia, i.e. blood supply to the cardiac muscle is insufficient.

[2]An overview of these CAD diagnostic procedures is presented in Appendix D

[3]Also, the use of OCT images to construct computational domains for blood flow simulations is gaining popularity.

Although there have been studies addressing the consistency between these two image modalities concerning the overall decision-making process [105], it has been largely acknowledged that these modalities feature several differences ranging from the economic cost and patient risk to the resulting anatomical definition [188, 195]. Moreover, the impact of the image modality on the conclusions drawn from CFD simulations has been overlooked.

Regarding the definition of boundary conditions, estimation of total coronary flow and flow distribution among branches are crucial to set reliable patient-specific simulations. This is of the utmost importance for clinical applications either in the estimation of FFR or wall shear stress (WSS).

1.1 Medicine assisted by scientific computing

Using an extremely simplified perspective, a big portion of the medical literature is based on finding correlations between the so-call clinical data[4] and disease (CAD) state, progression and outcomes. This is the basic mechanism to support or reject hypotheses. Recently, mathematical models started to be used to aid medical research in the understanding of underlying physical mechanisms, in the decision-making process, and in the development of therapeutic actions. Many of these mathematical models only remain at the level of basic research. Testing mathematical models in large clinical trails depends on several factors, i.e. availability of multidiciplinary research centers, project budgets, computational infrastructure, and so on. From the technical point of view, the scientific community is aware that research will ultimately rely on computational infrastructures capable of managing large sets of heterogeneous data, i.e. clinical information, raw images and patient-specific mathematical models parameterized from these data. Table 1.1 presents examples of projects worldwide, which make use of these kind of approaches to conduct research in cardiovascular-related topics.

Over the years, hemodynamics modeling tools have been used to quantify blood pressure, blood velocity and derived quantities such as FFR and WSS, in patient-specific arterial districts obtained from medical images. Nevertheless, not all of such tools were able to perform studies with moderate -large patient samples. Projects listed in Table 1.1 succeeded in this aspect of research. Remarkably, a lot of effort regarding geometric analysis and computational simulations of blood flow in arteries focusing on cerebral aneurysms can be found in the literature. In turn, studies with very large dataset of the heart do not consider coronary vasculature. Up to date, publications in collaboration or sponsored by the HeartFlow private company, reported roughly 250 patients [186, 247, 251], which is unprecedented for studies involving patient-specific computational models of arteries. Indeed, other research groups working in the same area than HeartFlow, published studies with at most 120 patients [76, 256, 137]. The private nature of HeartFlow resulted in technical publications which cursorily treated the methodological aspects behind the research [328], because they oriented the reported results to potential customers (clinical community). One of the main reasons behind the difficulty in reproducibility, assessment and scrutiny of their computational methodology for FFR estimation is that technical references inside documents presenting results describe different methods for blood flow simulations [182, 180, 181], and it is not clear which kind of methodology they actually are using. Moreover, to the best of our knowledge, geometrical analyses of the coronary arterial tree in patients samples of moderate size, have not been reported yet.

---

[4]Variables or phenotypes, that can be measured directly from the patient clinical records, procedures or images.

Name and main focus	Brief description
The Virtual Physiological Human (VPH) initiative (1997) [12]. Integration of models of all physiological systems and parameterization using patient-specific data in order to make possible personalized, predictive and integrative medicine.	The first and most ambitious project that accounts for patient clinical data, medical images and mathematical models of different spatial and temporal complexities. It can be defined as a framework of methods and technologies [118] that aims to integrate all information available for each patient and use it to parameterize computer models capable of predicting how the health of that patient will evolve under certain conditions. Database size (in number of patient) is not available.
Computational hemodynamics laboratory @GMU (2002)[240, 1]. Patient-specific blood flow modeling in cerebral aneurysms.	It is a research group which develops methods and techniques to model intracranial aneurysmal flow from 3D medical images. The group aims to: Understand the mechanisms responsible for the development, enlargement and rupture of cerebral aneurysms; enhance aneurysm risk assessment and patient diagnosis; evaluate endovascular devices and procedures such as flow diversion for minimally invasive treatment of brain aneurysms. Database size (in number of patients) is not available, although largest reported study of the group used 210 patients [64].
AneuRisk (2005) [289, 5]. Cerebral arteries (aneurysm) morphology, blood fluid dynamics and biomechanical properties of the vascular wall.	This project investigates the role of vessel morphology, vascular wall mechanics and hemodynamics on the pathogenesis of cerebral aneurysms. Processing tools are based on the vascular modeling toolkit (vmtk) [11]. Database consists of 99 patients.
Graphical Interface for Medical Image Analysis and Simulation (GIMIAS) (2007) [193, 9]. Workflow-oriented environment addressing biomedical image processing and visualization of computer simulation results.	It is an open source framework that allows extension through problem-specific software plug-ins. It integrates contributions from the Physiome community, and was specialized for cardiac and cerebral aneurysm modeling [193, 344]. For such applications the database size (in number of patient) is not available.
HeartFlow (2007)[3]. HeartFlow is a cardiovascular diagnostics company developing solutions for the non-invasive diagnosis of coronary artery disease.	The company offers FFR_{CT}, a technique to estimate fractional flow reserve from (noninvasive) computed tomography scan data. Since 2007, it is the first company (to our knowledge) that was able to transfer standard hemodynamic models to commercial applications. Database size (in number of patient) is not available, although major clinical trials reported incremental patient samples of 103, 252, 254 patients [186, 247, 251].
ARCH (2008)[61, 6]. Patient-specific image-based computational modeling for improvement of short- and long-term outcome of vascular access in patients on hemodialysis therapy.	The main goal of the project is to predict arteriovenous fistula function for improvement of surgical planning and management on hemodialysis therapy. This is done through hemodynamics simulation (using reduce models, 0D-1D) on image-based patient-specific computational models of the blood vessels in the arm. Last reported study [61] was performed with 98 patients.
euHeart (2008) [315, 2]. Development of individualized, computer-based, human heart models.	Most of the clinical applications designed within euHeart are prototyped within the GIMIAS application framework environment. The project focused activities on specific cardiovascular diseases: congestive, arrhythmias and abnormal myocardial tissue perfusion. Computational models of the heart do not include arterial structures. Database size (in number of patients) is not available.
Cardiac atlas project (2009) [109, 8]. Mapping and analysis of cardiac morphometry, with particular regard to spatio-temporal characteristics of regional heart wall motion.	It seeks to establish a structural and functional atlas of the heart. The project is dedicated to combine cardiac modeling and biophysical analysis methods with a structural database for the comprehensive mapping of heart structure and function. Patient-specific heart models are obtained from magnetic resonance images (MRI). Database contain over 3000 patients.

Name and main focus	Brief description
The Brain Vasculature database, BraVa (2013)[358, 7]. Characterization of healthy human brain arterial arborizations with extracted morphological measurements.	The projects aims to provide extended morphometric information of the cerebral vasculature in healthy adults. No computational hemodynamics data are reported on the samples. Database contains 61 patients.

Table 1.1: Summary of projects, research initiatives and companies developing computational tools and performing research on mathematical models related to the cardiovascular system. Projects were selected for using moderate-large patient samples (in related scientific publications) and or taking into account computational infrastructures for the management of clinical and modeling data.

1.2 Objectives

This Thesis pursues two main goals: (i) to propose methods for the geometrical characterization and comparison of coronary arterial trees; and (ii) to develop a methodology for the computational estimation of FFR (FFR$_{CE}$). Naturally, the achievement of such objectives implies several activities, and also specific goals, which are listed here:

1. Definition of a computational framework to perform a systematic and comprehensive assessment of the geometric features of coronary arteries from CCTA data. The methodology should embrace medical image segmentation, arterial vessel representation, characterization and comparison, data storage and analysis.

2. Processing of a sufficiently large sample of patient that allows data exploration and pilot studies.

3. Extraction of morphometric information of the coronary arterial tree based on a comprehensive set of geometric descriptors.

4. Definition of new geometric descriptors for arterial structures.

5. Exploration of the hypothesis of geometric risk factors for CAD.

6. Investigation of the hypothesis of heritability of arterial geometry. This will require that patients in the sample to be family relative, particularly, siblings.

7. Demonstration of illustrative examples of relevant applications of the geometric characterization of the coronary arterial tree.

8. Completion of the computational infrastructure (item 1), for the generation and processing of computational meshes suitable for fluid dynamic simulations. This will require a patient sample with specific information, e.g. hemodynamic variables and invasive measurements of FFR.

9. Definition of a methodology to perform patient-specific simulations of hyperemic conditions for the FFR$_{CE}$.

10. Study of the impact of medical image modalities, i.e CCTA and IVUS, in the outcome of blood flow simulations, in the context of the FFR$_{CE}$.

11. Study of the accuracy of 1D models to mimic 3D simulations in patient-specific coronary models, targeting cheap simulations in the context of FFR$_{CE}$.

12. Exploration of the diagnostic capabilities of the FFR_{CE} using invasive measurements of FFR as gold standard.

1.3 Outline of this document

This Thesis is organized into two parts according to the list of goals and activities presented in the previous section. Chapter 2 describes the computational framework and modeling tools that are, up to some extent, shared by both parts of the Thesis. The methodology embraces medical image segmentation, arterial vessel representation, characterization and comparison, data storage and analysis.

Part I focuses on the geometric characterization and comparison of coronary arterial trees. Chapter 3 presents the complete set of geometric features used to described arterial structures. Such set includes a comprehensive group of features from the literature, and a set of so-called non-conventional features developed in this work. Chapter 4 introduces the methods for arterial comparison, summarizes statistical tools used in the rest of the thesis and also briefly describes classification methods used in the first part. Chapter 5 is a compilation of results, comprising morphometrics of the coronary vasculature, arterial geometric likelihood and heritability of features in siblings, geometric risk factors for CAD and some exploratory data analysis on fractal analysis and power laws. Chapter 6 summarizes the contribution, discusses the implications and outlines the limitations of Part I.

Part II centers on the application of computational fluid dynamics for the estimation of FFR. Chapter 7 provides a summary of coronary physiology and ischemia. It is intended for readers that are not familiar with the basic concepts of coronary circulation, atherosclerosis and hyperemia. Chapter 8 centers on the FFR index, presenting the basic concepts, its derivation and limitations. A bibliographic summary of relevant clinical trails that explains why it is considered the gold standard for detecting risk of ischemia is presented. Then, the basic concepts and requirements for the FFR_{CE} are presented, followed by a critical review of the literature. Chapter 9 focuses on the modeling methodology. Specifically, the construction of patient-specific computational domains for fluid dynamic simulations. Then, the mathematical and numerical methods are detailed. The chapter concludes with the definition of patient-specific hemodynamic parameters and hypoteses to determine flow distribution, which defines boundary conditions. Chapter 10 is a compilation of results, starting with computational tests to ensure that computer simulations introduce minimum numerical error in the calculation of hemodynamic variables, e.g. FFR and WSS. The impact of image modality, i.e. CCTA and IVUS, on the outcomes of blood flow simulations is studied in detail. Then, a comparison between 3D and 1D models to perform numerical simulations in the coronary arteries is presented. The chapter ends by presenting the diagnostic capabilities of the proposed methodologies, comparing with invasive FFR measurements. Chapter 11 summarizes the contribution, discusses the implications and outlines the limitations of Part II.

1.4 Contributions

During the preparation of this Thesis, relevant results were compiled in 6 manuscripts and published in indexed journals. Preliminary results were presented in the form of 1 poster, 2 extended abstracts and 3 articles in national and international conferences.

Regarding Part I, methodological details and early preliminary results on the processing pipeline and geometrical characterization of the coronary arterial tree were presented at the *XXXIV Congresso da Sociedade Brasileira de Computação* [52] and the *XXXVI Iberian Latin-American Congress on Computational Methods in Engineering* [51]. The

final processing methodology presented in Chapters 2 and 4, together with the results presented Chapter 5, Sections 5.2, 5.4, regarding the geometric description and comparison mechanisms of coronary arteries in the patient sampling of siblings, were published in the *International Journal for Numerical Methods in Biomedical Engendering* (IJNMBE) [53]. The results of the association of geometric features and lesion presence in the LAD, see Chapter 5, Section 5.6, were published in the Journal of *Biomedical Signal Processing and Control* (JBSPC) [54]. Regarding the new set of non-conventional geometric descriptors proposed in Chapter 3 and tested in Chapter 5, Section 5.7, an article was submitted to JBSPC and is currently under review [57]. The study of heritability of geometric features in siblings, Chapter 5, Section 5.5, was published in the *International Journal of Cardiology* (IJC) [56].

The methodology to describe coronary arteries through geometric features is currently being used to characterize arterial models constructed from IVUS images. Although such study was not included in this Thesis, preliminary results were published in the *Revista Brasileira de Cardiologia Invasiva* [41] and were presented at the *Congresso da Sociedade Brasileira de Hemodinâmica e Cardiologia Intervencional* [38] and at the *V Congreso de Matemática Aplicada, Computacional e Industrial* [325].

Regarding Part II, methodological details on how to perform blood flow simulations with a novel boundary condition in the context of computational estimation of FFR using CCTA- and IVUS-derived models, see Chapter 9, and results on the impact of the image modality on the simulations, see Chapter 10, Section 10.5, were published in the *Journal of Biomechanics* (JBM) [55], and presented in the *Journal of the American College of Cardiology* (JACC) [39]. Although not presented in the Thesis, a comparison between CCTA- and IVUS-derived models using geometric features was explored, and preliminary results presented in the JACC [40].

Finally, the author co-authored a work presenting hybrid element-based approximation for the Navier–Stokes equations in pipe-like domains, published in IJNMBE [211]. Such numerical methods could be an intermediate alternative (between 3D and 1D) to perform blood flow simulations and estimate FFR and other relevant hemodynamic variables.

Chapter 2

From medical images to arterial models

"Winter is coming."

George R.R. Martin, *Game of Thrones*

The impact of computer systems in human society is undeniable; information and connectivity are redefining many aspects of our daily life. Particularly, clinical practice has benefited from many technological developments, i.e. digitalization of clinical history, computer aided equipment for image acquisition and processing techniques. In this sense, computational models bring additional and valuable information into the problem, since through mathematical equations and physical principles it is possible to predict quantitatively and qualitatively the behavior of variables of interests whose measurement is quite difficult, expensive, or even impossible because of technical or ethical aspects. Recently, such computational models of physiological systems have gained attention, because the potential application for improving diagnostic and prognostic accuracy, as well as they applicability for risk factor identification. In this context, three major stages can be identified: (i) basic research in mathematical models, (ii) clinical trials with a significant amount of patients to test medical hypothesis, and (iii) development of specialized software/hardware to apply such models in daily clinical practice. In stages (i-ii) the computational infrastructure is key. The present thesis aims to contribute with the development of models (stage (i)), and with data analysis to test medical hypothesis (stage (ii)). Furthermore, the work is structured within a computational framework, flexible enough to account for future modifications that would allow to use the tools here presented in clinical routine, stage (iii).

The computational approach used in this thesis is divided into two parts and covers: image segmentation, arterial representations (geometric models), characterization and comparison, hemodynamics simulations and data analysis. All major processing steps, involving the two parts of the thesis, are presented in this chapter. This chapter overviews the common methodological aspects employed all along the thesis.

2.1 Methodology overview

Problems covered in both parts of this work share the first stages of the workflows illustrated in Figure 2.1. The proposed processing pipelines for the geometric and functional analysis of coronary circulation consist of five stages:

1. *Input of medical data*, which includes patient, study and imaging modalities (e.g. CCTA, IVUS, AX, etc), as well as complementary information (see Section 2.2.1

9

for details on the medical image modalities used). For the FFR study, additional information containing specific data associated to the invasive procedure is recorded.

2. *Image processing*, which consists of the image segmentation pipeline (see Section 2.2.3), and whose standard output is a triangulated surface mesh representing the arterial lumen. This stage also accounts for the segmentation/estimation of other anatomical structures such as myocardial surface and volume (see Section 2.2.2).

3. *Arterial network modeling*, post-processing of the surface meshes results in the representation of vessels through their centerlines, also including arterial labeling and branching patterns (see Section 2.3). Note that multiple models may be generated from the same initial mesh, e.g. through normalization, as explained in forthcoming sections. For the FFR study, surface meshes must be further processed to obtain CFD-compatible[1] models (see Section 2.3.1).

4. The fourth step depends on the problem under study,

   - *Geometrical and anatomical characterization* of centerlines is performed, producing a variety of geometric descriptors (see Part I, Chapter 3) that are stored into a database.

   - *Hemodynamics simulations* using patient-specific boundary conditions are performed, and FFR is estimated from numerical results (see Part II, Chapter 9).

5. *Data analysis* is performed over application dependent data, see Part I, Chapter 5 for the geometric analysis and Part II, Chapter 10 for FFR results.

All image processing stages, as well as meshing and centerline processing, are performed using vmtk [11], ImageLab [4] and HeMoLab [4] softwares.

2.2 Image acquisition and processing

Tasks associated to the second step of the workflow in Figure 2.1a are detailed in this section. Specifically, we start by describing the image techniques and acquisition protocols used, then we explain how image-based measurements are estimated. The section ends by depicting the arterial segmentation pipeline employed.

2.2.1 Medical images

Due to the low risk (noninvasive) nature of the acquisition procedure, CCTA has been adopted as a tool for CAD detection and diagnosis, [323, 67]. CCTA images may have a resolution up to 0.23 mm, which is enough for visualization and measurement of arterial diseases on the main arteries of the heart. On the other hand, typical CCTA exams have very low or no time-related information, they comprise one or two snapshots of the cardiac structures at diastolic phase.

Alternative heart imaging techniques are Magnetic Resonance Image (MRI), coronary angiography (AX) and Intra-Vascular UltraSound (IVUS), among others. All three can provide time-dependent data. Nevertheless, MRI has poor spatial resolution which makes difficult to perform arterial segmentation. Although AX has better spatial resolution than CCTA, images are two-dimensional projections which lack from accurate three-dimensional modeling of arterial structures, and, furthermore, it is an invasive procedure. IVUS also needs catheterization, but can provide valuable information about arterial tissue

---

[1]CFD-compatibility must be understood in the sense of adequate triangular (surface) and tetrahedral (volume) meshes to obtain accurate results from numerical simulations.

(a)

(b)
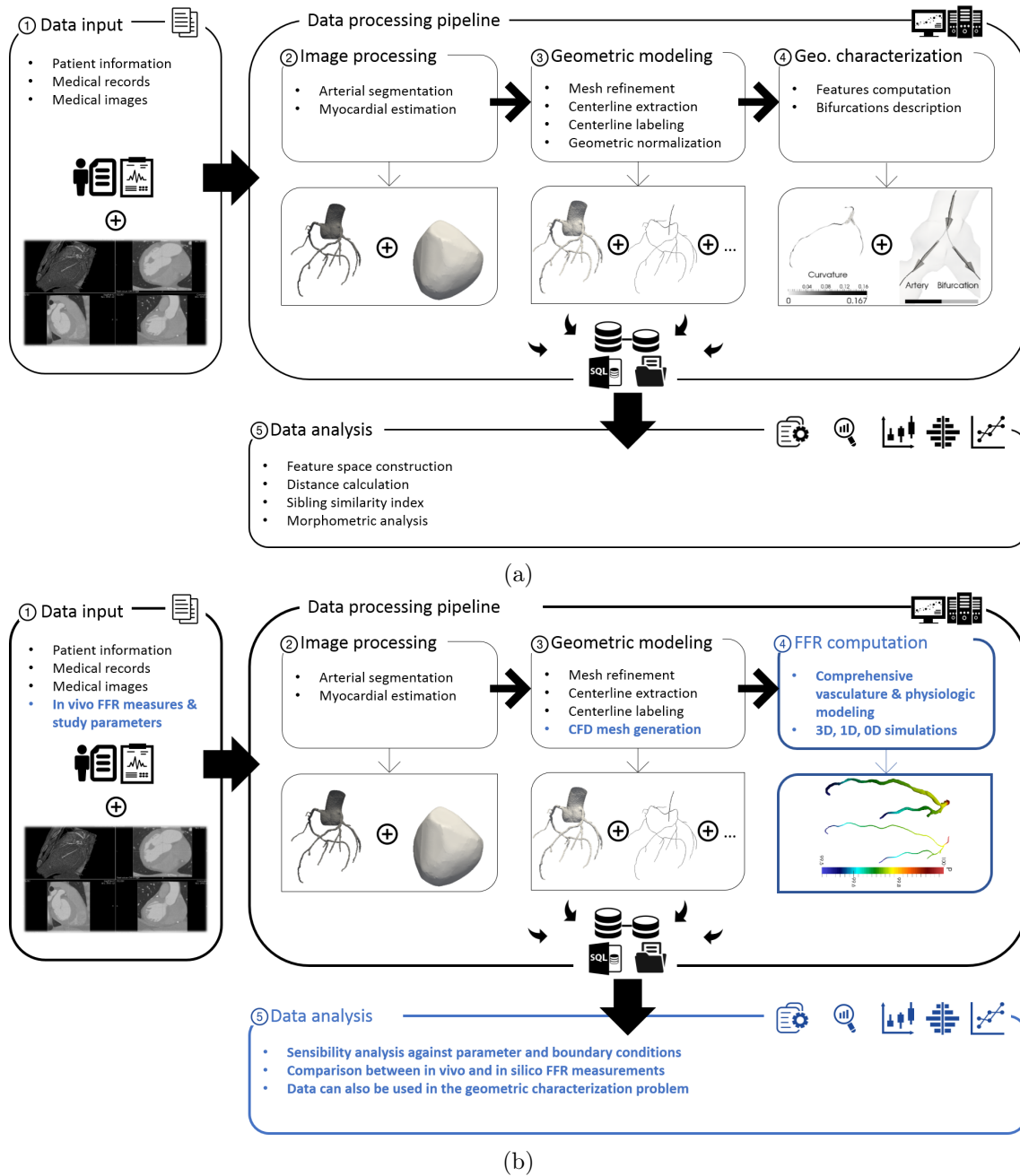
Figure 2.1: Overview of the workflows proposed for the geometric (top, Part I), and functional (bottom, Part II), analysis of the coronary circulation.

from inside the artery, with tremendous spatial resolution. Among the principal drawbacks are the high noise, loss of three-dimensional spatial orientation and the small number of arteries that can be acquired in a single procedure. Nevertheless, inPart II, Chapter 10 geometric models of coronary arteries imaged by means of IVUS+AX techniques are used to study the impact of geometry and branching patterns in hemodynamic simulations.

In this work, CCTA images were acquired following standard clinical procedures, ensuring patient heart rate below 65 bpm. Acquisitions were ECG-triggered prospectively at 75% of the cardiac cycle to keep the lowest possible radiation dose, and artifacts.

2.2.2 Myocardial volume estimation

Myocardial volume can be considered important towards the estimation of oxygen demand and, therefore, as an indirect measurement of blood flow requirement. Myocardial information, such us volume and area of external surface of the cardiac muscle, could be used for patient-specific parametrization in hemodynamic simulations (see Part II, Chapter 7). Furthermore, myocardial area can be used to perform a geometrical normalization of the arterial network, as explained in Section 2.3.

The myocardium is approximated through the convex hull (C) computed from a cloud of points manually selected over the medical image. This approach is valid for the computation of the myocardial external surface area, as it can be considered convex when it is relaxed, during diastole (when CCTA images are acquired). Furthermore, ventricular cavities can also be roughly approximated from the corresponding C, which are also obtained from the cloud of points defining each cavity. The C is computed using standard algorithms available in the VTK library [298]. Subtracting the myocardial and cavities volumes, the myocardial mass can be estimated. Figure 2.2 illustrates this procedure.

(a)   (b)   (c)
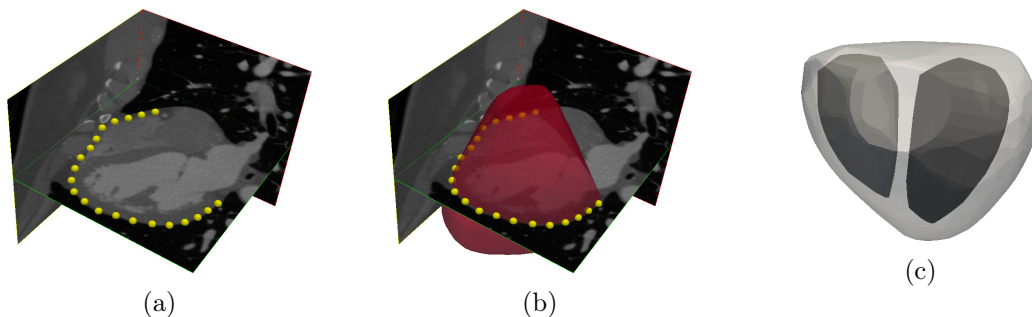
Figure 2.2: Illustration of the procedure to estimate myocardial and ventricular external surfaces. Panel (a) shows a set o points along the perimeter of the myocardium on a coronal plane, which were manually selected. By performing point specification in a small number of planes, the myocardial external surface is approximated. Panel (b) presents the convex hull of a point set. Panel (c) presents the resulting myocardial and ventricular external surfaces.

2.2.3 Arterial vessel segmentation

Segmentation of arterial vessels still remains as a challenging problem, strongly dependent on image modality and acquisition quality, for which several techniques were proposed over the years, see [198] for a comprehensive review. We adopted a methodology based on [21], which was refined and tuned to be used for the coronary arterial network. The proposed segmentation pipeline is based on implicit deformable models, which in the context of this work means a deformable surface $S(t) : \mathbb{R}^2 \times \mathbb{R}^+ \to \mathbb{R}^3$ described through the iso surface of the scalar function $\phi(\mathbf{x}, t) : \mathbb{R}^3 \times \mathbb{R}^+ \to \mathbb{R}$, such that $S(t) = \{\mathbf{x} \in \mathbb{R}^3, \phi(\mathbf{x}, t) = 0\}$. The technique used to calculate the temporal evolution of $S(t)$ is known as Level-Set, and the model for this evolution is described by a minimization process of a cost functional for which the associated partial differential equation is [21]

$$\frac{\partial \phi}{\partial t} = -w_p P(\mathbf{x})|\nabla \phi| + 2w_k K(\mathbf{x})\kappa(\mathbf{x})|\nabla \phi| - w_a \nabla A(\mathbf{x}) \cdot \nabla \phi, \qquad (2.2.1)$$

where the first term on the right-hand side represents surface inflation with a position-dependent speed given by $P(\mathbf{x})$, which can depend on image features or on shape constraints; the second term represents a smoothness constraint on the surface, being $\kappa(\mathbf{x}) =$

div $\frac{\nabla\phi}{|\nabla\phi|}$ the mean curvature of the zero-level surface affected by factor $K(\mathbf{x})$; and the last term represents advection of the surface by means of the given vector field $\nabla A(\mathbf{x})$. Weights w_p, w_k and w_a control the influence of each term in the pseudo-temporal surface evolution.

The Level-Set equation (2.2.1) is solved using the Insight ToolKit (ITK) [10] [2]. The current implementation uses spatial modifiers (P, K, A) based on the image gradient, hereafter called featured image (I_f). Then, by definition, I_f goes to zero in homogeneous regions of the image and increases its value near image boundaries, therefore we define

$$P(\mathbf{x}) = \frac{1}{1 + I_f(\mathbf{x})} = K(\mathbf{x}) = -A(\mathbf{x}), \qquad (2.2.2)$$

implying that the propagation term goes to zero near boundaries, the smoothing of the surface due to curvature increases in low gradient regions, and the potential field is such that convection of the iso surface is forced towards the boundaries.

In order to solve Equation (2.2.1), an initial solution must be given, which is obtained by the following semi-automatic procedure: For each arterial segment, (i) the user manually places two seeds, one at the beginning and the other at the end of the segment; (ii) the colliding front method [21] is used to obtain an initial segmentation of the vessel, which is a binary image identifying the arterial lumen from the rest of the domain; (iii) the output of the colliding front procedure is used as initial guess for the solution of the Level-Set equation.

The complete segmentation pipeline is illustrated in Figure 2.3a and is executed by performing five operations:

1. Extraction of the so-called Region Of Interest (ROI).

2. Standard curvature anisotropic filtering, as in [352], which is needed when the images present high levels of noise. Typical parameters values are 10 iteration, a time step of 0.0625 and conductance of 4.

3. Interactive initialization of individual arteries using colliding fronts [21].

4. Numerical approximation of the Level-Set equation. This needs the specification of four parameters. For the patients analyzed in Chapter 5 the mean and standard deviation of parameters used were: $w_p = 0.64 \pm 0.24$, $w_k = 0.59 \pm 0.20$, $w_a = 0.97 \pm 0.16$ and the number of iterations to solve the equation was 108 ± 46. These parameters depend on image quality and arterial characteristics. For example, noisy images are better segmented with larger values of w_k and more iterations, while small arteries are better defined with higher values of w_p. Arterial regions with conventional stents are challenging, and require more user interaction during initialization and smaller values of w_p.

5. Construction of surface mesh made of triangles using the marching cubes method [202].

Figure 2.3b features different coronary arterial networks extracted from patient-specific images using the present segmentation procedure. As a general rule, the aortic root and all visible arteries are segmented. Depending on image quality and vascular anatomy the number of arterial structures varies among medical images. For the patients analyzed in Section 5, the mean number of arteries for the coronary tree was 19 ± 6.

2.3 Geometric representation of arterial networks

Given a raw surface obtained from the segmentation process, two types of three-dimensional models can be generated: (a) high-quality triangular meshes suitable for en-

---

[2]The implementation use homogeneous Neumann boundary conditions.

(a)

(b)
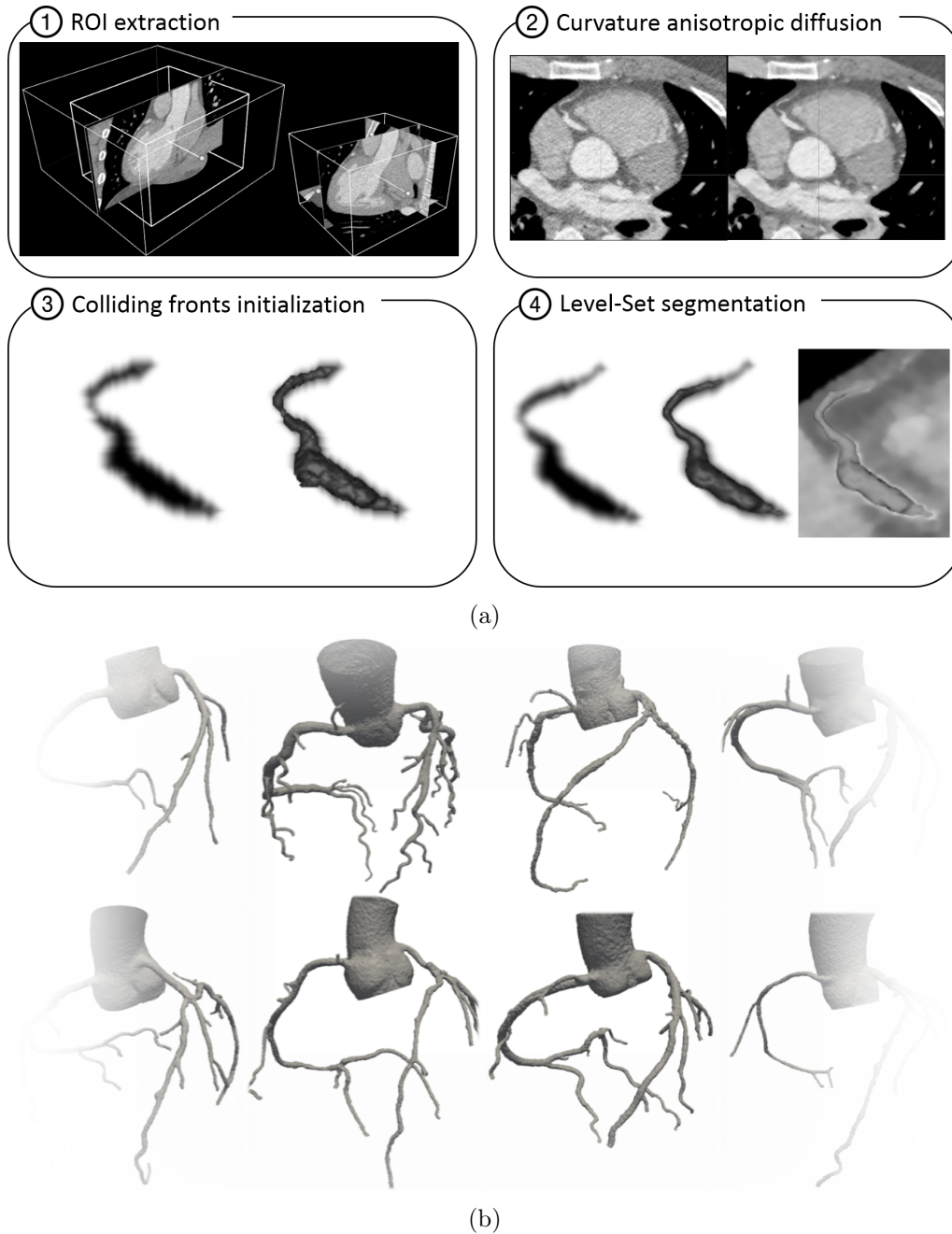
Figure 2.3: Panel (a) Illustration of the image segmentation pipeline: (1) extraction of the region of interest; (2) curvature anisotropic diffusion filtering to smooth out image noise; (3) colliding front method with the resulting binary scalar field and associated implicit surface for the proximal portion of a right coronary artery; (4) the Level-Set scalar field and zero-level surface. Panel (b) presents examples of coronary tree segmentations.

closing a three-dimensional volume in which hemodynamic simulations are to be performed (see Part II, Chapter 9) and (b) centerline models used for geometric characterization as well as for simplified 1D-0D (or 1D$^+$-0D, see [44, 211]) blood flow simulations (see Part II, Chapter 9). In this section, we present the pipeline used to construct these two classes of models.

2.3.1 Three-dimensional mesh processing

The image segmentation stage delivers a closed triangular surface, this raw geometry is the input of a processing pipeline that aims at improving mesh quality. The complete pipeline is detailed in Appendix A, and is briefly overviewed here.

- The raw triangulation is smoothed and opened[3] at terminal locations (outlets) and at the aortic root (inlet).

  - A centerline is computed using techniques and tools described in [20]. Then, it is used for the geometric characterization (see Section 2.3.2), and for dimensionally-reduced blood flow simulations see Part II, Chapter 9).

- Such surface with open inlet/outlets is re-meshed to improve triangulation quality, producing a refined contour to define the arterial lumen.

  - This improved surface encloses a volume in space, which is tetrahedralized to produce finite element volume meshes to perform CFD simulations, see Part II, Chapters 9.

2.3.2 Centerline model

Centerlines are widely accepted representations of arterial networks [252, 224, 372, 263, 48, 358, 241], because they retain most of the geometric characteristics of arteries in a more compact and simpler structure. Three-dimensional centerlines are represented by polylines with point-wise information (e.g. lumen radius for each point of the centerline). Furthermore, centerlines admit classic differential geometry analysis to compute, for example, point-wise curvature and torsion. Figure 2.4 illustrates how centerline geometric models are obtained
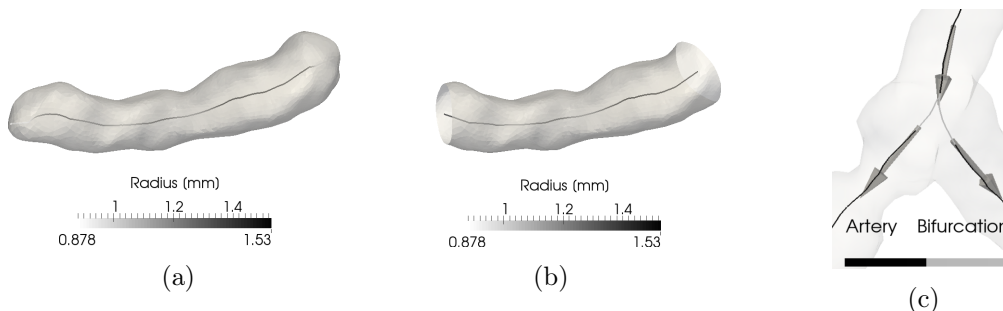
Figure 2.4: Illustration of the centerline extraction procedure. Panel (a) shows the raw surface of an arterial segment and the corresponding auxiliary centerline; Panel (b) shows the final surface with inlet and outlet and the resulting centerline model. Panel (c) shows a branching region, light gray centerline regions represent the bifurcation mask, the bifurcation in/out vectors are also shown.

---

[3]Using the HeMoLab [4] software.

Stenosis grade[*]	Tissue type	Lesion position
Normal	Soft tissue	Proximal
Minimal: $<25\%$	Calcification	Middle
Mild: 25% - 49%	Mixed	Distal
Moderate: 50% - 69%		
Severe: 70% - 99%		
Occluded		

Table 2.1: Parameters used by physicians for the characterization of stenotic lesions. [*]Stenosis grade is measured as the percentage of reduced maximal lumen diameter.

2.3.3 Arterial labeling

Labeling starts with detection of arterial tracks, which are polyline elements among branching points. Then, these arterial segments are manually labeled by a cardiologist using the HeMoLab software, and vessels with the same label are merged. Labeling is key for correct data storage, statistical analysis and comparison of arterial structures. Labeling is performed following standard guidelines [273] with some extra considerations presented in Appendix B.

2.3.4 Arterial lesion

Arterial lesion specification is also performed by physicians. Lesions are characterized according to [273] using a tuple of three variables, namely: stenosis grade, tissue type and lesion position, as seen in Table 2.1.

2.3.5 Bifurcation description

Bifurcation regions over the centerline are detected and masked using the procedure explained in [263]. Bifurcation vectors are then computed for the parent artery (in-vector) and the branches (out-vectors), as seen in Figure 2.4c. The out-vectors are computed by taking as origin the point at which the bifurcation mask ends, and as end point the weighted mean of N successive points[4], where weights are computed as $(N+1-i)^{-1}$, being $i \in [1, N]$ the index of the point. On the other hand, the in-vector is computed taking as end point the beginning of the bifurcation mask and as origin the n-th point over the parent centerline backwards from the end point.

2.3.6 Geometric normalization

Geometric normalization of centerlines is performed by affine transformations of the centerline geometry and associated scaling of the point-wise radii. The proposed methodology accounts for the computation and storage of different kinds of geometric normalizations. In the clinical literature normalization is commonly used, for example [94] studied the anatomy of coronary arteries and performed statistical analysis normalizing measurements by body surface area. The main idea behind all kind of normalization is that inter-patient variability, due to intrinsic difference in the anatomic size of hearts, is ruled out. Regarding centerline analysis, other normalization/registration techniques were proposed, see [290] and reference therein. In that work a warping-function procedure is

---

[4]In this work, $N = 10$, if the arterial segment has less than 10 points after bifurcation mask ended, the remaining points are extrapolated in the direction defined by the last two points.

performed for a single artery per patient, overcoming inter-patient variability in anatomic size.

In this work, we propose a scaling factor to perform normalization such that all patients have coronary trees centerlines enclosing a myocardium with the same surface area (denoted by $\mathcal{S}_{\mathrm{myo}}$), that is, a scaling of coronary geometry to perfuse a heart with the same size. This operation involves the computation of a dimensionless scale factor sf_{myo}, which multiplies centerline coordinates and radii. Particularly, the pre-defined myocardium area is $\mathcal{S}_{\mathrm{myo}} = 40000\mathrm{mm}^2$, and sf_{myo} has a mean value of 1.148 ± 0.0936 in our patient sample.

In this work, normalized geometries are only taken into consideration when assessing geometric similarity in siblings. In turn, statistics of the arterial morphometry are computed using raw geometries (see Part I, Chapter 5).

2.3.7 Geometric characterization

Centerlines model are characterized using a set of geometric descriptors. In this work, several point-wise and arterial-wide features are used. Several descriptors have already been described in the literature. Nonetheless, a novel set of descriptors are proposed based on thermodynamic concepts (see Part I, Chapters 3 and 5).

2.3.8 Database description

Adequate storage of input and generated data throughout the entire workflow is a major concern to the framework. Typical data analysis requires a wide range of information, from patient and medical input data to anatomical and geometric features generated during the processing pipeline. The heterogeneity of data types poses a challenge in terms of storage mechanisms. Furthermore, data mining and quantitative analysis typically require extraction of large amount of data from different sets of subjects satisfying specific conditions on patient, clinical and generated data, i.e. age, gender, presence of stenosis, arterial features, etc. These query requirements are better addressed by conventional relational databases, which in addition provide out of the box scalability and ease of access from web or standalone applications. Besides, current database engines can be extended to support storage and query on user defined data types. However our current implementation also stores sophisticated bulk data, i.e. raw and segmented medical images, three-dimensional arterial/myocardial meshes and centerlines (polylines with bifurcation and point-wise information) using standard DICOM and VTK file formats in a human-readable folder hierarchy defined by databases structure and identifiers. This allows storage of path as conventional strings in the database, ensuring direct access through queries, and facilitating usage of data from external applications for rapid prototyping and testing of new functionalities.

Data mining and analysis, which is the last stage in the workflow illustrated in Figure 2.1, is currently performed in MATLAB©, using a data warehouse constructed from the database.

Figure 2.5 presents a reduced version of our database Entity-Relationship Diagram (ERD) covering the following major entities.

- **Patient:** Contains invariant patient information like gender and date of birth.

- **FamilyRelatives:** Identifies familial aggregation between patients, i.e. parents, siblings, and so on.

- **MedicalStudy:** Contains medical data obtained during the clinical procedure that may change over time. Typical information agglomerated in this entity include the date of the study, copies of clinical reports, records of arterial pressure, weight, height, etc.

- **MedicalImage:** Depending on the imaging procedure and modality, more than one image may be associated to the procedure. Bulk data is stored on file hierarchy while information about quality, noise, artifacts and spatial resolution are stored on the database.

- **ImageSegmentation:** Abstract representation of the segmentation procedure, contains basic information about the method and parameters, the most relevant information is the path to the segmented image. In addition, a segmentation can represent arterial structures, myocardial, or any other physiological structure of interest.

- **SurfaceMesh** Different surface meshes may be generated from one segmentation. In order to keep track of mesh-precessing operation (resulting in meshes used for hemodynamics or geometric characterization), this entity allows a self-relations.

- **CenterlineModel** Each surface mesh may have various centerlines, e.g. given by different normalization procedures. Information about normalization and paths to the centerlines are kept in this entity.

- **ArterialSegment** A coronary tree is conformed of various arterial segment, each one is kept as a separate record identified by corresponding arterial labels.

- **ArterialFeature** geometric descriptors, stenosis and anatomical features of each artery are kept in series of tables, here grouped in an abstract entity for simplicity.

- **HeartModel** This entity accounts for patient-specific heart models, currently only the approximated surface for myocardial surfaces and ventricular cavities are considered, with corresponding surface and volumes.

- **HemodynamicModels** Computational fluid dynamics for (3|1|0)D models derived from surface meshes or centerlines are referenced in tables agglomerated in this entity. Models are associated to different simulation outcomes depending on physiological scenarios and definition of boundary conditions.

Note that the proposed schema allows high detailed querying over the patient populations, e.g. retrieving data of patients with specific arterial morphology and distribution, which empowers data mining and analysis. In addition, the relational model provides a natural mechanism for tracking down patient information, clinical data and model derived quantities.
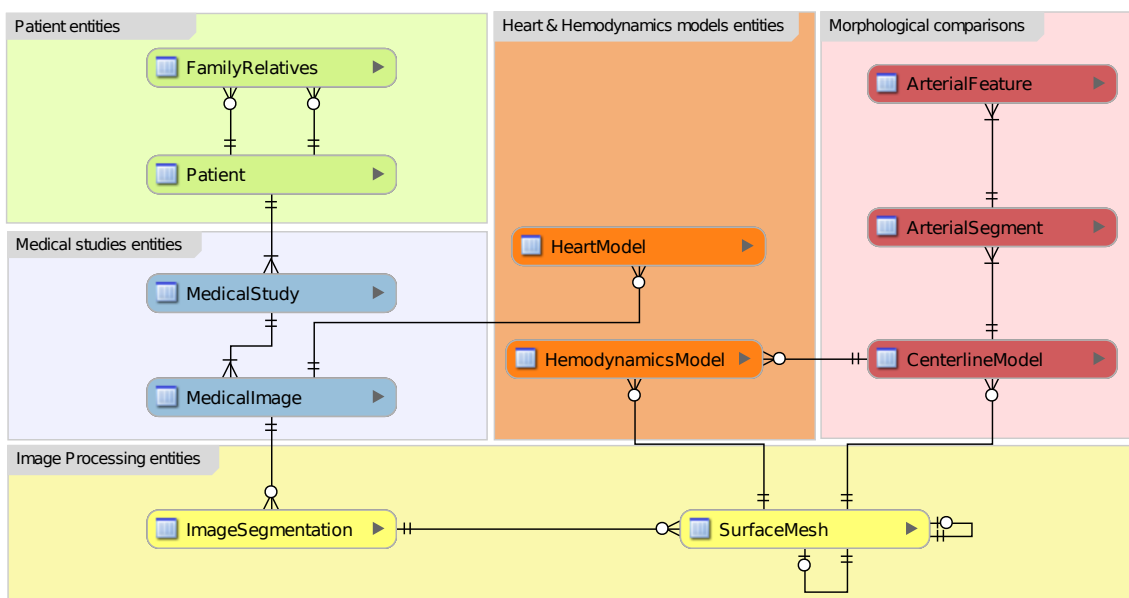
Figure 2.5: Illustration of the database schema.

Part I

Geometric analysis of coronary arterial trees

Chapter 3

Arterial geometry characterization

"He prescribed Euclidean geometry, followed by a dose of trigonometry and algebra. That should cure anyone, they both thought, from having too many artistic or romantic passions."

Walter Isaacson, *The Innovators: How a Group of Inventors, Hackers, Geniuses, and Geeks Created the Digital Revolution*

Ex-vivo anatomical characterization of coronary arterial trees from basic variables like vessel length and lumen radius was explored by the medical community elsewhere [94, 31]. Advances on medical imaging and processing tools allow further characterization from in-vivo data extracted from medical images. For instance, geometric characterization of healthy left anterior descending (LAD) and right coronary (RCA) arteries based on curvature, torsion and tortuosity was performed using AX images in [372]. Nevertheless, using AX images implies dealing with an invasive medical procedure and with a rather incomplete anatomic characterization. In contrast, as seen in Chapter 2, CCTA images provide a complete overview of the coronary arterial network with a moderate degree of invasiveness. To the best of our knowledge, complete coronary trees have not been geometrically characterized from in-vivo images. Several studies have employed geometric descriptors to characterize arterial centerlines from different parts of the body: Reference [252] emphasized the limitation of quantifying arterial geometry from planar projections and proposed a set of geometric parameters describing arterial branch origin, trajectory, and vessel curvature in 3D space, methods where tested using arteries in the abdominal aorta region. Reference [224] proposed two mathematical descriptors, namely torsion and curvature energy, to characterize the internal carotid artery shape. Reference [263] presented a new methodology for bifurcation patterns characterization and a set of computational tools for the geometric description of vascular structures based on classical differential geometry analysis, focusing on cerebral arteries and aneurysms. Reference [48] explored the characterization and classification of carotid arteries, using a set of standard features, i.e. length, tortuosity, radius, curvature, torsion, etc. Such work also made use of the large deformation diffeomorphic metric curve mapping (LDDMCM) [125], to provide correspondences between centerlines and to define a metric in shape space. Reference [358] performed statistical analysis of morphometric variables (e.g. size, distances, angles and branching structure) of the brain arterial vasculature; it was extended and complemented by [241] by describing the population-averaged shape and geographic distribution of the brain arterial trees based on a probabilistic vascular atlas.

As described in Chapter 2, centerline models of vascular trees are labeled, lesions are identified, and bifurcations are characterized by vectors and angles. These descriptors are invariant to rigid transformations of the geometry. As commented in Section 2.3.6,

normalization of the models are based on rigid transformations. Although the infrastructure employed in this work supports storing all kind of normalizations, we only used normalization by myocardial surface, and use it to test similarity in Chapter 5. When performing all other tests in Chapter 5 the raw geometric models are used. All these study cases are based on the geometric descriptors outlined in this chapter.

3.1 Conventional geometric features

In this work a collection of geometric and anatomical descriptors was selected among the wide variety of features available in the literature. Table 3.1 presents a formal definition and descriptions of the complete *conventional* set of features used in this work for any given artery denoted by A.

Feature	Definition
Parent: The label of the artery that gives rise to A according to the network topology. In some pathological cases, the coronary tree deviates from its normal topology, for example the left circumflex (LCx) and the left anterior descending (LAD) may branch directly from the aorta (Ao) in patients with absence of left main artery (LM).	$\text{parent}(A)$
Branch count: The number of arteries (in the centerline model) branching from A.	Υ
Length: The arc length of the curve in 3D space described by A.	ℓ
Tortuosity: [263] The relative increment in the length of a curve deviating from a straight line. Where d is the euclidean distance between the starting and ending points of A. The tortuosity defined in (3.1.1) has a minimum value (zero) when the vessel is straight, and increases as A is more tortuous.	$\chi = \dfrac{\ell}{d} - 1 \qquad (3.1.1)$
Radius: The arterial lumen radius, which is a point-wise variable defined along the *centerline abscissa* $s \in [0, \ell]$, the *minimum* (r_m), *maximum* (r_M) and *mean* ($\bar{r}$) values are then computed. The arterial radius is computed as the radius of the circumscribed sphere at s, which is the biggest sphere at the associated cross-section of the artery.	$r(s)$
Curvature: [263] It measures the deviation of the curve from a straight line (zero curvature). The *Frenet–Serret* theory of differential geometry provides the standard definition. Where $\mathbf{c}(s)$ is the centerline curve parametrized with the *curvilinear abscissa*, and $(\cdot)'$ indicates the derivative operator. As κ is defined for each point along the centerline, the *minimum* (κ_m), *maximum* (κ_M), *mean* ($\bar{\kappa}$) and *total* (κ_T, integral of the curvature over the centerline) values are computed.	$\kappa(s) = \dfrac{|\mathbf{c}'(s) \times \mathbf{c}''(s)|}{|\mathbf{c}'(s)|^3} \quad (3.1.2)$
Torsion: [263] It measures the curve local deviation from lying on the osculating plane, or equivalently, how sharply the line is twisting in space. The standard definition of torsion is analogous to curvature, the torsion is defined for each point along the centerline, therefore the *minimum* (τ_m), *maximum* (τ_M), *mean* ($\bar{\tau}$) and *total* (τ_T) values are computed.	$\tau(s) = \dfrac{|(\mathbf{c}'(s) \times \mathbf{c}''(s)) \cdot \mathbf{c}'''(s)|}{|\mathbf{c}'(s) \times \mathbf{c}''(s)|^2}$ $(3.1.3)$
Combined curvature: [252] It accounts for curvature and torsion at each point of the curve. As in the case of other point-wise defined variables, the *minimum* (ζ_m), *maximum* (ζ_M), *mean* ($\bar{\zeta}$) and *total* (ζ_T) values are computed.	$\zeta(s) = \sqrt{\kappa(s)^2 + \tau(s)^2} \quad (3.1.4)$
Aspect ratio: [241] It is the ratio between the arterial *length* and the *mean radius*.	$\Lambda_r = \dfrac{\ell}{\bar{r}} \qquad (3.1.5)$
Curvature ratio: [48] It is the dimensionless product of vessel *radius* with *curvature*, where N is the number of points in the centerlines that represents the artery.	$\Lambda_\kappa = \dfrac{1}{N} \sum_{i=1}^{N} \kappa_i^2 r_i^2 \qquad (3.1.6)$

Feature	Definition
Torsion ratio: [48] It is defined as the mean product between torsion and radius along the centerline.	$$\Lambda_\tau = \frac{1}{N}\sum_{i=1}^{N}\tau_i^2 r_i^2 \qquad (3.1.7)$$
Bending energy: [224] It is defined as the energy needed to bend a straight line into its curved shape. It corresponds to the average value of the square *curvature* scaled by the total arc *length* of the centerline under analysis. The ℓ^2 factor guarantees scale invariance (i.e., any circle will always have the same energy value), which is required for comparisons between curves with different lengths.	$$\xi_\kappa = \frac{\ell^2}{N}\sum_{i=1}^{N}\kappa_i^2 \qquad (3.1.8)$$
Twisting energy: [224] It is the energy needed to twist an straight line into its curved shape also in dimensionless form.	$$\xi_\tau = \frac{\ell^2}{N}\sum_{i=1}^{N}\tau_i^2 \qquad (3.1.9)$$
Fractal dimension: [358] It is defined as the slope of the linear regression obtained from the log-log scatter plot of *length* vs. euclidean distance, moving from the second to the last point along the centerline.	ϱ
Rising angle: It is the angle between the artery A and its parent. It is computed over the plane formed by the bifurcation vectors. Where $\mathbf{v}$ is the parent artery vector indicating the direction towards the branch and $\mathbf{w}$ the vector indicating the branching direction of A.	$\alpha = \arccos(\mathbf{v}\cdot\mathbf{w}) \qquad (3.1.10)$
Offspring mean raising angle: Defined as the mean of α over the offspring of A.	β
Lesions count: A list of arterial lesions defined by variables described in Table 2.1 is produced for each arterial segment, based on clinical data. From this list, the quantity of lesions is then obtained.	η

Table 3.1: List of standard geometrical and morphological descriptors, together with the mathematical definition and notation, as well as a description and a bibliographic reference that reports previous usage of the feature in the related literature.

It is worth noting that computation of curvature and torsion parameters is performed using finite differences over a smoothed centerline which is constructed using a Laplacian filter to get rid of spurious high-frequency noise, as detailed in [263]. This procedure is only employed for the computation of derivatives with respect to the parametric coordinate. Alternatively, high-order continuous representation of centerlines could be achieved using *free-knots regression splines* [291], which allows analytic computation of derivatives.

3.2 Non-conventional geometric features

The so called non-conventional geometric descriptors are a new set of arterial features, designed and developed in this work. These features are demonstrated to be useful for RCA shape identification and LAD healthy/diseased classification, as shown in Chapter 5.

3.2.1 Average distal curvature

Although mean curvature of arteries is commonly used in the literature [372], it is usually computed using the total length of the arterial centerline. Medical literature usually establishes criterion for discriminating proximal, middle and distal arterial segments of the main coronary arteries based on branching points of specific vessels. Note that anatomical variability may introduce an observer bias on the identification of such dividing points. However, this division facilitates anatomical descriptions and simple measurements from

medical images (such as AX or CCTA) or ex-vivo dissections without quantitative models of vessels, e.g. lesion location or arterial radius at the beginning of segment [94]. Curvature patterns in these three segments of the LAD, LCx and RCA have been characterized for healthy arteries elsewhere [372].

Average distal curvature ($\bar{\kappa}_d$) is presented in this work as a geometric descriptor of the LAD artery associated to lesion presence. The rationale behind this feature was inspired by visual inspection of medical data from the patient sample described in Chapter 5 (see Section 5.1). Patients were divided in two groups, healthy (H, n=21) and diseased (D, n=27) LAD arteries. The behavior of the point-wise curvature for each class, D and H, was explored by averaging the variables over each subsample at each position $s \in [0, 1]$ over the centerlines[1].

The formal definition of average distal curvature is as follows,

$$\bar{\kappa}_d = \text{mean}(\kappa(s >= d)), \qquad d \in (0, 1), s \in [0, 1], \tag{3.2.1}$$

where d defines the beginning of the distal segment of the artery. Although our study focused on LAD vessels (see Chapter 5), the value of $\bar{\kappa}_d$ can be computed for any arterial vessel.

3.2.2 Thermodynamics of curves

The theory known as *thermodynamics of plane curves* was originally proposed by Mendès France [223, 98]. The core idea was to characterize planar curves with classical thermodynamics quantities, e.g. entropy, temperature and pressure, preserving analogies to the corresponding physical laws. The very foundation of the theory relies on a theorem from the field of *integral geometry*, known as the Cauchy-Crofton theorem [80], which states that the expected number of intersections ($\bar{n}$) between a plane curve Γ and a random line intersecting it, is related to the length (ℓ) of Γ and the perimeter (C) of its convex hull. The link to thermodynamics came from an *information-theory* based analysis of the discrete probability distribution (p_n) of the intersection count function.

Over the years the ideas behind the theory of *thermodynamics of plane curves* were further explored in close relation to fractal theory, with strong theoretical flavors and a modest number of applications. For example, [235] revisited the theory for planar curves and related the entropy to the notion of dimension of curves. [169] used the rationale behind thermodynamic analogies to define the temperature of non-random maps. Almost two decades after the introduction of the theory, [92] adapted the concept of entropy for application in time/spatial series, showing practical examples in geological data processing; specifically it was shown that the entropy of time series obtained from vibrations of drilling equipment can be used to localize stationary zones and assess the degree of homogeneity of geological formations. The same research group then used entropy of time/spatial series to the identification of functional relationships between atmospheric pressure and carbon dioxide in the cave of Lascaux [91]. More recently, [29, 30] adapted the entropy of curves, generalizing it to an arbitrary number of dimensions, with application to analysis and classification of dynamical systems. [17] recently presented applications of the $\bar{n}$, also known as inconstancy, to numerical sequences and proposed some practical applications. More recent contributions in the area focused on the use of other well known entropy definitions, like Rényi's [95].

It is worthwhile to remark that neither the entropy adaptations for time/spatial series [92], nor the one proposed by [29] for curves in $\mathbb{R}^n$, are linked to the expected number of intersection ($\bar{n}$) between a curve and hyperplanes, which is a cornerstone of the

---

[1]The normalized arc-length coordinate s is discretized in an evenly-spaced scale and linearly interpolated for each patient in the range $[0, 1]$.

original theory. In fact, both works proposed a new definition of the entropy function based on the series/curve characteristics, without considering any probability distribution. This strays those contributions from the original notion: an information-theory-based entropy with analogy to statistical mechanics.

In this section, a natural extension of the thermodynamic-based descriptors to curves in three-dimensional (3D) space is presented. In order to do that, the probability distribution p_n is used directly, instead of the Cauchy-Crofton theorem. Then, a computational approximation of p_n allows the numerical estimation of the entropy, temperature and pressure descriptors of a 3D curve. The use of probability distributions also inspired a generalization of these thermodynamic descriptors for characterizing curves from spatially distributed information, e.g. curvature, torsion. In Chapter 5, such descriptors are used for the characterization of human coronary arteries.

3.2.2.1 Basic theory

The theory of *thermodynamics of plane curves*, as presented by Mendès France, relies on the Cauchy-Crofton theorem [80], which states that the expected number of intersections between a plane curve Γ and a random line intersecting it, is given by

$$\bar{n} = \sum_{n=1}^{\infty} np_n = \frac{2\ell}{C}, \tag{3.2.2}$$

where p_n is the probability of a line intersecting Γ at n points, ℓ is the length of Γ and C is the perimeter of the convex hull of Γ. If the curve is a straight line, then $C = 2\ell$, and $\bar{n} = 1$. The analogy to thermodynamics can be made when the entropy of the probability distribution is computed using Shannon's measure of entropy from information theory [306],

$$H = -\sum_{n=1}^{\infty} p_n \log p_n. \tag{3.2.3}$$

In physics, finding the probability distribution p that maximizes Shannon's information entropy H, is the basis of the so called MaxEnt thermodynamics principle, developed by Edwin T. Jaynes [157, 158], which explains statistical mechanics and equilibrium thermodynamics as inference processes. Maximization of H subjected to a restriction on the mean value was first tackled by J. Willard Gibbs [121]. The classical solution, known as Gibbs algorithm, makes use of Lagrange multipliers to find the stationary points of the functional

$$\mathcal{L}(p) = -\sum_{n=1}^{\infty} p_n \log p_n - \phi \left(\bar{n} - \sum_{n=1}^{\infty} np_n \right) - \lambda \left(1 - \sum_{n=1}^{\infty} p_n \right). \tag{3.2.4}$$

Solving the equation $\mathcal{L}' = 0$ yields

$$p_n = (\mathrm{e}^\phi - 1)\mathrm{e}^{-\phi n}, \quad \phi = \log\left(\frac{\bar{n}}{\bar{n}-1} \right), \quad \mathrm{e}^{-1-\lambda} = \mathrm{e}^\phi - 1, \tag{3.2.5}$$

then, the maximum entropy corresponds to a planar curve in "thermodynamic equilibrium", and can be written in terms of the mean number of intersection points as

$$H_{max} = \log(\bar{n}) + \frac{\phi}{\mathrm{e}^\phi - 1} = \bar{n}\log(\bar{n}) - (\bar{n}-1)\log(\bar{n}-1). \tag{3.2.6}$$

In quantum thermodynamics, p_n usually represents the probability that a system of particles (e.g., atoms or molecules) is in the discrete energy level E_n. Furthermore, the classical

definition of temperature is $T = k\phi^{-1}$, where k is the Boltzmann constant (hereafter taken equal to one). In the present context the temperature is defined by analogy as

$$T = \frac{1}{\phi} = \left[\log\left(\frac{\bar{n}}{\bar{n}-1}\right)\right]^{-1}. \tag{3.2.7}$$

In an attempt to push further the analogy with physics, the "volume" V and "pressure" P of a curve are defined by the length ($V := \ell$) and perimeter of the convex hull ($P := 1/C$). For planar curves, using the Cauchy-Crofton theorem equation (3.2.2), the "equation of state" of a curve can be written as

$$T = \left[\log\left(\frac{2V}{2V - P^{-1}}\right)\right]^{-1} \quad \Rightarrow \quad PV = \frac{1}{2}\left(1 - e^{-\frac{1}{T}}\right)^{-1}. \tag{3.2.8}$$

When the temperature vanishes ($T = 0$), the curve freezes to a straight line and $PV = \ell/C = 1/2$. Furthermore, the entropy also vanishes ($H = H_{max} = 0$), which agrees with classical thermodynamics, where at zero temperature the entropy of the system vanishes. On the other hand, when the temperature is increased, the approximation $PV \sim T/2$ is valid, resulting in the state equation of a perfect gas.

Following Mendès first proposal, publications in the field usually express the thermodynamic quantities of curves in terms of $2\ell/C$, through expression (3.2.2). However, observe that given p_n, the thermodynamics can be defined for any curve in any dimension. It is the use of the Cauchy-Crofton theorem, and the lack of an extension of such theorem to higher dimensions, what has limited the theory to the plane. Since we are interested in applying the thermodynamic analogy to curves in 3D, we propose to overcome this limitation by defining the pressure of a curve in terms of its entropy, equation (3.2.3), and its temperature, equation (3.2.7), in analogy with the thermodynamics of ideal gases, that is:

$$H = \frac{\gamma}{1 - \gamma}\log T + \log P, \tag{3.2.9}$$

where γ is the ratio of specific heats, and the universal gas constant is set to one. P and γ will be taken as parameters that, hopefully, remain the same for a given class of curves (e.g., with similar shape). Note that $\gamma(1-\gamma)^{-1}$ is the slope of the linear approximation in a ($\log T$ vs. H) plot.

3.2.2.2 Extended framework

As shown in Section 3.2.2.1, the thermodynamics of curves can be computed from a discrete probability distribution function (DPDF). In the original theory of Mèndes France, the DPDF accounts for the number of intersections between a plane curve and a random line. This notion can be naturally extended to 3D curves intersected by a random plane. Given a curve Γ, the procedure to produce a generalized thermodynamic characterization is as follows:

i. Choose a random variable (X) associated to the geometry of the curve, e.g. the number of intersection points of Γ with random planes. Note that in the context of the thermodynamics analogy, $X \in \mathcal{G} \subset \mathbb{R}$ represents the "energy levels" of the curve. Here, $\mathcal{G}$ represents the subset of admissible energy levels.

ii. Compute the probability distribution, $p(X, \Gamma) = p$, for the given curve Γ. This step strongly depends on the choice of the random variable X.

iii. Compute curve descriptors based on the probability function, for example

    i. Statistical moments of p, such as the mean.

ii. Entropy (H) of p. In this work Shannon's entropy is used, but other definitions like [335] or [284] entropies may be used as well.

iii. Using the mean, thermodynamic descriptors can be calculated using equations (3.2.3), (3.2.7) and (3.2.9).

3.2.2.3   Probability distribution for intersection counting

As said, the generalization of the thermodynamic framework is done by defining X as the intersection count between the curve and random planes. This generalization allows direct use of thermodynamics descriptors defined in equations (3.2.3), (3.2.7) and (3.2.9), since the probability distribution p and the mean value of X, hereafter $\bar{n}$, are known. Nonetheless, estimation of p requires a computer simulation. The following methodology generalizes the computation of p for any parametric function, not just planes.

i. Choose a parametric function $\{\mathcal{F}(\mathbf{m}) \in \mathscr{F}^N \mid \mathcal{F} : \mathbb{R}^N \to \mathbb{R}^3\}$, where $\mathbf{m} \in \mathbb{R}^N$ is the vector of parameters. And $\mathscr{F}^N$ is the space of all parametric functions with N parameters. Particularly, for planes $N = 3$.

ii. Define a functional operator $\{\mathcal{O}(\Gamma, \mathcal{F}) \in \mathscr{O} \mid \mathcal{O} : \mathscr{F}^1 \times \mathscr{F}^N \to \mathcal{G}\}$. Where $\Gamma \in \mathscr{F}^1$ is a curve parametrized by arc length; $\mathcal{F} \in \mathscr{F}^N$ is the test parametric function; $\mathcal{O}$ is the functional operator which retrieves an admissible energy level $X \in \mathcal{G}$.

iii. Define an exploration set of parameters $S = \{\mathbf{m}_1, \mathbf{m}_2, \ldots, \mathbf{m}_J\}$. In theory, S would be an infinite set. In practice, the cardinality of S is finite and equals J. The selection of S must ensure an homogeneous spatial distribution of the parametric function. This means that no spatial region of $\mathbb{R}^3$ should be privileged with a higher density of functions covering the region.

iv. Compute a histogram for the random variable X, hereafter called hist(X). This is performed by applying the functional operator to the complete set of parametric functions spanned by S. That is, $X_j = \mathcal{O}(\Gamma, \mathcal{F}(\mathbf{m}_j))$, $j = 1, 2, \ldots, J$.

v. Compute p from hist(X).

In the present work, (i) the parametric functions are intersecting planes, and so $N = 3$. (ii) The functional operator is the operation through which the number of intersections (n) between a plane and the curve is counted. The number of intersections is the chosen random variable ($X = n$). (iii) The set of parameters S, in this work, has cardinality $J = 440000$ and was defined from a regular grid containing all possible curves. A series of rotations of the grid in azimuthal and polar angles is performed, and for each grid configuration the normal vectors to the planes are also rotated in both directions. This procedure ensures a homogeneous density of planes in the region where the curves are defined.

3.2.2.4   Pseudo-probability distribution based on curve features

The thermodynamics of a curve, as defined in this work, depends on the DPDF of a random variable X. When X stands for the number of intersections between a planar curve and a random line, the thermodynamics proposed by Mendès is recovered. In this section we exploit spatially distributed information which can be associated to the curves, e.g. curvature or lumen radius, to construct a probability distribution and use it to compute thermodynamic descriptors. Such DPDF is computed in four steps:

i. Define a spatial partition of the curve into M buckets, called B_i, $i = 1, \ldots, M$.

ii. List the buckets in ascending order according to the natural order of the curve.

iii. For a given spatially distributed feature f, compute the cumulative value (F_i) of f for each bucket $B_i, i = 1, \ldots, M$, namely

$$F_i = \sum_{j=1}^{L_i} f_j, \quad i = 1, \ldots, M,$$

for a given bucket B_i, containing L_i points.

iv. Compute the discrete pseudo-probability distribution

$$p_i = F_i \left(\sum_{j=1}^{M} F_j \right)^{-1}. \tag{3.2.10}$$

Note that in this case, the discrete random variable, $X = B$, represents the bucket index with expected value $\bar{B} = \sum i p_i$. Given p_i and $\bar{B}$, the entropy, temperature and pressure as defined in equations (3.2.3), (3.2.7) and (3.2.9) can be calculated. In this work, (i) each arterial vessel to be analyzed is divided into $N = 20$ equally sized buckets, (ii) bucket order starts in the points of the vessel near the heart (proximal) and increases towards the distal location, following the blood flow direction, and particularly (iii) we emphasize the analysis when using the curvature as the spatially distributed feature ($f = \kappa$).

3.2.2.5 Convergence of the numerical strategy for intersection-counting-based thermodynamic variables calculation

Convergence tests were performed to ensure that the computational methodology presented in Section 3.2.2.3 does not introduce errors in the statistical analysis of the thermodynamics variables. For the parameters used in this work, it was found that the mean relative difference in all thermodynamic variables for a set of 144 curves[2] was significantly higher (thirty to sixty times) than the mean of relative convergence difference for successive planes of intersection. These results ensure that errors due to the numerical procedure used in the computation of thermodynamic variables are negligible compared to the differences among different curves. Figure 3.1 presents the evolution of the difference for successive intersection planes for the 3D curves. The median and interquartile range for the 144 curves are displayed.

---

[2]Such set contains the LAD, RCA and RCA arteries of 48 patients, see Section 5.1 for a description of the population sample.

3.2.3 Summary of non-conventional features

The thermodynamics features derived in previous sections and used in this work are summarized in Table 3.2.

Feature	Definition	
The average of point-wise curvature in the distal quarter of the artery.	$\bar{\kappa}_d = \text{mean}(\kappa(s >= 0.75))$	(3.2.11)
The expected number of intersections between a given centerline and a random plane.	$\bar{n}$	
The Shanon entropy based on the probability distribution of number of intersection points between a given centerline and a random plane.	$H_n = -\sum_{n=1}^{\max_n} p_n \log p_n$	(3.2.12)
The temperature of the centerline associated to $\bar{n}$	$T_n = \left[\log\left(\dfrac{\bar{n}}{\bar{n}-1}\right)\right]^{-1}$	(3.2.13)
The pressure of the centerline associated to T_n and H_n	$P_n = e^{H_n - \gamma(1-\gamma)^{-1}\log T_n}$	(3.2.14)
The Shanon entropy based on the pseudo-probability distribution derived from point-wise curvature.	$H_\kappa = -\sum_{i=1}^{N=20} p_i \log p_i$	(3.2.15)
The temperature of the centerline associated to the point-wise curvature.	$T_\kappa = \left[\log\left(\dfrac{\bar{B}}{\bar{B}-1}\right)\right]^{-1}$	(3.2.16)
The pressure of the centerline associated to T_κ and H_κ	$P_\kappa = e^{H_\kappa - \gamma(1-\gamma)^{-1}\log T_\kappa}$	(3.2.17)

Table 3.2: List of non-conventional geometric features used in this work.
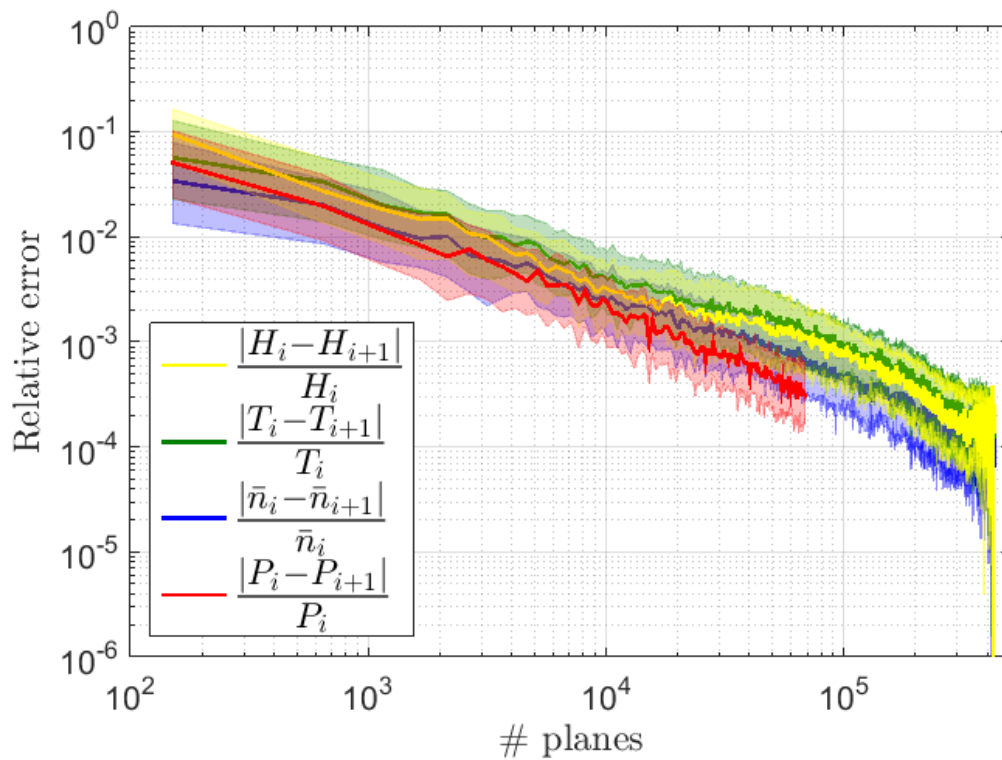
Figure 3.1: Relative error evolution for all intersection-counting-based thermodynamic variables. The set of intersecting planes is the same for all curves and the number of planes that effectively intersect each curve is different. Therefore, the pressure P was computed using all 144 curves until the minimum number of intersecting planes for all 144 curves.

Chapter 4

Comparison of arterial structures

"One can state, without exaggeration, that the observation of and the search for similarities and differences are the basis of all human knowledge."

Alfred Nobel

The geometric characterization of arteries presented in Chapter 3 is the first step towards a broad spectrum of quantitative and statistical analysis that can be performed to evaluate clinical hypotheses. Some examples of such analyses are presented in Chapter 5. In this chapter, a methodology to establish similarity and comparison of arterial geometry is presented. Furthermore, some statistical concepts and classification techniques which are used in Chapter 5, are summarized.

Geometric assessment of vascular structures has been employed to study other vascular territories, i.e. the AneuRisk [5] project investigated the role of vessel morphology, vascular wall mechanics and hemodynamics on the pathogenesis of cerebral aneurysms [263, 290, 262, 257]; the BraVa project [7] aimed to provide extended morphometric information of the cerebral vasculature in healthy adults [358, 241].

4.1   Arterial comparison

This section presents a feature-based criterion to perform comparisons of arterial vessels. The concept of comparison implies seeking for similarities, which can be assessed for any two given patients. Furthermore, for a sample of patients, relative likelihoods can be established using ranking (ordering). The set of features presented in Tables 3.1 and 3.2 is used to construct an euclidean space $\mathscr{F}$, in which comparison is defined through an euclidean distance.

After computing the features, an array of real numbers for each artery is obtained. The goal is to construct a mathematical environment suitable for quantifiable comparisons which is performed in four steps, as explained next.

1. **Arterial selection**: A subset of arteries ($\mathcal{S}_{\mathscr{A}}$) is used to represent each patient. In Chapter 5 (see Section 5.4) we provide examples considering the left anterior descending (LAD), left circumflex (LCx) and right coronary (RCA) arteries, either separately or altogether.

2. **Feature selection**: A subset of features $\mathcal{G}_{\mathscr{D}}^{\mathscr{A}}$ is chosen to characterize each artery $\mathscr{A}$, for which $\mathscr{D}$ is an identifier of the set of features of artery $\mathscr{A}$, i.e. *all* and *min*, as used in Chapter 5 (see Section 5.4). Then each patient is represented by a vector $\hat{\mathbf{p}}$ constructed from the concatenation of features per artery, this is $\hat{\mathbf{p}} \in \mathbb{R}^n$, with $n = |\mathcal{G}_{\mathscr{D}_1}^{\mathscr{A}_1}| + \cdots + |\mathcal{G}_{\mathscr{D}_m}^{\mathscr{A}_m}|$, where $m = |\mathcal{S}_{\mathscr{A}}|$ is the cardinality of the arterial subset.

In Chapter 5 (see Section 5.4) we present results for $\mathcal{G}_{\mathscr{D}}^{\mathscr{A}} = \mathcal{G}_{\text{all}}^{\mathscr{A}}$ (the complete set of features, presented in Table 3.1, for each artery $\mathscr{A}$), and for $\mathcal{G}_{\mathscr{D}}^{\mathscr{A}} = \mathcal{G}_{\text{min}}^{\mathscr{A}}$ which is the subset of features that minimizes a given metric for each artery $\mathscr{A}$.

3. **Feature space construction**: As features differ in metric units and magnitude, a normalization of each feature (adimensionalization) is required. Given a vector $\hat{\mathbf{p}}$, the normalization results in a vector $\mathbf{p}$, whose components are $p_f = (\hat{p}_f - \hat{\mu}_f)/\hat{\sigma}_f$, $f = 1, \ldots, n$, where $\hat{\mu}_f$ is the mean value of feature f for all the patients and $\hat{\sigma}_f$ is the corresponding standard deviation for the entire set. The resulting euclidean space is called *feature space* and is denoted by $\mathscr{F} = \mathscr{F}(\mathcal{G}_{\mathscr{D}}^{\mathscr{A}})$. Note that the zero element of $\mathscr{F}$ is that associated to the arterial structure with all geometric features equal to the mean values, and therefore, patients are characterized as a deviation from the average geometry of the population. This interpretation is key to understand the upcoming definition of likelihood.

4. **Elements of the feature space**: Each patient is normalized and its vector representation in $\mathscr{F}$ is computed. Once all patients are represented in the feature space, distances and likelihoods between patients are straightforwardly obtained.

In this work we define arterial comparison through the euclidean norm (denoted by $|| \cdot ||$) in the feature space. Given two patients $\mathbf{a}, \mathbf{b} \in \mathscr{F}$, the distance between them, denoted by $\mathsf{d}(\mathbf{a}, \mathbf{b})$, is defined as

$$\mathsf{d}(\mathbf{a}, \mathbf{b}) = ||\mathbf{a} - \mathbf{b}|| \tag{4.1.1}$$

Note that $\mathsf{d} \to 0$ means proximity (similarity) between patients. This approach leads to the concept of ranking $\mathsf{r}(\mathbf{a}, \mathbf{b}), \mathbf{a}, \mathbf{b} \in \mathscr{F}$, an index that measures how similar patient $\mathbf{b}$ is to $\mathbf{a}$ relative to all patients in $\mathscr{F}$. For a given patient $\mathbf{a}$, the ranking for the sample is computed in three steps,

- Compute distance $\mathsf{d}(\mathbf{a}, \mathbf{c})$, $\forall \mathbf{c} \in \mathscr{F}$ generating a list of distances.

- Sort (in ascending order) the list.

- For each patient $\mathbf{c} \in \mathscr{F}$, compute the ranking referred to $\mathbf{a}$ as the position of $\mathsf{d}(\mathbf{a}, \mathbf{c})$ in the sorted list.

The ranking is a positive natural number, $\mathsf{r} \in \mathbb{N}^+$, and its maximum value depends on the cardinality of the patients sample (denoted by $|\mathscr{P}|$). Note that r can be used to query the m patients in the database which are more similar to a given one. This information can be used, for example, to assess if patients sharing some external characteristic tend to cluster in $\mathscr{F}$. In Chapter 5 (see Section 5.4) we show that for a given patient, his/her sibling tends to present low ranking positions, thus having similar geometric attributes. Computing the median of the ranking of each patient with the corresponding sibling leads to what we call the Siblings Ranking Index,

$$\mathsf{SRI} = \text{median}(\mathsf{r}(\mathbf{a}, \mathbf{b})), \forall \mathbf{a} \in \mathscr{F}, \tag{4.1.2}$$

where $\mathbf{b} = \text{sib}(\mathbf{a})$ is sibling of $\mathbf{a}$. The SRI assesses likelihood at population level. In order to decouple the SRI from $|\mathscr{P}|$, a further normalization is performed, which leads to the relative sibling ranking index, $\mathsf{rSRI} = \mathsf{SRI}/|\mathscr{P}|$. Given two patients who are siblings, say $\mathbf{a}$ and $\mathbf{b}$, it would be expected that $\mathsf{d}(\mathbf{a}, \mathbf{b}) \to 0$ and $\mathsf{r}(\mathbf{a}, \mathbf{b}) \to 1$, which is analogous to $\mathsf{rSRI} \to 0$.

4.2 Statistical analysis

Several statistical tests are performed in Chapter 5 and Part II, Chapter 10. Most of such tools are standard and taught in introductory statistics courses. For the sake of completeness, this section provides a brief summary of the concepts and tools used in this work.

4.2.1 Difference in the mean value of two samples

Given a continuous variable (x) and two defined classes, e.g. healthy (H) and diseased (D) arteries. It can be determined, to a certain level of statistical significance (the so called p-value), if the mean value of the variable is different between both classes. In our example, consider that x is larger in H than in D arteries. Depending on the probability distribution of the continuous variable, several tests can be performed. Particularly, when the variable is normally distributed, a Student's t-test [321] is the common choice. The Mann-Whitney U test[1] [210] can be used when the probability distribution of the variable is not known.

4.2.2 Association of categorical variable

When assessing significant association of two categorical variables, e.g. shape of the RCA and lesion presence, of the same population, a chi-square (χ^2) test for independence is used. In that example the test can confirm, with a significance level (p-value) whether the shape is associated to the presence of lesion in the the RCA.

4.2.3 Correlation coefficient

In statistics, the strength of a relation (association or dependence) between two random variables (or observed data values), can be quantified through the so called correlation coefficient. Typically, such coefficient takes values in the range $[-1, 1]$, where zero indicates no association, 1 states a perfect positive correlation and -1 perfect negative correlation. Types of correlation coefficients include: (a) Pearson product-moment correlation coefficient (r), which measures the strength and direction of the linear relationship between two variables. (b) Spearman's rank correlation coefficient (ρ), which measures how well the relationship between two variables can be described by a monotonic function. Spearman's coefficient, is usually preferred to assess discrete and ordinal variables, and it also can capture non-linear association between variables.

4.2.4 Bland-Altman plots

In data analysis, Bland-Altman plots [46] are extensively used to evaluate the agreement between two different instruments or two measurements techniques. The method allows to detect any systematic difference between the measurements, i.e. fixed bias, and to identify possible outliers. The mean difference is the estimated bias, and the standard deviation (SD) of the differences measures the random fluctuations around this mean. If the mean value of the difference differs significantly from 0 on the basis of a paired t-test or U-test, this indicates the presence of fixed bias. When comparing methods, or assessing repeatability, it is important to calculate confidence intervals for 95% limits of agreement (average difference $\pm 1.96 \times$ SD). If the differences within the confidence intervals are not relevant in the context of the measurements, the two methods can be used interchangeably.

---

[1]Also called the Mann-Whitney-Wilcoxon (MWW), Wilcoxon rank-sum test, or Wilcoxon-Mann-Whitney test.

4.2.5 Association of features between siblings

The distance (d) and related ranking indexes (rSRI) defined in Section 4.1 can be used to assess similarity between siblings using an arbitrary number of features. Restricting the cardinality of the feature space to 1, it allows as to use a broad spectrum of statistical indexes to explore for heritability landmarks. Most of these indicators are designed to work with categorical or binary variables, i.e. patient has a disease or not. Indicators under this category are marked with a (**D**) symbol in the following subsections. Nevertheless, continuous or ordinal variables can be dichotomized, and such indicators can also be used. In this study, the only binary variable are the presence or absence of lesion, and the shape of the RCA. In Chapter 5 (see Section 5.5), dichotomization is performed in relation to the mean value of the feature among the patient sample.

In the context of heritability assessment, arterial features are phenotypes, and saying that a patient tested positive for a given phenotype, means that the feature value is larger than the mean of the sample. Therefore, these types of tests should be interpreted as association of the feature between siblings relative to the mean value of the feature.

Nevertheless, other indicators are designed for continuous or ordinal variables, and are identified with (**C**) symbol in the following subsections. Such indicators directly measure the relationship among variables.

4.2.5.1 ProbandWise ratio, PBWR [D]

Probability that a patient tests positive given that his sibling tested positive. Proband-Wise and CaseWise (CWR) ratios measure the same probability. In cases when double assertion in diagnosis is used, and there is a chance of discordance in diagnosis, the PBWR proved to be the best choice for establishing the concordance rate between pairs of patients [220]. Nevertheless when such discordance is not possible, as in this work, the PBWR and CWR are algebraically equivalent. Such probability is computed as

$$\text{PBWR} = \frac{2B}{2B + O}, \tag{4.2.1}$$

where B and O are, respectively, the number of sibling pairs where both patients tested positive and where only one sibling tested positive.

4.2.5.2 Similarity Index, SimI [D]

Probability that both siblings have the same test results. It is defined as

$$\text{SimI} = \frac{B + E}{B + O + E}, \tag{4.2.2}$$

where B and O are the same as in Equation (4.2.1), and E is the number of sibling pairs where neither patient tested positive.

4.2.5.3 Relative sibling ranking index, rSRI [C]

Introduced in Section 4.1 this indicator measures how similar (in terms of a given feature) siblings are in relation to the rest of the sample. A value of 0.5 implies that siblings are as similar as they are to the general population. There is no statistical significance p-value asssociated to this index.

4.2.5.4 p-value of the Mann-Whitney U-Test, p-UTest [C]

The test assesses if distance (in terms of the feature) between siblings is smaller than between non-sibling patients. A non-parametric Mann-Whitney U-Test [210] is used. In this work, p-UTest < 0.05 are statistically significant. This test is used in Chapter 5 (see Section 5.4) to assess similarity in different feature spaces, here, the feature spaces contain one feature only.

4.2.5.5 Intraclass correlation coefficient, ICC [C]

It describes how strongly siblings resemble each other. The One-way random single measure is used [219]. In addition to estimation of ICC, a hypothesis test is performed with the null hypothesis that ICC = 0. In this work, p-ICC < 0.05 indicates statistical significance on the ICC value.

4.2.5.6 Risk-ratio or relative-risk, RR [D]

In epidemiological terms [282], RR is the risk to test positive for individuals with a given susceptibility genotype (in this case the susceptibility genotype is that the sibling tested positive), divided by the risk of disease for those without it. In addition, the confidence interval (RR_CI), can be computed to test for statistical significance. If the confidence interval (CI) contains the value 1, then the RR has no statistical significance.

4.2.5.7 Odds-ratio, OR [D]

The odds ratio (OR) quantifies how strongly the presence or absence of property A is associated with the presence or absence of property B in a given population. If each individual in a population either does or does not have property "A", (e.g. "patient has lesion"), and also either does or does not have a property "B" (e.g. "sibling has lesion") where both properties are appropriately defined, then a ratio can be formed which quantitatively describes the association between the presence/absence of "A" (patient has lesion) and the presence/absence of "B" (sibling has lesion), for individuals in the population. This ratio is the OR [78].

Furthermore, an associated confidence interval (OR_CI) can be computed to test for statistical significance. If the interval contains the value 1, then the OR is not statistically significant.

4.2.5.8 Association Parameter, PHI [D]

If the OR_CI does not encompass the value OR=1, then the Bayesian Credibility Assessment [285] of the test is computed. If the test is credible, the Association Parameter PHI is computed.

$$\text{PHI} = \sqrt{\frac{\chi^2}{N}}, \tag{4.2.3}$$

where χ^2 is the associated chi-square statistic of the contingency table used to compute the OR. PHI > 0 implies positive association (risk factor). PHI < 0 implies negative association (protective factor). $|\text{PHI}| \leq 0.3$ is considered a weak association. $0.3 < |\text{PHI}| \leq 0.7$ is considered moderate association. $|\text{PHI}| > 0.7$ is considered a strong association.

4.2.5.9 Critical Odds Ratio, COR [D]

While the OR statistical significance criterion is a widespread indicator to assess the efficacy of the OR, in some cases, statistical significance is not a good indicator of

the *credibility* of a finding (that is, the extent to which it provides convincing evidence for efficacy), as it fails to take full account of the size of the trial, or of pre-existing insights [216]. The *credibility* of any given OR with statistical significance can be assessed using a Bayesian method [216]. For a given result to meet this standard, the prior evidence for efficacy must exceed a specific level; this level is captured by the Critical Odds Ratio (COR). The assessment of a given clinical trial result can then proceed as follows:

- If the stated 95% CI excludes an OR of 1.00 (corresponding to no effect), the result can be deemed statistically significant at the 95% level;

- If OR is at least as impressive as that indicated by the COR, the result can also be deemed credible at the 95% level.

Typically, when the number of patients is large, the COR is undemanding and the OR easily covers the credibility criterion. This is justified on the basis of current knowledge. On the other hand, when the number of patients is relatively low, the associated COR demands a substantial amount of prior evidence before the new result can be deemed credible.

4.2.5.10 Power, Pw [D]

It is the probability of detecting an effect, given that the effect is really there. Or likewise, the probability of rejecting the null hypothesis when it is in fact false [285]. It is recommended a $Pw \geq 0.8$, which means that if we perform a study N times, we would see a statistically significant difference 80% of the times.

4.3 Classification

Classification is defined as the action or process of assigning a category to something according to shared qualities or characteristics. The most general form of the classification problem belongs to the field of pattern recognition. In machine learning and statistics, classification refers to the identification of the class to which a new observation belongs, by means of an algorithm tuned with data (observations) whose category membership is known a priori. Such algorithms are known as classifiers.

Depending on the number of categories to which a classifier has to map the data, two types of problems are defined: binary and multiclass classification. In the former, only two classes are involved, whereas the later involves more than two. Particularly, in this work, examples of binary classifications are given in Chapter 5.

The most common way to model data for classification is through a so called feature vector containing the measurable properties of the data. In the context of this thesis, the vector of geometric features described in Section 4.1 spanning the feature space, can be used directly for classification purposes.

4.3.1 Linear classification

The use of a linear function to map the feature vector ($\mathbf{f} \in \mathbb{R}^n$) to a real number ($c \in \mathbb{R}$) and classification using threshold ($t \in \mathbb{R}$) on c is one of the simplest and used classification techniques. Such linear function takes the form of a linear combination of the feature vector and a vector of weights ($\mathbf{w} \in \mathbb{R}^n$),

$$c = \mathbf{f} \cdot \mathbf{w}. \tag{4.3.1}$$

For this kind of classifiers, the determination of $\mathbf{w}$ and of the threshold used on c are key.

4.3.2   Kernel density classification

Kernel density estimation (KDE) is an unsupervised learning procedure, which leads naturally to a simple family of procedures for nonparametric classification, the so called kernel density classification (KDC). A good review of these methods, can be found in [112, Chapter 6]. Given a random sample $X = \{x_1, \dots, x_N\}$ drawn from an unknown probability density function $f_X(x)$, one can estimate f_X at any given point x_0 by means of the KDE method. In $\mathbb{R}^p$ using the Gaussian product kernel yields

$$\hat{f}_X(x_0) = \frac{1}{N(2\lambda^2\pi)^{\frac{p}{2}}} \sum_{i=1}^{N} e^{-\frac{1}{2}\left(\frac{||x_i - x_0||}{\lambda}\right)^2}, \tag{4.3.2}$$

where $\phi_\lambda(x_i, x_0) = e^{-\frac{1}{2}\left(\frac{||x_i - x_0||}{\lambda}\right)^2}$ is the so called Gaussian kernel with mean zero and standard deviation λ. In this work, a value of $\lambda = 0.75$ was chosen by rule of thumb. Many kernel functions ϕ_λ were proposed in the literature, being the Gaussian function the simplest and most popular. Note that the estimation $\hat{f}_X(x_0)$ is smooth, due to the weighting average of the observations closed to x_0, with weights that decrease with distance from x_0.

Multivariate, multiclass classification from the probability estimate (4.3.2) is straightforward using Bayes' theorem. Given a problem with J classes, and a training data set of N samples, three steps are needed. First, the density estimation is computed (separately) for each class, this is $\hat{f}_j(X_j)$, with $j = 1, \dots, J$. Given the sample proportions π_j. Then, the posterior probability of a new data x_0 belonging to class j is estimated as

$$\hat{P}_j(\text{class} = j | X = x_0) = \frac{\pi_j \hat{f}_j(x_0)}{\sum\limits_{k=1}^{J} \pi_k \hat{f}_k(x_0)}. \tag{4.3.3}$$

Finally, x_0 is assigned to the class with the biggest probability $\hat{P}_j$.

Taking into account that the size of the available data sample is small and that trained classification algorithms often produce overoptimistic assessments, all uses of KDC in Chapter 5 are evaluated by means of an standard leave-one-out cross validation test (LOOCV). Such cross-validation technique performs classification of each data object by training the classifier with the rest of the data sample.

4.3.3   Classification performance

Many metrics have been developed to evaluate the performance of binary classifiers, see [142] for a good review on the subject. For a given set of data with known class membership, any classification output on such data can be summarized using the so called confusion or misclassification matrix, see Table 4.1. Given two classes C_0 and C_1, for each data object, the classification outcome can be positive (i.e. C_1) or negative (i.e. C_0). The classifier result for each data object may, or may not, match the actual class. In such a general setting, where positives can be interpreted as identified and negative as rejected, there are four possible outcomes, namely: True Positive (TP, correctly identified), False Positive (FP, incorrectly identified), True Negative (TN, correctly rejected) and False Negative (FN, incorrectly rejected).

Accuracy (Acc), is the proportion of true results (both TP and TN) among the entire sample.

$$\text{ACC} = \frac{\text{TP} + \text{TN}}{\text{TP} + \text{TN} + \text{FP} + \text{FN}} \tag{4.3.4}$$

		True class	
		C_1	C_0
Predicted class	C_1	True positive (TP)	False negative (FN)
	C_0	False positive (FP)	True negative (TN)

Table 4.1: Illustration of a confusion matrix.

Sensitivity (Sen), refers to the classifier's ability to correctly detect TP. The sensitivity of a classifier is the proportion of data objects classified as C_1 among those which actually belong to C_1. Mathematically, this can be expressed as:

$$\text{Sen} = \frac{TP}{TP + FN}, \tag{4.3.5}$$

which is equal to the conditional probability $P(\text{predicted} = C_1 | \text{true} = C_1)$.

Specificity (Spe), relates to the classifier's ability to correctly detect TN. The specificity of a classifier is the proportion of data objects known to belong to C_0, which will be classified as C_0. Mathematically, can be written as:

$$\text{Spe} = \frac{TN}{TN + FP}, \tag{4.3.6}$$

which is equal to the conditional probability $P(\text{predicted} = C_0 | \text{true} = C_0)$.

The **positive** and **negative predictive values** (PPV and NPV, respectively) are the proportions of positive and negative classifier results that are true positive and true negative results. The PPV and NPV are not intrinsic to the test; they depend also on the **prevalence** (Prev) of C_1 over the entire data sample. Mathematically, these indexes are written as:

$$\text{PPV} = \frac{TP}{TP + FP}, \tag{4.3.7}$$

$$\text{NPV} = \frac{TN}{TN + FN}. \tag{4.3.8}$$

$$\text{Prev} = \frac{TP + FN}{TP + TN + FP + FN}. \tag{4.3.9}$$

For threshold-based classifiers, one of the most widely used measures of classification performance is the **area under the receiver operating characteristic curve** (AUC). It is simply the probability that a randomly chosen member of class C_0 has a lower score than a randomly chosen member of class C_1.

The receiver operating characteristic or ROC curve is a plot of the cumulative distribution of class C_0 on the vertical axis against the cumulative distribution of class C_1 on the horizontal axis. Sometimes alternative axes are used, but the principles remain the same. For the labeling we have introduced, this implies that the ROC curve is a plot of specificity against 1-sensitivity. Then the AUC is simply the area under this curve. Where each point of the curve is computed by performing classification of the complete data sample with different values of the threshold value t.

Chapter 5

Data analysis examples

"In God we trust; all others must bring data."

William Edwards Deming

In this chapter, several data analyses making use of the framework proposed in previous chapters are presented. First, the specification of the medical protocols used in the selection of the patient sample used in all studies of the chapter is detailed in Section 5.1. A demographic summary in terms of clinical data associated to the sample is also shown. Section 5.2 presents extended statistical morphometric information of the coronary tree; furthermore inter- and intra-arterial correlation among descriptors is explored. Section 5.3 presents the application of geometric features to identify the characteristic shape of the RCA. In Section 5.4 it is shown how the similarity criterion between arterial structures can be used to provide insight about medical hypotheses, specifically the existence of similar geometric attributes between siblings. In Section 5.5 the heritability of individual geometric features for the main coronary arteries through a set of indexes is explored. In Section 5.6 the rationale behind the distal average curvature feature for the LAD artery is explained. In Section 5.7 the association between stenotic lesions and geometric features is addressed. Finally, in Section 5.8 it is shown that models of coronary arterial networks obtained from noninvasive medical images can be used to construct descriptive power laws, rooted in fractal theory. Regarding the denomination of arterial vessels along this chapter, the reader is referred to Appendix B for a complete description of the notation and to Appendix C for the basic knowledge of coronary anatomy.

5.1 Patient sample

All patients were referred to Coronary Computed Tomography Angiography (CCTA) between February 2008 and March 2013 to the Radiology Department at the Heart Institute (InCor), University of São Paulo Medical School, Brazil. Eligible patients had suspected or known coronary artery disease. The InCor database was queried for patients with CCTA using the terms: age gap of 10 years AND same name of the mother AND father. Exclusion criteria included a history of allergy to iodinated contrast material or contrast-induced nephropathy, hepatic failure, serum creatinine > 2 mg/dL or calculated creatinine clearance of <60 mL/min, dyspnea at rest, known neoplasm and pregnancy. A total of 48 patients were selected for this study, consisting of 24 pairs of siblings, 4 sisters, 14 brothers and 6 female/male siblings. Making a total of 14 females and 34 males patients with an average age of 53 ± 13 years old. The demographics of these patients are summarized in Table 5.1, where continuous variables are expressed as means $\pm$ SD. Normality was assessed using Shapiro-Wilk test [307]. Categorical data are described as number (percentage).

	Group 1	Group 2	p-value
Age, years $\pm$ SD	53.4 ± 14.4	53.6 ± 12.1	0.82
Female, n(%)	7(29.2)	7(29.2)	1.00
BMI, Kg/m^2 $\pm$ SD	28.4 ± 3.9	29.6 ± 6.24	0.73
Hypertension, n(%)	17(70.8)	20(83.3)	0.30
Diabetes, n(%)	6(25)	4(16.7)	0.47
Dyslipidemia, n(%)	20(83.3)	19(79.2)	0.71
LDL	127.5 ± 35.4	118.6 ± 38.5	0.41
HDL	48.9 ± 10.8	44.9 ± 10.1	0.18
Colesterol	192.6 ± 46.6	188.3 ± 41.1	0.73
Smoking, n(%)	8(33.3)	6(25)	0.52
Family history, n(%)	12(50)	11(45.8)	0.77
Previous MI, n(%)	4(16.7)	3(12.5)	0.68
Previous PCI, n(%)	4(16.7)	1(4.2)	0.17
Previous CABG, n(%)	2(8.3)	1(4.2)	0.50
LVEF, % $\pm$ SD	63.2 ± 3.9	63.1 ± 3.7	0.97

Table 5.1: Demographic summary for sibling subdivision of patient sample. Abbreviations stand for: Body mass index (BMI); Low-density lipoprotein (LDL); High-density lipoprotein (HDL); Myocardial infarction (MI); Percutaneous coronary innervation (PCI); Coronary artery bypass graft (CABG); Left ventricle ejection fraction (LVEF).

Comparisons of continuous variables were made using Student's t-test or Mann-Whitney U-test [210] for parametric and non-parametric data, respectively, and χ^2 test or Fisher's exact test for categorical ones. All these tests were performed using STATA 11.0 software (StataCorp., Texas, USA). Groups in Table 5.1 separate family members (in a random fashion), for all comparisons a two tailed p-value <0.05 was considered as statistically significant. It was found no statistically significant difference between groups, and all patients have at least one of the major CAD systemic risks factors (smoker, hypertension, diabetes or dyslipidemia).

As stated in Chapter 2 (see Section 2.3.4), the existence of arterial lesions in the arteries was specified by physicians, and the lesions are characterized according to [273] using a tuple of three variables, namely: stenosis grade, tissue type and lesion position. In all data analyses presented in this work, an artery was consider as diseased when a stenotic lesion of any grade, tissue and position was present in the artery. For each one of the major arteries (LAD, LCx and RCA), two subgroups can be classified according to presence of at least one stenosis (disease, class D) as opposed to the complete absence of stenosis (healthy, class H). The demographics of these classes are summarized in Table 5.2, where continuous variables are expressed as means $\pm$ SD. Categorical data are described as numbers (percentage). Comparisons of continuous variables were made using non parametric two tailed Mann-Whitney U-test. A χ^2 test was used for categorical ones.

In our sample, it was found that: (i) for the LAD artery, statistically significant difference between groups was found for previous percutaneous coronary intervention (PCI) and left ventricle ejection fraction (LVEF); (ii) the LCx presented statically significant differences for the gender, previous myocardial infarction (MI) and previous coronary artery bypass graft (CABG); (iii) in turn, lesioned RCA were associated to dyslipidemia, previous MI, PCI and CABG. Furthermore, presence of lesion in one of the major arteries (LAD, LCx or RCA) was strongly associated to lesion in at least other of the remaining two arteries.

In addition, all patients have at least one of the major CAD systemic risks factors (smoker, hypertension, diabetes or dyslipidemia). Despite the familial relationship present in the data set, it is shown in Section 5.2 that the patient sample is representative from the point of view of the anatomical description of the coronary vasculature, i.e. circulation dominance, lumen radius measurements and arterial occurrence.

Baseline Characteristics	All (n=48)	LAD			LCx			RCA		
		H (n=21)	D (n=27)	p-value	H (n=36)	D (n=12)	p-value	H (n=29)	D (n=19)	p-value
Age, years±SD	53.0±13.1	49±14	56±12	0.096	52.7±13.8	54.1±11.1	0.849	50.4±14.0	57.1±10.7	0.116
Male, n (%)	34 (70.8)	12 (57.1)	22 (81.5)	0.066	22 (61.1)	12 (100)	**0.010**	18 (62.1)	16 (84.2)	0.099
BMI, Kg/m²±SD	29.0±5.2	28.8±5.8	29.2±4.8	0.467	29.0±5.1	29.1±5.7	1.000	29.4±5.7	28.4±4.4	0.841
Hypertension, n (%)	37 (77.1)	15 (71.4)	22 (81.5)	0.411	26 (72.2)	11 (91.7)	0.165	21 (72.4)	16 (84.2)	0.342
Diabetes, n (%)	10 (20.6)	3 (14.3)	7 (25.9)	0.325	6 (16.7)	4 (33.3)	0.218	3 (10.3)	7 (36.8)	**0.027**
Dyslipidemia, n (%)	39 (81.2)	16 (76.2)	23 (85.2)	0.428	29 (80.6)	10 (83.3)	0.831	23 (79.3)	16 (84.2)	0.671
LDL	123.1±36.9	125.3±40.2	121.3±34.8	0.835	123.0±38.4	123.3±33.8	0.748	121.1±38.5	126.1±35.1	0.541
HDL	46.9±10.6	46.7±10.8	47.0±10.6	0.950	47.4±11.5	45.2±7.3	0.489	47.8±11.5	45.4±9.1	0.364
Cholesterol	190.4±43.6	192.0±50.4	189.2±38.3	0.934	186.4±43.7	202.6±42.5	0.225	187.3±44.9	195.3±42.1	0.429
Smoking, n (%)	14 (29.2)	6 (28.6)	8 (29.6)	0.936	9 (25.0)	5 (41.7)	0.271	7 (24.1)	7 (36.8)	0.344
Familiar CAD Hist., n (%)	23 (47.9)	9 (42.9)	14 (51.9)	0.536	16 (44.4)	7 (58.3)	0.404	13 (44.8)	10 (52.6)	0.597
Previous MI, n (%)	7 (14.6)	1 (4.8)	6 (22.2)	0.089	3 (8.3)	4 (33.3)	**0.034**	1 (3.4)	6 (31.6)	**0.007**
Previous PCI, n (%)	5 (10.4)	0 (0)	5 (18.5)	**0.037**	2 (5.6)	3 (25.0)	0.056	0 (0)	5 (26.3)	**0.004**
Previous CABG, n (%)	3 (6.2)	0 (0)	3 (11.1)	0.115	0 (0)	3 (25.0)	**0.002**	0 (0)	3 (15.8)	**0.027**
LVEF, %±SD	63.7±3.7	65.0±3.4	62.7±3.7	**0.033**	63.6±3.8	64.3±3.4	0.777	64.2±3.7	63.1±3.7	0.256
Lesion?, n (%)	28 (58.3)	-	-	-	-	-	-	-	-	-
Lesioned LCx/RCA, n (%)	-	1 (4.8)	19 (70.4)	**0.000**	-	-	-	-	-	-
Lesioned LAD/RCA, n (%)	-	-	-	-	16 (44.4)	12 (100)	**0.001**	-	-	-
Lesioned LAD/LCx, n (%)	-	-	-	-	-	-	-	9 (31.0)	19 (100)	**0.000**

Table 5.2: Summary of the patient sample demographics when considering lesion in the LAD, LCx and RCA arteries. Abbreviations stand for: Body mass index (BMI); Low-density lipoprotein (LDL); High-density lipoprotein (HDL); Myocardial infarction (MI); Percutaneous coronary innervation (PCI); Coronary artery bypass graft (CABG); Left ventricle ejection fraction (LVEF).

5.2 Morphometry of coronary vasculature

Quantitative measurement of the geometry and anatomy of coronary arteries can also be useful in clinical practice as well as to provide researchers with physical parameters to set up computational models. The medical literature is vast in terms of qualitative description of the coronary system [345, 108, 204], but quantitative information is more likely presented in terms of simple variables [94, 31]. The arrival of highly detailed models of the human circulatory system [42, 43] is a clear example of scientific research exploiting morphometric information. In this section, we provide statistics and quantification of the geometric features introduced in Chapter 3. First we show point-wise (spatially distributed) information for the LAD, LCx and RCA arteries, and then we show arterial-level features for a bigger set of arterial branches, finally we present correlation among features.

5.2.1 Morphometric information

Figure 5.1 presents the point-wise average and standard deviation of radius and curvature for the LAD, LCx and RCA arteries. The well known tapering behavior of arteries is observed in the radius plots. Ostium and distal values agree with those previously reported in [94, 31]. Point-wise curvature shows different behavior in each artery: the LAD tends to have a fairly straight proximal third, while curvature increases as it describes a meandering path; the LCx rises from the LM with high curvature as it deviates to the left atrioventricular sulcus, traverses the sulcus at a fairly constant curvature and only presents large variations at the most distal part; in turn, the RCA does not present a region of constant mean curvature, which is due to the mix of patients with C and Σ-shaped arteries.

For the patient sample considered in this work, a total of 92 different arteries were labeled, the mean frequency of appearance was $\bar{F} = 10 \pm 14$. Figure 5.2 presents the frequency (F) of arteries such that $F_{\mathscr{A}} \geq \bar{F}$. The main arteries, LAD, LCx and RCA are present in all patients, while the left main artery (LM) is absent in one patient, in which the LCx branches from the right sinus of valsalva (pathology known as anomalous origin of coronary artery from opposite sinus (AOCAOS) [108], which is rare). The ramus intermedius artery (RI) was identified in cases of trifurcations of the LM artery, and was present in 27% of patients, which agrees with data reported in [345]. The high frequency of the right posterior descending arteries (RPD) and right posterolateral segment arteries (RPLSA) relative to their left counterparts is explained by circulation dominance. For our patient sample, 87.5% has right-dominant, 6.25% left-dominant and 6.25% has co-dominant circulation, which agrees with the literature [108]. The criterion used to identify circulation dominance was the following: Right, if the RPD1[1] artery was present and the {LPLSA[2], LPDA1[3]} are not present, for patients were image quality did not allow segmentation of RPDA and do not have LPLSA neither LPDA1, but the RCA was larger than the mean (120 mm) right dominance was assumed; Left, if the patient has LPLSA and LPDA1 arteries but does not have RPDA1, left-dominance was considered; Co-dominant circulation was identified when patients are neither left nor right dominant. The artery to the sinoatrial was identified as the first atrial branch of the RCA or of the LCx (labels RCA_AB1 and LCx_AB1) which was found in 54% and 33% of the patient population, respectively, and which also agrees with anatomical reports [108]. These data suggest that we are using a representative sample in terms of anatomical description of the coronary vasculature.

Image quality and resolution limits the segmentation of small arteries to small proximal segments, which are sufficient to compute rising angles, but not to perform significant

---

[1]First right posterior descending artery.
[2]Left posterolateral segment artery.
[3]First left posterior descending artery.
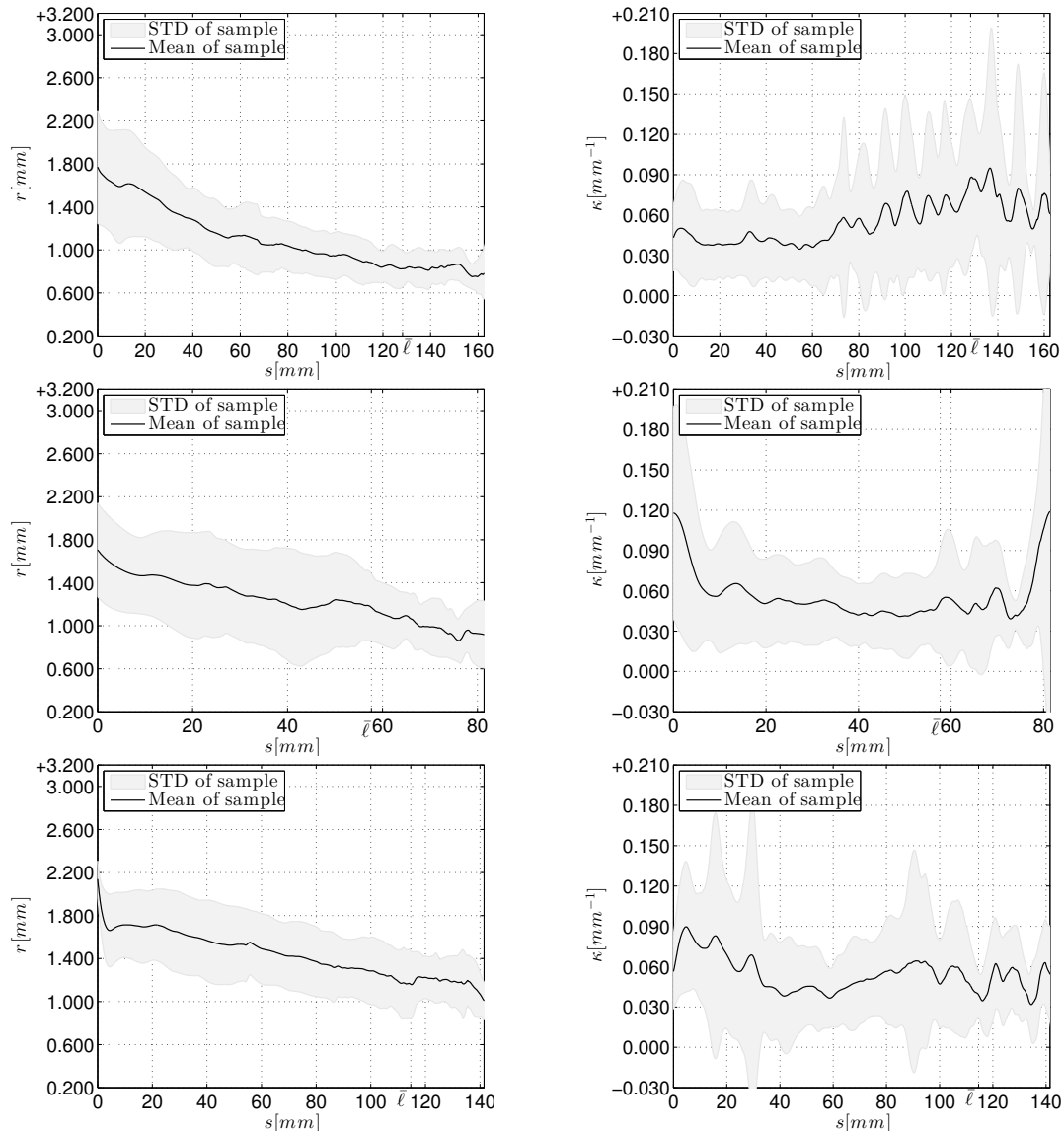
Figure 5.1: Point-wise variables, radius (left column) and curvature (right column) along LAD (top row), LCx (mid row) and RCA (bottom row).

geometric characterization of such small arteries. Figure 5.3 presents box plots of some geometric descriptors for relevant arteries. In the construction of these plots, only arteries larger than 15 mm in length were taken into account.

Our data indicates that the major coronary arteries (LAD, LCx and RCA) have a mean length of roughly 130, 60 and 120 mm, respectively, which matches anatomical data [349, 345]. Mean lengths of diagonal and obtuse branches of the LAD and LCx tend to decrease from proximal to distal, while proximal branches of the RCA are shorter than mid-distal ones.

Arterial radius is commonly discriminated among ostium and proximal-middle-distal tracks, because arteries generally taper in diameter, and usually, measures are taken at a single point for clinical usage [94, 345, 31]. This explains underestimation of the mean radius feature, when compared to the literature, and the smaller $\bar{r}$ value of the LAD when compared to the other two major arteries. As expected, mean radii of bifurcating branches are smaller. The RPDA and RPLSA typically rise from the end point of the RCA and
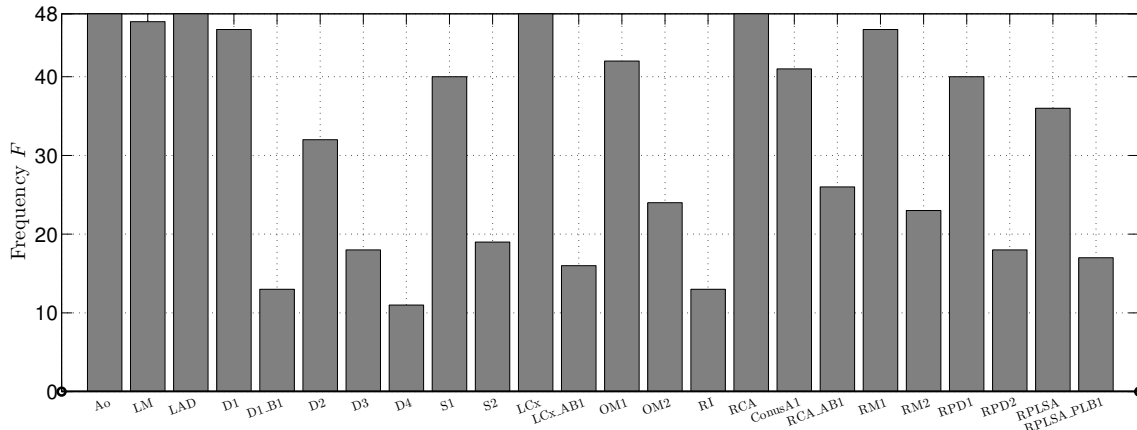
Figure 5.2: Appearance frequency of arteries with $F_{\mathscr{A}} \geq \bar{F} = 10$. For notation, refer to Appendix B.

therefore are continuations rather than side branches (ConusA[4], RM[5]), this explains the increase in mean radius of those arteries compared to proximal branches of the RCA.

Tortuosity of the major arteries is larger than those of branching vessels mainly because of their path over the myocardium surface. By definition, see equation (3.1.1), larger values of length and small euclidean distance between ostium and terminal points imply larger tortuosity. These conditions are present in all three major arteries: the RCA and LCx traverse the atrioventricular sulcus towards the crux, which is reached by the RCA in most cases (right circulation dominance), which explains the higher tortuosity of the RCA when compared to the LCx. The LAD artery travels into the upper portion of the interventricular sulcus, and continues towards the apex of the heart, in the cases when the artery passes the apex, the euclidean distance decreases, resulting in increased tortuosity. These loop-back paths are characteristics of these long arteries, and explain smaller tortuosity in the other branches.

On the other hand, mean curvature shows a different distribution when compared to tortuosity. Although the main arteries have similar mean curvatures, the branches tend to have larger values as their bending is more pronounced in space. It was found that the left subtrees (originating from the LAD and LCx) have similar mean curvature and were smaller when compared to those of the right subtree.

Clinical literature addressing bifurcation angle quantification can be based on in-vivo images or ex-vivo dissections. There are many forms of measuring angles. For example, in three-dimensional images three angles of take-off of the RCA and LM can be considered. They are measured in relation to the axis of the aortic root in three planes: seen from above (equivalent to the transversal plane), seen from lateral (equivalent to the sagittal plane) and seen from the front (equivalent to the coronal plane) [345]. The angle measuring technique employed in this work is objective and well defined for all arteries (see Chapter 2, Section 2.3.5). It was found that the septal branches of the LAD had wider bifurcation angles than the diagonals, while the latter had larger rising angles than the obtuse marginals of the LCx artery. The LCx had a wider rising angle than the LAD, which is sometimes considered as the LM continuation [108]. In the right tree, branches arise with larger angles except for the terminal branches.

---

[4]Conus artery

[5]Right marginal artery.
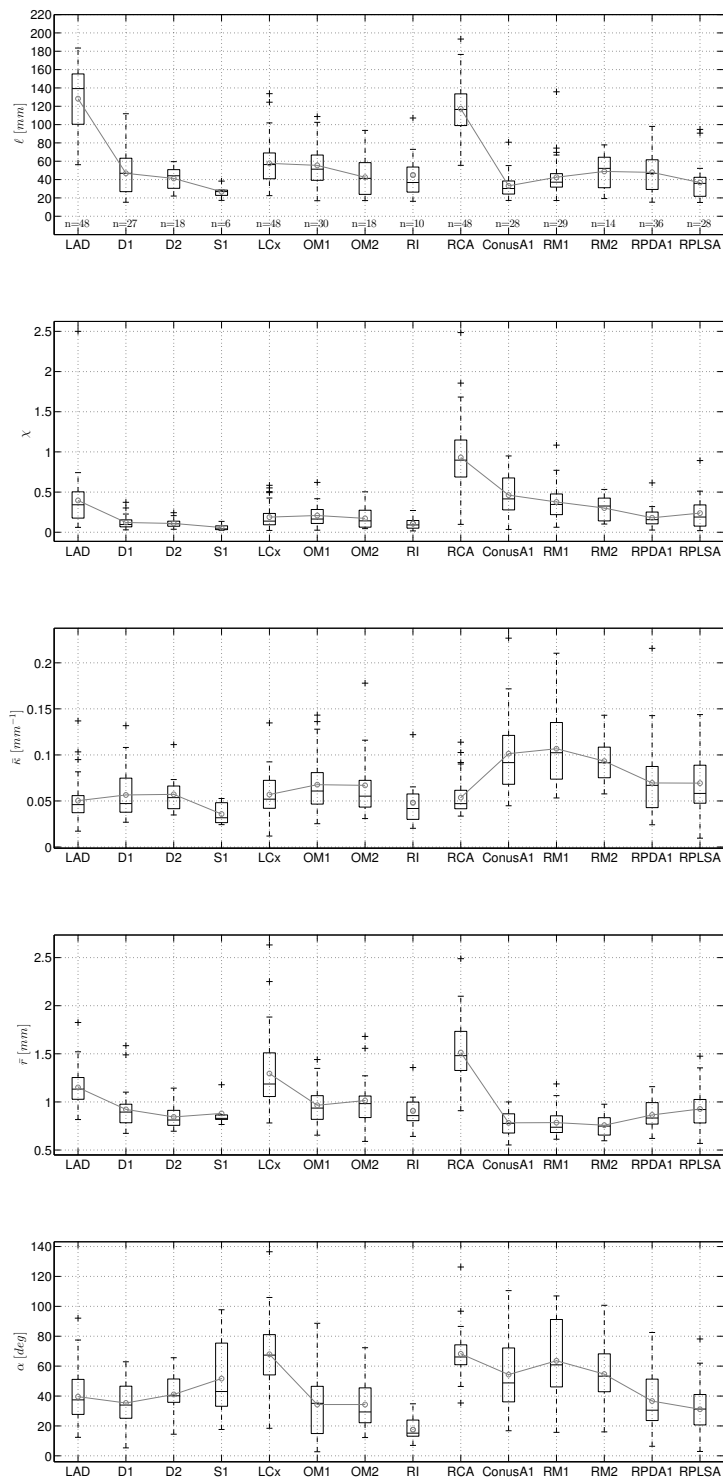
Figure 5.3: From top to bottom, box plots of length, tortuosity, mean curvature, mean radius and rising angle distribution along the most relevant coronary arteries that satisfied a cut-off criterion of $\ell \geq 15$ mm. The occurrence of each artery (n) is presented in the length plot. Gray circles and lines indicate mean values, and link connected arteries.

5.2.2 Association among geometric features

In Chapter 3, we have incorporated morphometric descriptors to complement the simpler measures reported in the specialized literature. But we can further analyze the feature space by identifying relationship between descriptors intra and inter arteries. Figure 5.4 presents significant feature correlations ($p < 0.01$) through hive and arc plots for the three major arteries. The Spearman correlation coefficient was used for continuous and ordinal variables. Features representing minima and maxima were skipped. In all plots, red links between arteries stand for positive correlation, and blue ones for negative correlation.

5.2.2.1 Intra-arterial correlation

Similar association patterns are observed in the three arc graphs in Figure 5.4, i.e:

- Correlation among curvature derived features;

- Lack of strong association between lesion number (η) and any geometric feature, for the chosen level of significance;

- Negative correlations involve entropy (H_κ) and pressure (P_κ) derived from point-wise curvature;

- Mean and total torsion ($\bar{\tau}, \tau_T$) only correlate with each other. This behavior is attributed to the fact that point-wise τ can be positive or negative, but the absolute value is not accounted in these two features, while τ^2 is used in the other torsion derived features;

Most of the feature associations were somehow expected since many features depend on point-wise or average values of other features, e.g. $\bar{\kappa}, \kappa_T, \bar{\zeta}$, or ℓ and χ, indicating that two descriptors characterize similar geometric aspects. Besides, it is observed that features of the RCA are more correlated when compared to the LAD and LCx, the latter presenting fewer strong correlations.

Nevertheless, there are some relationships that are characteristics of each artery, e.g.:

- Angle α only correlates with other features (particularly the $\bar{\kappa}$) in the LCx;

- In the LCx and LAD, the number of visible (large) branches Υ is positively correlated to the mean rising angle of the offspring (β). Although Υ increases with $\bar{r}$ in the three arteries, only in the LCx a strong correlation exists between Υ and ℓ;

- An expected negative correlation is present between $\bar{r}$ and Λ_r in the LCx and RCA, but it is not present at the LAD with the current level of statistical confidence;

- The average distal curvature $\bar{\kappa}_d$, presents more associations with other features in the LAD than in the other arteries;

- Curvature-derived thermodynamics, present different association patterns in the three arteries, i.e. few correlations in the LCx, more positive correlations involving T_κ in the LAD, and more negative correlations involving P_κ in the RCA. These differences may be explained by the characterized point-wise distribution of κ in the arteries (see Figure 5.1)

5.2.2.2 Inter-arterial correlation

Several observations can be made from the analysis of inter arterial feature correlation, summarized below:

- Curvature derived features are correlated among the three arteries;

- Mean radius and aspect ratio are somehow related among the three arteries, suggesting a global relationship of vascular caliber;

- Positive lesion correlation among the three arteries suggests an increasing risk of developing three vessel disease, when individual arteries are compromised. These result agrees with the fact that all patient present at least one systemic risk factor, which increase risk of atherosclerosis at a systemic level;

- The high number of association between features of the LCx and RCA, when compared to the LAD, can be explained by the fact that both arteries run analogous paths over the heart anatomy, travel the left and right atrioventricular sulcus respectively. Therefore, a global geometric similarity is expected,

These findings suggest that descriptors reflect a global geometrical structure, where the complete coronary tree tends to present larger or smaller arterial curvature and lumen radius.
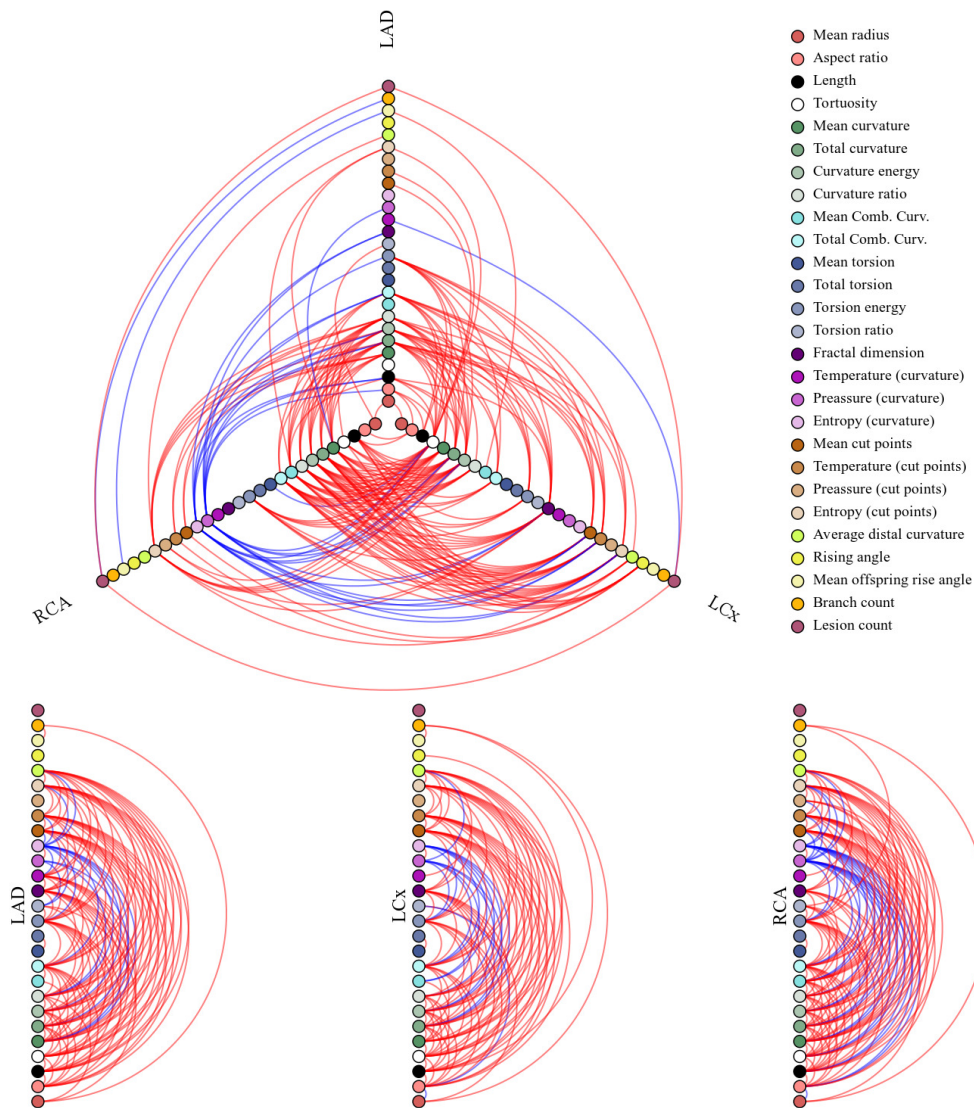
Figure 5.4: Features relationship for the LAD, LCx and RCA arteries. Inter arterial features correlation in a hive plot at the top, intra arterial features correlations at the bottom.

5.3 Geometric features of the RCA

Up to date, the shape of the coronary arteries is not to be a known risk factor for CAD. In turn, there is evidence that the shape of the right coronary artery (RCA), which is known to be C or Σ shaped, is influential. Dvir et. al. [100] first pointed out that short RCA where associated to arterial narrowing. In a successive work [101], the RCA shape was studied by the first time, exploring the association to the length and the presence of lesions. Thus, it was found that C-shape are shorter than Σ-shape RCAs and also associated to lesion presence. More recently, [23] reported that flow-mediated endothelium-dependent dilation in the brachial artery is significantly higher in Σ-shaped compared to C-shaped, suggesting a potential mechanism whereby C-shaped RCA are susceptible to atherosclerosis. Other groups [89], showed that C-shape is an independent predictor of significant CAD. All these studies rely on invasive angiographic images, and manual measurements to classify the RCA shape. In this section, the association between RCA shape and the geometric features, introduced in Chapter 3, is explored. Shape classification methods, based on the true geometry of the RCA obtained from noninvasive

CCTA images, are tested with encouraging results.

The RCA shape was classified by an specialized cardiologist from the constructed geometrical models. Different classification criteria had been used in the literature. For example, some authors [101, 89] define shape from manual measurements of distance in the angiographic image, which must be acquired following a specific protocol. In this work, the criterion defined in [23] was used: Σ-*shape arteries have an indentation of at least the width of the artery. Any RCA that did not comply with this definition is defined as C-shape RCA.*

From the original sample of 48 patients, one arterial model could not be classified because the RCA was too short. This patient and the associated sibling were removed from the sample used in the section. Expert classification resulted in 30 C and 16 Σ shaped arteries.

Geometric descriptors association to RCA-shape can be identified by standard Mann-Whitney U-Test. Figure 5.5 presents box-plots of features with statistically significant ($p < 0.05$ in the U-Test) difference in the mean values between C-shape and Σ-shape RCA. Note that feature values have been normalized to have sample-wide zero mean and unitary standard deviation. Minimum-maximum based features where not included in this test. Results indicate that:

- With the exception of the entropy derived from curvature (H_κ) and the associated pressure (P_κ), all the other feature values are greater for the Σ-shape group.

- The rising angle of the RCA (α), branch count (Υ) and offspring mean rising angle (β) are not associated to the RCA shape.

- Although the mean radius ($\bar{r}$) is not directly associated to the RCA shape, the curvature and torsion ratios ($\Lambda_\kappa, \Lambda_\tau$), which combine spatially distributed radii with curvature and torsion respectively, are different between groups.

- Curvature derived features are strongly associated to the RCA-shape.

- Regarding the thermodynamic descriptors introduced in Chapter 3 (see Section 3.2.2), it was found that all, except for curvature-derived temperature (T_κ), are associated to the RCA shape. Particularly, the entropy associated to the number of intersections between the curve and planes (H_n) obtained the second smallest p-value.

- The number of lesions is not different between groups. Furthermore, association between lesion presence and RCA shape was tested using the standard χ^2 test, resulting in no significant association ($p \simeq 0.7$). The lack of agreement with reported data in the literature [101] could be related to the small sample size.

The Andrew's plot [19] is a widespread visualization method in data mining that allows inspection of multidimensional data in two dimensions. In a nutshell, the technique transforms each *observation* to a function $A(t)$ of a dummy variable $t \in [0, 1]$. In this context, an observation is a RCA defined by a real vector, $\mathbf{f} \in \mathbb{R}^n, \quad n = 17$, constructed from the values of the subset of geometric descriptors listed in Figure 5.5. In this work, we use the following Andrew's transformation

$$A(t) = \frac{f_{(1)}}{\sqrt{2}} + \sum_{i=1}^{\lfloor n/2 \rfloor} f_{(2i)} \sin(2i\pi t) + \sum_{i=2}^{\lceil n/2 \rceil} f_{(2i-1)} \cos(2(i-1)\pi t) \quad \forall t \in [0, 1]. \qquad (5.3.1)$$

The Andrew's function of each RCA are presented in Figure 5.6a, and the median and quantiles enclosing the 50% of each group are presented in Figure 5.6b. From this

representation the difference among the C and Σ shapes are better appreciated in the extremes of the mapped function, where the Σ shaped arteries achieve higher values; a general difference in the phase of the functions can also be visualized.
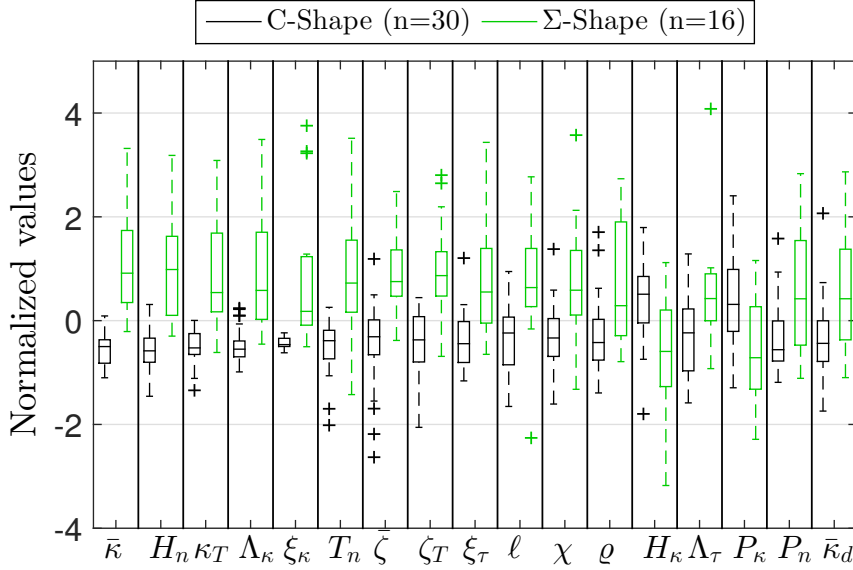
Figure 5.5: Sub-set of features with statistically significant ($p < 0.05$) difference in mean values for the C and Σ shaped RCA. Features are sorted from left to right in ascending order of the associated p-value.
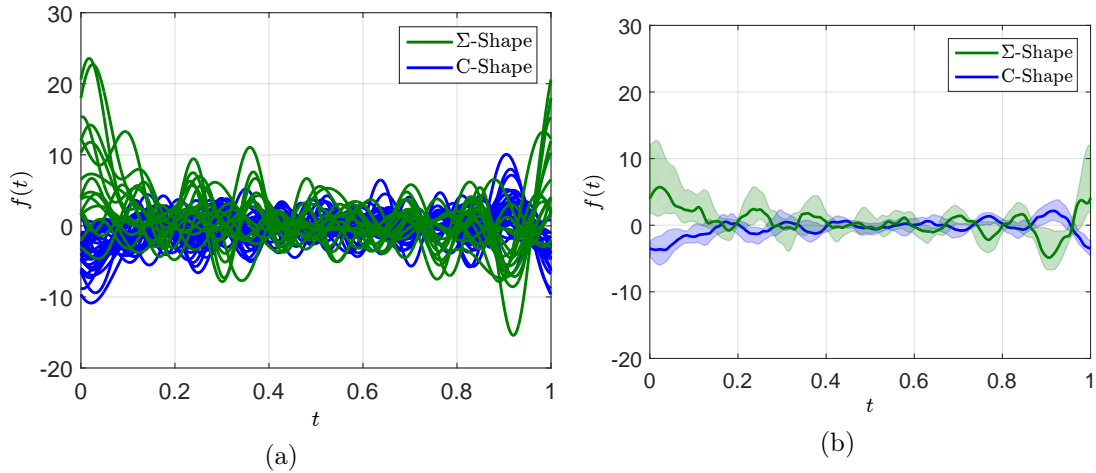
Figure 5.6: Panel (a) presents the Andrew's plot of the individual 46 analyzed RCAs. Panel (b) shows the medians and quantiles enclosing the 50% of the samples of each group.

The association between the subset of features in Figure 5.5 and RCA shape indicates that classification is possible. As a proof of concept, a linear and a kernel density classifiers were tested. For the linear case, recalling Chapter 4 (see Section 4.3.1) the classification variable c for each artery is defined as $c = \mathbf{w} \cdot \mathbf{f}$, where $\mathbf{f} \in \mathbb{R}^n$ is the features vector ($n = 17$), and $\mathbf{w} \in \mathbb{R}^n$ is a weighting vector. In this example, $w_i = -1 \quad \forall i \neq \{H_\kappa, P_\kappa\}$ and $w_i = 1$ otherwise. Recalling Figure 5.5, and considering the given weight vector, it is expected that Σ-shape RCAs score smaller c values than C-shape arteries. Therefore, given a threshold value $\hat{c}$, the classifier identifies $c < t$ as a Σ-shape artery. Figure 5.7a shows the classifier score for different values of the cut-off variable t. The percentage of Σ-shape in the patient sample accordingly to the expert classification is 34.78% (prevalence). Particularly,

for $t = -2$, it was found that

- The proportion of correctly identified Σ-shape arteries is 87.50% (*sensitivity*).

- The proportion of correctly identified C-shape arteries is 96.67% (*specificity*).

- The proportion of correctly classified RCAs is 93.48% (*accuracy*).

The receiver operator curve (ROC) of the classifier is presented in Figure 5.7b. The ROC illustrates the performance of the classifier for different values of the threshold parameter (t). A random classification would produce a diagonal line known as the line of no-discrimination. A perfect classification would produce a line from $(0,1)$ to $(1,1)$. To quantify the ROC, the area under the curve (AUC) is used. In the context of this example, the AUC measures the probability that a randomly selected Σ-shape artery scores a c value lower than a randomly selected C-shape. For the chosen weighting vector, the AUC=0.9490, which is very close to 1 (the AUC of a perfect classifier).

$$(a) \qquad\qquad\qquad (b)$$
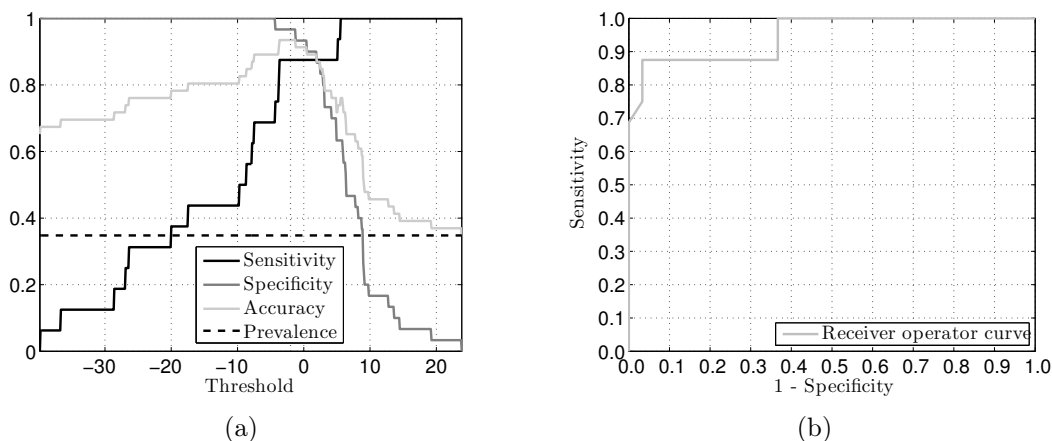
Figure 5.7: Panel (a) presents the sensitivity, specificity and accuracy of the binary classifier for a wide range of cut-off values. Panel (b) shows the associated receiver operator curve.

Regarding multivariate kernel density classification[6] (see Chapter 4, Section 4.3.2), a feature selection problem was solved in order to choose the feature set such that classification score is maximum. We tested the standards sequential (forward and backward) feature-selection strategies, also the features sets containing the complete set (25 features), only geometric (19 features), only thermodynamic (6 features), and the one specified by the U-Test, Figure 5.5. All of these sets resulted in suboptimal classification scores when compared with a "brute force" search of a 6-feature set that maximizes the average of the LOOCV classification scores. We call such feature set $\mathscr{F}_{B6}$ and, for the sake of clarity, we only present results using such set.

Table 5.3 presents the performance of the classifier using leave-one-out cross-validation. The brute-force search yields $\mathscr{F}_{B6} = \{\bar{\kappa}, \zeta_T, \Lambda_r, \Lambda_\tau, T_n, H_n\}$.

This results emphasizes the association between geometric features of the RCA and the characteristic shape of the artery, demonstrating that automatic classification is possible. Further analysis on the heritability of the RCA shape between siblings are presented in Section 5.5.

---

[6]Tests using the well-known naive KDC were also performed, but with sub-optimal results when compared to multivariate KDC.

	$\mathscr{F}_{B6}$ (34.8%)
Acc.	0.96
Sen.	0.88
Spe.	1.00
PPV	1.00
NPV	0.94

Table 5.3: Multivariate kernel density classification scores for LOOCV. The prevalence indicated in parentheses, of the Σ-shape is 34.8%.

5.4 Arterial geometric likelihood in siblings

In this section, we make use of the mathematical framework and similarity indexes introduced in Chapter 4 (see Section 4.1) to test for relative likelihood of coronary arterial geometry between siblings. In this section, only the conventional features listed in Table 3.1 were used. Table 5.4 presents the subsets of features that minimize the rSRI for each arterial selection. Those minimizing subsets were found through a brute force algorithm, except $\mathcal{G}_{\min}^{3A}$, which is defined as the union of the minimizing subsets for each artery.

$\mathcal{S}_{\mathscr{A}}$	$\mathcal{G}_{\min}^{\mathscr{A}}$	
$\mathcal{S}_{\text{LAD}}$	$\mathcal{G}_{\min}^{\text{LAD}}$	$= \{\chi, \bar{r}, r_m, \kappa_M, \tau_m, \bar{\zeta}, \zeta_m, \zeta_M, \xi_\kappa, \Upsilon\}$
$\mathcal{S}_{\text{LCx}}$	$\mathcal{G}_{\min}^{\text{LCx}}$	$= \{r_M, \kappa_T, \tau_m, \zeta_m, \beta\}$
$\mathcal{S}_{\text{RCA}}$	$\mathcal{G}_{\min}^{\text{RCA}}$	$= \{\bar{r}, \kappa_T, \zeta_M, \Lambda_r, \varrho, \beta\}$
$\mathcal{S}_{3A}$	$\mathcal{G}_{\min}^{3A}$	$= \{\mathcal{G}_{\min}^{\text{LAD}} \cup \mathcal{G}_{\min}^{\text{LCx}} \cup \mathcal{G}_{\min}^{\text{RCA}}\}$

Table 5.4: Subsets of features that minimize the SRI for each arterial subset.

In order to show the impact of geometric normalization, we perform some tests using two population samples, namely $\mathscr{P}_r$ and $\mathscr{P}_n$, both containing the entire patient sample, the former is based on the raw centerlines and the latter contains the normalized geometries, as explained in Chapter 2 (see Section 2.3.6). The entire set of features for the main coronary arteries ($\mathcal{G}_{\text{all}}^{3A}$) is used for each population, which produces the associated feature spaces $\mathscr{F}^p = \mathscr{F}(\mathcal{G}_{\text{all}}^{3Ap})$, where the subscript $p = \{r, n\}$ stands for the raw or normalized population. It is worthwhile to mention that the construction process of the feature space ensures a zero mean and unitary standard deviation in each dimension. Therefore, measuring dispersion through total variance is not an option, and the generalized variance is zero, suggesting strong correlation between variables. We make use of the ranking definition to estimate how much the normalization affects inter-patient distances. First, we compute the ranking matrices $\mathbf{M}^p \in \mathbb{R}^{|\mathscr{P}| \times (|\mathscr{P}|-1)}$ for each feature space, where row i contains the ranking list for patient i. Then, we subtract $\mathbf{M} = \mathbf{M}^r - \mathbf{M}^n$ and count the number of nonzero entries (z). Hence, we can calculate what we call the ranking dispersion index $\text{RDI} = z/(|\mathscr{P}| \times (|\mathscr{P}|-1)))$, which is zero when ranking remains identical as predicted by both feature spaces (with and without normalization), and has a maximal unitary value when the pattern of the ranking list of the patients has completely changed, i.e., all entries have nonzero values. Therefore, a value of RDI close to one indicates that normalization significantly changes the relative distances between patients. In this test we obtain $\text{RDI} = 0.7735$, indicating that the 77% of the ranking positions changed after the geometric normalization, furthermore, it was found that all patients changed position in some ranking list at least once.

Now, we proceed to show evidence of geometric likelihood between siblings when

compared to the rest of the population. This will be assessed using two tests, first we test if distance $d(\mathbf{a}, \mathbf{b})$ is smaller when $\mathbf{a}$ and $\mathbf{b}$ are siblings, and second we present results of the relative sibling ranking index (rSRI, see definition in Chapter 4, Section 4.1).

We performed a standard one-tailed Mann-Whitney U-Test, to show that the mean distance between siblings is smaller than the mean distance between non-sibling patients in the sample. Figure 5.8 presents box plots of the sibling and non-sibling distances, with means and the p-values for the test. The test was performed for the $\mathcal{G}_{\text{all}}^{3A}$ and $\mathcal{G}_{\text{min}}^{3A}$ features subsets using raw and normalized data. In all tests, the mean distance between siblings is smaller within the 5% of significance level. Furthermore, the result holds for both feature spaces, raw and normalized.

Figure 5.9 presents values of the rSRI for different feature sets (with and without normalization), constructed from the LAD, LCx and RCA arteries separately and considering the three vessels altogether, taking into account all features ($\mathcal{G}_{\text{all}}^{\mathscr{A}}$) and feature subsets that minimize the rSRI for each individual artery ($\mathcal{G}_{\text{min}}^{\mathscr{A}}$). The rSRI evaluation agrees with the U-Test outcomes, in the sense that it also points out the existence of a geometric likelihood between siblings when compared to the rest of the population.

Figure 5.10a presents the centerlines corresponding to the coronary networks for the entire raw data set. Centerlines were translated to have the origin in their aortic root, and rotated to register a reference geometry using the coherent point drift registration method [243]. Clustering of the main arteries (LAD, LCx and RCA) can be seen in the corresponding anatomical regions of the myocardium. Figure 5.10b presents a random patient $\mathbf{a} \in \mathscr{F}^r$ (in black), his sibling denoted by $\text{sib}(\mathbf{a}) \in \mathscr{F}^r$ (in green), the most similar $\mathbf{b} \in \mathscr{F}^r$ such that $r(\mathbf{a}, \mathbf{b}) = 1$ (in cyan) and the most different $\mathbf{c} \in \mathscr{F}^r$ such that $r(\mathbf{a}, \mathbf{c}) = |\mathscr{P}| - 1$ (in red). In this example, $r(\mathbf{a}, \text{sib}(\mathbf{a})) = 3$ indicating a strong similarity between both siblings, which can be qualitatively appreciated by the proximity of the black and green centerlines of the RCA, LAD and LCx (in that order). Patient $\mathbf{c}$ is clearly different from $\mathbf{a}, \text{sib}(\mathbf{a})$ and $\mathbf{b}$, for example the LCx and LAD are significantly shorter, and the RCA is clearly Σ-shaped while in the other patients RCA is C-shaped.
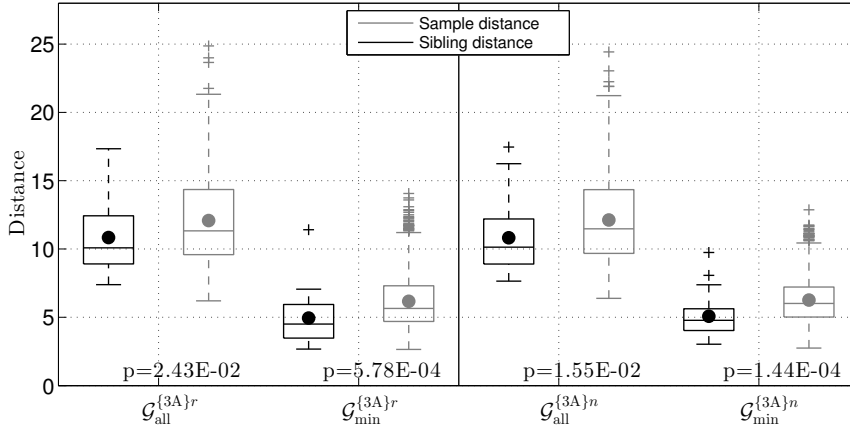
Figure 5.8: Box plot of the distance distribution between siblings (black-boxes) and characteristic distances among patients (gray-boxes) for different feature sets, using raw data (r, left) and normalized data (n, right). Mann-Whitney U-Test p-values are presented between the compared distributions, circle markers stand for the mean values.
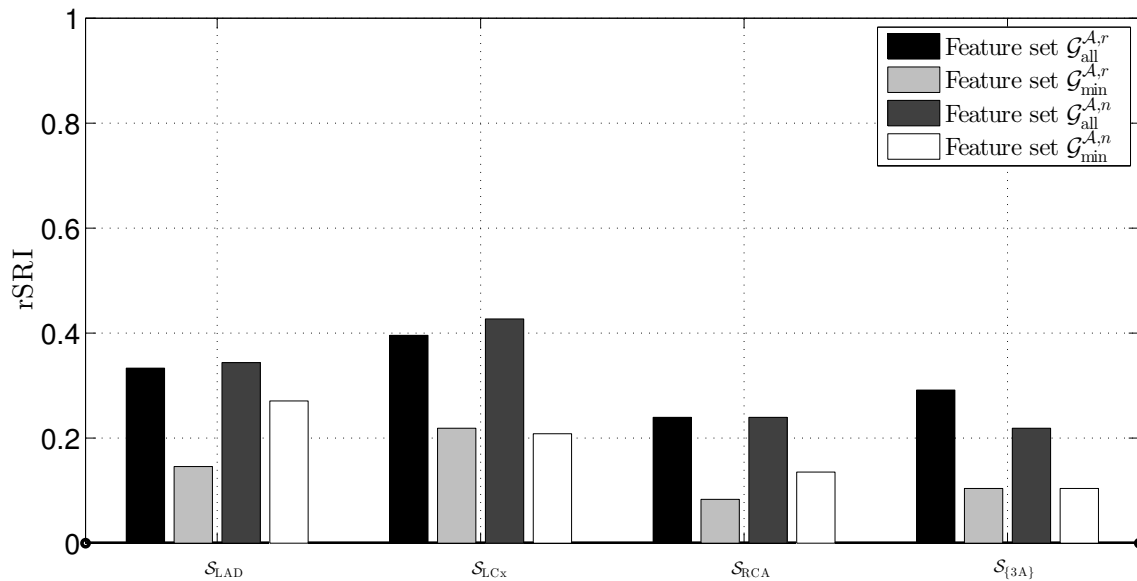
Figure 5.9: rSRI, for different arterial and features subsets, for raw and normalized data.

(a)

(b)
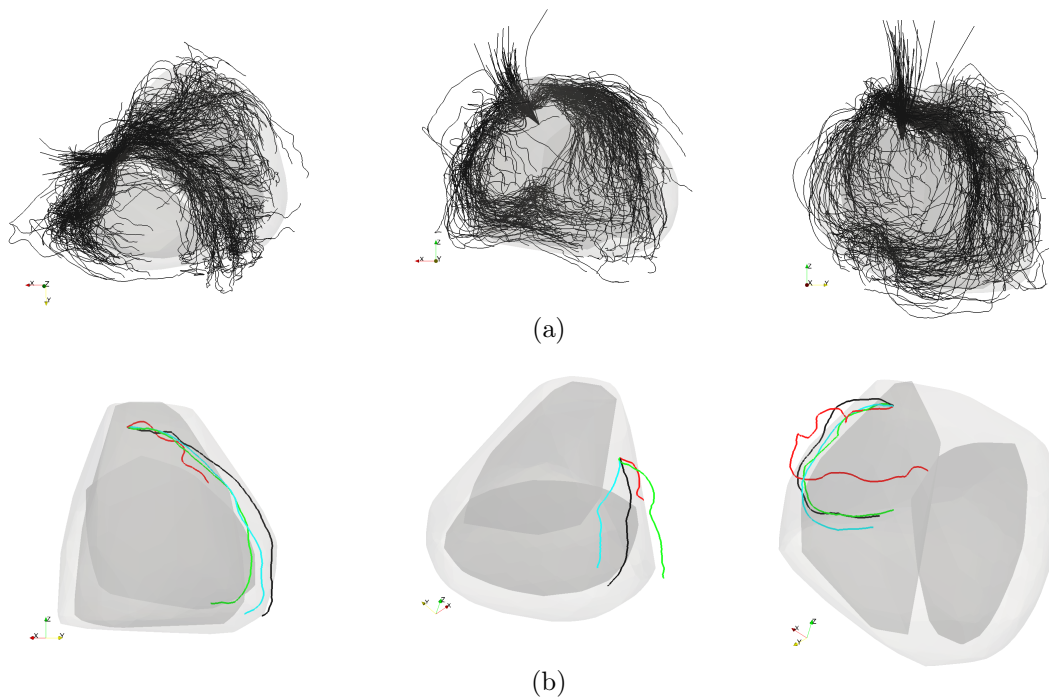
Figure 5.10: Panel (a) shows centerlines of the complete coronary networks for the entire patient sample, from left to right: transverse, coronal and sagital views; Panel (b) shows the LAD, LCx and RCA arteries of a random patient $\mathbf{a}$ (in black), his sibling sib($\mathbf{a}$) (in green), the most similar $\mathbf{b}$ such that $r(\mathbf{a}, \mathbf{b}) = 1$ (in cyan), and the most different $\mathbf{c} \in \mathscr{F}^r$ such that $r(\mathbf{a}, \mathbf{c}) = |\mathscr{P}| - 1$ (in red).

5.5   Heritability of individual features

Standard statistical indicators, summarized in Chapter 4 (see Section 4.2.5), are used to analyze the different arterial descriptors for each one of the major coronary arteries. In the context of this section, geometric feature, variable and phenotype are used interchangeably. Recalling that statistical indicators for binary and continuous variables are employed, binary features were tested directly, while continuous features were tested after being dichotomized, using the mean value of the feature for the patient sample as a cutoff value (i.e. hereafter, saying that a patient tested positive for a given feature, means that the feature value is larger than the mean of the sample); therefore, these types of tests should be interpreted as an association of the feature between siblings relative to the sample-mean value of the feature.

Association between phenotypes and presence of lesion is assessed by means of standards two-tailed χ^2 and Mann-Whitney (U) tests. Statistical significance is assumed at 95% confident interval.

5.5.1   Geometric features of the LAD in siblings

Table 5.5 presents the quantitative values for all indicators presented in Chapter 4 (see Section 4.2.5), when assessing individual geometric features of the LAD in the patient sample. From these results, it can be inferred that there is a relationship between geometric descriptors of the LAD artery between siblings, particularly, it is noteworthy to remark the following.

- The *lesion presence* in the LAD, which is a binary phenotype, obtained the highest values of PBWR, indicating that the probability of a patient having a lesion in the LAD increases if his sibling has a lesion in the same artery. The SimI test also indicates the chances of both siblings having the same LAD status (healthy or diseased) is high (70%). It was found that the RR is high (2.22) and statistically significant (CI=[1.16,4.23]). Furthermore, the OR=5.71 (CI=[1.63, 19.95]) is also significant and credible (COR=3.62), with a moderate positive association (PHI=0.36), and a high Pw=0.82. These results agree with the literature reporting that familial history of CADs is a risk factor [9, 10].

- When dichotomizing continuous variables by the mean in the sample, it was found that:

  - Several geometric features score high PBWR.
  - The RR and OR result in statistically significant association, around 2 and 3.9 respectively, for the mean radius ($\bar{r}$), the mean combined curvature ($\bar{\zeta}$) and curvature-derived entropy (H_κ) although none of them satisfied the credibility criterion.
  - In turn, SimI> 0.5 for several features indicates that the probability of both siblings having feature values greater or lower than the mean is high, especially for the tortuosity (χ) and lesion presence.

- Tests for continuous variables render the following results:

  - Pearson's correlation coefficient (ρ), scores significant values ($p_\rho < 0.05$) for tortuosity (χ), total curvature (κ_T) and bending energy (ξ_κ).
  - The ICC presented weak (but significant association) for the total curvature and torsion (κ_T, τ_T) , the bending energy (ξ_κ) and for the intersection counting temperature and entropy (T_n, H_n).

57

– The p-UTest is only significant (<0.05) for the curvature-derived entropy (H_κ). Recalling results of Section 5.4, these findings indicate that standalone features are not sufficient to show a significant similarity, when similarity is measured through distance in feature spaces.

– Although the rSRI < 0.5 for several variables, most of the scores were close to 0.5, indicating that the patients tend to be ranked slightly below half of the sample when comparing distances among the patient sample.

- Association between LAD phenotypes and presence of lesion showed significant levels for the following set of descriptors $\{\ell, \kappa_T, \zeta_T, \xi_\kappa, \varrho, \Upsilon, \beta, \bar{\kappa}_d, T_\kappa, T_n, H_n\}$. From this set, only the subset $\{\kappa_T, \zeta_T, \xi_\kappa, T_n, H_n\}$ scored some kind of heritability (ICC or ρ) different from the SimI. Section 5.7 explores in more detail the association of features and lesion in the LAD, and provides results for classification of healthy/diseased arteries from feature values.

Feature	PBWR	SimI	ρ	p-ρ	rSRI	p-UTest	ICC	p-ICC	RR	RR_CI_L	RR_CI_U	OR	OR_CI_L	OR_CI_U	PHI	COR	Pw	p- Chi^2	p-U-Test
Length	0.552	0.458	0.127	0.556	**0.417**	0.169	0.147	0.239	0.806	0.515	1.262	0.568	0.169	1.911	NaN	NaN	0.143	**0.026**	**0.005**
Tortuosity	0.400	**0.750**	**0.438**	**0.032**	**0.427**	0.109	0.108	0.301	2.533	0.881	7.284	3.556	0.765	16.528	NaN	NaN	0.403	0.067	0.062
Mean radius	0.636	**0.667**	0.300	0.154	**0.333**	0.074	0.312	0.062	**2.068**	**1.072**	**3.991**	**3.938**	**1.182**	**13.117**	0.287	9.096	0.631	0.633	0.448
Mean curvature	0.375	**0.583**	0.335	0.109	**0.479**	0.467	0.305	0.066	1.200	0.531	2.711	1.320	0.375	4.645	NaN	NaN	0.066	0.081	0.088
Total curvature	0.316	0.458	**0.474**	**0.019**	0.552	0.476	**0.371**	**0.032**	0.704	0.324	1.530	0.568	0.169	1.911	NaN	NaN	0.143	**0.028**	**0.014**
Mean torsion	0.571	**0.625**	0.180	0.401	**0.417**	0.094	0.187	0.182	1.714	0.895	3.282	2.667	0.821	8.659	NaN	NaN	0.375	0.289	0.448
Total torsion	0.571	**0.625**	0.355	0.089	**0.427**	0.288	**0.358**	**0.037**	1.714	0.895	3.282	2.667	0.821	8.659	NaN	NaN	0.375	0.289	0.357
Mean Comb. Curv.	0.636	**0.667**	0.179	0.403	**0.406**	0.137	0.186	0.183	**2.068**	**1.072**	**3.991**	**3.938**	**1.182**	**13.117**	0.287	9.096	0.631	0.533	0.498
Total Comb. Curv.	0.480	0.458	0.087	0.686	**0.490**	0.481	0.102	0.310	0.849	0.493	1.462	0.710	0.228	2.216	NaN	NaN	0.085	0.081	**0.037**
Aspect ratio	0.571	0.500	0.078	0.719	0.500	0.300	0.098	0.317	0.952	0.589	1.540	0.889	0.277	2.854	NaN	NaN	0.039	0.190	0.194
Curvature ratio	0.429	**0.667**	0.317	0.132	0.500	0.432	0.303	0.067	1.821	0.774	4.288	2.438	0.650	9.145	NaN	NaN	0.276	0.212	0.159
Torsion ratio	0.222	0.417	0.178	0.405	0.500	0.389	0.193	0.174	0.476	0.185	1.225	0.327	0.087	1.226	NaN	NaN	0.387	0.299	0.448
Bending energy	0.333	**0.667**	**0.725**	**0.000**	**0.479**	0.428	**0.338**	**0.047**	1.500	0.548	4.105	1.750	0.417	7.346	NaN	NaN	0.130	**0.017**	**0.008**
Twisting energy	0.476	**0.542**	0.174	0.417	0.531	0.561	0.194	0.173	1.169	0.617	2.214	1.322	0.419	4.176	NaN	NaN	0.069	0.088	0.074
Fractal dimension	0.522	**0.542**	0.188	0.379	**0.448**	0.270	0.183	0.188	1.186	0.657	2.140	1.388	0.445	4.329	NaN	NaN	0.081	**0.021**	**0.020**
Branch count	0.609	**0.625**	0.177	0.409	**0.406**	0.240	0.182	0.189	1.691	0.912	3.133	2.765	0.859	8.907	NaN	NaN	0.403	**0.018**	**0.036**
Rising angle	0.500	0.500	(0.006)	0.980	0.510	0.743	0.013	0.474	1.000	0.568	1.761	1.000	0.323	3.101	NaN	NaN	0.025	0.884	0.892
Mean offspring rise angle	0.545	**0.583**	0.032	0.882	0.542	0.781	0.052	0.401	1.418	0.764	2.631	1.920	0.606	6.080	NaN	NaN	0.196	**0.028**	0.060
Average distal curvature	0.316	0.458	0.057	0.790	**0.490**	0.615	0.048	0.408	0.704	0.324	1.530	0.568	0.169	1.911	NaN	NaN	0.143	**0.003**	**0.002**
Temperature (curvature)	0.417	0.417	(0.234)	0.270	0.573	0.892	(0.227)	0.864	0.714	0.399	1.278	0.510	0.162	1.608	NaN	NaN	0.207	**0.004**	**0.006**
Preassure (curvature)	0.667	**0.625**	0.067	0.756	**0.385**	0.186	0.077	0.355	1.556	0.887	2.727	2.667	0.821	8.659	NaN	NaN	0.375	0.493	0.607
Entropy (curvature)	0.692	**0.667**	0.196	0.359	**0.240**	**0.041**	0.167	0.209	**1.904**	**1.035**	**3.501**	**3.938**	**1.182**	**13.117**	0.287	9.096	0.631	0.755	0.665
Temperature (cut points)	0.571	**0.625**	0.396	0.055	**0.427**	0.251	**0.344**	**0.044**	1.714	0.895	3.282	2.667	0.821	8.659	NaN	NaN	0.375	**0.034**	**0.030**
Preassure (cut points)	0.615	**0.583**	0.180	0.401	**0.406**	0.337	0.121	0.279	1.354	0.782	2.345	1.920	0.606	6.080	NaN	NaN	0.196	0.271	0.291
Entropy (cut points)	0.609	**0.625**	0.404	0.050	**0.385**	0.173	**0.363**	**0.035**	1.691	0.912	3.133	2.765	0.859	8.907	NaN	NaN	0.403	0.051	**0.048**
Lesion Presence	0.741	**0.708**	NaN	NaN	**0.385**	0.185	NaN	NaN	**2.222**	**1.166**	**4.234**	**5.714**	**1.636**	**19.957**	**0.365**	**3.626**	**0.825**	NaN	NaN

Table 5.5: Statistical indicators of similarity of individual geometric features for the LAD artery.

5.5.2 Geometric features of the LCx in siblings

Table 5.6 presents the quantitative values for all indicators presented in Chapter 4 (see Section 4.2.5) when assessing individual geometric features of the LCx in the patient sample. In agreement with the results presented in Section 5.4, the LCx shows less heritability than the LAD and RCA (see Section 5.5.3). Particularly, we remark the following.

- The lesion presence in the LCx does not present statistically significant values of RR nor OR. Furthermore the PBWR and Pw are small. Such results indicate that for any given patient, it would not be appropriate to assume risk of lesion in the LCx, given that his sibling has a lesion in the same artery.

- When dichotomizing continuous variables by the mean of the sample yields:
  - Some geometric features score high PBWR.
  - The number of features with statistically significant values of RR and OR is reduced to four $\{\bar{\kappa}, \kappa_T, \zeta_m, T_\kappa\}$, and only the last one did not satisfy the credibility criterion.
  - The RR and OR scored significant values for the mean and total curvature $(\bar{\kappa}, \kappa_T)$ and T_n. Nevertheless, the credibility criterion was only satisfied by the $\bar{\kappa}$ and κ_T, both with good Pw, 82.5% and 78.5%.
  - In turn, SimI> 0.5 for several features indicates that the probability of both siblings having feature values larger or lower than the mean is high. Particularly for $\bar{\kappa}$ and κ_T.

- Test for continuous phenotypes was not statistically significant for any phenotype.

- Although the rSRI < 0.5 for several variables, most of the scores were close to 0.5, indicating that the patients tend to be ranked slightly below half of the sample when comparing distances among the patient sample.

- Association between LCx phenotypes and presence of lesions showed significant levels only for P_n and Λ_τ, none of which scored any kind of heritability.

Feature	PBWR	SimI	ρ	p-ρ	rSRI	p-UTest	ICC	p-ICC	RR	RR_CI_L	RR_CI_U	OR	OR_CI_L	OR_CI_U	PHI	COR	Pw	p- Chi^2	p-U-Test
Length	0.545	**0.583**	0.055	0.800	**0.323**	0.076	0.068	0.371	1.418	0.764	2.631	1.920	0.606	6.080	NaN	NaN	0.196	0.094	0.229
Tortuosity	0.476	**0.542**	(0.066)	0.758	**0.490**	0.440	(0.047)	0.587	1.169	0.617	2.214	1.322	0.419	4.176	NaN	NaN	0.069	0.240	0.080
Mean radius	0.526	**0.625**	(0.069)	0.750	**0.271**	0.128	(0.058)	0.608	1.696	0.850	3.382	2.469	0.747	8.163	NaN	NaN	0.320	0.394	0.439
Mean curvature	0.667	**0.708**	0.292	0.166	**0.344**	0.197	0.307	0.065	**2.571**	**1.270**	**5.208**	**5.714**	**1.636**	**19.957**	**0.365**	**3.626**	**0.825**	0.614	0.748
Total curvature	0.632	**0.708**	0.126	0.557	**0.365**	0.131	0.130	0.265	**2.617**	**1.260**	**5.435**	**5.388**	**1.525**	**19.029**	**0.347**	**4.169**	0.785	0.865	0.186
Mean torsion	0.462	0.417	(0.174)	0.417	0.552	0.808	(0.154)	0.771	0.725	0.430	1.222	0.490	0.153	1.565	NaN	NaN	0.223	0.738	0.642
Total torsion	0.480	0.458	(0.066)	0.761	0.510	0.481	(0.046)	0.585	0.849	0.493	1.462	0.710	0.228	2.216	NaN	NaN	0.085	0.868	0.660
Mean Comb. Curv.	0.545	**0.583**	0.401	0.052	**0.427**	0.074	0.404	0.021	1.418	0.764	2.631	1.920	0.606	6.080	NaN	NaN	0.196	0.316	0.300
Total Comb. Curv.	0.545	**0.583**	0.133	0.536	**0.479**	0.343	0.100	0.314	1.418	0.764	2.631	1.920	0.606	6.080	NaN	NaN	0.196	0.094	0.131
Aspect ratio	0.400	0.375	(0.098)	0.649	0.583	0.680	(0.072)	0.635	0.613	0.348	1.079	0.356	0.110	1.149	NaN	NaN	0.413	0.868	0.877
Curvature ratio	0.250	0.500	(0.095)	0.660	0.552	0.392	(0.067)	0.624	0.667	0.255	1.740	0.556	0.146	2.119	NaN	NaN	0.126	0.480	0.398
Torsion ratio	0.444	**0.583**	0.057	0.791	**0.479**	0.377	0.071	0.366	1.333	0.647	2.748	1.600	0.482	5.313	NaN	NaN	0.119	**0.016**	**0.020**
Bending energy	0.286	**0.583**	0.007	0.975	**0.375**	0.092	0.005	0.490	0.971	0.365	2.584	0.960	0.243	3.794	NaN	NaN	0.028	0.714	0.186
Twisting energy	0.375	**0.583**	(0.109)	0.613	**0.458**	0.194	(0.081)	0.650	1.200	0.531	2.711	1.320	0.375	4.645	NaN	NaN	0.066	0.480	0.098
Fractal dimension	0.476	**0.542**	0.004	0.984	**0.479**	0.351	0.024	0.452	1.169	0.617	2.214	1.322	0.419	4.176	NaN	NaN	0.069	0.065	0.098
Branch count	0.500	**0.583**	0.320	0.128	**0.375**	0.081	0.262	0.100	1.400	0.722	2.716	1.800	0.559	5.792	NaN	NaN	0.165	1.000	0.769
Rising angle	0.522	**0.542**	0.223	0.294	**0.448**	0.191	0.218	0.144	1.186	0.657	2.140	1.388	0.445	4.329	NaN	NaN	0.081	0.617	0.915
Mean offspring rise angle	0.500	**0.583**	0.070	0.746	**0.490**	0.446	0.077	0.354	1.400	0.722	2.716	1.800	0.559	5.792	NaN	NaN	0.165	0.499	0.202
Average distal curvature	0.375	**0.583**	0.219	0.304	**0.438**	0.288	0.235	0.126	1.200	0.531	2.711	1.320	0.375	4.645	NaN	NaN	0.066	0.480	0.660
Temperature (curvature)	0.333	0.333	(0.256)	0.228	0.542	0.645	(0.237)	0.874	**0.500**	**0.266**	**0.941**	**0.250**	**0.075**	**0.830**	0.375	0.125	0.645	0.505	0.766
Preassure (curvature)	0.667	**0.583**	0.089	0.680	0.521	0.591	0.106	0.303	1.200	0.739	1.948	1.600	0.482	5.313	NaN	NaN	0.119	0.731	0.385
Entropy (curvature)	0.667	**0.583**	(0.053)	0.806	**0.448**	0.296	(0.034)	0.563	1.200	0.739	1.948	1.600	0.482	5.313	NaN	NaN	0.119	0.731	0.279
Temperature (cut points)	0.545	**0.583**	0.034	0.873	0.510	0.525	0.055	0.394	1.418	0.764	2.631	1.920	0.606	6.080	NaN	NaN	0.196	0.094	0.194
Preassure (cut points)	0.462	0.417	(0.076)	0.725	0.531	0.612	(0.059)	0.610	0.725	0.430	1.222	0.490	0.153	1.565	NaN	NaN	0.223	**0.019**	**0.019**
Entropy (cut points)	0.545	**0.583**	0.037	0.865	0.521	0.511	0.057	0.391	1.418	0.764	2.631	1.920	0.606	6.080	NaN	NaN	0.196	0.094	0.179
Lesion Presence	0.167	**0.583**	NaN	NaN	0.531	0.581	NaN	NaN	0.600	0.152	2.362	0.520	0.097	2.802	NaN	NaN	0.095	NaN	NaN

Table 5.6: Statistical indicators of similarity of individual geometrical features for the LCx artery.

5.5.3   Geometric features of the RCA in siblings

Table 5.7 presents the quantitative values for all indicators presented in Chapter 4 (see Section 4.2.5), when assessing individual geometric features of the RCA in the patient sample. A large amount of statistically significant associations of feature between siblings was found. These results agree with those reported in Section 5.4, where it was shown that the RCA presents higher similarities between siblings than when compared to non siblings. Particularly, we remark the following.

- The lesion presence in the RCA, has moderate values of PBWR and SimI, 52% and 62% respectively. Nevertheless the RR and OR are not statistically significant.

- Dichotomization of continuous variables by the sample mean shows that:

    - Several geometric features score high PBWR, above 70%.

    - The number of features with significant values of RR and OR is larger than in the LAD and LCx cases, several of which also satisfied the credibility criterion and featured high Pw values.

    - Furthermore, it was obtained SimI> 0.5 for several features, resulting in larger values than in the LAD and LCx arteries for the same phenotypes. Particularly, for the bending energy (ξ_κ) reached a SimI$= 97\%$, scoring a perfect Pw.

- Test for continuous variables yielded:

    - Pearson's correlation coefficient (ρ) scored significant values ($p < 0.05$) for features in the set: $\{\ell, \chi, \bar{r}, \bar{\kappa}, \kappa_T, \zeta_T, \Lambda_r, \Lambda_\kappa, \xi_\kappa, \xi_\tau, \varrho, \bar{\kappa}_d, T_n, H_n\}$.

    - The ICC also scored statistically significant values for these features and for the mean offspring rise angle (β).

    - The p-UTest is also significant for a large subset of these features, emphasizing the results presented in Section 5.4.

    - It is worth noting that the rSRI < 0.5 for several features, like for the LAD and LCx; however, for the RCA smaller values are obtained.

- Finally, the RCA has two extra phenotypes, the Σ-shaped (binary variable) and classifier c variable studied in Section 5.3. The dichotomization of the c continuous variable was performed according to $t = -2$. Observe that a high degree of heritability of the arterial shape is indicated by almost all tests, for both phenotypes. Moreover, using the dichotomized value of the c variable produces better results. This indicates that, although two sibling patients may have different RCA-shapes (according to the expert observer), the shape characterized by the geometric features are similar enough to be classified in the same group by the binary classifier. For the c variable, it is observed that, the PBWR is high (> 0.65); the SimI indicates that is highly probable (87% chance) that both siblings have the same shape (C or Σ); The RR=8.267 (CI=[2.739, 24.954]) and OR= 37.333 (CI=[6.570, 212.132]) are statistically significant and the OR satisfied the credibility criterion (COR=2.587); showing a moderate positive association (PHI=0.654), and a high Pw=0.999. These results strongly indicate that the RCA shape may have a genetic contribution.

- None of the RCA phenotypes presented significant association to presence of lesions.

Feature	PBWR	SimI	ρ	p-ρ	rSRI	p-UTest	ICC	p-ICC	RR	RR_CI_L	RR_CI_U	OR	OR_CI_L	OR_CI_U	PHI	COR	Pw	p- Chi^2	p-U-Test
Length	0.696	**0.708**	**0.555**	**0.005**	0.302	**0.015**	**0.539**	**0.002**	**2.484**	**1.253**	**4.925**	**5.878**	**1.692**	**20.421**	**0.374**	**3.427**	**0.844**	0.951	0.899
Tortuosity	0.636	**0.667**	**0.480**	**0.018**	0.438	0.230	**0.489**	**0.006**	**2.068**	**1.072**	**3.991**	**3.938**	**1.182**	**13.117**	0.287	9.096	0.631	0.444	0.950
Mean radius	0.636	**0.667**	**0.622**	**0.001**	0.281	**0.002**	**0.586**	**0.001**	**2.068**	**1.072**	**3.991**	**3.938**	**1.182**	**13.117**	0.287	9.096	0.631	0.675	0.541
Mean curvature	0.667	**0.792**	**0.607**	**0.002**	0.417	0.094	**0.617**	**0.000**	**4.400**	**1.819**	**10.641**	**11.200**	**2.668**	**47.015**	**0.467**	**2.883**	**0.955**	0.551	0.555
Total curvature	0.714	**0.833**	**0.823**	**0.000**	0.354	**0.007**	**0.800**	**0.000**	**6.071**	**2.282**	**16.150**	**18.750**	**3.941**	**89.209**	**0.546**	**2.665**	**0.991**	0.317	0.704
Mean torsion	0.370	0.292	(0.189)	0.375	0.594	0.953	(0.161)	0.781	**0.458**	**0.268**	**0.780**	**0.138**	**0.036**	**0.529**	**0.481**	**0.291**	**0.892**	0.315	0.487
Total torsion	0.429	0.333	(0.161)	0.453	0.625	0.922	(0.130)	0.733	**0.536**	**0.331**	**0.866**	**0.188**	**0.050**	**0.707**	0.414	0.178	0.753	0.212	0.423
Mean Comb. Curv.	0.522	**0.542**	(0.025)	0.909	**0.354**	0.107	(0.018)	0.533	1.186	0.657	2.140	1.388	0.445	4.329	NaN	NaN	0.081	0.514	0.658
Total Comb. Curv.	0.727	**0.750**	**0.629**	**0.001**	0.344	**0.002**	**0.626**	**0.000**	**3.152**	**1.493**	**6.652**	**8.889**	**2.402**	**32.900**	**0.455**	**2.662**	**0.955**	0.863	0.643
Aspect ratio	0.571	**0.625**	**0.579**	**0.003**	**0.333**	**0.027**	**0.563**	**0.001**	1.714	0.895	3.282	2.667	0.821	8.659	NaN	NaN	0.375	0.315	1.000
Curvature ratio	0.750	**0.833**	**0.446**	**0.029**	0.406	**0.040**	**0.417**	**0.018**	**6.000**	**2.299**	**15.660**	**21.000**	**4.493**	**98.161**	**0.578**	**2.474**	**0.997**	0.835	0.720
Torsion ratio	0.435	0.458	0.063	0.771	**0.448**	0.407	0.064	0.379	0.836	0.459	1.522	0.710	0.228	2.216	NaN	NaN	0.085	0.597	0.264
Bending energy	0.800	**0.917**	**0.836**	**0.000**	0.354	**0.006**	**0.769**	**0.000**	**15.200**	**3.808**	**60.665**	**72.000**	**8.778**	**590.536**	**0.684**	**3.285**	**1.000**	0.155	0.628
Twisting energy	0.556	**0.667**	**0.523**	**0.009**	0.406	0.209	**0.508**	**0.004**	**2.083**	**1.011**	**4.293**	**3.438**	**1.002**	**11.790**	0.244	>>3.43	0.517	0.939	0.613
Fractal dimension	0.588	**0.708**	**0.483**	**0.017**	0.375	**0.042**	**0.493**	**0.005**	**2.605**	**1.214**	**5.590**	**4.898**	**1.360**	**17.639**	0.317	5.741	0.714	0.433	0.643
Branch count	0.667	**0.708**	0.316	0.133	0.302	**0.040**	0.284	0.081	**2.571**	**1.270**	**5.208**	**5.714**	**1.636**	**19.957**	0.365	**3.626**	**0.825**	0.853	0.983
Rising angle	0.421	**0.542**	0.065	0.762	**0.458**	0.404	0.066	0.375	1.110	0.549	2.243	1.190	0.366	3.872	NaN	NaN	0.048	0.372	0.158
Mean offspring rise angle	0.476	**0.542**	0.374	0.072	**0.344**	0.060	**0.391**	**0.025**	1.169	0.617	2.214	1.322	0.419	4.176	NaN	NaN	0.069	0.683	0.088
Average distal curvature	0.526	**0.625**	**0.472**	**0.020**	0.375	0.060	**0.472**	**0.008**	1.696	0.850	3.382	2.469	0.747	8.163	NaN	NaN	0.320	0.135	0.461
Temperature (curvature)	0.519	0.458	0.117	0.587	0.531	0.753	0.133	0.259	0.838	0.511	1.374	0.663	0.208	2.114	NaN	NaN	0.101	0.110	0.332
Preassure (curvature)	0.538	0.500	0.259	0.222	0.469	0.313	0.264	0.098	0.987	0.586	1.663	0.972	0.311	3.039	NaN	NaN	0.028	0.675	0.850
Entropy (curvature)	0.593	**0.542**	0.301	0.153	0.542	0.539	0.301	0.069	1.131	0.677	1.891	1.322	0.419	4.176	NaN	NaN	0.069	0.853	0.784
Temperature (cut points)	0.700	**0.750**	**0.519**	**0.009**	0.344	0.092	**0.458**	**0.010**	**3.267**	**1.520**	**7.021**	**8.556**	**2.297**	**31.871**	**0.443**	**2.772**	**0.943**	0.960	0.966
Preassure (cut points)	0.273	0.333	(0.054)	0.804	0.563	0.679	(0.117)	0.711	**0.443**	**0.210**	**0.935**	**0.234**	**0.069**	**0.799**	0.385	0.143	0.671	0.675	0.365
Entropy (cut points)	0.625	**0.750**	**0.732**	**0.000**	0.427	0.154	**0.602**	**0.001**	**3.333**	**1.475**	**7.531**	**7.222**	**1.879**	**27.755**	0.391	**3.496**	**0.866**	0.404	0.950
Lesion Presence	0.526	**0.625**	NaN	NaN	**0.448**	0.367	NaN	NaN	1.696	0.850	3.382	2.469	0.747	8.163	NaN	NaN	0.320	NaN	NaN
Σ-Shaped	0.625	**0.739**	NaN	NaN	0.326	**0.024**	NaN	NaN	**3.125**	**1.390**	**7.025**	**6.667**	**1.727**	**25.737**	**0.377**	**3.935**	**0.832**	0.702	0.715
Σ-Shaped (classifier c var.)	0.903	**0.870**	**0.664**	**0.001**	**0.402**	**0.023**	**0.637**	**0.000**	**4.516**	**1.631**	**12.507**	**37.333**	**6.570**	**212.132**	**0.654**	**2.587**	**1.000**	0.445	0.876

Table 5.7: Statistical indicators of similarity of individual geometrical features for the RCA artery.

5.6 Average distal curvature of the LAD

The behavior of the point-wise variables $r(s)$ and $\kappa(s)$ for each class, diseased (D) and healthy (H), of the LAD artery, was explored by averaging the variables over each subsample at each position s, which is discretized in an evenly-spaced scale and linearly interpolated for each patient. Figure 5.11 shows the point-wise average for radius and curvature, when normalizing the arc length to the interval $[0, 1]$. It can be observed that the average curvature in the distal section and the average radii in the proximal section of the subsample D are smaller than those of the subsample H. The behavior of the proximal radii is somehow expected since most of the stenoses of the sample are proximal or mid-vessel. Obviously, stenotic lesions are essentially related to the lumen area in the vicinity of the lesion. However, previous evidences have unequivocally documented the diffusiveness of the atherosclerotic process, being frequently present even in normal-looking vessel segments [84]. Therefore, using the vessel radius directly or implicitly to assess the relation to stenosis presence may be questionable.

In order to quantify the efficiency of the curvature as a risk indicator of stenosis, the average curvature of each artery $\bar{\kappa}_d$ was calculated over the distal portion of the segment. The fraction s_d that defines the distal length for averaging is taken as the control parameter. Figure 5.12 presents the area under the receiver-operator characteristic curve (AUC) of a classifier method based purely on $\bar{\kappa}_d$ for each value of s_d. In addition, right tailed Mann-Whitney U-Tests were also performed to assess statistically significant differences between healthy and diseased distributions of $\bar{\kappa}_d$. The results of these tests are also presented in Figure 5.12. It can be seen that an optimal partition exists when $s_d = 0.75$, that is, averaging over the distal 25% length of the artery.

(a)

(b)
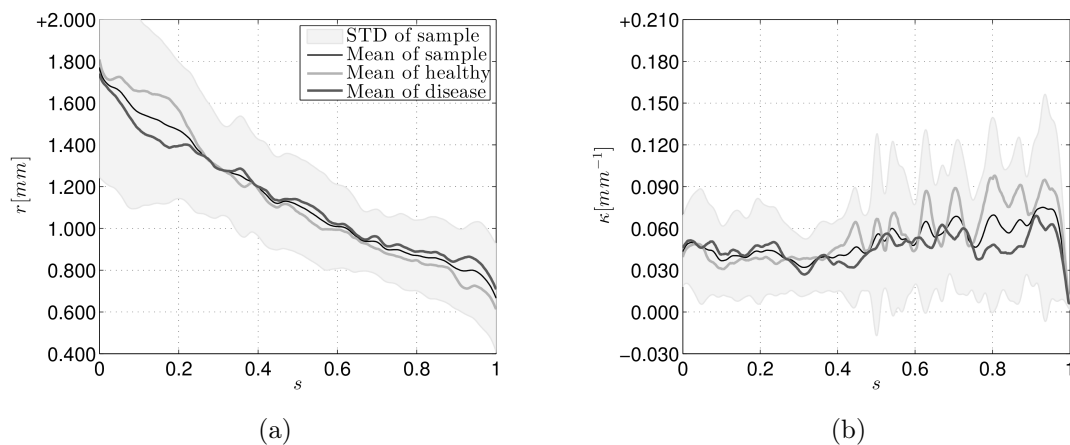
Figure 5.11: Comparison of the point-wise averages (curves) and STD (light-gray band) of the entire sample, the healthy and diseased subsamples. Artery inner radius (a) and curvature (b).

5.6.1 Arterial curvature analysis

Figure 5.13a presents a box plot of the distribution of $\bar{\kappa}_d$ for healthy and diseased LADs. Note that patients in the H group scored higher values (in average) than the D group ($p < 0.01$), implying that diseased vessels have, in average, less curved shape. Figure 5.13b shows statistical measures of the performance of the classifier as a function of the discriminating threshold of $\bar{\kappa}_d$. It was found that using a threshold $\bar{\kappa}_d = 0.0537 mm^{-1}$ maximizes the accuracy, sensitivity and specificity of the classifier. The associated receiver operator curve is displayed in Figure 5.13c. The optimal AUC score is 0.753. Table 5.8

Statistical summary	
Cut-off value	$0.0537\ mm^{-1}$
Sensitivity	0.7037
Specificity	0.8095
Accuracy	0.75
AUC	0.7531
PPV	0.8261
NPV	0.68
Median H	$0.067891\ mm^{-1}$
Median D	$0.048876\ mm^{-1}$
U	427
p-value	0.0012
Mean H	$0.07712\ mm^{-1}$
Mean D	$0.04795\ mm^{-1}$

Table 5.8: Mann-Whitney U-Test and classifier output associated to $s_d = 0.75$. The prevalence of the disease in the population is 56.25%.

details the classifier output and the right tailed U-Test used to determine if the mean value of $\bar{\kappa}_d$ was significantly higher in the H group, all using $s_d = 0.75$.

Figure 5.14 presents the centerlines of healthy and diseased LADs, and illustrates the difference between them. It can be qualitatively appreciated by visual inspection that the diseased arteries seem to be more straight than healthy ones.

The patient sample used in the present work is composed of siblings. Therefore, some standard test for heritability can be performed. When using the sibling condition (healthy or diseased LAD) as a boolean phenotype, it was found: (i) a high probability that a patient has a lesion given that his sibling has a lesion, given by the probandwise ratio [220] (PBWR=74%); (ii) the risk ratio or relative risk (RR) is statistically significant RR= 2.2 (with CI= [1.2, 4.2]); (iii) the odds ratio (OR) also scored a significant value OR= 5.7 (with CI= [1.6, 20.0]), satisfying the credibility criterion [216] (with a critical odds ratio COR= 3.6).

In turn, the average distal curvature ($\bar{\kappa}_d$), when used as phenotype, yielded no statistically significant outcomes for the Pearson's correlation coefficient (ρ), nor the interclass correlation coefficient (ICC). Furthermore, if the cut-off value $0.0537mm^{-1}$ is used to dichotomize the $\bar{\kappa}_d$ into a binary phenotype, none of the aforementioned indexes (PBWR, RR and OR) scored significant values.

Figure 5.15 presents a scatter plot of $\bar{\kappa}_d$ for each pair of siblings. Healthy and diseased LADs are represented with empty and filled circles respectively, the classifier cut-off value is also displayed. The lack of a strong heritability of the mean distal curvature as a standalone geometric descriptor suggests that this feature may be an independent predictor for CAD.

5.6.2 Association between curvature and lesion

Curvature patterns in LAD arteries have been characterized before by Zhu et al. [372] using a sample of healthy LADs. In that study, the distal section of the artery is defined as the fraction of the artery from the second diagonal branch to the arterial end, which in most cases brackets distal segments longer than the last 25% of the artery length. In that work, the reported median distal curvature of healthy LADs is $0.057mm^{-1}$, which is within the range of healthy arteries found in the present study, i.e. $\bar{\kappa}_d > 0.0537$.

Although the statement that LADs with straighter distal segments are more prone to present stenotic lesion appears counterintuitive at first sight, similar results have been
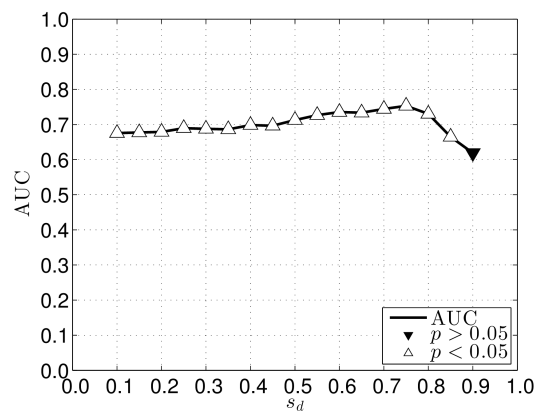
Figure 5.12: Area under the receiver-operator curve (AUC) and U-Test p-values for each partition point s_d.

(a)

(b)

(c)
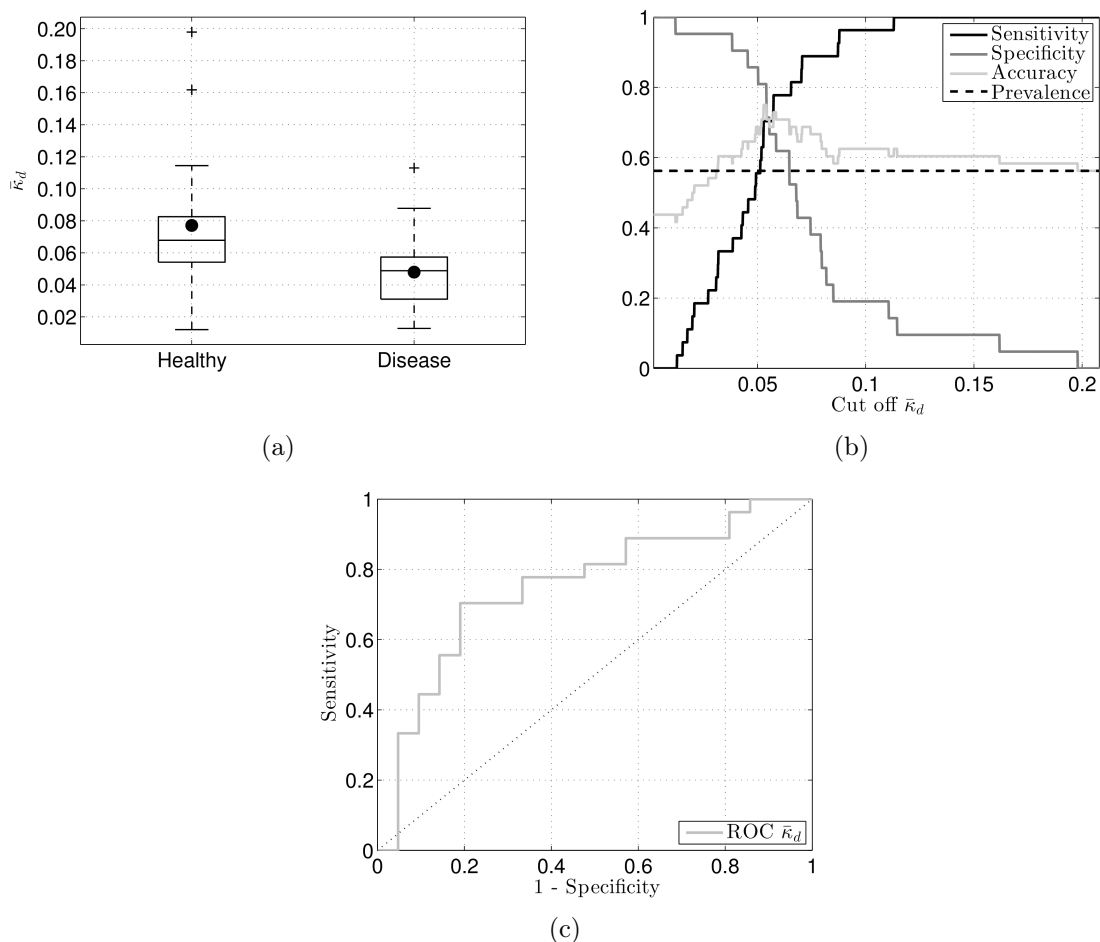
Figure 5.13: Panel (a) shows the box plot for $\bar{\kappa}_d$ distribution among healthy (H) and diseased (D) LADs, patients in the H group scored higher values (in mean) than the D group ($p < 0.01$). Panel (b) presents the performance of the classifier for a range of the $\bar{\kappa}_d$ cut-off value. Panel (c) shows the associated receiver-operator curve. Data correspond to a partition point $s_d = 0.75$.
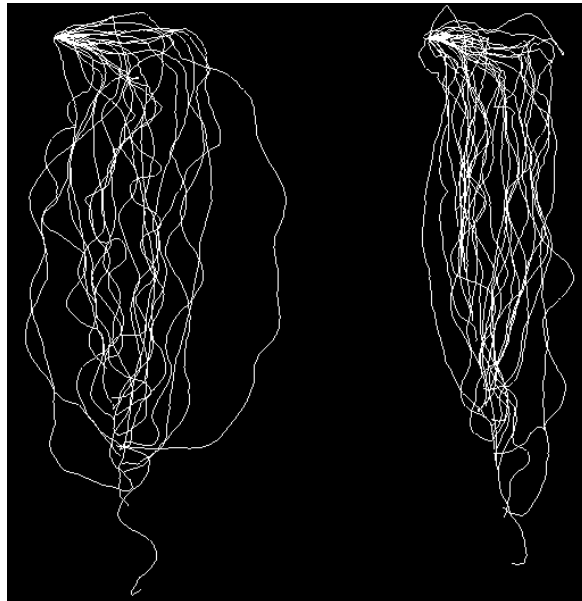
Figure 5.14: Illustration of the entire patient sample data. Healthy LAD centerlines are on the left, and diseased over the right.
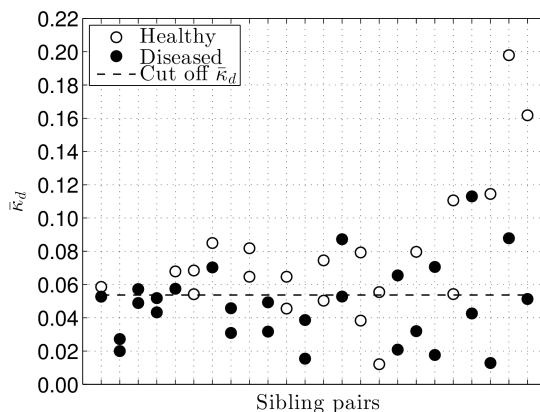
Figure 5.15: Scatter plot of average distal curvature ($s_d = 0.75$) for each pair of siblings.

previously reported for the right coronary artery (RCA). Dvir et al. [101] reported that C-shaped RCAs are associated with more atherosclerotic disease than Σ-shaped RCAs. Demirgab et al. [89] showed that C-shape is an independent predictor of significant CAD. Arbel et al. [23] reported that flow-mediated endothelium-dependent dilation in the brachial artery is significantly higher in Σ-shaped compared to C-shaped, suggesting a potential mechanism whereby C-shaped RCA are susceptible to atherosclerosis. In this context, it can be conjectured the existence of a global anatomical behavior of the coronary arterial network associated to plaque formation. The results of the present study support this conjecture. Following this rationale, we have recently shown [53] that curvature derived features in the main coronary arteries are positively correlated.

On the other hand, considering that the present study included a high-risk population, with all patients presenting at least one of the major systemic risk factor (smoker, hypertension, diabetes and/or dyslipidemia), one might hypothesize that high distal curvatures may represent a potential physiological protective mechanism against plaque formation in LAD arteries.

It is also possible that straightness of the distal LAD arteries is a consequence, not a cause, of the atherosclerotic process. In this scenario, the ultimate morphology of a coronary vessel would be shaped by the disease (as hypothesized in [23] for the RCA), and accordingly, atherosclerosis would cause arteries to change geometry over time. To the best of our knowledge, there is no register in the literature which has documented this trend so far, which indicates that this topic deserves further investigation.

5.7 Association between lesions and geometric features

Over the years, several risk factors for CAD has been identified, and a rough classification can be made as next: (i) Systemic factors, which comprise (i.a) modifiable risk factors (cigarette smoking, diabetes mellitus, hypertension, hypercholesterolemia, etc.), (i.b) non-traditional atherosclerosis predictors (C-reactive protein, lipoprotein(a), brinogen, homocysteine, etc.) [139], (i.c) familial history [314, 167, 148] and genetic contribution to susceptibility for CAD [253, 132, 104, 285, 287, 221]. (ii) Biomechanical predictors, which are expressed in terms of several indexes, e.g. wall shear stress and oscillatory shear index [120], and have been supported by evidence [189, 365, 123, 71, 82]. (iii) geometric risk factors [113], which suggest that the geometric variability of the human vasculature contributes to the development of atherosclerosis. In the context of this work, we highlight that several clinical observations back up the geometric hypothesis [153, 114, 371, 100, 101, 89, 23].

The amount of CVD explained by systemic risk factors is still controversial [143, 206, 60, 217], mainly because they do not explain the localization and non-uniformity of atherosclerosis distribution [141, 69]. These medical observations are the motivation behind the research developed in topics such as biomechanical and geometric risk factors.

Up to date, the shape of the coronary arteries is not to be a known risk factor for CAD. However, there is evidence that the shape of the RCA is influential [100, 101, 89, 23]. Remarkably, in our dataset was found no statistical significant association between the RCA shape and lesion, see Section 5.3. The focus of this section is to explore the association of geometric features and arterial lesion on the principal coronary arteries.

The patients sample used in this study is described in Section 5.1, consists in 48 patients (24 pairs of siblings), and demographics data are shown in Table 5.1.

5.7.1 Identification of relevant thermodynamic and geometric features

Association between lesion presence and descriptors can be established with a standard Mann-Whitney U-Test. The LAD artery shows significant association of disease with descriptors. Figure 5.16 presents box-plots of descriptors with significant ($p < 0.05$) difference in the mean value between healthy and diseased LAD according to the U-Test. Feature values have been normalized to have sample-wide zero mean and unit standard deviation. The results indicate that:

- The average distal curvature ($\bar{\kappa}_d$), scores the best results in the U-Test.

- A few conventional features were found to be associated to lesion presence: bending energy (ξ_κ), branch count (Υ), fractal dimension (ϱ), arterial length (ℓ), total curvature (κ_T) and offspring mean rising angle (β).

- Some of the thermodynamic descriptors are significantly different in healthy and diseased vessels. Specifically, the curvature-based temperature (T_κ) and random plane intersection temperature (T_n).

- All the associated features present smaller mean values for diseased LAD vessels than for healthy ones.

Regarding the RCA, no statistically significant (95% confident interval) association was found between lesion presence and thermodynamic/geometric features. On the other hand, the LCx presented association between disease and two features: intersection counting pressure (P_n) and torsion ratio (Λ_τ).
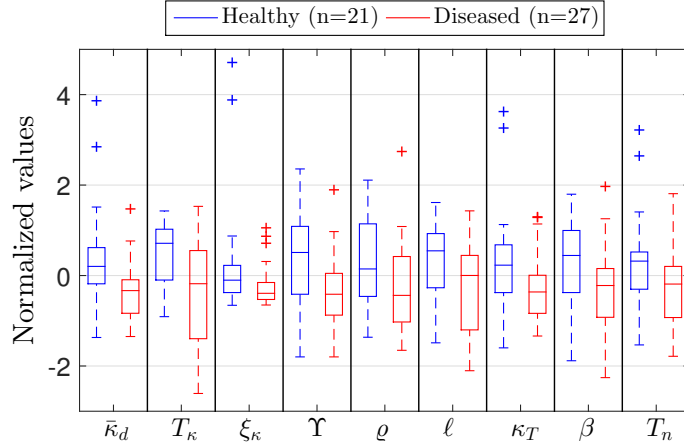
Figure 5.16: Subset of features with statistically significant ($p < 0.05$) difference in mean values for the healthy and diseased LAD arteries. Features are sorted from left to right in ascending order of the associated p-value.

Following the same rationale used in Section 5.3 to identify the RCA shape, binary classification can be performed to distinguish healthy and diseased LADs. Linear classification (see Chapter 4, Section 4.3.1) was performed, but with suboptimal results compared to multivariate kernel density classification[7]. As in Section 5.3, a feature selection problem was solved in order to choose the feature set such that classification scores are maximized. Standard sequential (forward and backward) feature-selection strategies were tested along with the feature sets containing the complete set (25 features), only geometric (19 features), only thermodynamic (6 features), and the one specified by the U-Tests for each artery. All of these sets resulted in suboptimal classification scores when compared with a "brute force" search of a 6-feature set that maximizes the average of the LOOCV classification scores. Such feature set is called $\mathscr{F}_{B6}$ and, for the sake of clarity, we only present results using such set.

Table 5.9 presents the performance results of the kernel density classifiers when using LOOCV. The brute force search for the 6 features maximizing classification output resulted in: (i) $\mathscr{F}_{B6}^{\mathrm{RCA}} = \{\zeta_T, \Lambda_\kappa, \xi_\tau, \beta, H_\kappa, H_n\}$; (ii) $\mathscr{F}_{B6}^{\mathrm{LAD}} = \{\kappa_T, \bar{\zeta}, \Lambda_r, \Lambda_\tau, \xi_\kappa, \beta\}$; (iii) $\mathscr{F}_{B6}^{\mathrm{LCx}} = \{\ell, \bar{\zeta}, \Lambda_\tau, \Upsilon, P_n, H_n\}$.

	$\mathscr{F}_{B6}^{\mathrm{RCA}}$ (41.3%)	$\mathscr{F}_{B6}^{\mathrm{LAD}}$ (56.3%)	$\mathscr{F}_{B6}^{\mathrm{LCx}}$ (26.1%)
Acc.	0.78	0.83	0.88
Sen.	0.74	0.89	0.50
Spe.	0.81	0.76	1.00
PPV	0.74	0.83	1.00
NPV	0.81	0.84	0.86

Table 5.9: Multivariate kernel density estimation classification scores for LOOCV. The prevalence of the disease is indicated in parentheses for each type of artery.

The results of the U-Tests show that healthy LAD arteries have a more complex geometry than diseased ones. In this context, complexity is understood as an increase of in the values of descriptors (see Figure 5.16). On the other hand, the LCx artery showed a weaker association in the U-Test, while the RCA artery showed no statistically significant difference in the U-Test. Classification performance depends strongly on the

---

[7]Tests using the well-known naive KDC were also performed, but with sub-optimal results when compared to multivariate KDC.

arterial sample, and the following conclusions can be drawn from Table 5.9:

- The LCx artery scored the highest accuracy (88%), although the probability of lesion identification was low (i.e. 50% sensitivity). However, the specificity and PPV reached 100%, which means that all healthy LCx were correctly classified, with no false positives.

- The LAD artery scored the highest sensitivity (89%), and the overall classification accuracy was 83%. The probability of correct classification of healthy arteries was 76%. The positive and negative predictive values were high (83% and 84%), indicating low rates of false positive/negative classifications.

- The RCA showed the worst classification scores. Nevertheless, the accuracy is 78%, with acceptable diseased/healthy detection rates, i.e. 74% sensitivity and 81% specificity. The positive and negative predictive values were 74% and 81%, respectively.

It is important to remark that sets of features for LCx and RCA arteries include thermodynamic descriptors, namely H_κ and H_n for LCx, and P_n and H_n for the RCA.

5.8 On fractal analysis and power laws

All applications of geometric analysis presented in this work have been performed using descriptors from Tables 3.1 and 3.2. Although the amount of descriptors presented here is more comprehensive than previous works available in the current literature, it is worthwhile to remark that further geometric analysis can be performed. Particularly, tools and descriptors rooted in fractal theory can be applied to arterial centerlines. Fractality concepts were used to study and construct models of arterial networks [364, 34, 230, 229, 259].

Although we used a definition for the fractal dimension (ϱ) of the centerline [358], there are many ways to define fractality. The basic fractal expression is a summarizing statement describing a recursion. Such expressions are found to define figures which show "infinite" amounts of detail and have "infinitely" complicated boundaries with "infinite" lengths [33]. The general ideas of fractal systems have been described by Mandelbrot [208, 209].

The characteristic repetition of the bifurcation process gives arterial trees its first fractal character but only in the most rudimentary sense. What is meant by "fractal properties" of an arterial tree depends fundamentally on whether the tree structure is being described by whole arteries or arterial segments (defined between branches) [364]. For example, the fractal dimension feature (ϱ) used in this work is defined for a whole artery.

Rossitti [280], summarized how the principle of minimum work (PMW)[8] for least energy cost for blood flow is also compatible with the spatial constraints of arterial networks according to concepts derived from fractal geometry. The PMW in this context was first described in [239], and is widely known as the Murray's law, which relates (i) flow to vessel diameter and (ii) diameter of vessels sharing a bifurcations through a power law. Power laws are commonly related to fractal analysis because they are rooted in log-log plots, which is typically used in the analysis of different scales, which are the basis of fractal theory.

Zamir [364] studied the fractal properties of a resin cast human RCA tree (diameters in the range 3.48 to 0.007 mm), and reported that the tree structure was found to have "pseudo-fractal" properties, in the sense that vessels of different calibers displayed the same branching pattern but with a range of values of the branching parameters, rather than constant.

A particular example of the use of fractal geometry is in explaining myocardial flow distribution via delivery of blood through an asymmetric fractal branching network [34]. Perfusion heterogeneity as a general problem was also found to have fractal properties when using constrained constructive optimization (CCO) algorithm to construct arterial networks [174]. Power laws associating flow to arterial diameter in computational models of coronary circulation of pigs hearts, reconstructed from partial measures using fractal algorithms [230], were presented in [229].

Several studies of blood flow simulations in computer generated models of fractal branching networks can be found in the literature [116, 50, 324]. Self-similar networks can mimic the structure and hierarchy of vessels in the microvascular regime (radii in the range 500-10 μm), and were used to improve the descriptive capabilities of lumped boundary conditions for 1D simulations of arterial networks [259].

Fractal analysis can also be found in allometric laws[9]. For example, quantification

---

[8]Also known as the energetic optimum principle, it is a parametric optimization model for the growth and adaptation of arterial trees.

[9]Allometry is the study of the relationship between body size and shape. Theoretical developments are carried out in the field of statistical shape analysis, and practical applications in biology for are very common, i.e. growth rates of the parts of a living organism.

of the coronary vessel diameter, length, volume and flow in relation to myocardial mass, in pigs, was characterized by power laws in [75].

River basins are examples of naturally organized flow architectures whose scaling properties were noticed long ago in the field of hydrology [317]. In the work of Horton [149, 150], several relations of stream lengths and bifurcation ratios were developed, the so called Horton's model for description and construction of river models was proposed. Mittal et. al. [230] used such model for construction of coronary arterial networks. Maybe, the best known fractal-like result in hydrology is the so called Hack's law [138, 277], which relates the basin area to the longest stream length of a river, in a power fashion.

Here we present an example on how the data obtained through the computational methodology detailed in Chapter 2 can be used to derive power laws from noninvasive medical images of human hearts.

Figure 5.17 presents a log-log plot relating the total length (ℓ_T, in mm) of the coronary tree models to the surface area of its convex hull (C, in mm^2) for each patient in the sample. Information such as gender, age, presence of lesion and kin pair are presented through marker type, size and color. A power law of the type $C = a\ell_T^b$, with $a = 1196, b = 0.48$ can be inferred from the plot, with a significant (p-value $\ll 0.01$) Pearson's correlation of $r = 0.7$. Although visual inspection of Figure 5.17 does not provide associations of age, sex or lesion presence with the power law prediction (black line), some interesting remarks can be made in relation to the patient's kin. It can be observed a general tendency to line out patients along the power law prediction, which could be an indication that similarity of arterial geometry is reflected in the power law by different values of the a parameter. This hypothesis is also supported by the 67% chance that both siblings are above or below the power law prediction.

An analogous test linking ℓ_T to the surface area of the myocardium resulted in no significant correlation. Such lack of association could be due to the incompleteness of the arterial models. Therefore, noninvasive patient-specific models of the coronary tree from medical images are not enough to derive allometric power laws such as the ones reported by [75] (in that case for pig heart). Nevertheless, the fractal nature of vasculature, even at the level of the major arteries, can be recognized by the existence of a power law analogous to that of the Hack's law for river basins.

As other morphometric information, allometric laws can be useful for the development of computational strategies for the generation of coronary networks.
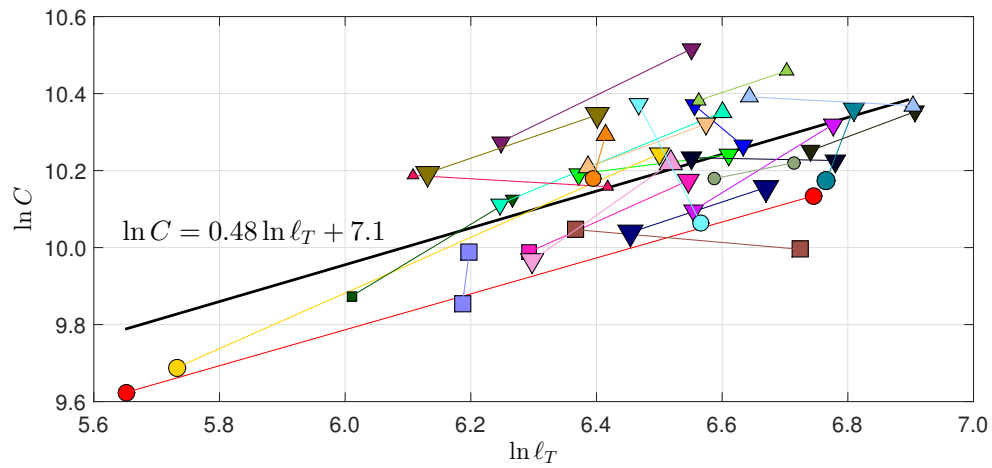
Figure 5.17: Scatter plot relating the total arterial length (ℓ_T), which is the sum of the lengths of all vessels that compose the coronary network, to the surface of the convex hull of the coronary tree (C) in a log-log fashion. Sibling pairs are matched by color and linked by a strike line. The size of the markers increase with the age of the patients. Males are identified with up-pointing triangles when healthy and down-pointing triangles when some artery have lesion, analogously, healthy females are marked with circles and diseased ones with squares.

Chapter 6

Geometric description and comparison of coronary arteries: Final comments

"The aim of an argument or discussion should not be victory, but progress."

Joseph Joubert

Through Chapter 5, a comprehensive analysis of the geometric characteristic of the coronary arterial tree has been presented. Such studies comprised morphometric analysis of the coronary arteries, similarity metrics based on geometry, heritability of arterial geometric characteristics and exploration of geometric risk factors for CAD. This section addresses such results to provide a global perspective of the first Part of this Thesis.

6.1   Non-conventional geometric characterization

A generalization of the theory of *thermodynamics of plane curves* to curves in 3D space, as well as an adaptation for using spatially distributed (point-wise) information attached to the curves was presented in Chapter 3 (see Section 3.2.2). Examples of applications have been presented through Chapter 5. It was found that some thermodynamic descriptors have different mean values for healthy/diseased LAD and LCx, as well as for Σ/C-shaped RCA arteries. Some of the thermodynamic descriptors contributed to the optimal indicator sets for KDC, see Chapter 5, Sections 5.7, 5.3. It is believed that the tools proposed here provide a suitable approach to further extend the range of applications of the thermodynamics of curves.

6.2   Morphometry of the coronary vasculature

Morphometric data of coronary arterial trees is key to understand the potential risk of geometry in the genesis and progression of stenotic lesions, which is an open problem in the medical community, as well as for the setting of computational models and definition of criteria to specify boundary conditions to hemodynamic simulations (see Part II, Chapter 9).

In Section 5.2, statistical information of several geometric descriptors were presented for the major coronary arteries and their principal branches. Morphometric data reported here complements the existing literature with a new set of geometric descriptors (see, Chapter 3, Section 3.2) that goes beyond length, radius and branching angle. It was shown that

the major arteries present different curvature patterns, lengths and lumen radius. Such data can be used to guide the generation of vascular models for simulation and to determine morphometric-based criteria to provide models with physiologically consistent boundary conditions. Curvature data can also be definitely useful in setting more sophisticated models of blood flow which require this information as input parameter, see for example [111]. Results indicate that subtrees also present different patterns for features such as α, $\bar{r}$, $\bar{\kappa}$. Nevertheless, a strong intra-arterial correlation among curvatures and torsion derived features was found, indicating a global constraint over the morphological aspects of the entire coronary network.

Different geometrical patterns could help to explain some known clinical facts, i.e. why the left coronary tree is more prone to develop stenotic lesions than the right [69]; or the reported association [101], that C-shaped RCAs are more susceptible to atherosclerotic disease than Σ-shaped RCAs.

The strong correlation between variables reported in Section 5.2, may be an indication of redundancy. Feature selection techniques and dimensionality reduction methods such as principal component analysis can be applied to reduce the number of variables, analogous to results presented in the study of similarity between siblings (see Chapter 5, Section 5.4) or for shape and arterial lesion classification (see Chapter 5, Sections 5.3 and 5.7).

The analysis of RCA shape presented in Section 5.3 showed remarkable results. The U-Test identified 17 features with significant difference in the mean value among classes, five of which are thermodynamic descriptors. Furthermore, the shape of the RCA is intrinsically defined from arterial geometry, therefore, a good classification performance is expected. In turn, classification scores show 96% of correctly identified shapes (accuracy), 88% of correctly classified Σ-shaped RCAs (sensitivity), 100% of correctly identified C-shaped RCAs (specificity), none incorrectly classified C-shape (100% of PPV), and a low number of Σ-shape classified as C-shape (94% of NPV). Furthermore, two thermodynamic descriptors (T_n, H_n) are included in the $\mathscr{F}_{B6}$, which is the set that maximizes the classification scores. Although in the present patient sample there is no statistically significant association between shape and disease, such association was reported elsewhere [101]. Interestingly, there are two descriptors shared between the features sets ($\mathscr{F}_{B6}$) used for KDC of lesions (see Chapter 5, Section 5.7) and shape of the RCA (see Chapter 5, Section 5.3), namely H_n and ζ_T. Further analysis with larger sample sizes are mandatory to reach conclusive results on the association of the RCA shape and lesions.

6.3 Similarity of geometric features in siblings

This work explored, for the first time, association of coronary artery morphology among sibling patients. More than 20 geometric descriptors were used to characterize the RCA, LAD and LCx arteries of 48 patients (24 siblings). In Chapter 5 (see Section 5.4), it was shown that the proposed geometric normalization (see Chapter 2, Section 2.3.6) directly impacts the morphology of the underlying feature space, through a direct modification in the ranking list of all patients. Then, it was shown that the mean distance between siblings is smaller than the mean distance to non-sibling patients, which holds true for the raw geometries of the principal coronary arteries as well as for the case in which normalization by myocardial area was performed. The U-Test clearly shows that more similar arterial structures are observed between siblings in comparison to the rest of the sample, when similarity is defined through distance in the feature space. Furthermore, this likelihood pattern is noticed when all features are used ($p < 0.025$), and when the rSRI is minimum for each independent artery ($p < 0.01$).

From the results on arterial comparisons through the set of features (see Chapter 5,

Section 5.4) on the rSRI, displayed in Figure 5.9, it can be stated for both, raw and normalized geometries, that (i) the RCA obtained the best scores for rSRI while LCx the worst ones, which indicates that possible manifestation of geometric heritability may be stronger in the RCA, followed by the LAD, than in the LCx; (ii) individual scores of rSRI are below 0.5 for all cases, indicating that arteries of sibling patients tend to be ranked below half of the sample; (iii) when studying all three arteries together the RCA and LAD similarities compensate the LCx likelihood, producing rSRI ~ 0.1 which indicates that half of siblings obtained ranking position within the 10% of the sample.

It is widely accepted that familial history of CAD increases cardiovascular risk [314, 167, 148], and previous works have suggested the heritability of stenosis characteristics such us localization, extent and morphology, as well as risk of coronary events in siblings [106, 107]. The outcomes of data exploration techniques presented here strongly indicate a geometrical likelihood between siblings that transcends geometric normalization. This result suggests that geometric characteristics of the major coronary arteries could be inheritable, as was hypothesized in [153, 114]. Linking our findings to the theory of geometric risk factors [113], it is possible that the so-called familial risk factor may be explained, at least to some extent, by heritable geometric risk factors. It is important to highlight that the alleged association between atherosclerosis and geometric variables must be taken as a second type of risk factor, which acts at the arterial level instead of the systemic level, accounting for the local interaction between hemodynamic forces and the ultimate target for the atherosclerotic process, which is the vessel wall.

When arterial features where assessed individually for indications of heritability (see Chapter 5, Section 5.5), it was found that the RCA scored positive for the largest number of phenotypes, followed by the LAD. The LCx presents the weaker association of morphology between siblings. The LAD was the only artery showing positive association of stenotic lesion between siblings. Moreover, few descriptors indicated some kind of correlation between siblings. Although the lesion presence in the RCA showed no association, the shape (C/Σ) as well as more than 15 geometric descriptors scored positive association between siblings. The LAD artery presented association between phenotypes and presence of lesion in more than 10 phenotypes, while the LCx presented such association only for 2, and the RCA featured no association. Such differences could be related to the intrinsic differences in the hemodynamics loads in the arteries. These results are encouraging, and strongly suggest that morphology of the coronary arterial tree may have genetic mediators.

These studies open the door for a new kind of analysis of coronary artery disease. Noninvasive visualization of the coronary tree may provide insights on the evaluation of anatomy, geometry, and functionality. Increasing knowledge of these features in patients may offer an opportunity to infer similar disease distribution in their family relatives.

6.4 Geometric risk factors

Identification of risk factors for coronary artery diseased is key for medical applications involving prevention and risk assessment. Estimation of such risks from noninvasive medical imaging, could have major implications in future medical practice.

There are many known CAD risk factors. Particularly, all patients used in this work have at least one of the modifiable risk factors, as commented in Section 5.1. Nevertheless, healthy/diseased classification presented in Section 5.7 is performed in terms of arterial descriptors alone. Therefore, an incomplete description of patients is used, and there are many descriptors that are not used, i.e. systemic risk factors (hypertension, hypercholesterolemia, diabetes, smoking, etc.), genetic (familial history) and hemodynamics. Thus, a very high classification accuracy is unlikely to happen using such reduced sample quantity. In this context, classification performance of the LAD and LCx arteries using

only geometry-derived data is satisfactory. Finally, in Chapter 5 (see Section 5.5), it was verified that lesion presence has an heritable association between siblings.

Regarding classification (see Chapter 5, Section 5.7), it is worth noting that sets of differential features for LCx and RCA arteries include thermodynamic descriptors, namely H_κ and H_n for LCx and P_n and H_n for the RCA.

The results presented in Chapter 5 (see Sections 5.7 and 5.6) show that healthy LAD arteries have a more complex geometry than diseased ones. In this context, complexity is understood as an increase in the values of descriptors (see Figure 5.16). Particularly, it was found that the increased distal average curvature of the LAD presents potential role as a protective geometric feature, analogous to the Σ-shape RCAs. Whether straightness of distal portion of the LAD is a geometrical risk factor or a consequence of atherosclerosis proliferation is subject of further investigation. In turn, the LCx artery showed a weaker association between geometry and disease, while the RCA artery showed no statistical significance for such associations.

To date, the shape of the coronary arteries is not an acknowledged risk factor for CAD. Data analysis presented in Chapter 5 (see Sections 5.7 and 5.6), suggest that there is a correlation between coronary plaques and shape of the LAD.

6.5   Power laws

In Section 5.8 it was shown that coronary network models obtained from noninvasive medical images can be used to explore descriptive laws of the vasculature, analogous to those used in the field of hydrology. Clearly, the results presented here are preliminary and much work is still needed. Nevertheless, a fractal nature in the morphology of the coronary vasculature can be identified by the power law associating the length of the arterial tree to the surface of its convex hull in three-dimensional space. The patterns described by siblings alienation to the power law prediction are also interesting and worth of further research.

6.6   Limitations

All examples of data analysis presented in Chapter 5 were performed with the same study sample. Therefore, they share limitations regarding the methodology used to construct arterial models, namely: (a) image artifacts due to calcified plaque, stents or patient movement can introduce noise into the segmentation and therefore in the centerline model, and ultimately affect geometrical features; (b) image resolution and quality limits the segmentation of small branches constraining the analysis to what is seen in the medical image. Such points originate from technological limitations in the image acquisition process, and can only be addressed by performing cautious segmentation and discarding images with poor quality. Regarding limitations associated with the data analysis examples, it should be taken into account that: (c) a relatively modest number of patients was used. In this regard, in Chapter 5 (see Section 5.2), it was shown a very close agreement with several population broad statistics of anatomical variables, e.g. circulation dominance and presence of the RI artery, lengths and radii, indicating that the sample is representative of the human coronary arterial tree. Although the patient sample is small to perform definite conclusive statistical analysis, at the same time, it is sufficiently large so as to serve as proof of concept of the various morphometric, statistical and classification tests. In future studies with larger samples, dimensionality reduction techniques, like principal component analysis, are recommended to explore classification in the transformed spaces. Incorporation of patient descriptors such as systemic risk factors could also help to improve classification tests. Since all patients were referred to a CCTA study due to high risk of

coronary artery disease, the sample may be biased towards diseased. Nevertheless, in obtaining a sample with asymptomatic patients, would require volunteers. This preliminary, prospective analysis may serve as a proof of concept towards conducting such study. The possible bias of the patient sample should be considered when interpreting lesion heritability in the LAD, since prior chances of concordance are already latent. In turn, the RCA and LCx arteries presented no heritability of lesion presence. Overall, this study presented the first attempt to explore heritability of geometric characteristic of coronary arteries.

6.7   Concluding remarks for Part I

A systematic approach for extraction, processing and analysis of coronary tree geometries was presented and tested. The coronary arterial tree of a representative sample of 48 patients (comprising 24 pairs of siblings) was geometrically characterized. One of the contributions of this work is the development of a complete morphometric analysis of coronary arteries, not only addressing standard statistical data but exploring correlations among geometric descriptors. Methods for comparison of arteries using those descriptors were presented and tested. Non-conventional geometric features were proposed and successfully used in several applications. Remarkably, from analyzing the data, it was found a strong indication that geometric features of the main coronary arteries are more similar between siblings than among non-relatives, and several indications of geometric heritability of the principal coronary arteries were found.

More sophisticated data analysis tools deserve to be explored in the present context. For example, dimensionality reduction and classification techniques (i.e. principal component analysis and support vector machine, among others). Nevertheless, the use of such trained-based algorithms also requires a larger sample size to avoid bias using training and test samples, which poses challenges from the point of view of the automation of image segmentation.

Finally, the comprehensive approach for geometric characterization and analysis of vessels can be generalized to other arterial territories and diseases, e.g. cerebral arteries and cerebral aneurysms, or aorta artery and aortic aneurysms.

Part II

Computational Simulation of Fractional Flow Reserve

Chapter 7

Coronary physiology and ischemia

"The heart has its reasons, which reason does not know..."

Blaise Pascal, *Pensées*

Physiology is the branch of biology that deals with the normal functions of living organisms and their parts. Ischemia means an inadequate blood supply to an organ or part of the body. The study of coronary physiology has a long history. The discovery of coronary flow inhibition during systole due to myocardium contraction in 1695 is usually considered as a starting point in coronary physiology. Since then, advances in technical methods marked the understanding of physiology in four phases. According to Spaan [316], the early phase ended in the 1940s, where much of the basic understanding of the field was formulated with great difficulty and with crude methods. The second phase endured up to the 1960s, and was characterized by the development of instruments for high fidelity registration of coronary flow and pressure. The third phase extended to the 1990s, and was marked by techniques for measuring regional myocardial blood flow, enabling major advances in understanding of the physiology and pathophysiology of coronary circulation. The current phase is not based on new measuring techniques but on (i) the introduction of information about the micro-circulation and (ii) advances on coronary circulation models. Furthermore, clinical diagnosis and decision-making process for the treatment of coronary artery disease can be based on physiological principles.

Computational models and numerical simulation techniques to study blood circulation in the cardiovascular system is an active area of research which has benefited from the development of sophisticated mathematical and numerical models as well as from the raise in computational power available. Currently, we are entering a phase where computational simulations are being tested as new diagnostic tools, with imminent translation to the operating room, see Chapter 8, Section 8.4. Specifically, it is the concern of this thesis the use of computational models for the noninvasive estimation of fractional flow reserve to assess risk of myocardial infarction.

This chapter is intended to provide the reader with the basics concepts on coronary anatomy, physiology and pathophysiology. It aims to provide complementary data for the concepts developed in the rest of the thesis, but it cannot be considered an ultimate complete review of the field. The associated literature is extensive, for instance, some remarkable compilation of anatomical knowledge is presented by von Lüdinghausen [346, 347], while coronary physiology is explained in detailed by Spaan [316]. An early compilation by Pijls and De Bruyne [268] focuses on coronary pressure assessment, fractional flow reserve rationale and related topics.

7.1 Basic concepts of coronary circulation

The heart propels blood to the entire body through the vascular system. When the heart fails completely, awareness is gone within seconds and brain death occurs within minutes. The mechanical work needed for pumping blood is performed by the heart muscle, also called myocardium. In adult humans, typical heart rate, cardiac output and aortic mean pressure are 70 beats/min, 5 liters/min and 100 mmHg. An average human heart will beat 2.6×10^9 times, and pump 2×10^{11} liters in a lifetime span. During severe exercise, cardiac output may increase by a factor of 4 to 6.

As for every other organ, the heart depends on blood, which is supplied by the coronary arteries. About 5 to 10% of the cardiac output is shunted through these coronary vessels to make cardiac functioning possible [316]. The coronary system starts within the region of the aortic valve structure, with two major vessels. These vessels, run over the surface of the heart, giving rise to branches that penetrate the heart muscle and, in turn, branch into smaller vessels in order to supply the capillary network of the heart with blood. The capillary network is very dense, with average inter-capillary distance of 20μm, and a mean capillary diameter of 5μm through which the red cells flow in a single line.

A brief summary of the coronary arterial tree anatomy is presented in Appendix C. Basic understanding of coronary anatomy is mandatory for image segmentation, arterial modeling and simulation. References [346, 108, 31, 204] are recommended for the interested reader.

Regarding coronary fluid mechanics, a clear distinction between right and left coronary networks is observed. While the right coronary flow signal follows the aortic pressure signal during systole, the left coronary is low or even retrograde in systole. Such inhibition of coronary arterial flow during systole originates in the interaction of myocardial muscle contraction and perfusing arterioles and capillaries during systole.

Regulation mechanisms of coronary flow strongly depend on myocardium oxygen consumption, basically, increased oxygen demand produces an increase in blood flow. The coupling between coronary flow and oxygen consumption is often referred to as exercise or functional hyperemia.

Coronary flow is controlled at the arteriolar level by vessel dilation. Vessels state is referred to as "tone", which accounts for the wall tension of these vessels being modulated by the smooth muscle in their walls and also by transmural pressure. Since wall tension is impossible to measure, an index is needed to reflect its effect; generally this index is the concept of vessel resistance and is regarded as equivalent to tone. In general, flow and pressure in the coronary arteries are the quantities available from which resistance can be estimated simply by computing the ratio between average pressure and average flow rate.

7.1.1 Collateral circulation

Collateral blood flow has been subject of study in the medical community for a long time. A complete review on the relevance of coronary collateral circulation can be found in [175]. Pioneer efforts to characterize collateral vessels go as far as 1956 [32], using a corrosion method on a set of human hearts (healthy and diseased). Collateral anastomoses are classified as homo-coronary when they connect branches of one single coronary artery in contrast to inter-coronary when they connect branches from two coronary vessels. More than 20 different collateral pathways were identified in [199].

In normal hearts [32], homo-coronary anastomoses present average lengths of 1-5cm and diameters of 0.02-0.25mm, connecting vessels with diameters in the range of 0.5-1mm, typically in the subepicardial regions. Normal left ventricles present at least one homo-coronary collateral per arborization with diameter range 0.5-1mm, while right ventricles present less collaterizations. Inter-coronary anastomoses are found in border

regions supplied by branches from both coronary vessels. Collateral vessels have an average length of about 2-3cm and diameters in the range of 0.02-0.35mm. An average of 25 anastomoses were observed per region (septum, anterior and posterior walls).

In pathological hearts [32], collateral circulation is generally more developed. The longer the history of angina, the larger the number of large-caliber coronary collaterals at postmortem examination [115]. Collateral vessel diameters in the range of 0.4-2mm can be found [32]. The process of arteriogenesis leads to the positive remodelling of an arteriole into an artery up to 12 times its original size [301]. This growth in structural vascular size goes along with a decreasing number of collateral arteries during CAD development, a process called pruning. Pathophysiologically, and in the sense of the Poiseuille law, pruning may be interpreted as a way of effectively reducing vascular resistance to collateral flow, because a large caliber increase of a few vessels is more efficient for bulk flow augmentation than a small increase in size of numerous vessels [301].

After rapid coronary occlusion, collateral vessels develop rapidly and are generally observable within 2 weeks. Therefore, it is possible for patients suffering myocardial infarction to present collaterals that were not completely developed at the time of the event [299].

Although the functional significance of coronary collateral vessels in patients with acute myocardial infarction (in-vivo) has been recognized from long time [354], the use of collateral blood flow into clinical practice is relatively recent. Such methodological delay is attributed to the fact that collateral blood vessels, if present, do not significantly react to drugs, and moreover since they are close to ischemic tissue they are already maximally dilated when a major artery is acutely occluded [296].

7.1.1.1 Quantification of coronary collateral circulation

Assessing the collateral circulation is challenging, and there is currently no technique to quantify it noninvasively in humans [222]. There are three methods being used which have demonstrated predictive value in clinical practice. All of them involve balloon occlusion of the compromised artery, if it is not already occluded. (i) Semiquantitative visual assessment of collateral arteries by coronary angiography [276]. This method has several limitations: it is not objective, it is influenced by blood pressure and the force of contrast injection as well as the duration of filming; furthermore, in practice the artery is not always closed by a balloon. (ii) A boolean evaluation of the electrocardiogram ECG [86]. ST-segment elevation ≥ 0.1mV during a 1 to 2 minute vessel occlusions are taken as insufficient collateralization. Although it is the cheapest methods, it is not accurate enough. (iii) The so called collateral flow index (CFI), is considered the most accurate method to assess the collateral circulation. The CFI is defined as the ratio between flows during total occlusion, and after angioplasty (hypothetic normal flow without lesion). Therefore, it represents the percentage of normal blood flow that can be supplied via collateral circulation during vessel occlusion. The CFI can be estimated by Doppler velocity measurements or by pressure sensor, the former is more accurate and more commonly used.

To prevent myocardial ischemia during acute vessel occlusion, a CFI of 0.2-0.25 is considered sufficient to supply myocardial demand at rest. Although, there is still controversy whether collateral circulation is sufficient to meet myocardial demand during exercise after coronary occlusion [222].

7.1.1.2 Mechanisms of collateral growth (arteriogenesis)

Vasculogenesis refers to the initial events in vascular growth. The term angiogenesis was formerly used to describe the formation of new capillaries. Currently, angiogenesis is considered the subsequent growth, expansion, and remodeling of primitive vessels into a complex, mature vascular network. Finally, arteriogenesis refers to the transformation of

preexisting (collateral) arterioles into functional (muscular) collateral arteries, as a thick muscular coat is added, concomitant with acquisition of viscoelastic and vasomotor properties [185].

The process of arteriogenesis is mediated mechanically through an increase in shear stresses. For example, in the event of a hemodynamically relevant stenosis of a main feeding artery, a pressure gradient is created and collateral arteries are recruited. Because of the decrease in arterial pressure distal to the stenosis, blood flow is redistributed through the preexistent arterioles that now connect a high-pressure with a low-pressure area. This results in an increased flow velocity and therefore increased shear stress in the preexistent collateral arteries. Subsequently, several morphological changes and vascular remodeling occur [185].

Collateral flow can be reduced and even reverted if atherosclerosis progresses in the donor artery, a process called the "collateral steal" [373].

Collaterals often disappear after the recanalization of chronic total occluded arteries. Although coronary collaterals, once established, are believed to persist and are able to be re-recruited, such re-recruitment is not immediate. Well-developed collateral vessels close when the pressure gradient across the collateral network disappears, and the time needed to reopen such closed collaterals after re-establishment of the pressure gradient seems to be directly related to the time interval between coronary occlusions [373].

7.1.1.3   Collaterization as a therapeutic treatment

Well-developed coronary collateral function is related to reduced mortality in patients with CAD. Therapeutic promotion of coronary collateral function is, thus, a promising concept, and potential arteriogenic approaches are mater of current research in the field. Many reviews on coronary collaterals explore the therapeutic potential of collateral circulation [222, 301, 175, 373]

7.1.2   Rest and hyperemia

In humans, coronary blood flow can increase up to 5 times the basal[1] flow to meet increased demand. Such an increase in blood flow is referred to as a hyperemic response, and in humans is commonly observed in response to ischemia and exercise [343]. It is an autoregulatory response mediated by arteriolar vasodilation. Thorough reviews on the autoregulatory mechanisms of the heart can be found in [183, 147, 316].

The coronary vascular system is normally a low-flow/high-resistance circulation at rest conditions. In turn, during coronary hyperemic conditions, it turns into a high-flow/low-resistance system [127]. Under such hyperemic conditions, coronary stenoses (even mild ones) have greater effects on maximum flow supplied to the myocardium. This is the reason why, as will be presented later, the functional impact of a stenosis on the circulation is assessed during hyperemia.

7.2   Atherosclerosis

Atherosclerosis is a chronic disease that remains asymptomatic for decades, and it is the primary etiology of CVD. It is characterized by an arterial wall thickening as a result of the accumulation of fatty material, called atheromatous plaque, which forms as a time-dependent response to chronic arterial injury. The atheromatous plaque is divided into three distinct components: (i) the atheroma, which is the nodular accumulation of a soft, flaky, yellowish material at the center of large plaques, nearest the lumen of the

---

[1]Flow at rest or normal conditions.

artery; (ii) underlying areas of cholesterol crystals; and (iii) calcification at the outer base of older/more advanced lesions. Arterial narrowing is also called stenosis.

Despite great efforts from the research community, there is a lack of understanding of the true pathogenic mechanisms of the disease. That is, known risk factors do not completely determine the probability of disease, and revascularization merely delays the inevitable [120, 69, 72, 342].

The extreme complexity of the vascular biomechanical environment includes shear stresses continuously acting over the endothelium as well as internal arterial wall stresses which develop in response to the pulsatile nature of blood pressure and flow. It is believed that such stimuli provides a mechanism by which systemic factors, i.e. diabetes mellitus, smoking, and dyslipidemia can result in a localized disease such as atherosclerosis [342].

7.2.1 Detection of coronary artery disease

Coronary artery narrowing, induced by atherosclerosis, compromises the blood supply to the heart. At first, the decreased blood flow may not cause symptoms. As plaque continues to build up, however, signs and symptoms can be detected, including: chest pain (angina), shortness of breath, abnormal heart rhythm (arrhythmia) and heart attack.

Over the years, several clinical tests were developed to detect the presence of CAD, with increase interest in quantifying the functional significance of stenosis. Such procedures can be roughly divided into three categories: (i) exercise test with monitoring of CAD symptoms or direct observation of coronary flow, i.e. stress test, stress echocardiography and exercise test with thallium scanning; (ii) invasive and none invasive medical images, i.e. coronary angiography (AX), quantitative coronary angiography (QCA) and coronary computed tomography angiography (CCTA); and (iii) functional assessment of lesion through physiologic response, i.e. absolute/relative coronary flow reserve (CFR)[2] and fractional flow reserve (FFR). An overview of these CAD diagnostic procedures is presented in Appendix D. Since this work focuses on FFR, Chapter (8) is devoted to overview this technique with an associated Appendix (E).

7.2.1.1 Coronary Flow Reserve (CFR)

Diagnostic tests based on physiological principles try to estimate the impairment of maximal myocardial blood flow due to stenotic lesions. The capacity of coronary arteries to increase their blood flow three- to four-fold after transient ischemia was recognized in 1939 [177]. The concept of absolute coronary flow reserve (A-CFR or CFR for short) was introduced in 1960 [77] to describe the capacity of the coronary circulation to conduct maximal hyperemic blood flow. Four years later, the physiologic framework of CFR was established through the notion of coronary autoregulation [238]. CFR provides a method for describing the capacity of the coronary circulation to conduct maximal hyperemic blood flow. In most studies, CFR is estimated as the ratio between hyperemic and resting blood flow, generally estimated from coronary blood flow velocity measurements (CBFV). However, it was not until 1974, that CFR was proposed as a useful index for prediction of stenotic lesion functionality, marking a key point in diagnosing CAD through physiologic data. A comprehensive review on CFR assessment and clinical implications is presented in [343].

7.2.1.2 Fractional Flow Reserve (FFR)

FFR is a quantitative index to determine the likelihood that an stenosis impedes oxygen delivery to the associated myocardial bed. It is defined as the quotient between

---

[2]Which can be assessed by perfusion magnetic resonance imaging, for example.

maximal current flow and maximal flow in the absence of disease. Practically, it is estimated from pressure measurements during invasive catheterization. Hence, it is computed as the ratio between post- and pre-stenosis pressures averaged in time during drug-induced hyperemia. The procedures yields is a dimensionless value with an unequivocal maximum value of 1 under normal flow conditions and a minimum positive value known as wedge pressure. An FFR value of 0.80 means that a given stenosis causes a 20% drop in blood pressure during hyperemic flow regime, and consequently has an associated impact in the flow delivery through the diseased vessel. Several clinical trails identified ≤ 0.8 as considered abnormal, indicating a functionally significant stenosis. An comprehensive review on FFR technical details, as well as clinical trails demonstrating its potential are presented in Chapter 8.

7.2.1.3   Computational FFR

FFR-guided percutaneous coronary intervention improves patient outcomes and reduces stent procedures and cost; yet, due to several practical and operator related factors, it is used in $< 10\%$ of percutaneous coronary intervention procedures [237]. Such scenario motivated researchers in the field of applied computational fluid dynamics (CFD) to use modeling and simulation tools to reach an in-silico estimate of patient-specific FFR. Briefly, anatomical and physiological information are required. Particularly, (i) arterial geometry is generated from medical images[3]; (ii) such arterial models are further processed to create CFD meshes; (iii) boundary conditions (BC) for the CFD simulations are established using physiological information; and, finally (iv) simulations are performed, and velocity/pressure fields are obtained, from which the computational FFR is computed. The correct determination of BC is crucial for the accuracy of FFR estimation. Ideally, definition of BC accounts for the measurement of blood velocities at all vessels in the generated geometric model. However, this is not possible in current practice, and this is why such BC must also be estimated by taking into account data such as cardiac output, systemic pressure, and myocardial blood flow demand during hyperemia. Further details regarding computational assessment of FFR are presented in Chapter 8.

7.3   Considerations for the modeling of hyperemia

In humans, the hyperemic response to ischemia or exercise can increase up to 5 times the basal flow [343]. Medical literature reports drug-induction of cardiac hyperemia using two techniques, intra-coronary (ICA_{VD}) and intra-venous (IVA_{VD}) administration of vaso-dilator. Currently, adenosine is the most commonly used agent [194], and the clinical guidelines from both, the European Society of Cardiology [93] and the American Heart Association [200] recommend ICA_{VD} over IVA_{VD}, arguing cost-efficiency and fewer side effects.

7.3.1   Adenosine

It has been demonstrated that the use of adenosine is safe via both the ICA_{VD} and IVA_{VD} routes and that it could reliably induce near-maximal coronary hyperemia in most patients, with little effect on systemic blood pressure [355].

Layland et al. [194] present a discussion regarding safety of adenosine use to achieve coronary hyperemia, and briefly review novel agents used to that goal. Adenosine is a fundamental component of human biology, with far-reaching effects as an extracellular

---

[3]Applications using computed tomography angiography (CCTA), quantitative coronary angiography (QCA), intra-vascular ultrasound (IVUS) or optical coherent tomography (OCT) have been presented int the literature, see Chapter 8, Section 8.4.2 for an overview on current approaches.

signaling molecule, inducing vasodilation in most vascular beds, regulating activity in the sympathetic nervous system and having anti-thrombotic properties.

Adenosine administration has been widely adopted as the gold-standard method for diagnosing cardiac ischemia. Practically, the ideal hyperemic agent should have a rapid onset and short duration of action, low cost with no significant side effects. Particularly, adenosine is rapidly transported into vascular endothelial cells, and adenosine levels can rise rapidly in ischemic tissue.

Sato et al. [295] examined the mechanism of adenosine-induced vasodilation in coronary arterioles from patients with heart disease. It was found that vasodilation caused by adenosine is not influenced by underlying diseases (coronary artery disease, hypertension, hypercholesterolemia, diabetes mellitus, myocardial infarction, or congestive heart failure), sex, or age.

Regarding administration procedures, there is still controversy and mixed findings (see Section 7.3.3). For example, at the lower "standard" doses, 10% of vessels with an initial FFR value > 0.75 had a subsequent value smaller than this cutoff point with higher ICA_{VD} doses or IVA_{VD} [63]. In turn, IVA_{VD} results in variable changes in systemic blood pressure, which can lead to alterations in FFR lesion classification [326]. Measures of FFR must be performed under stable hyperemia (not peak hyperemia), although the FFR measure during stable hyperemia may be higher than the one measured at peak hyperemia [326].

Intra-coronary administration of adenosine has a peak effect in less than 10 seconds after administration, and it has a duration of approximately 20 seconds. On the other hand, intra-venous administration produces a more stable and prolonged hyperemic state (reached after approximately 60 seconds with a duration of approximately 60 seconds) [160]. While both methods produce a slightly drop on mean systemic blood pressure, IVA_{VD} is associated with a greater increment in heart rate than ICA_{VD}. Side effects are more common during IVA_{VD} than ICA_{VD}, and may include flushing, dyspnea, chest pain, gastrointestinal discomfort, headache, atrio-ventricular block, arrhythmias and bronchospasm.

7.3.2 Vasodilation

It is well established that the coronary micro-circulation is a key regulator of myocardial blood flow. Jayaweera et al. [156] studied the role of capillaries in coronary circulation, and they found that at rest condition, approximately 60% of resistance is provided by the arteriolar level, 25% by the capillary level, and the remaining 15% in the venular compartment. During hyperemia, total resistance decreases across the coronary circulation by 70%. In the arteriolar and venular compartments, resistance decreases by 86% and 98%, respectively, resulting in minimal alteration of capillary hydrostatic pressure such that the capillaries offer the most resistance to coronary blood flow during hyperemia. The arteriolar and capillary resistances now comprise 25% and 75% of the total resistance, respectively. Thus, capillaries provide the ceiling for the hyperemic response.

Adenosine exerts its predominant vasodilatory effect at arteriolar level, on coronary microvessels $< 150\mu m$ in diameter [194].

In the presence of severe stenoses (greater than 80% luminal reduction), there is a limited vasodilatory response to adenosine such that basal flow may equal hyperemic flow [338]. In such conditions, affected downstream microvessels do not respond to adenosine, probably because a maximum vasodilation state was achieve already to counteract the added resistance provided by upstream stenotic vessels.

7.3.3 Clinical observations

Effects of both ICA_{VD} and IVA_{VD} of adenosine on global hemodynamic variables, i.e. mean systemic blood pressure (MSBP) and heart rate (HR), have been reported since the pioneering work of Wilson et al. [355]. Note that MSBP and HR are important to estimate, for example, the cardiac output (CO), as well as all other quantities needed for a patient-specific parametrization of coronary circulation models. Table 7.1 summarizes clinical literature reporting hemodynamic response (in terms of MSBP and HR) for different administration methods and doses of adenosine. It is well established that adenosine-induced hyperemia, in average, reduces MSBP, for both administration doses, in approximately 4 mmHg. Regarding HR, IVA_{VD} produces higher increase of hyperemic to basal HR (18 beat/min), when compared to ICA_{VD} which, in average, decreases the HR in 1 beat/min.

Discordances in ΔHR^4 can be explained by the fact that IVA_{VD} administration produces a systemic reach of adenosine, therefore not only myocardial tissue increases blood flow demand, and consequently to accommodate the increased systemic flow demand, the HR must be incremented. In turn, when ICA_{VD} is used, adenosine reaches myocardial beds irrigated by the coronary vessels in which the adenosine was administrated, having thus a more focal vasodilatory impact, and almost null effect on HR.

Several works addressing the computational simulation of FFR model hyperemic conditions by increasing overall myocardial blood flow (see Chapter 8, Section 8.4.2) justifying this choice by the clinical observations of Wilson et al. [355], which reported changes in myocardial blood flow and resistance measured in the middle section of arteries. Hyperemic flow was reported to has a 4.5 fold increase in relation to a basal condition. The paper is not clear whether the LM and RCA arteries were measured standalone, although it specifies that ICA_{VD} adenosine was injected in the ostium of such arteries. Therefore, changes in blood flow of one coronary tree when ICA_{VD} adenosine in the opposite tree is used, are not documented. Nevertheless, IVA_{VD} adenosine ensures myocardial-wide reaching of the drug, and similar increments in blood flow were recorded.

Taking into account this finding, computational models can safety assume IVA_{VD} induced hyperemia. Although two key points are not considered by studies dealing with computational evaluation of FFR. (i) The spatial heterogeneity of myocardial blood flow reserve: anterior and lateral regions have similar demands which are greater than demands from septum and inferior regions [68]. (ii) Arteries with impaired flow feature a reduction in the increased flow during hyperemia ($\sim$ 3 instead of $\sim$ 4.5) [355]. Therefore, the assumption of homogeneous increment of coronary blood flow intrinsically induces error in the estimation of FFR, since the flow may be overestimated in compromised arteries.

---

[4]The difference between rest and hyperemic HR.

Paper (n of patients, n of lesioned arteries)	Administration	ΔHR (beats/min)	ΔMSBP (mmHg)	ΔSBP (mmHg)	ΔDBP (mmHg)
[288] Lesioned (n=50, 56)**	ICA[†]	0.8±3.4	-3.2±5.1	-3.8±7.9	-3.4±7.0
	IVA[†]	5.0±5.6	-10.0±12.8	-15.6±16.3	-9.6±6.8
[197] Lesioned (n=45, 50)	ICA[†] (600μg)	-8.0	-5.0	1.0	-3.0
	IVA[†] (140 μg/kg/min)	5.0	-5.0	-7.0	-4.0
[160] Lesioned (n=52, 60)	ICA[‡] (24μg)	0.6±3.6	-0.3±5.1	-3.3±8.2	-3.2±6.9
	IVA[†] (140 μg/kg/min)	5.6±6.8	-13.0±10.3	-17.3±14.6	-10.3±6.8
[228] Healthy (n=348)*	IVA[†] (140 μg/kg/min)	24.0	-2.0	-1.0	-3.0
[355] Healthy	ICA[‡] (16 μg, LAD, n=20)	3.0±3.0	-7.0±5.0	N/A	N/A
	ICA[‡] (12 μg, RCA, n=5)	0.0±1.0	-17.0±3.0	N/A	N/A
	IVA[†] (140 μg/kg/min, n=25)	24.0±14.0	-6.0±7.0	N/A	N/A
[355] Lesioned	ICA[‡] (16 μg, LAD, n=5)	-1.0±2.0	-9.0±5.0	N/A	N/A
	ICA[‡] (12 μg, RCA, n=3)	-3±4	-11±6	N/A	N/A
	IVA[†] (140 μg/kg/min, n=5)	12.0±10.0	-3.0±6.0	N/A	N/A
Average	ICA	-1.4	-3.8	-2.2	-3.2
	IVA	18.5	-4.4	-4.8	-4.6

Table 7.1: Summary of reported effects of adenosine IVA_{VD} and ICA_{VD} on hemodynamic variables. Values are difference (hyperemic minus basal states). Inter-study averages where computed as weighting average by number of observations.

* Healthy patients without evidence of obstructive coronary artery disease were imaged with positron emission tomography.

** ICA_{VD} consecutive doses of 60, 100 and 120μg were administrated until maximal hyperemic state was reached, hemodynamic variables should be considered as related to maximum hyperemia, which was obtained with different adenosine dose for each patient. Analogous with IVA_{VD} (140, 160 and 180μg/kg/min).

[‡] Infusion administration.

[†] Bolus administration.

7.3.4 Estimation of patient-specific resting blood flow

Estimation of patient-specific coronary basal blood flow is key for a correct estimation of hyperemic flow. The resting coronary blood flow in humans averages 225 ml/min, which is about 4-5% of the total cardiac output [136, 268]. Wieneke et al. [353] measured and reported coronary flow in-vivo for a sample of 28 adult humans. Total coronary resting flow was found to be 197±72 ml/min (range: 59-376 ml/min). In that work, it was also stated that no specific method can currently be regarded as the "gold standard" for the assessment of total coronary flow in humans, and no normal values have been established so far. This poses a clear limitation for any methodology aimed at estimating the resting total coronary flow. In a recent study, Sakamoto et al. [286] measured coronary blood flow in 496 patients combining information from AX and IVUS images. They found significant association of blood flow in the LCx and RCA arteries and circulation dominance, while the LAD artery presented none. Total coronary resting flow was found to be 270±82 ml/min.

Moreover, patient-specific resting myocardial blood flow can be estimated by the cardiac output or from myocardial mass, as discussed in detail next.

7.3.4.1 Estimation through systemic hemodynamic variables

Total cardiac output can be estimated from hemodynamic variables. The pressure at the inlet of the coronary tree is considered to be the pressure at the aortic arch. It is known that the mean systemic blood pressure (MSBP) is a good approximation of the mean aortic pressure at rest. It is also known that the coronary blood flow at rest is approximately 4.5% of the cardiac output (CO). Given the heart rate (HR, in beats/min) and the stroke volume (SV in ml/beat), the CO (in ml/min) is computed as

$$\text{CO} = \frac{\text{HR} \times \text{SV}}{1000}.$$

The HR can be measured noninvasively, and the stroke volume can be estimated [87] from patient data as

$$\text{SV} = \text{PP}^* \times (0.013 \times \text{W} - 0.007 \times \text{A} - 0.004 \times \text{HR} + 1.307),$$

$$\text{PP}^* = 0.49 \times \text{PP} + 0.30 \times \text{A} + 7.11,$$

where PP is the pulse pressure[5] (in mmHg), PP* is an adjusted value for PP, A is the age of the patient (in years) and W is the weight (in Kg). Then, the total flow demanded by myocardium Q (in ml/min) is estimated as

$$Q = 0.045 \times \text{CO}. \tag{7.3.1}$$

7.3.4.2 Estimation through myocardial mass

Myocardial mass blood demand has been reported in the past. Anderson et al. [18] reported resting flow through the left main artery of 58±15 (range: 27-103) ml/min/100g of left ventricular mass, using a simplistic estimation formula (originally adjusted for dogs), which is used in coronary flow models for estimation of FFR [308, 275]. The total coronary flow at rest is estimated as

$$Q = \underbrace{(8 \times (0.0007 \times (\text{HR} \times \text{SBP}) - 0.4)/100)}_{\text{Estimate of blood flow, in ml/min/100g.}} \times \underbrace{1.5 \times \text{LVMM}}_{\text{LV is 2/3 of total myo. mass.}}, \tag{7.3.2}$$

---

[5]Systolic blood pressure (SBP) minus diastolic blood pressure (DBP).

where LVMM is the left ventricle mass (in grams), which can be estimated from the myocardial volume times its density (1.05 g/cm^3 [203]).

Perfusion values ranging from 72 to 117 ml/min/100g have been reported with positron emission tomography [304, 99, 271]. Flow data is rather similar to invasive measurements performed in [353], which reported 91±30 ml/min/100g.

Regarding normal myocardial mass, Lorenz et al. [203] reported values in humans estimated from magnetic resonance imaging, and validated them to an extensive series of published works with both autopsy and imaging measurements of myocardial mass. The RV free wall mass averaged 50±10 g in males and 40±8 g in females. Mean LV total mass was 178±31 g in males and 125±26 g in females. Yielding total ventricular myocardial mass averages of 228/165 g for males/females.

Choy et al. [75] presented allometric laws of hemodynamic and anatomical parameters as a function of myocardial mass from experimental measurements in pigs. It was reported that global coronary blood flow (in ml/min) can be estimated as

$$Q = 0.71 \times m^{3/4}, \tag{7.3.3}$$

where m is the myocardial mass, in grams. Taylor et al. [328], implies that uses equation (7.3.3) for the estimation of patient-specific resting coronary blood flow.

7.3.4.3 Resting myocardial flow estimation in our patient sample

Details of the complete patient population used in this work can be found in Chapter 10, Section 10.1. In order to compare the methods for estimation of resting myocardial blood flow, a subset of patients (IDs in the range $[6, 35]$) comprising 20 adult individuals (3 females and 17 males) with mean age $60 \pm 10[43, 84]$ years.

Table 7.2 summarizes statistical data of various hemodynamic variables used to estimate the resting myocardial flow with equations (7.3.2),(7.3.3) and (7.3.1). Although total ventricular myocardial mass matches reported data [203], estimations of resting coronary blood flow with equations (7.3.2) and (7.3.3) significantly underestimate normal values [136, 353, 286]. In turn, using the proposed methodology, which does not make use of myocardial mass, yields values within the physiological range according to [136, 353, 286]. Therefore, all estimations of patient-specific myocardial blood flow are performed using the proposed method, Equation (7.3.1).

7.3.5 Estimating hyperemic blood flow.

Chareonthaitawee et al. [68] studied the regional heterogeneity of resting and hyperemic myocardial blood flow (MBF) in healthy humans, through positron emission tomography. Basal and hyperemic MBF is heterogeneous both, inter and intra-individual. Furthermore under both blood flow conditions, similar degree of spatial heterogeneity was found. Anterior and lateral regions have similar demands and greater than septum and inferior regions. Such variabilities produce myocardial region dependence of the CFR index, and rise concern about the use of a global CFR threshold for ischemia indicator in clinical practice. The study also suggests that some regions may be operating near maximal capacity in the resting state, becoming more susceptible to injury when demand exceeds supply.

Moreover, myocardial perfusion seems to depend on patient age. Smaller values of CFR are associated to elders adults [304].

More than twenty studies reporting CFR were summarized in [165]. Weighted averages of mean CFR for lesioned (1.98±0.61) and nonischemic (2.57±0.61) arteries were reported. It should be noted that values as large as CFR=6 have been recorded in vivo. The relation between CFR and FFR is studied in [165, 102], both studies support the

	Age [years]	W [kg]	H [cm]	SBP [mmHg]	DBP [mmHg]	MBP [mmHg]	HR [min^{-1}]	PP [mmHg]
AVG	60.37	85.11	172.37	113.89	69.79	84.74	70.21	44.11
STD	10.35	17.10	10.90	13.63	9.57	9.89	8.13	7.28
MIN	43.00	52.00	147.00	80.00	50.00	65.00	58.00	30.00
MAX	84.00	119.00	192.00	139.00	84.00	102.00	88.00	57.00

	PP* [mmHg]	SV [ml/beat]	CO [l/min]	m [g]	Q, Eq.(7.3.2) [ml/min]	Q, Eq.(7.3.3) [ml/min]	Q, Eq.(7.3.1) [ml/min]
AVG	46.83	79.33	5.57	217.73	91.36	39.98	250.67
STD	5.68	10.15	0.94	57.53	29.40	8.06	42.43
MIN	38.96	60.37	3.85	113.76	36.24	24.73	173.17
MAX	57.24	94.22	7.35	326.22	140.60	54.50	330.71

Table 7.2: Statistical data of hemodynamic variables in a patient sample of the population, consisting of 20 patients, 3 females and 17 males.
W: Weight; H: Height; SBP: Systemic systolic blood pressure; DBP: Systemic diastolic blood pressure; MBP: Systemic mean blood pressure; HR: Heart rate; PP: pulse pressure; PP*: Adjusted PP; SV: Stroke volume; CO: Cardiac output; m: Myocardial mass; Q: Resting myocardial blood flow.

existence of differentiated patterns of ischemic heart disease that combine focal and diffuse coronary narrowing with variable degrees of micro-circulatory dysfunction.

Taking these findings into account, a comprehensive methodology for estimating patient-specific CFR should take into account heterogeneous CFR values per artery. Such behavior should depend on supplied territory, lesion characteristic (focal or diffuse) and, eventually, microcirculatory dysfunctions. Furthermore, the CFR should also be adjusted using patient data, e.g. age.

In this thesis, a simplified approach to estimate CFR is considered, see Chapter 9, Section 9.3 for details.

Chapter 8

Fractional flow reserve

> *"Water shapes its course according to the nature of the ground over which it flows; the soldier works out his victory in relation to the foe whom he is facing."*

<div align="right">

Sun Tzu, *The art of war.*

</div>

8.1 Basic concepts

The ideal diagnostic test to assess stenosis functionality and aid the clinical decision-making process should be expressed in the form of a quantitative index featuring the following characteristics [268, Chapter 4]: (a) independence of blood pressure, heart rate, and contractility; (b) definition within in a range of values independent of patient and coronary artery; (c) ability to identify lesions which are capable of causing ischemia from those which are not; (d) consideration for the effects of collateral circulation; and finally (e) easy-to-compute. These desired features discouraged the used of CFR and motivated the development of the fractional flow reserve (FFR), which was introduced in the early 90's by Pijls et al. [266].

FFR is defined as the maximally achievable flow in the presence of a stenosis divided by the maximum flow expected in the absence of the lesion. Figure 8.1 presents a schematic representation, simplifying heart circulation with a purely resistive electrical model. A healthy artery (with aortic input pressure P_a and a given flow Q_a) that bifurcates into a stenotic artery (s) and a healthy one (b), with blood flow rate Q_s and Q_b, respectively. Both branches reach separate myocardial vascular beds, with myocardial resistance R_{m1} and R_{m2}. After myocardial resistance, pressure drops to venous pressure P_v. Additionally, an anastomosis at the arteriolar level models a collateral path between the two arterial branches. Such connection has resistance R_c with an associated collateral flow (Q_c) from the healthy to the stenotic branch. Albeit simple, this electric-analog model allows the understanding and derivation of FFR and related indexes.

In his seminal work, Pijls et al. [266], presented a collection of three indexes to estimate the functional severity of a stenosis. Although such indexes conceptually represent relationships between blood flows, they can be estimated from pressure measurements. To correctly estimate flow from pressure, resistances R_{m1} and R_{m2} must remain constant and minimal, as is the case during maximal vasodilation (myocardial hyperemic state).

All indexes are calculated from pressure measurements in the aorta, transtenotic, wedge[1] and venous/right atrium (as illustrated in Figure 8.1). These pressures are averages

---

[1]The wedge pressure is the transtenotic pressure in the scenario of total occlusion, which can be forced by a balloon at the time of angioplasty.

along a cardiac cycle. Furthermore, indexes are dimensionless, because they express relative quantities.

The following notation is used for the introduction of the hemodynamic indexes:

- The supra-index N stands for normal condition, i.e. without stenosis, in such a case, $Q_s = Q_{m1}$ and no collateral flow is present, i.e. $Q_c^N = 0$.

- The wedge pressure is the distal (transtenotic) pressure during stenosis total occlusion, i.e. $R_s = \infty, Q_s = 0$ and therefore $Q_c \neq 0$.

A detailed derivation of each index is given on Appendix E.

(a)   (b)
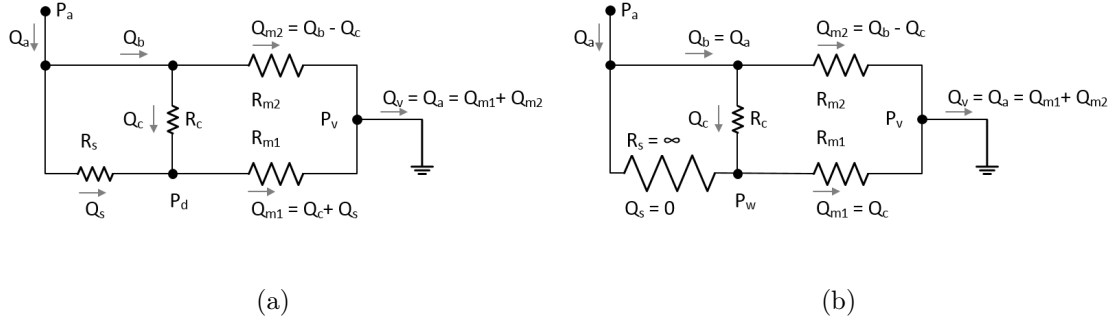
Figure 8.1: Schematic representation of coronary circulation using a purely resistive electric-analog model. Panel (a) represents a stenotic condition, while panel (b) stands for a total occlusion condition.

Coronary fractional flow reserve ($\mathbf{FFR_{cor}}$)   This index expresses the relative maximum flow through the stenosis relative to the maximum flow in the absence of it. Therefore, it takes values in the range $[0, 1]$, and can be mathematically defined as

$$\text{FFR}_{\text{cor}} \quad = \frac{Q_s}{Q_s^N} = \frac{P_d - P_w}{P_a - P_w}. \tag{8.1.1}$$

In order to calculate FFR_{cor} from pressures, a total occlusion of the stenotic artery is needed, therefore in clinical practice the FFR_{cor} can only be measured during angioplasty (balloon inflation).

Myocardium fractional flow reserve ($\mathbf{FFR_{myo}}$)   Also known simply as FFR, it expresses the myocardium maximal achievable flow in the presence of a stenosis in relation to the maximum flow expected in the absence of the stenosis. It takes values in the range $[0, 1]$, and is defined as

$$\text{FFR}_{\text{myo}} \quad = \frac{Q_{m1}}{Q_{m1}^N} = \frac{P_d - P_v}{P_a - P_v}. \tag{8.1.2}$$

By definition, FFR_{myo} only makes use of transtenotic (P_d) aortic (P_a) and venous (P_v) pressures, therefore, it can be calculated without total occlusion of the lesioned artery, meaning that no angioplasty is needed to estimate FFR_{myo}.

Collateral flow reserve ($\mathbf{FFR_{col}}$)   Also named collateral flow index (CFI), it represents the contribution of collateral flow to myocardial flow in presence of stenosis relative to the normal myocardial flow. It is calculated as

$$\mathrm{FFR_{col}} \quad = \frac{Q_c}{Q_{m1}^N} = \mathrm{FFR_{myo}} - \mathrm{FFR_{cor}} = \frac{P_w - P_v}{P_a - P_v}. \tag{8.1.3}$$

By definition, $\mathrm{FFR_{col}}$ needs pressure measurements during total occlusion ($\mathrm{FFR_{cor}}$), therefore its clinical applications are limited.

Practical considerations Since FFR is clinical obtained from coronary pressure measurements, some prerequisites associated to the interpretation of coronary pressure measurement are pertinent [268]:

1. Reliable intra-coronary pressure recording needs the used of ultra thin pressure-monitoring guide wires [85].

2. Pressure measurements are only meaningful at maximum coronary hyperemia. Furthermore, it is sufficient to study blood flow only in the arteries affected by the stenotic lesion.

3. It is not the gradient, but the remaining distal coronary pressure which determines myocardial perfusion.

Independence of FFR of hemodynamic loading conditions Reproducibility is a crucial characteristic of any diagnostic test. A measurement which is either difficult to obtain, of little clinical relevance, or highly variable, has no clinical value. Chapter 9 of [268] compiles several studies demonstrating the independence of FFR from changes in heart rate, blood pressure, and contractility. Nonetheless, questions remain regarding FFR repeatability and stability during intravenous infusion ($\mathrm{IVA_{VD}}$) because of systemic effects that can alter driving pressure and heart rate [326]. A recent study [163] showed that $\mathrm{IVA_{VD}}$ produced 3 general patterns of P_d/P_a response, with associated variability in aortic and coronary pressure and heart rate during the hyperemic period. Nevertheless, FFR – when chosen appropriately – proved to be a highly reproducible value. Therefore, operators can confidently select the "smart minimum" FFR for patient care.

8.2   The roadmap of FFR

The three hemodynamic indexes were first presented in [266], and were validated to direct flow measures in dogs. The results indicated that, under maximal vasodilation, estimation of flow by pressure measurements were precise, encouraging later investigations. In a posterior study [83], the estimation of FFR from pressure measurements was validated in humans.

The capability of pressure-estimated $\mathrm{FFR_{col}}$ to predict ischemic events was first studied by Pijls et al. [264]. It was confirmed that during acute stenosis or even total occlusion, collateral flow must be considerable or at least sufficient to meet the metabolic demands of the myocardium at rest. The study was conducted in patients with stable angina and positive exercise test, ensuring well developed collateral flow and suitability for angioplasty. It was detected that ischemia during occlusion was manifested in patients with $\mathrm{FFR_{col}} < 0.25$, while patients exceeding this threshold did not suffer ischemic events. A relation between visible collateral flow with the quantitative value of $\mathrm{FFR_{col}}$ could not be established. Furthermore, the study discarded wedge pressure (P_w) alone as a good index for collateral flow capability. It was concluded that the major limitation of $\mathrm{FFR_{col}}$ is that it can only be measured during angioplasty and not as a diagnostic procedure because P_w must be recorded during coronary artery occlusion. Validation of $\mathrm{FFR_{col}}$ against myocardial perfusion images was later performed by Matsuo et al. [215].

Pijls et al. [267] stated that FFR can be used to reliably discriminate coronary stenosis functional severity, i.e. whether it is associated with inducible ischemia or not. The study consisted in FFR measurements before and after angioplasty on a group of patients with positive stress test. A week after the procedure, the stress test was repeated. Normal outcomes of this second test indicate that the pre-angioplasty value of FFR was associated with inducible ischemia and the post value not. The study clearly found that FFR values < 0.75 are associated to myocardial ischemia. More evidence supporting the clinical value of the FFR, and the 0.75 threshold, was presented by comparing it to other diagnostic tests [2] frequently employed to detect myocardial ischemia [270].

The first long-term study of the implications of angioplasty decision-making driven by FFR was presented in [35] and continued in [269], and it is known as the DEFER (deferral of percutaneous coronary intervention) study (with two and five years of patients follow up). The study was performed in 12 hospitals in Europe and 2 hospitals in Asia between June 1997 and December 1998. Patients undergoing the study had 1) more than 50% diameter stenosis in a native coronary artery[3]; and 2) no evidence of reversible ischemia had been documented by noninvasive testing within the last 2 month. The results reinforced the validity of FFR ≥ 0.75 as an index to deferral angioplasty, stating that when percutaneous coronary intervention (PCI) was performed when FFR ≥ 0.75, the patients probability of having any cardiac event or death was not improved, and neither the chance of suffering chest pain.

The second multi-center clinical trail, known as FAME (Fractional Flow Reserve Versus Angiography in Multivessel Evaluation) [332], took place in 20 medical centers in the United States and Europe from January 2006 until September 2007. It was conducted in patients with multiple stenoses with at least one with 50% occlusion (determined by visual inspection). All patients were randomly assigned into two groups, one underwent PCI guided by angiography in all stenotic vessels (PCI group), and the other only received angioplasty in arteries with FFR < 0.8 (FFR group). Results showed that, although the average time per procedure was the same for both groups, almost a double of stents per patient were placed in the PCI group, and around 10% more contrast agent was used in the PCI group. In average, the number of dead, infarction, need for repeated revascularization was smaller in the FFR group. After one year follow up, several statistics, e.g. suffering from angina or any cardiac event, still favored the FFR group. In addition, the average cost of the procedure was U$D 700 lower and the mean length of stay in the hospital was also reduced.

A posterior study [333] using a subsample of data from the original FAME trail, concluded that: patients with multi-vessel CAD, visual inspection and stenosis percentage reduction based on coronary angiography results in an inappropriate tool to identify ischemia-producing stenosis as detected by the FFR. This discrepancy between angiographic and functional stenosis severity is present in stenosis featuring between 50% to 90% of lumen diameter reduction. The study reinforced the need for functional analysis of stenosis, over pure geometrical (visual inspection) methods. Recently, results of a 5-year follow up of the original FAME patients were published [341]. Authors claim the long-term safety of FFR-guided PCI in patients with multivessel disease.

Such clinical evidence has turned FFR into the new gold standard for myocardial ischemia risk assessment. Nevertheless, for various reasons, it is used in less than 10% of the patients [237]. Either way, there is an increasing interest from the medical community in predicting FFR threshold from geometric characteristics of arterial lesions imaged from coronary angiography (AX), intra-vascular ultrasound (IVUS), optical coherent tomography (OCT) or coronary computed tomography angiography (CCTA). Several studies

---

[2]Exercise test and thallium scanning, Stress echocardiography, quantitative coronary angiography.
[3]The term native, refers to arteries that were not surgically implanted, e.g. bypass grafts.

focused on the FFR prediction capabilities of several geometric variables, e.g. lumen area, percentage of stenosis, lesion length, plaque burden, and so on [348, 126, 205].

Given large impact on the practice of cardiology and the increasing used of FFR as the guidance tool for revascularization, controversy naturally arises. A critical review of the evidence for the concept of FFR-guided revascularization is presented by Arbab-Zadeh in 2014 [22]. Mainly, he argues that: (a) the limitations of the FAME studies are sufficiently significant to cast doubt on the validity of the FFR-guided PCI concept; (b) neither FAME studies provided conclusive evidence that FFR guidance of PCI reduces myocardial infarction or death other than by lowering the number of PCIs and does not provide proof that FFR guidance does so better than chance alone. Nevertheless, it is irrefutable that FFR can identify coronary stenoses that trigger angina, avoiding PCI in lesions that would not result in symptomatic relief. Furthermore, the DEFER and FAME studies did demonstrate the absence of merit in performing PCI in coronary artery stenoses without hemodynamic significance, which has led to decreasing numbers of stent procedures overall. This represents a major achievement of the FFR paradigm and an important step in the direction of incorporating functionality to medical images in order to improve diagnosis and therapeutic strategies.

8.3   Limitations of FFR

Pijls et al. [265] summarize the potential pitfalls of invasive coronary pressure measurements and the impact on FFR estimation. Although most of such are associated to the procedure, e.g. drug administration, recording synchronization, catheter positioning, etc; there are some known pathophysiologic conditions limiting the use of pressure measurements, e.g. coronary steal and microvascular disease.

Coronary steal occurs when one critically narrowed or occluded coronary artery, receives collaterals from another vessel which is stenotic itself (but not critically stenotic). To correctly assess FFR in such condition, the drug induced hiperemia should be enforced in both vessels, i.e. intravenous administration of vasodilator [268].

The most important conceptual limitation of FFR is the presence of microvascular disease distal to place were P_d is measured. This can be manifested in the presence of diabetes, but may also play a role after myocardial infarction and in diffuse coronary atherosclerosis. Under such conditions, the hypothesis for normal flow estimation, see Section 8.1, does not hold. Nonetheless, even under these conditions, the FFR still expresses the extent to which the flow supply will be improved by a revascularization procedure. This consideration is a key difference between FFR and CFR, since the later may indicate epicardial disease, microvascular disease, or both. However, it cannot separately distinguish between these entities. Associations between FFR and CFR were initially presented in [83]. More recently, in [165], a linear relation between CFR and FFR was found. The relative contributions of focal and diffuse disease define the slope and values along the linear CFR and FFR relation. Discordant CFR and FFR values reflect divergent extremes of focal and diffuse disease, not failure of either tool. A posterior study [102], supported the existence of differentiated patterns of ischemic heart disease that combine focal and diffuse coronary narrowings with variable degrees of micro-circulatory dysfunction.

Also, there is increasing interest in novel indexes that are able to account for a more comprehensive assessment of coronary physiology [162, 340], in which flow is measured directly and not estimated from pressure. In such paradigm, the CFR and the hyperemic flow are combined to quantify and stratify ischemia risk.

The interested reader will find updated reviews about the different aspects of the FFR index in [339, 171, 161].

8.4 Computational assessment of FFR

Despite the controversy and limitations surrounding the FFR, a large part of the community supports the concept of coronary revascularization guided by FFR. Such statement is sustained by the fact that several international guidelines emphasize ICA with the measurement of FFR as the standard of reference for determining the functional significance of individual coronary artery stenoses [258, 27]. However, these invasive procedures carry the risk of serious complications such as bleeding, stroke, coronary artery dissection, allergic reaction to dye or medication, kidney damage and myocardial infarction, among others [249]. Furthermore, the short-term cost of the procedure is increased in relation to the traditional angiography alone because of the need for pressure wire and hyperemic drugs. Also, the FFR is used in less than 10% of suitable scenarios [88, 237] even in the United States and the Europe Union, where the rates of use of FFR are among the highest.

At the same time, thanks to advances in scanner technology [323, 67], CCTA became a popular noninvasive method for direct visualization of CAD. However, there is a weak association between severe stenosis detected by CCTA and ischemia [227]. Therefore, although useful to rule out stenotic vessels, CCTA alone is not enough to guide revascularization. As a consequence, other diagnostic noninvasive tests are usually performed following CCTA to help with the physiological assessment of CAD and, at the same time, avoid invasive procedures. It is in this context in which the idea of using tools from computational fluid dynamics (CFD) to estimate the FFR noninvasively from CCTA image was conceived, yielding the foundation of the medical software start-up known as HeartFlow [3]. In recent years other research groups and health-care equipment manufacturers around the world are actively working to develop methods and techniques to estimate the FFR from medical images, without the use of the pressure wire. This section aims (a) to state the key steps needed to estimate FFR using CFD simulation tools and (b) to summarize the most relevant contributions to the field. This prepares the groundwork for the proposed strategy to estimate FFR from medical image, as will be discussed in Chapter 9.

8.4.1 Requirements

Since the conceptual determination of FFR amounts to characterize the resistive features of stenotic lesions (recall the FFR paradigm is based on an purely resistive electric-analog circuit), targeting the computation of FFR, it is standard to assume that vessels do not deform during the cardiac cycle. In such context, a complete model for the coronary arterial circulation should take into account several aspects of the physical phenomenons taking part, mainly:

- The governing equations of fluid dynamics are the well known Navier-Stokes equations (8.4.1), which characterize the velocity ($\mathbf{v}$) and pressure (p) of a fluid in each spatial position ($\mathbf{x}$) of a given three-dimensional (3D) domain (Ω) at each time instant (t) during the cardiac cycle. These equations read

$$\begin{cases} \rho\dfrac{\partial \mathbf{v}}{\partial t} + \rho(\nabla\mathbf{v})\mathbf{v} - \mu\triangle\mathbf{v} + \nabla p = 0 & \text{in } \Omega, \\ \operatorname{div}\mathbf{v} = 0 & \text{in } \Omega, \\ \mathbf{v} = 0 & \text{on } \Gamma_w, \\ + \text{ Appropriate BC (see Chapter 9)} & \text{on } \Gamma_p \text{ and } \cup_{i=1}^{N_o}\Gamma_i \end{cases} \tag{8.4.1}$$

  In the equations above, the actual physical properties of blood, fluid density (ρ) and viscosity (μ), are assumed known and constant (flow is incompressible, and fluid is assume to be Newtonian), which are standard hypotheses for large vessels such as the coronaries arteries. The domain Ω is constant in time, with boundary Γ_w

representing the arterial wall, Γ_p the proximal boundary (the inlet at the aortic root) and Γ_i, $i = 1, \ldots, N_o$, the N_o outlet boundaries, and $\mathbf{n}$ the normal vector. Although equation (8.4.1) models flow in a 3D domain, dimensional reductions (for example 1D models) targeting blood flow were proposed in the past [28, 151, 319], and are currently being used to simulate blood flow in extremely large arterial networks comprising the entire arterial vasculature [42, 43]. In such simplified models, part of the physical phenomena is neglected by the model, e.g. transversal flow circulation. Finally, BC stand for boundary conditions, which will be discussed next.

- The fluid domain (Ω) represents the arterial lumen. A comprehensive model of the arterial wall mechanics and the fluid structure interactions, which cause deformation of the lumen, is a challenging and expensive task [24]. Furthermore, during the heart beat, the spatial location of the arteries changes due to the movement imposed by the heart [255, 170]. The effects in the pressure field of such lumen variations were studied in [90], and it was shown that modeling such phenomena does not substantially contribute to the average pressure required by the calculation of the FFR. Therefore, as said in this work, the arterial domain Ω is considered fixed in time (arteries are considered rigid).

- The coronary arterial circulation is not an isolated system, it is coupled to the rest of the cardiovascular system at both, the inlet and outlet. A comprehensive review of physiological aspects of coronary circulation can be found in [316]. Basically, the pressure at the inlet of the coronary arterial tree is given by the aortic root pressure, while the flow signatures are shaped by myocardial microcirculatory compression patterns due to cardiac contractions along the heart beating [81]. Therefore, an isolated model of the coronary arterial circulation, needs of the imposition of appropriate hemodynamic conditions at the domain boundaries, the so called boundary conditions (BC). Over the arterial wall no-slip BC are assumed, meaning that the blood adheres to the wall, that is blood velocity is zero. There are different approaches to impose hemodynamic conditions at the inlets and outlets, e.g. traction (pressure), flow, resistance and so on (see Chapter 9). Note that modeling resting or hyperemic blood flow requires the appropriate setting of such BC, because they fully determine the blood demand from the downstream myocardial tissue. In such context, using time-dependent BC results in time-dependent flow, and thus in the need for transient simulations, where the cardiac cycle is simulated. However, since the FFR relies on average pressure values over the cardiac cycle it is also possible to perform steady state simulations, achieved by setting BC which are constant in time.

- The use of numerical methods for solving fluid dynamic problems is the definition of the so called Computational Fluid Dynamic (CFD) field of research. With more than 50 years of existence, the impact of CFD in a broad range of applications is invaluable. The first applications of 3D CFD for simulating blood flow in arterial domains where performed in the early 90's [260] as an alternative to study wall shear stress in an in-silico manner. Maybe the most used numerical method to solve the Navier-Stokes equations are Finite Element Methods (FEM), as well as Finite Volume Methods (FVM), Finite Difference Methods (FDM) and Lattice-Boltzmann Methods (LBM). Accuracy and computational cost of numerical methods depend on the so call refinement of the computational domain[4], also known as computing mesh. Furthermore, the dimensionality of the model, e.g. 3D or 1D, directly impact on the computational cost required to perform the simulation.

---

[4]The computational domain is the discrete counterpart of the continuum domain Ω, achieved after partitioning Ω into basic units usually referred to as elements, or cells.

A comprehensive review of different aspects regarding computational models for coronary circulation, focusing in myocardial-vessel interaction due to left ventricle contractility is presented by Kassab et al. [176]. Moreover, solving the Navier-Stokes equations in a patient-specific fashion needs the specification of the arterial domain Ω and, equally fundamental, the definition of BC matching the patient hemodynamic features, namely:

- Computational domains of the coronary arteries are obtained using image processing techniques from medical images. Several imaging modalities can be used, e.g. coronary computed tomography angiography (CCTA), intra-vascular ultrasound (IVUS), optical computed tomography (OCT), coronary angiography (AX) and rotational coronary angiography (ROC). Each modality presents different challenges as for the image processing techniques to be used, and also have advantages and disadvantages regarding the quality and spatial definition of the resulting geometric model. In this work, special detail has been given to the processing of CCTA images in Chapter 2 to produce geometrical models for the Part I of this Thesis. From such geometric models, computational meshes for CFD can be constructed by standard mesh operations, as can be seen in Appendix A. The accuracy of the computational domain has an obvious direct effect on the results delivered by CFD simulations.

- Depending on the type of BC to be used, appropriate patient data needs to be measured or estimated. Arterial pressure, flow rates, cardiac frequency and peripheral resistances are examples of relevant hemodynamic parameters that can be used to prescribe patient-specific BC. Note that such parameters vary depending on hemodynamic load conditions, e.g. rest and hyperemia.

- Finally, once the domain and BC are prepared, the Navier-Stokes equations must be solved, and the simulation results must be processed to extract the pressure field (average over the cardiac cycle) to obtain an scalar field representation of the FFR in the arterial domain. Assuming the image was accurately processed, it is then evident that BC directly impact the result of CFD simulations, and therefore, the correctness of the computational assessment of FFR is directly, and mostly in our experience, related to the BC, as will be seen in Chapter 10.

8.4.2 Critical literature review

Since 2011, several computational methodologies to estimate FFR using CFD methods have been proposed. Some of these approaches gained recognition in the medical community (moreover, some are boosted up by private health care companies) and produced clinical trials with relatively large patient samples, and many others are still in the phase of preliminary tests. A comprehensive bibliographic review about the computational assessment of FFR is presented in this section. First, in Table 8.1, current approaches are reviewed from a methodological point of view. Then, in Table 8.2, the results in terms of comparisons against invasive FFR measurements are summarized. Note that references are grouped by research teams to provide a global perspective about the different methodologies. The interested reader is referred to [237, 337], for reviews on current approaches on CFD-derived FFR.

Group Study (year)		Summary	Medical image	Modeling considerations
Worldwide multicenter (hospitals) - Using of HeartFlow Software	DISCOVER-FLOW [186],[360],[146] (2011, 2012, 2013)	• Presentation of the FFR$_{CT}$ index, the first noninvasive (computational) estimation of the FFR. • The first medical trial assessing the accuracy of a computational approach to estimate the FFR [186]. Prospective, multicenter blinded study. • Lesions of any degree were used. • It Compares cdiagnostic capabilities of CT (%stenosis≥50%) against FFR$_{CT}$ and invasive FFR. • A subgroup of patients was used to compare diagnostic capabilities against Trans-luminal Attenuation Gradient (TAG, see Appendix D) [360]. • Another subgroup of patients was used to make economic cost projections following hipothetic clinical decision scenarios guided by different diagnostic strategies, including FFR$_{CT}$ [146]. It was reported that a strategy of using FFR$_{CT}$ to guide the selection of patients for ICA and PCI might reduce costs and improve clinical outcomes in patients with suspected coronary artery disease. • Overall, noninvasive FFR$_{CT}$ provides better diagnostic performance for lesion-specific ischemia compared to CCTA %stenosis and TAG, taking as gold standard invasive FFR. • It is reported that simulation runtime is 5 hs/exam.	CCTA, (≥64-detector row CT scanners). It is not stated if the geometrical models consist of all arteries or the subtree affected by the disease.	• *Collaterization* not used, not mentioned. • *Model dimension* 3D. • According to references cited within the studies [182, 180, 181], *boundary conditions* are modeled with lumped windkessel elements; simulations compute *transient* regimes (the number of cardiac cycles is not reported); coupled with systemic circulation through a closed loop (with heart and pulmonary circulation models), although reference [182] is based on an open loop system; it is not specified whether the model accounts for compliant arterial walls or rigid, although references [180, 181], use compliant models. • It is not specified how hyperemic conditions are simulated, although the work [355] is cited, mentioning that microcirculation reacts predictably to maximal hyperemic conditions.
	DeFACTO [225],[226],[247] (2011, 2012, 2013)	• Rationale [225] and results [226, 247] of a prospective, multicenter blinded study to evaluate the diagnostic performance of FFR$_{CT}$. • Stenosis (in the range of 30% to 90% obstruction) were included in [226], while only intermediate stenosis (in the range of 30% to 70% obstruction) where used in [247]. • It is reported that simulation runtime is 6 hs/exam.		
	NXT [119, 251, 250] (2013, 2014, 2015)	• Rationale [119] and results [251] of the prospective, multicenter blinded NXT trial. • The main purposes are: (i) test the influence of improvements in HeartFlow software on the diagnostic accuracy of FFR$_{CT}$, (ii) investigate prospectively the FFR$_{CT}$ accuracy in patients with non-critical coronary artery lesions, and (iii) test the methodology in a real-world scenario by using site coronary CTA reads rather than core laboratory reads. • Criterion for patient exclusions are %stenosis>90% or %stenosis<30%, previous cardiac interventions, and poor image qualities. • Using a subgroup of patients [250], the impact of calcium scores in the FFR$_{CT}$ index was assessed. In a subsample of arteries with higher calcium score, comparisons between invasive FFR and FFR$_{CT}$ results in smaller correlation and larger dispersion. • It is reported that simulation runtime is 1-4 hs/exam.		The following methodological points differ from previous studies (DISCOVER-FLOW and DeFACTO): • The methodological references now are [180, 181, 328]. • The new reference [328] suggests that an open loop model of the circulatory system is used. • It is not clear whether compliant or rigid arterial wall models are used, reference [328] suggests rigid while [180, 181] suggest compliant. • The methodology for simulating hyperemia is still not well documented, although reference [328], suggests that microcirculatory resistance of all arterial terminals is reduced by a factor of ∼ 0.25 according to [355].
	PLATFORM [96, 145] (2015)	• This medical trial uses the FFR$_{CT}$ methodology in a real-world scenario, where diagnostics were performed either by usual care or FFR$_{CT}$. • It was reported that FFR$_{CT}$ was a feasible and safe alternative to invasive coronary angiography (ICA) and was associated with a significantly lower rate of invasive angiography showing no obstructive CAD [96]. • Furthermore, an evaluation strategy based on FFR$_{CT}$ was found to be associated with less resource usage and lower costs within 90 days than evaluation with ICA. Also, it was associated with greater improvement in quality of life than evaluation with usual noninvasive testing.		• Methodological details associated to the computation of FFR$_{CT}$ are not presented, citations to [328] are provided instead, which is not informative.

Group	Study (year)	Summary	Medical image	Modeling considerations
Siemens	[155, 308] (2012)	• Two methodological papers, make use of only a single patient-specific model. • First attempt to use 1D models for the FFR computational estimation [155]. • Adds a parameter estimation strategy for the peripheral resistances of the lumped parameter model [308]. • It is reported that simulation runtime is 1 min [308].	CCTA. No details nor references regarding the image segmentation and geometric model construction are given.	• *Collaterization* not used, not mentioned. • *Model dimension* 1D. The proposed model is composed of axisymmetric 1D elements. Stenosis regions are modeled using the pressure drops known as the Young model [362]. • *Boundary conditions* are modeled with lumped windkessel elements of the coronary and systemic circulation, coupled with a heart model to include the effects of the myocardial contraction on the coronary flow (and provide the inflow), in an open loop fashion; simulations compute *transient* regimes (the number of cardiac cycles is not reported); to distribute the total resistance to the various lumped models at the outlets, the Murray's law is used; the 1D model implicitly accounts for the compliance of arterial walls. • For simulating drug-induced intracoronary hyperemia, only the lumped parameters of the artery of interest are adapted by a scale factor [155] which is then adjusted by a control strategy to fit pressure data. [308].
	[275, 76] (2014)	• Two independent trials, introducing the Siemens Healthcare approach to estimate FFR from noninvasive images (cFFR), using a software (version 1.4) not commercially available at the moment of publications, installed on a regular workstation. • Retrospective, single center blinded studies. • The cFFR was compared against invasive FFR and to CCTA (%stenosis≥50%). It was found that cFFR outperforms CCTA for the detection of hemodynamically significant stenosis. • Including data set processing and flow simulation, reported runtime is 37.5±13.8 minutes [275]. According to [76], image processing/mesh generation takes 20-120 minutes depending on image quality, while solving the 1D model takes 5-10 minutes.	CCTA. A quality index is used in order to decide whether images are to be processed or not.	Modeling details are not well documented, instead, citations to [155, 308] are provided.
	[334] (2016)	• The first trial from Siemens Healthcare introducing the so called FFR$_{angio}$, an estimation of FFR from angiogram images. • Retrospective, single center blinded studies. • Low inter-observer variability. • It is reported that simulation runtime is 40 seconds.	AX, acquired at rest from 2 views at angulations at least 30° apart. 3D model of the coronary lesion is contructed using a commercially available software (syngo IZ3D; Siemens AG, Healthcare, Forchheim, Germany). The main vascular branch and, if appropriate, one side branch could be included in the model. The centerline to create the 1D model is then extracted.	Modeling details are not well documented, instead, citations to [155] are provided. Particularly, it is not clear how the inflow is determined, since input data is different from the one used in [155].

Group	Study (year)	Summary	Medical image	Modeling considerations
Toshiba	[184] (2016)	• First trial, introducing CT-FFR, the Toshiba Medical Systems Corp. approach for estimation of FFR from noninvasive images. Using proprietary software installed in regular workstations. • It is reported that total processing time per patient averages 24.07±7.54 min. • Single-center study with a small sample of subjects and vessels. • The CT-FFR was compared against CCTA, QCA and visual ICA (%stenosis≥50%). It was found that CT-FFR outperforms all three methods for the detection of hemodynamically significant stenoses, taken invasive FFR as gold standard. • Boundary conditions are determined with nonstandard method, accounting for the structural deformation changes in the coronary lumen and adjacent aorta across the entire diastolic phase of the cardiac cycle. • It is not clear if hyperemic or resting conditions are simulated, the iFR concept is mentioned, and there are no comments on adapting the BC for hyperemia. • Performed in a blinded fashion, with intra- and inter-observer variability, -0.02 ± 0.05 and 0.03 ± 0.06, respectively.	CCTA. Pre-processing is performed using FC03 reconstruction kernel (SurePlaque, Toshiba Medical Systems Corp.). Vessel centerline and luminal contours were automatically processed. Manual adjustments were performed as required. Four CT images were reconstructed (at 70%, 80%, 90%, and 99% of R-R interval). Each millimeter of the coronary tree from the vessel inlet to outlet (up to 1.8 mm in diameter) was registered and permitted calculation of structural data including the cross-sectional luminal deformation, volume variation in the vessels and aortic root.	• *Collaterization* not used, not mentioned. • *Model dimension* 1D. Blood was modelled as a non-Newtonian fluid using the Herschel-Bulkley fluid constitutive model. • Fluid dynamics solved with FEM using dedicated software. • The paper lacks methodological and modeling details, instead a citation to [144] is presented.
Sheffield, United Kingdom	VIRTU-1 [236] (2013)	• First trial using AX images, introducing the so called vFFR index. • Only lesions with %stenosis>50% detected in angiograms are used. • It is reported that simulation runtime is $\sim$ 24 hs/exam.	AX. 3D model is constructed from two projections at 90° angulation. Image quality is an excluding factor. Image processing performed in a Philips 3D workstation. Geometric models were meshed into $\sim$ 1 M internal tetrahedral.	• *Collaterization* not used, although it is mentioned in discussions. • *Model dimension* 3D. Computational domains only take into account the artery of interest without branches. • Fluid dynamics solved with the FVM using commercial software [14]. • *Boundary conditions* are modeled with lumped windkessel at the outlet and pressure curve at the inlet, in an open loop fashion. Generic windkessel parameters were used for all patients, such parameters were obtained by averaging the values over the same patients, initially calculated to fit data acquired from pressure measurements. The inlet pressure waveform was also averaged from all patients. • The flow is determined by the generic windkessel, therefore all patients are simulated with the same blood flow, disregarding the artery and patient-specific physiology. • Simulations compute *transient* regimes (the number of cardiac cycles is not reported) • Although not specified, it is suggested that rigid walls are used.

Group Study (year)	Summary	Medical image	Modeling considerations
Lediden, Netherlands [336] (2014)	• First work introducing FFR$_{QCA}$, another computational estimation of FFR. • Flow boundary conditions are obtained from the AX using image processing techniques. • Low inter- and intra- observer variability was reported. • Only arteries with diameter stenosis within 40-70% according to visual inspection of angiograms were used. Bifurcation lesions were discarded. • Simulation run time ~ 5 min/exam.	AX. 3D model is constructed from two projections at 25° angulation. Only large branches are included. It is reported that CFD meshes of ~ 780000 element are constructed in 2 minutes.	• *Collaterization* not used. The justification is that collateral flow development would be rather infrequent in the case of intermediate lesions. Furthermore, disagreement to invasive FFR is attributed to abnormal microcirculatory resistance or downstream collateral circulation. • *Model dimension* 3D. • No details on the numerical method used to solve the CFD problem, although the FLUENT (version 1.4, ANSYS Inc [15]) software is used. • Blood density and viscosity are patient-specific measurements. • *Steady state* simulations are performed; patient-specific *boundary conditions* are used, mean pressure and flow at the inlet and flow at the outlet. All flows are estimated using the TIMI (Thrombosis in myocardial infarction) technique and frame count. • Although not specified, it is suggested that arterial walls are assumed to be rigid.
Univ. of Ioannina, Greece; Imperial College London, UK [256] (2014)	• Introduction of the virtual functional assessment index (vFAI), defined as the area under the curve relating pressure ratio (P_d/P_a) to flow rate (Q). Which is estimated from the relation $\Delta P = f_v Q + f_s Q^2$, where the coefficient for pressure lost due to viscous and separation effects are obtained from pressures resulting from CFD simulations at fixed flow rates $Q = \{1,3\}$ [ml/s]. • Only arteries with diameter stenosis within 30-70% according to visual inspection of angiograms were used. • It is reported that the complete pipeline (processing and simulation) takes < 15 min/exam. Segmentation time 5 min. Mesh generation time 3 min	AX. 3D model is constructed from two projections 30° apart. Side branches are not included.	• *Collaterization* not used, not mentioned. • *Model dimension* 3D. Computational domains only take into account the artery of interest without branches. • No details on the numerical method used to solve the CFD problem. • *Steady state* simulations are performed with *boundary conditions* of 100 mmHg at the inlet, and flow was imposed at the outlet (1 and 3 ml/s). • Although not specified, it is suggested that arterial walls are rigid.
Yonsei University, Seoul, Korea [137] (2016)	• First study using OCT image derived computational models, introducing the so called FFR$_{OCT}$ index. • The use of OCT allows the most accurate lumen model of the main artery under study. • Only LAD arteries with diameter stenosis within 40-70% according to visual inspection of angiograms were used. • It is reported that the complete pipeline (processing and simulation) takes < 10 min/exam.	OCT.	• *Collaterization* not used, not mentioned. • *Model dimension* 3D. Computational domains only take into account a small region near the stenosis disregarding branches, in a rectified manner (no spatial orientation is performed). • Commercial software (ADINA v 9.0.7 [13]) is used to solve the CFD problem with FEM and rigid wall models. • *Steady state* simulations are performed, and a generic, simplified one-size-fits-all approach to *boundary conditions* is used [236]. Patient-wide averages of pressure and flow at the outlet and inlet were used. Flow is estimated by using TIMI from angiogram at rest conditions, and hyperemia is not simulated.

Group	Study (year)	Summary	Medical image	Modeling considerations
Indiana Univ. Purdue Univ. Indianapolis, Indianapolis, USA	Huo et al. [152] (2012)	• Analytical model for pressure drop across stenosis. • Good agreement with in-vivo and in-vitro measurements. • Flow pulsatility and stenosis shape (e.g. eccentricity, exit angle divergence, etc.) had a negligible effect on FFR. The pressure drop across a stenosis remained relatively unchanged (less than 5%), between pulsatile and steady-state flow in in-vitro experiments. • Entrance effect in a coronary stenosis was found to contribute significantly to the pressure drop.	Lack of use of medical images from human patients. Experimental measurements of in-vitro arterial models and in-vivo (swines) are used.	• *Collaterization* not used. It is mentioned as a source of disagreement in significant stenosis between the model and patient measurements. • Analytical equation. • Needs the specification of the inflow.
Universities from Singapore, USA, China	[368] (2016)	• First trial, introducing FFR_{SS}, an approach for estimation of FFR from noninvasive images. • It is reported that total processing time per patient between 0.5 and 2 hs. • Single-center study with a small sample of subjects and vessels. • The FFR_{SS} was compared and outperformed area and diameter of stenosis, taken invasive FFR as gold standard. • The analytical approach proposed by Huo et al. [152], now named FFR_{AM} was also evaluated, and obtained similar results than FFR_{SS} compared to invasive FFR. Although a direct comparison between both (FFR_{SS}, FFR_{AM}) was not presented. • Boundary conditions are determined with nonstandard method, using a generalized Murray's law [370, 367].	CCTA. Details on the image segmentation technique are provided. Computational mesh of ∼ 0.8 tetrahedral are constructed with commercial software ANSYS workbench.	• *Collaterization* not used, not mentioned. • *Model dimension* 3D. Blood was modeled as a Newtonian fluid, the Navier-Stokes equations were solved using commercial software, FLUENT^{TM}. • *Boundary conditions* of pressure at the inlet and pure resistive at the outlets where used, to simulate steady state flow. Resistances are estimated using a generalized Murray's law [370], and an iterative strategy to adjust resistance values is employed, see [367]. • Hyperemia was modeled by multiplying the resistances by a factor of 0.21, based on [355].

Table 8.1: Summary of publications addressing the computational estimation of FFR.

Research group	Study (year)	#Patients/ #Arteries	Prev	AUC	Prediction value [%] Acc	Sen	Spe	PPV	NPV	Corr. r	Difference $m_{BA} \pm SD_{BA}$
HeartFlow	DISCOVER-FLOW [186] (2011)	103 / 159	36.5	90.0	84.0	87.9	82.2	73.9	92.2	0.68	0.022 ± 0.116
	Yoon et al. [360] (2012)	65 / 82	39.0	94.0	89.0	81.3	94.0	89.7	88.7	0.70	-
	DeFACTO [226] (2012)	252 / 406	54.4	81.0	73.0	90.0	54.0	67.0	84.0	0.63	0.058 ± -
	Nakazato et al. [247] (2013)	82 / 150	23.3	79.0	69.0	74.0	67.0	41.0	90.0	0.50	0.050 ± 0.200
	NXT [251] (2014)	235 / 484	20.7	90.0	81.0	86.0	79.0	65.0	93.0	0.93	0.020 ± 0.074
Siemens	Renker et al. [275] (2014)	53 / 67	29.8	92.0	-	85.0	85.0	71.0	93.0	0.66	-
	Coenen et al. [76] (2014)	106 / 189	42.3	83.0	74.6	87.5	65.1	64.8	87.7	0.59	-0.040 ±0.130
	Tröbs et al. [334] (2016)	73 / 100	29.0	93.0	90.0	79.0	94.0	85.0	92.0	0.85	0.008 ± 0.063
Toshiba	Ko et al. [184] (2016)	30 / 56	33.9	83.9	88.0	77.8	86.8	73.7	89.2	0.57	0.065 ± 0.137
Univ. of Sheffield, UK	VIRTU-1 [236] (2013)	19 / 35	20.0	-	97.0	86.0	100.	100.	97.0	0.84	0.020 ± 0.080
Lediden, Netherlands	Tu et al. [336] (2014)	68 / 77	29.9	93.0	88.0	78.0	93.0	82.0	91.0	0.81	0.000 ± 0.060
Univ. from Greece and UK	Papafaklis et al. [256] (2014)	120 / 139	37.4	92.0	86.0	79.0	90.0	82.0	88.0	0.78	-0.004 ± 0.085
Univ. of Yonsei, Korea	Ha et al. [137] (2016)	92 / 92	26.1	93.0	88.0	68.7	95.6	84.2	89.0	0.72	-0.030 ± 0.080
Univ. from Singapore, USA, China	Zhang et al. [368] (2016)	21 / 32	31.2	95.5	90.6	80.0	95.5	88.9	91.3	0.84	0.026 ± 0.050

Table 8.2: Summary of results available in the literature comparing invasive FFR and computational estimations. All listed publications used a threshold value of 0.8 to diagnose risk of ischemia in both invasive and computational FFR indexes. Correlation, prediction and differences indexes computed in a per-artery basis.

From the bibliographic review, it is clear that the FFR_{CT} index from HeartFlow is leading the race for the computational assessment of FFR. This statement is based on the evolution of clinical trials, i.e. DISCOVER-FLOW [186], DeFACTO [247], NXT [251] and PLATFORM [96]. Through these trials, (i) the FFR_{CT} was compared to other diagnostic techniques, and outperformed them for detecting ischemia when invasive FFR was taken as gold standard; (ii) FFR_{CT} as a measure alone was used in the decision making progress; (iii) The economics and quality-of-life impact in the use of FFR_{CT} compared to other clinical tests was analyzed. In turn, the rest of the approaches summarized in Table 8.1 are in stage (i) and with smaller patient samples.

Nonetheless, a close review of the publications behind FFR_{CT} reveals some points that are worth discussing, and motivates further research in the area. It is noteworthy that all publications of HeartFlow's FFR_{CT} were made in medical journals, which is proper when reporting trials results. Then, since such publications lack of methodological details, citations to more "technical" papers are to be expected. Particularly, until the year 2013, such technical references were [182, 180, 181], in which incremental complexity in the modeling of hemodynamics is presented, including FSI, closed loop circulatory system and regulatory mechanisms among others. After the year 2013, HeartFlow published three methodological papers [366, 133, 328] which are referenced in subsequent trials publications. But all three of them were published in medical, instead of bioengineering journals, and therefore the level of detail regarding each step for patient-specific hemodynamic is not rigorously documented, and moreover, the same technical papers, i.e. [182, 180, 181], are cited within such apparently "methodological reports". The lack of a critical review, from the appropriate community, on the methodology behind FFR_{CT} detracts reproducibility of the index. A clear example can be found in [119], where it is mentioned that HeartFlow software version 1.4 will be used in the NXT trial, instead of version 1.2 (which was used in previous trials). The implications on the modeling and numerical methodologies of such software version change are not known.

Since the methodology is not properly reported, from [366, 133, 328], although not explicitly said, one can infer that peripheral resistances are estimated with a Murray-law relation, the coronary flow is estimated with an allometric law based on [75], and hyperemia is obtained reducing peripheral resistances by a factor of ~ 0.25 according to [355]. It is reported that version 1.4 of the HeartFlow software computes the FFR in 4 hs per exam. From the practical point of view, it should also be taken into account that approximatly 13% of CCTA studies are discarded for not reaching the minimum image quality requirements so that it can be used in the calculation of FFR_{CT} [251].

From the big health care companies, Siemens seems to be taking the lead in terms of a framework to computationally estimate the FFR. Currently with two approaches (cFFR and FFR_{angio}), they aimed to estimate the FFR from CCTA or AX images. Both techniques use 1D models of the coronaries. These models allow fast estimations of FFR. According to the methodological description, both approaches are based on [155, 308], i.e. on a special stenosis model (based on Young et al. [363]), on a flow distribution based on Murray's law, and with boundary conditions which are implemented with windkessel elements in an open loop model, while the coronary flow is estimated from myocardial mass. It is not clear, however, how the coronary flow is estimated when using AX images. Hyperemic conditions are obtained by reducing resistance terminals with an optimization problem [308]. Although cFFR is noninvasive, the use of FFR_{angio} requires catheterization (AX image modality) but does not need of drug-induced hyperemia. Both approaches provide the FFR estimation within 1 hs including image processing and mesh preparation. In turn, Toshiba Medical Systems Corp. recently joined the race with the so called CT-FFR [184] with a clinical-like publication with a relative small patient sample. Their methodology used 1D models of patient-specific coronary trees constructed from 4D-CCTA

images. The mathematical and numerical methodology to impose boundary conditions is not clear, but they cite a more methodological work from the same group [144].

Computational assessment of FFR from AX images was first introduce in the VIRTU-1 trial [236], by researchers from the University of Sheffield, United Kingdom. The methodology is called vFFR, the 3D computational domain does not include side branches. The most notorious feature that differs from the other approaches is that the boundary conditions used for all patients are the same, pressure at inlet and flow at the outlet, which were estimated as the mean of best-fits for each patient. It was reported that simulations are performed in ~ 24 hs. Furthermore, the methodology requires catheterization (AX image modality) but does not need of drug-induced hyperemia.

The first work using artery specific flow derived from AX images to impose boundary conditions was presented in [336], by a group from the Leiden University, Leiden, the Netherlands. The approach is called FFR_{QCA}, since the 3D computational model is constructed from AX images and includes large branches. The blood density and viscosity are obtain from patient-specific measurements. This is the first approach in which steady state simulations are performed. The computational times reported for mesh preparation and simulation are within 10 minutes, which would allow in-site computation of FFR_{QCA}. The reported methodology requires catheterization (AX image modality) and drug-induced hyperemia.

A different approach was proposed in [256], by researchers from University of Ioannina, Greece and various other centers in Europe and the Unite States. They proposed the so called virtual functional assessment index (vFAI), based on CFD simulations. The index correlates well with invasive measurements of FFR. Simulations are performed in 3D domains of the lesioned artery, without branches, which is obtained from AX images. Steady state simulations are performed with the same boundary conditions for all patients. Reported computational times are within 15 minutes, accounting for image processing and mesh generation, which would allow for in-place utilization of vFAI. Nevertheless, the use of AX images requires catheterization, but does not need drug-induced hyperemia.

The use of OCT images to estimate functional significance of stenoses was first presented in [134]. Researchers from such study declared associations to Boston Scientific. The study introduces the so called vascular resistance ratio (VVR) index, derived from a lumped resistance model based on OCT arterial diameters. This is the only work in which the influence of considering branches in flow distribution is assessed. In turn, the use of 3D computational models derived from OCT image modalities was first presented in [137], by researchers of the Yonsei University, Seoul, Korea. They named the index FFR_{OCT}, and compared it to invasive measurements of FFR. Although the methodology is detailed, it is suggested that boundary conditions correspond to patient-wide (retrospective group) measurements of flow (using TIMI frame count) and pressure at rest. In that case, the FFR_{OCT} is not obtained simulating the hyperemic conditions associated to the invasive FFR.

Other approaches for the computational assessment of FFR have been reported, such efforts are still in pilot studies stages, and therefore were not included in Tables 8.1 nor 8.2.

A group from the University of Ioannina, Greece, presented the first attempt to computationally estimate the FFR from IVUS+AX medical images [313] in the year 2013. The pilot study consisted of 7 arteries from 6 patients, with invasive FFR > 0.9 for all of them. 3D models did not include side branches, and CFD meshes had a density of ~ 3000 tetrahedral/mm^3, determined after a mesh sensitivity analysis. Steady state flow regime with rigid walls were assumed. Neither details on the numerical methods used for solving the CFD problem nor the computational times were reported. Furthermore, this approach does not simulate an hyperemic state. In contrast, it is based on the iFR paradigm (see Appendix D). Boundary conditions are patient-specific average pressure at the inlet and

average coronary blood flow under resting condition at the outlet (averages are computed during the diastolic wave-free period). At a later pilot study (year 2015) from the same research group [312], 5 arteries were used (all with invasive FFR> 0.9). The study used the methodology detailed in [256] to compute the vFAI, i.e. boundary condition of 100 mmHg at inlet and flow (1 and 3 ml/seg) at the outlet. Steady-state with rigid walls simulations were assumed. They compared the results using 3D meshes reconstructed purely from AX (as in [256]) and reconstructions using IVUS+AX. Such differences were below the 3%, although differences in the volume of the meshes were $\sim 20\%$ (with greater volumes achieved using IVUS+AX).

A group from the University Hospital La Paz, Madrid, Spain presented in 2014 [62] the methodology to estimate the FFR from steady-state CFD simulations with rigid walls from IVUS+AX images. The study consisted in 1 patient with pre- and post-stent data. They report that the CFD mesh are created in ~ 180 min and simulations is done in ~ 130 min using ANSYS Release 14.5 software [15]. The boundary conditions were constant 100 mmHg pressure at the inlet and image-derived flow at the outlet.

Recently, in the year 2015, two independent groups presented approaches to computationally estimate the FFR using compliant 1D models. Boileau and Nithiarasu [49], presented an open-loop model using an average description of the human coronary geometry. The work has no novel contribution in terms of modeling or numerical methods. No special stenosis elements were employed, and the parameters associated to the stenosis were manually tuned to match pressure measurements. A pressure curve was imposed at the inlet and windkessel elements accounting the intra-myocardial pressure at the outlets. In turn, Gamilov et al. [117] presented a methodology based on CCTA image data. No special stenosis elements were employed, although a Poiseuille pressure drop is considered at the junctions and an autoregulatory mechanism is incorporated in the model.

The work by Huo et al. [152] is also relevant as an alternative to enrich stenosis elements in reduced order modeling (1D). In that work, good correlation ($r = 0.99$ and $r = 0.75$) and agreement (bias of -0.59 ± 2.61 and -1.01 ± 3.6 mmHg) were obtained against in-vitro and in-vivo measurements of pressure drops. See Chapter 9, Section 9.2.2 for more detail on stenosis models for 1D models. In a joint effort between researchers from Singapore, USA and China [368], the so called FFR$_{SS}$ was presented and, for the first time, the analytic model of Huo et al. [152] now named FFR$_{AM}$, was tested with human data. The results showed, in a modest patient sample, that FFR$_{AM}$ and FFR$_{SS}$ obtain similar and good agreement against invasive measurements of FFR. The methodology behind FFR$_{SS}$, requires steady state 3D simulation patient-specific models constructed from CCTA. It uses a generalization of the Murray's law to obtain resistive values for BC, the methodology is detailed in [367].

Finally, recent publications from HeartFlow [292, 293, 294] and Siemens [154], indicate that both groups are exploring the use of machine learning techniques to perform fast calculation and prediction of FFR values based on large databases of studies. Moreover, it is noteworthy that some researchers are patenting the methodology employed for estimating the FFR using computer simulations, e.g. HeartFlow [327, 330, 110] and Siemens [309, 310, 311].

Chapter 9

Modeling methodology

> *"Essentially, all models are wrong, but some are useful."*
>
> **George E. P. Box**, *Empirical Model-Building and Response Surfaces.*

Patient-specific hemodynamic simulations rely on two fundamental issues: (i) computational domains and (ii) boundary conditions. Vascular geometries are obtained using imaging methods: coronary computed tomography angiography (CCTA) [73, 278, 328] or angiograms (AX), which can be utilized alone [59, 237], or in combination with either intra vascular ultrasound (IVUS) [70, 187, 320, 313] or optical coherence tomography (OCT) [103, 137]. In turn, definition of boundary condition requires knowledge of global and local hemodynamic information, i.e. systemic pressure, heart rate and blood flow distribution.

In this work, CCTA and IVUS image modalities are used to obtain patient-specific models of the coronary vasculature, and modeling methodologies to simulate patient-specific hemodynamics are proposed. This Chapter outlines the complete methodology: First, the pipeline used to construct arterial domains from medical images, is presented in Section 9.1. The numerical methods used to solve the fluid dynamic governing equations are detailed in Section 9.2. Finally, the methodology proposed to estimate hemodynamic parameters from patient-specific data is presented in Section 9.3.

9.1 Vascular models from patient-specific data

This section presents the most relevant aspects of the image processing techniques used for CCTA and IVUS image modalities. Further details can be found in Chapter 2 for CCTA and in [214] for IVUS.

9.1.1 CCTA image processing

CCTA images were acquired following standard procedures using ECG-triggered imaging at 75% of the cardiac cycle (late diastole) and ensuring patient heart rate lower than 65 bpm. The slice thickness was set to 0.3 mm with in-plane square pixel resolution of 0.415 ± 0.049 mm, depending on the equipment.

Segmentation of CCTA images is achieved using the methodology detailed in Chapter 2, Section 2.2.3. Briefly, the pipeline starts with the extraction of a region of interest on top of which curvature anisotropic filtering [352] is applied for noisy images. Segmentation is performed using a level-set method, initialized using a colliding front algorithm [21]. The segmented lumen is defined using a marching cubes method [202]. This procedure results

in a triangulated raw surface of the coronary tree. Such coarse mesh is further processed to obtain the computational mesh suitable for the CFD simulations.

Surface mesh processing steps include: (a) smoothing, using a Laplacian algorithm with no shrinking restriction (a relaxation factor of 0.63 and 30 iterations are used) [192]; (b) incorporation of tube extensions at inlet/outlets (at boundaries near bifurcations or in boundaries with non-convex enclosing curves) to reduce boundary effects in the simulation [124], such extensions have circular cross-section with the same area of the boundaries that are extending in the direction of the outward normal; (c) adaptive refinement, which is a function of vessel radius. Finally, a tetrahedral volume mesh is constructed for the CFD simulations.

All image processing stages, as well as meshing and centerline processing, are performed using vmtk [11], ImageLab [4] and HeMoLab [192, 4] softwares. Both, surface and volume meshes were generated using vmtk [11]. Appendix A presents an expanded explanation of the mesh processing pipelines used to obtained the CFD meshes.

9.1.2 IVUS image processing

IVUS images were acquired with the Atlantis^{TM} SR Pro Imaging Catheter 40 MHz synchronized with an ECG signal and connected to an iLab^{TM} Ultrasound Imaging System (Boston Scientific Corporation, Natick, MA, USA). The acquisition was performed with a frame rate of 30 FPS during an automated constant velocity pullback at 0.5 mm/s. The IVUS frames of 512×512 pixels in cartesian coordinates yield a resolution of 17.5μm $\times$ 17.5μm per pixel. In addition, gating of IVUS images is performed to retrieve a specific cardiac phase from the IVUS dataset [213]. Specifically, the diastolic phase was employed. The vessel geometry is defined in a system of intrinsic transducer coordinates which demands integration with angiographic images to register and place the transducer in 3D space.

Two orthogonal AX films were acquired synchronized with the ECG signal when the IVUS sensor was at the initial pullback position. The views were taken along the cranial-caudal plane to minimize dye overlapping between the different coronary vessels. The films span over 8 heartbeats to ensure the acquisition along the whole respiratory period. Finally, a specialist selected images from the films at the same respiratory phase (full exhalation) and at the end-diastolic cardiac phase, to perform a time-space consistent reconstruction of the vessel.

An in-house software developed in Matlab was used to retrieve the end-diastolic cardiac phase from the ECG-gated IVUS images. Luminal area (from all end-diastolic IVUS frames) was manually segmented by a specialist using cubic splines. The length of the segmented pull-backs was 153.81 ± 45.76 gated frames, which corresponds to 67.19 ± 17.89 mm of vessel length. Then, the transducer path was segmented from the orthogonal AX images using a biplane snakes method [233]. The segmented cross-sectional areas were positioned in the transversal plane of the recovered transducer path, using an interframe spacing dictated by the acquisition time of the frame and by the pullback velocity. Segmentation of side branches from IVUS images was also manually performed, creating a mesh in intrinsic transducer coordinates for each branch. These branches were spatially positioned in the transversal plane already determined for the parent vessel.

To account for catheter rotations, we rotate all contours around the axis described by the transducer path. The rotation angle of each frame is the one that minimizes the mismatch between the projected luminal area from IVUS and the contrast in the same part of the vessel which is observed in the AX. After this process, a specialist verifies and, if necessary, corrects the rotation angle by matching the branches and main artery with the projection resulting in the AX.

At this point, IVUS processed data consist in several disconnected tiangulations,

one for the parent vessel and one for each branch. Each mesh is improved following the thee steps described in Section 9.1.1. Then, all surfaces are merged using union surface operations described in [272]. Finally, a tetrahedral volume mesh is constructed for the CFD simulations using also vmtk.

9.1.2.1 Vessel rectification due to catheter deployment

It should be notice that CCTA and IVUS models of the same patient could differ in several aspects: (i) lumen radii can be underestimated in CCTA due to image resolution and artifacts produce by calcifications, while IVUS provides a more reliable radii information; (ii) side branches, while IVUS models retain more side branches, the rising angle and lumen of such branches can be distorted when compared to CCTA; (iii) the 3D path of the IVUS models may differ from CCTA models in terms of geometric descriptors, e.g. curvature and torsion. Although not presented in this Thesis, preliminary results of the quantification of geometric differences between CCTA and IVUS models were presented in [40], and is a current research topic. All these kinds of differences will produce discrepancies in the outcome of blood flow simulations, see Chapter 10, Section 10.5.

The (iii) source of differences between IVUS and CCTA models is the less intuitive, and we have found no documentation on the subject. Therefore, some empirical evidence is presented here. Due to the insertion of intravascular instrumentation, it is observed a rectification of the vessel under IVUS inspection. In Figure 9.1, the LCx and LAD arteries feature larger curvature when the transducer is not deployed yet (e.g. sites marked by the arrows). Particularly, a more pronounced rectification is seen in the LCx comparing to the LAD. Note that in this analysis we assume that the catheter matches the centerline of the artery.

(a)   (b)
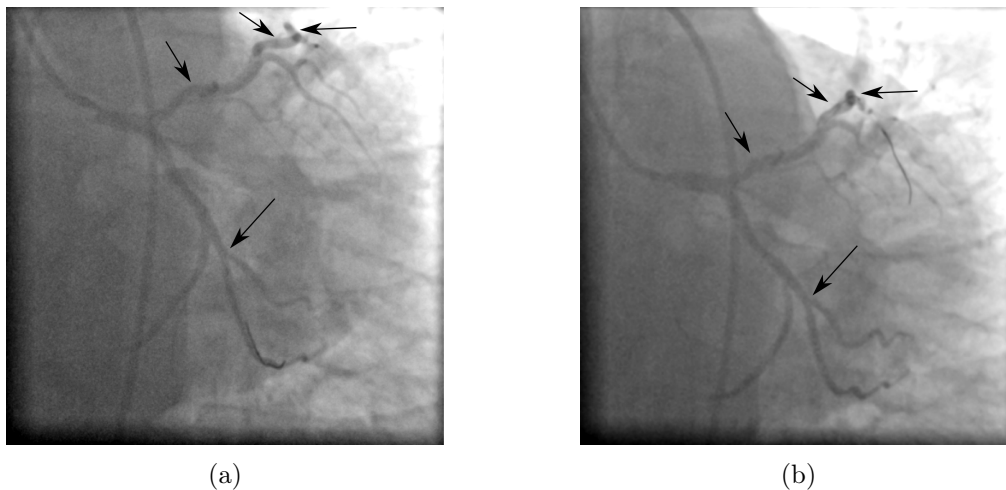
Figure 9.1: Rectification of the vessel due to catheterization: (a) LAD transducer deployment; (b) LCx transducer deployment.

9.1.3 1D mesh generation

Meshes for 1D simulations are built on top of centerline models of the coronary arterial trees, which are generated following procedures explained in Chapter 2. Such centerlines are discretized with a point spacing of 0.05 cm, and contain the radii of the maximum circumscribed sphere at each point, we call this variable r_s[cm]. Note that the cross-sectional area at each point can be retrieved by slicing the 3D mesh at each centerline point, the radius of the circle with equivalent area is denoted as r_a[cm]. Note that r_a is

not well defined in junction regions, see Figure 9.2, and in arterial regions with circular cross sections (such as inlet-outlet extensions), $r_s = r_a$.

As described in Section 9.2.2, junctions and stenosis regions can be treated with special mathematical models. Therefore, two masks are added to the centerline to mark regions inside junctions and delimiting stenotic lesions. The process to generate both masks is fully automatic to ensure reproducibility.
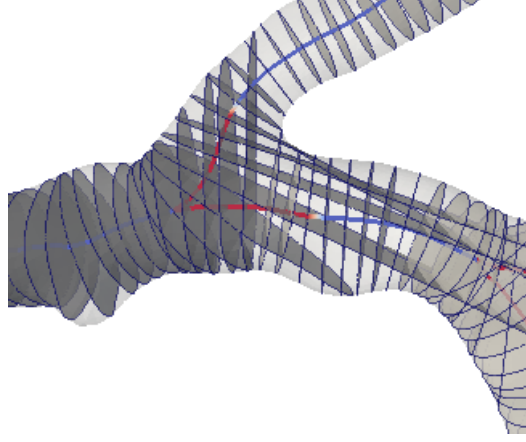
Figure 9.2: Example of cross-sectional lumen areas in arterial segments and junction regions (red indicates in the centerline) of a CCTA 3D model, patient ID 6.

The junction mask is zero at each centerline point outside a junction region, and is greater than zero for each point p_i satisfying

$$||\mathbf{x}(p_i) - \mathbf{x}(p_j)|| \leq r_s(p_i) + r_s(p_j), \tag{9.1.1}$$

where $\mathbf{x}(p)$ is the spatial coordinate of centerline point p, and p_j is any point of the centerline not belonging to the parent of the artery containing p_i. Additionally, a correction is performed to ensure that the ratio (in terms of r_a) between the last point of a junction mask and the first of the associated segment is less than $3/4$, which is done expanding the junction mask if necessary. This is performed to avoid numerical errors in the simulation, due to artificial discontinuities in the cross-sectional area. Bifurcation vectors are computed using the points with zero junction mask.

The stenosis mask assumes non-zero value in regions of focal lesions and zero values elsewhere. It is generated after the junction mask, and therefore points outside junctions are used, i.e. there are no intersection between masks. We implement a modified version of the algorithm proposed in [305] to detect stenosis regions. Briefly, for each arterial segment, containing n points, the true lumen radius at each point i is defined as $r_i = r_a(p_i)$. Then, the "healthy" radius ($\hat{r}$) of the arterial lumen is defined by applying a robust weighted Gaussian kernel regression to the true lumen r.

$$\hat{r}_i = \frac{\sum_{j=1}^{n} N(j|i,\sigma_i)w_j r_j}{\sum_{j=1}^{n} N(j|i,\sigma_i)w_j} \quad \forall i \in [1,n], \tag{9.1.2}$$

where w is a weighting function and N a Gaussian kernel, such that

$$w_i = M(r_i | r_i^{\text{MAX}}, \sigma_r), \tag{9.1.3}$$

$$r_i^{\text{MAX}} = \frac{\sum\limits_{j=1}^{n} N(j|i, \sigma_{\max}) r_j}{\sum\limits_{j=1}^{n} N(j|i, \sigma_{\max})}, \tag{9.1.4}$$

$$N(j|i, \sigma) = \frac{1}{\sigma\sqrt{2\pi}} e^{-\frac{(j-i)^2}{2\sigma^2}}, \tag{9.1.5}$$

$$M(r_i | r_i^{\text{MAX}}, \sigma_r) = \begin{cases} N(r_i | r_i^{\text{MAX}}, \sigma_r) & \text{if } j \leq i, \\ a & \text{otherwise} \end{cases} \tag{9.1.6}$$

Here, M is a modified kernel used to weight the radius function when its value is smaller than an approximation of the maximum radius at the location r_i^{MAX}. In the original algorithm [305], $M = N$, the modification was introduced because the original version attenuated radius values greater than the estimation of r_i^{MAX}. Also, when the algorithm was presented in [305], it was not clear the scale in which radius and vessel length were taken, which is crucial for the definition of the parameters. Therefore, in this work, previous the estimation of $\hat{r}$, the 1D functions representing the true lumen radius r and the arterial intrinsic length are re-sampled in 100 points and normalized in the range $[0, 1]$. Then, the healthy radius is computed $\hat{r}$, note that an abuse of notation is used when calling the Gaussian Kernel function in the arterial length space $N(i|j, \cdot)$, i and j represent the length from the arterial ostium to the points with index i and j. After computing $\hat{r}$, a postprocessing is performed to interpolate $\hat{r}$ in the original points of the centerline and in the correct range of radii, i.e. a de-normalization. The following parameters were chosen in a trial and error basis, $\sigma_i = 0.08, \sigma_r = 0.1, \sigma_{\text{MAX}} = 1, a = 10$.

The percentage area of stenosis is defined as

$$\Theta_i = 1 - \left(\frac{r_i}{\hat{r}_i}\right)^2, \tag{9.1.7}$$

and stenosis regions are detected using two threshold parameters, Θ_1, Θ_2. A stenosis is defined between two point p_i, p_j satisfying:

- $\Theta_i >= \Theta_1$ and $\Theta_j >= \Theta_1$,

- $\Theta_{i-1} < \Theta_1$ and $\Theta_{j+1} < \Theta_1$,

- $\forall k \in [i, j], \Theta_k >= \Theta_1$.

- $\exists k \in [i, j], \Theta_k >= \Theta_2$.

The following parameters were chosen in a trial and error basis, $\Theta_1 = 0.1$ and $\Theta_2 = 0.4$.

The final 1D mesh is constructed using the centerline, by truncating all points with junction mask different from zero. If stenosis elements are employed, see Section 9.2.2, points with stenosis masks are truncated and the arterial segment is divided in two computational domains (pre- and post-lesion), connected by a lumped parameter node modeling the stenosis. Each arterial segment represents a one-dimensional domain, discretized using a regular mesh, i.e. constant Δx. A nodal basis defined by second order Lagrange polynomia interpolating Gauss-Lobatto quadrature nodes is used for the spatial discretization within each computational cell. The arterial radius is interpolated at each node of the basis function. The mismatch between computational nodes and centerline nodes requires a post-processing of the simulation result, in which the solution is quadratically interpolated

into the centerline nodes. For centerline points that are masked as stenosis points, and therefore not considered as one-dimensional domains, the pressure is linearly interpolated between upstream and downstream results.

9.2 Fluid dynamics

This section presents the mathematical and numerical models used for 3D and 1D simulations.

9.2.1 3D Model

Blood flow was modeled using the Navier-Stokes equations for rigid domains, i.e. arterial compliance was neglected. Let Ω be the arterial domain, with boundary $\Gamma = \Gamma_w \cup \Gamma_p \cup \Gamma_1 \cdots \cup \Gamma_{N_o}$, where Γ_w is the boundary corresponding to the arterial wall, Γ_p is the inlet boundary at the proximal location, and Γ_i, $i = \{1, \ldots, N_o\}$ are the N_o outlet boundaries. All boundaries have unit outward normal vector denoted by $\mathbf{n}$. Let $\mathbf{v}$ and p be the velocity and pressure of the fluid, which are in proper function spaces called $\mathcal{V}$ and $\mathcal{P}$, respectively. Then, given the initial condition $\mathbf{v}(\mathbf{x}, t = 0)$ and given the resistances $\mathcal{R}_i(t)$, $i = \{1, \ldots, N_o\}$, the time-dependent problem consists in finding $(\mathbf{v}, p) \in \mathcal{V} \times \mathcal{P}$ for each $t \in [0, T]$, such that

$$\int_\Omega \left[\rho \frac{\partial \mathbf{v}}{\partial t} \cdot \hat{\mathbf{v}} + \rho (\nabla \mathbf{v}) \mathbf{v} \cdot \hat{\mathbf{v}} + 2\mu (\nabla \mathbf{v})^s \cdot (\nabla \hat{\mathbf{v}})^s - \hat{p} \operatorname{div} \mathbf{v} - p \operatorname{div} \hat{\mathbf{v}} \right] d\Omega =$$

$$- \int_{\Gamma_p} P_p \mathbf{n} \cdot \hat{\mathbf{v}} \, d\Gamma - \sum_{i=1}^{N_o} \int_{\Gamma_i} \left[\mathcal{R}_i(t) \left(\int_{\Gamma_i} \mathbf{v} \cdot \mathbf{n} \, d\Gamma \right) + P_{\text{ref}} \right] \mathbf{n} \cdot \hat{\mathbf{v}} \, d\Gamma$$

$$\forall (\hat{\mathbf{v}}, \hat{p}) \in \mathcal{V} \times \mathcal{P}, \quad (9.2.1)$$

where ρ and μ are the fluid density and viscosity, respectively, P_p is the normal traction at the inlet boundary (i.e. aortic pressure), P_{ref} is a reference value for the normal traction at terminal outlets (i.e. venous pressure), and $(\mathbf{E})^s$ denotes the symmetric part of the second order tensor $\mathbf{E}$. The approach presenting here assumes that P_p and P_{ref} are constant over time, but the method to impose boundary conditions is general enough to be used with time dependent data. Since the flow model assumes rigid walls, P_p is kept constant in time, because the results are insensitive to this consideration. In the present study the function spaces are defined as

$$\mathcal{V} = \{[H^1(\Omega)]^3; \ \mathbf{v}|_{\Gamma_w} = 0\}, \qquad (9.2.2)$$

$$\mathcal{P} = L^2(\Omega). \qquad (9.2.3)$$

Note that in variational formulation (9.2.1) a resistance boundary condition is being applied at each outlet Γ_i, $i = \{1, \ldots, N_o\}$. In fact, we can introduce the variable P_i defined as

$$P_i(t) = \mathcal{R}_i(t) \left(\int_{\Gamma_i} \mathbf{v} \cdot \mathbf{n} \, d\Gamma \right) + P_{\text{ref}}, \qquad (9.2.4)$$

which stands for the total normal traction at Γ_i (i.e. the pressure at each outlet). Then, since the flow rate is $Q_i(t) = \int_{\Gamma_i} \mathbf{v} \cdot \mathbf{n} \, d\Gamma$, we have

$$Q_i(t) = \frac{P_i(t) - P_{\text{ref}}}{\mathcal{R}_i(t)}, \qquad (9.2.5)$$

Resistance $\mathcal{R}_i(t)$ is computed as follows. Consider the resistances given by the Murray's law, denoted by $\bar{R}_i^*$, estimated from the mean inflow ($\bar{Q}_T$, which is a datum) as

$$\bar{Q}_T = \sum_{i=1}^{N_o} \bar{Q}_i^*, \tag{9.2.6}$$

$$\bar{Q}_i^* = \beta r_i^\gamma, \tag{9.2.7}$$

$$\bar{R}_i^* = \frac{(P_p - P_{\text{ref}})}{\bar{Q}_i^*} = \frac{(P_p - P_{\text{ref}})}{\bar{Q}_T} \frac{1}{r_i^\gamma} \sum_{j=1}^{N_o} r_j^\gamma, \tag{9.2.8}$$

where $\beta = \bar{Q}_T / (\sum_{i=1}^{N_o} r_i^\gamma)$ is the proportionality constant, γ is the Murray's exponent and r_i is the radius of outlet Γ_i.

Consider now a flow signature $Q(t)$ with mean value $\bar{Q} = 1$ ml/s, and with a prescribed physiological value for the pulsatility index (PI) which is defined as

$$\text{PI} = \frac{Q_{\text{max}} - Q_{\text{min}}}{\bar{Q}}, \tag{9.2.9}$$

where Q_{max} and Q_{min} are the maximum and minimum values of the curve over a cardiac cycle. Figure 9.3 shows the flow signature used in the present work for the left and right coronary trees, with PI values of 1.0 and 0.75 respectively [140].
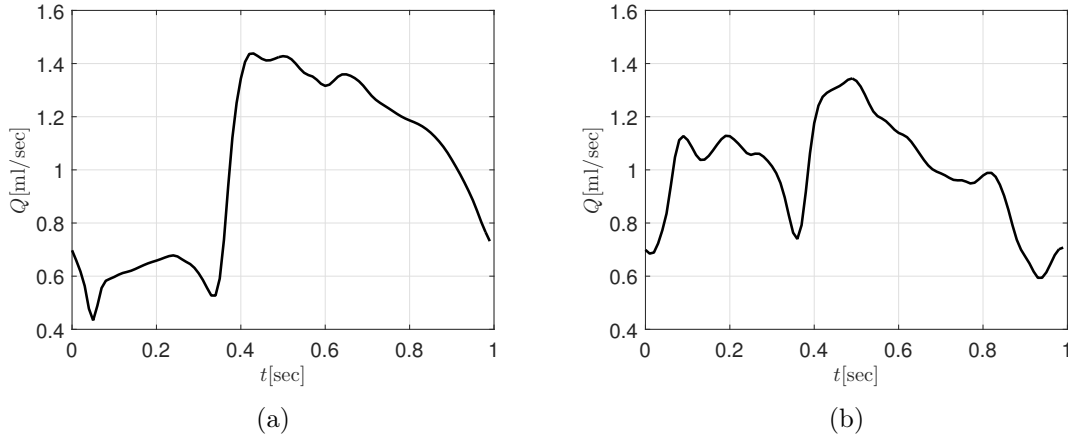
Figure 9.3: Coronary flow signature for the left (a) and right (b) coronary trees. The mean flow is $\bar{Q} = 1$ ml/s for both signatures, and the PI is 1.0 and 0.75 for (a) and (b), respectively. Estimated from a velocity profile in [140].

Then, a time dependent Murray's resistance is computed for each outlet i

$$R_i^*(t) = \frac{\bar{Q}}{Q(t)} \bar{R}_i^*. \tag{9.2.10}$$

Then, the terminal resistance $\mathcal{R}_i(t)$ is obtained as follows

$$\mathcal{R}_i(t) = \alpha(t) R_i^*(t), \tag{9.2.11}$$

where $\alpha(t)$ is such that the total flow at the inlet $\sum_{i=1}^{N_o} Q_i(t)$ matches the prescribed total coronary flow

$$Q_T(t) = \frac{\bar{Q}_T}{\bar{Q}} Q(t). \tag{9.2.12}$$

The computation of $\alpha(t)$ in the approximate problem is performed at each time-instant (t^n). The value of $\alpha(t^n) = \alpha^n$, is found along the Picard iterations performed to converge the nonlinearities already present in the Navier-Stokes equations, that is

$$Q_T(t^n)\alpha^{n,k} - \sum_{i=1}^{N_o} \frac{P_i^{n,k}}{\alpha^{n,k-1}R_i^*(t^n)} = -\sum_{i=1}^{N_o} \frac{P_{\text{ref}}}{\alpha^{n,k-1}R_i^*(t^n)}, \qquad (9.2.13)$$

where $Q_T(t^n)$ and $R_i^*(t^n)$ are the data for flow and resistance at time instant t^n, $\alpha^{n,k}$ is the value of $\alpha(t^n)$ at the current iteration k and $\alpha^{n,k-1}$ is the value of $\alpha(t^n)$ at the previous iteration $k-1$.

This way, terminal resistance (9.2.11) is computed from the value of α at the previous iteration, that is

$$\mathcal{R}_i^{n,k-1} = \alpha^{n,k-1}R_i^*(t^n), \qquad (9.2.14)$$

where $\mathcal{R}_i^{n,k-1}$ is the value of the terminal resistance that used in problem (9.2.1), linearized by Picard iterations, at the current iteration k at the current time time t^n.

Therefore, after discretizing in time by backward Euler, and linearizing using Picard iterations, we arrive at the following discrete-in-time linearized variational problem

$$\int_\Omega \left[\rho\frac{\mathbf{v}^{n,k}}{\Delta t} \cdot \hat{\mathbf{v}} + \rho(\nabla\mathbf{v}^{n,k})\mathbf{v}^{k-1} \cdot \hat{\mathbf{v}} + 2\mu(\nabla\mathbf{v}^{n,k})^s \cdot (\nabla\hat{\mathbf{v}})^s - \hat{p}\operatorname{div}\mathbf{v}^{n,k} - p^{n,k}\operatorname{div}\hat{\mathbf{v}} \right] d\Omega$$

$$+ \sum_{i=1}^{N_o} \int_{\Gamma_i} \mathcal{R}_i^{n,k-1}\left(\int_{\Gamma_i} \mathbf{v}^{n,k}\cdot\mathbf{n}d\Gamma \right)\mathbf{n}\cdot\hat{\mathbf{v}}d\Gamma = \int_\Omega \rho\frac{\mathbf{v}^{n-1}}{\Delta t}d\Omega - \int_{\Gamma_p} P_p\mathbf{n}\cdot\hat{\mathbf{v}}d\Gamma - \sum_{i=1}^{N_o}\int_{\Gamma_i} P_{\text{ref}}\mathbf{n}\cdot\hat{\mathbf{v}}d\Gamma$$

$$\forall(\hat{\mathbf{v}},\hat{p}) \in \mathcal{V} \times \mathcal{P}, \quad (9.2.15)$$

where $\mathbf{v}^{n,k}$ and $p^{n,k}$ are the fluid velocity and pressure at time t^n and at the current iteration k, $\mathbf{v}^{n-1}$ is the velocity at the previous time step t^{n-1} and $\mathcal{R}_i^{n,k-1}$ is given by (9.2.14). The semi-discrete variational problem (9.2.15) is then discretized in space using finite element with equal order interpolation and bubble enrichment for the velocity field (i.e. the mini element).

Steady-state simulations are run by replacing $R_i^*(t)$ by $\bar{R}_i^*$ in (9.2.11).

Statistical results regarding the values adopted by the α parameter are presented in Chapter 10, Section 10.5.

In this work, the implementation of the novel BC was done in the context of an in-house general purpose parallel solver, based on the finite element method, which is under continuous development by the HeMoLab research group [4].

9.2.2   1D Model

The computational domain Ω for the 3D model, is condensed in a so called 1D computational domain denoted as $\bar{\Omega}$, as explained in Section 9.1.3, which consists of arterial segments, or vessels, connected through a set of junctions. The spatial coordinate in such vessels is denoted by x. The inlet boundary Γ_p is now simply denoted by the inlet point I, and the outlet boundaries Γ_i are denoted by O_i, $k = 1,\ldots,N_o$.

Given a generic domain $\bar{\Omega}$ consisting of: N_v arterial segments of size L_k, $k = 1,\ldots,N_v$; N_J junctions, in this work we use only bifurcations, junction points are denoted as B_j, $j = 1,\ldots,N_J$; an inlet point I and N_o outlet points O_i, $i = 1,\ldots,N_o$. The governing 1D

equations are the following

$$
\begin{cases}
\dfrac{\partial A}{\partial t} + \dfrac{\partial Q}{\partial x} = 0 & \text{in each vessel, } x \in [0, L_k], \ k = 1, \ldots, N_v, \\[3mm]
\dfrac{\partial Q}{\partial t} + \dfrac{\partial}{\partial x}\left(\dfrac{Q^2}{A}\right) + \dfrac{A}{\rho}\dfrac{\partial P}{\partial x} + \dfrac{\varpi \pi \mu U}{\rho} = 0 & \text{in each vessel, } x \in [0, L_k], \ k = 1, \ldots, N_v, \\[3mm]
P = P_0 + \beta\left(\sqrt{\dfrac{A}{A_0}} - 1\right) & \text{in each vessel, } x \in [0, L_k], \ k = 1, \ldots, N_v, \\[3mm]
P = P_p & \text{at inlet } I, \\[3mm]
Q = Q_{\text{out}}^i & \text{at each outlet } O_i, k = 1, \ldots, N_o, \\[3mm]
\text{Mass conservation and continuity of} & \\
P_{\text{tot}} = P + \tfrac{1}{2}\rho U^2 & \text{at each bifurcation } B_j, \ j = 1 \ldots N_J,
\end{cases}
\tag{9.2.16}
$$

where Q is the flow rate, A is the lumen area, P is the average pressure in the lumen cross section, $U = Q/A$ is the mean velocity, ϖ is a parameter that characterizes the assumed velocity profile in the 1D model, β is an effective stiffness which characterizes the compliance of the arterial wall through a linear elastic relation, being P_0 a reference external pressure for which the lumen area is A_0. Since the present study is only concerned with pressure loses predicted by 1D models β is set at a high value to simulate 1D flow in a quasi-rigid domain (therefore $A \approx A_0$). Furthermore, the velocity profile is assumed to be parabolic, therefore $\varpi = 22$ [49, 244].

In order to properly approximate mechanical and geometrical variations along vessels, system (9.2.16) is reformulated to obtain a non-conservative hyperbolic system of partial differential equations [234, 245] and discretized using a third-order one-step Discontinuous - Galerkin scheme [97] with a local time-stepping strategy and path-conservative numerical fluctuations [244, 246].

For this work, the above mentioned numerical schemes are implemented in a different solver with respect to the one used for 3D simulations. The 1D solver is also an in-house parallel software, based on the finite volume and Galerkin methods, which is under continuous development by the HeMoLab research group [4].

9.2.2.1 Stenosis modeling

The pressure drop produced by sudden area variations, i.e. stenosis, can not be accurately captured by the 1D model presented in Eq. (9.2.16). To our knowledge, the so called Young model for stenoses, initially proposed in [362, 363] for steady and transient flow conditions, is the most widespread model to estimate pressure drops across this kind of geometric singularities. To be precise, stenoses are modeled using the lumped parameter approach proposed in [363]. That is, the pressure drop across a constriction is

$$
\Delta P = K_v \frac{\mu}{D} U + K_t \frac{\rho}{2}\left[\frac{A}{A_s} - 1\right]^2 |U|U + K_u \rho L_s \frac{dU}{dt},
\tag{9.2.17}
$$

where U and A (D the diameter) are the velocity and lumen area in the unobstructed part of the vessel, L_s is the stenosis length, A_s is the minimum stenosis area, and K_v, K_t and K_u are model parameters characterizing viscous, turbulent and inertial effects,

respectively. Geometric parameters (L_s, A_s) are obtained from the centerline model in the region delimited by the stenosis mask, see Section 9.1.3. In turn, K_v is the constant that accounts for viscous pressure losses and is strongly dependent on geometry; the K_t constant accounts for turbulence effects and weakly depends on geometry; finally, the coefficient K_u accounts for pressure drag due to accelerations plus any correction to the viscous-turbulence terms that are proportional to $\frac{dU}{dt}$.

The Young model was initially validated with in-vitro experiments in [362, 363], where the constant parameters were adjusted to match experimental data. In a later study, the model was validated in-vivo, inducing stenosis in femoral arteries of dogs [361]. The reported results supported the applicability of the model to predict pressure drops on arterial stenoses. Up to that point, model parameters known to depend on geometry were determined by curve fitting. In [300], analytical forms for the model parameters based on geometrical characteristics, and in-vitro steady flow experiments have been presented. In that work, the applicability of the model for consecutive stenoses was also studied. The results suggested that in order to increase pressure drop prediction accuracy, the parameters should take the form

$$
\begin{cases}
K_u & = 1.0, \\
K_t & = 1.52, \\
K_v & = 32\dfrac{L_a}{D}\left[\left(\dfrac{A}{A_s}\right)_a\right]^2, \\
L_a & = 0.83L_s + 1.64D_s, \\
\left(\dfrac{A}{A_s}\right)_a & = 0.75\left(\dfrac{A}{A_s}\right) + 0.25.
\end{cases}
\tag{9.2.18}
$$

To our knowledge, the incremental work of Gould [128, 127, 129] in the 80's, was the first to make use of the Young model to predict pressure drops in human coronary arteries. More recently, the Young model was used in several computational models [350, 318].

9.2.2.2 Junctions modeling

Pressure losses at junctions are modeled using the lumped parameter approach proposed in [242]. In such model, at any junction point B_j, the continuity of total mechanical energy between the inlet and any outlet is expressed as

$$
\begin{cases}
P_1 + \frac{\rho}{2}U_1^2 & = P_k + \frac{\rho}{2}U_k^2 + P_{\text{loss},k} \quad k = 2,\ldots,N_j, \\
P_{\text{loss}} & = K_{1,k}\frac{\rho}{2}U_1^2,
\end{cases}
\tag{9.2.19}
$$

where N_j is the number of converging segments at the junction, in this work $N_j = 3$, the pressure loss $P_{\text{loss},k}$ models energy dissipation through coefficient $K_{1,k}$ which depends on geometrical parameters of the branches, i.e. angulation between branches, see [242] for details. Although the original approach proposed in [242] is for planar bifurcations, patient-specific arterial networks rarely present such bifurcation pattern. Nonetheless, in this work, bifurcation angles are computed between branch pairs in the plane formed by the corresponding bifurcation vectors.

9.2.2.3 Parameter estimation using Kalman filter

The process by which the state of a numerical model is updated through the incorporation of observations of the actual system being modeled is called data assimilation. The Kalman filter [173, 168, 232] is a widely used tool for data assimilation applications, by estimating values of unknown parameters to improve results of computational simulations

using available measurements on a given system. Such filter is based on a sequential approach, in which the error between the available measurement and the current simulation result is used to correct the model parameters at each time step of the simulation.

The 1D solver used in this work provides an out of the box parameter estimation method based on Kalman filter [58]. Specifically, the reduced-order unscented Kalman filter (ROUKF) [231] is used, which employs an efficient sampling of the parameter space to improve performance. Regarding applications of ROUFK for blood flow simulations, estimation of the mechanical properties of the aorta was presented in [37], and tunning of boundary conditions parameters (0D models) for 3D simulations using patient-specific data were presented in [254].

In this work, we use the ROUKF only in the context of the Young stenosis model, to estimate the K_v parameter, in order to match the pressure drop, denoted by ΔP^{3D}, observed in the 3D simulation, at each stenosis location.

Details on the formulation and implementation of the ROUKF in the context of the 1D blood flow model used here, can be found in [58]. Briefly, from a general point of view, writing the 1D model in the form of a dynamical system

$$
\begin{cases}
X_{n+1} & = \mathcal{F}(X_n, \theta), \\
X_0 & = Y + \xi^X,
\end{cases}
\tag{9.2.20}
$$

where X_n contains, for the time step t_n, the state variables (i.e. flow, pressure and cross-sectional area) at each computational node along the arterial network and the state variables of the parameters to be estimated (i.e. K_v) at each stenosis node; $\mathcal{F}$ is an operator involving the numerical solution of equations (9.2.16) and (9.2.17); θ contains the parameters to be estimated, i.e. K_v; finally, Y stands for the initial condition, and ξ^X is a random variable that takes into account the uncertainty of the initial state.

Given a measurement vector $Z_n \in \mathbb{R}^M$, i.e. the ΔP^{3D} for M estenoses, at each time step t_n, the method assumes that the model can reproduce such state, this is

$$
Z_n = \mathcal{H}(X_n) + \xi^Z,
\tag{9.2.21}
$$

where $\mathcal{H}$ is an observation operator, which retrieves compatible measurements from the model. i.e. the ΔP^{1D} for the M stenoses; and ξ is an intrinsic noise[1] of the measurement Z_n, assumed independent at all times and Gaussian with zero-mean.

Assuming that parameters do not change over time, the idea behind the Kalman filter is to apply a prediction-correction scheme to an augmented state (X_n, θ_n). Namely, a prediction is obtained via a forward propagation

$$
\begin{cases}
X^-_{n+1} & = \mathcal{F}(X^+_n, \theta_n), \\
\theta^-_{n+1} & = \theta_n.
\end{cases}
\tag{9.2.22}
$$

In turn, the correction takes into account the differences between the observations and measurements

$$
\begin{cases}
X^+_{n+1} & = X^-_{n+1} + K_X \left(Z_n - \mathcal{H}(X^-_{n+1}) \right), \\
\theta^+_{n+1} & = \theta^-_{n+1} + K_\theta \left(Z_n - \mathcal{H}(X^-_{n+1}) \right).
\end{cases}
\tag{9.2.23}
$$

The Kalman matrices K_X and K_θ are defined in order to minimize the distance between observations and measurements in a proper norm, which depends on the confidences in both the measures and the model.

The interested reader will find more details on the implementation and performance

---

[1]In a clinical setting, the main contribution to the observation noise is given by error statistics of measurement devices.

of the ROUKF in [58].

9.3   Patient-specific hemodynamic parameters

For all the 3D simulations performed in this work, whose results are summarized in Chapter 10, the following set of parameters was used: $\rho = 1.05$ g/cm^3, $\mu = 0.04$ cP, $P_{\text{ref}} = 10$ mmHg. The Murray's exponent was set to $\gamma = 2.66$ motivated by allometric laws relating flow to volume of tissue [45, 351].

Patient data included resting heart rate (HR) and mean arterial pressure (MAP, used as the aortic pressure P_p in Section 9.2). The coronary blood flow (CBF) is estimated from patient data as detailed in Chapter 7, Section 7.3.4.1. The inflow $\bar{Q}_T$ used in Section 9.2 can be estimated from the CBF following different approaches, details are given later in this section.

Maximum myocardial hyperemia was modeled changing these parameters according to bibliographic data presented in Table 7.1. Specifically, for intra-coronary or intra-venous administration of adenosine, $HR^H = HR - 1.4$ bpm and $MAP^H = MAP - 3.8$ mmHg or $HR^H = HR + 18.5$ bpm and $MAP^H = MAP - 4.4$ mmHg respectively, here superscript H indicates hyperemic condition and absence of superscript corresponds to rest condition. Regarding the coronary flow reserve (CFR), see Chapter 7, Section 7.3.5, we assume two simple but slightly different strategies, see Sections 9.3.1 and 9.3.2.

Once the value of the CBF is known, a flow distribution among all outlets of the computational model is defined. This distribution is manifested in the mathematical models through the outlet boundary conditions. Since the radii of the terminal arteries is known, the most common approach to define flow distribution is the Murray's law [239]. Other criteria can be used by means of perfusion data, as explored in [297]. In this work, four approaches to define flow distribution were explored in closed relation to the image modality. In our approaches, flow distribution is determined for rest conditions, therefore in order to simulate hyperemic conditions, the CFR needs to be defined. These approaches are detailed next.

9.3.1   Flow distribution in CCTA

CCTA images provide geometric information, i.e. lumen radii, of the left and right coronary trees. We tested two methods to estimate flow distribution from such information:

Distal Murray Distribution (DMD): The flow at the inlet boundaries of the major vessels, as stated by the Murray's law, is determined by the terminal vessel radii located downstream to these vessels, e.g. the flow into the LM is defined by the vessel radii of all related terminals (diagonals, septals, obtuse marginals, etc). Revisiting Section 9.2.1, the strategy to define terminal resistances R_i^*, is employed for CCTA models in a straight forward manner using all outlets and the total CBF to estimate Murray's resistances.

Proximal Murray Distribution (PMD): This method was designed to account for tapering in long segments lacking side branches. Such situation may be a problem in models constructed from CCTA images with low-quality. Murray's law assumes that arterial segments (defined as the portion of artery between two branches) in a network have no tapering, and therefore wall shear forces are homogeneously distributed, satisfying a principal of minimum work. Moreover, Murray's law does not account for the viscous dissipation of major vessels. In such cases this hypothesis is not valid. In such an ideal and complete network, with a known inflow, estimating flow distribution from all outlets using Murray's law would be equivalent to applying Murray's law at each bifurcation traveling downstream from the root. In practice, proximal radii of arterial segments are more reliable than terminal radii, because of technical limitations such as image resolution

and noise. Moreover, the absence of small side branches and associated sub-trees in long arterial segments produce artificial tapering, directly impacting the flow distribution, if calculated using all outlet radii only. In turn, if Murray's law is recurrently used at each branching point, a more realistic flow at the inlet of large-proximal branches for truncated networks should be expected. Since the PMD strategy requires to travels through a coronary network from the root (the Ao for CCTA models), it can be easily adapted to account for physiological flow distributions in specific branches. We take advantage of such property, and introduce some physiological restrictions regarding the Ao-RCA-LM and LM-LAD-LCx branching points. Basically, the PMD algorithm detects such branching points in the labeled network and checks if the local Murray's distribution satisfies average flow distributions reported in the literature [286]. If not, the flow distribution is modified as little as possible to match mean±STD physiological values. More details can be found in Appendix F.

Generalizations and adaptations of the Murray's law to take into account stenoses in branches and downstream characteristics of the vasculature had been explored in [370, 135].

Regardless the flow distribution strategy (DMD or PMD), in this work all simulations performed with CCTA models adopt the same definition for the hyperemic flow ($\bar{Q}_T^H$). It is assumed that all branches have the same CFR, and therefore $\bar{Q}_T^H = \text{CFR} \times \bar{Q}_T$.

9.3.2 Flow distribution in IVUS

Two approaches were adopted for defining the flow distribution in IVUS models, which comprise a section of the artery of interest, e.g. LAD, LCx or RI starting at the LM ostium, and include more side branches than CCTA models. Both strategies rely on Murray's law (DMD) to determine the flow distribution inside the artery of interest. The difference between both strategies is how the inflow to such artery is determined.

CCTA - Simulation Result Distribution (CSRD): This strategy was developed to perform adequate comparisons between CCTA and IVUS derived computational models, see Chapter 10, Section 10.5, and is aware of the flow distribution obtained from a CCTA simulation. Figure 9.4 illustrates a typical IVUS model starting at the LM artery, the most proximal side branch is the LCX and the rest of the arterial domain corresponds to the LAD artery and its side branches, the associated CCTA model is also shown. The CSRD strategy utilizes the result of the CFD simulation of the associated CCTA model to determine the inflows to the LCx and LAD branches. Then Murray's law is used to determine the resistances of all the outlets associated to each one of the major vessels, in Figure 9.4 this is one resistance for the LCx and nine resistances for the LAD outlets. In practice, each of these inlets is associated to an α variable coupling the corresponding outlet resistances, such that the simulation total inflow is the same to that in the CCTA model.

Therefore, the anatomical data extracted from the IVUS model is used to determine only the *relative* flow distribution in these models according to the same Murray's law. In turn, the *total* flow into the artery of interest in the IVUS model (LAD, LCx or RI) is forced to be equal to that obtained from the corresponding CCTA simulations, making both CCTA and IVUS simulations comparable. Such flow given by the CCTA simulation is not exactly the one dictated by Murray's law, because of the resistance of major vessels. This is the reason why IVUS simulations are performed just once the corresponding CCTA simulation is finalized, so exactly the same inflow can be prescribed, at the inlet of the major arteries of interest.

Note that, since the CSRD strategy is lined to a CCTA simulation, the CFR is intrinsically defined, since that simulation was performed for a hyperemic state.

Physiological Distribution (PD): In turn, the second strategy can be used when

the geometry of the coronary arterial tree is partially known[2], and includes statistical information about flow distribution among the major arteries from the literature. The work of Sakamoto et al. [286] was taken to set the criterion called PDC, and based on it, a variation was performed based on clinical observations pointed out by a team of specialized cardiologists, such method is identified as PDP. Table 9.1 presents the percentage of the CBF for each one of the major arteries depending on the circulation dominance for both distribution criteria, PDC and PDP.

Criterion	Circ. Dominance	RCA	LAD	LCx
PDC	Right	40	35	25
	Left	30	36	34
	Co	20	35	45
PDP	Right	35	45	20
	Left	20	45	35
	Co	30	45	25

Table 9.1: Percentage of the CBF per artery depending on circulation dominance and distribution criterion (PDC or PDP). If a RI artery is present, only the LCx percentage is modified, such that it gives 15% of the CBF to the RI for te PDC criterion and 10% in the PDP criterion.

Since the PD strategy estimates flow distributions for a resting scenario, the CFR must be defined in order to perform simulation of an hyperemic state. The same strategy used for CCTA simulations can be used, i.e. assume that all branches have the same CFR and therefore $\bar{Q}_T^H = \text{CFR} \times \bar{Q}_T$. Another alternative is to assume that the CFR is a function of patient-specific data and the artery of interest. Particularly, a team of specialized physicians defined a criterion to determine the CFR based on clinical observations [172, 196, 178, 26, 25, 190, 207]. Briefly, estimation of CFR is performed taking into account patient data such as: age, clinical condition and the coronary territory analyzed (LAD, LCx or RCA). The CFR would be higher on young, healthy patients and in LAD territories. Although, it would be smaller on elderly, with comorbidities and in non-LAD territories. So the following strategy has been designed

$$
\begin{cases}
\text{CFR} & = 2.3 + X + Y + Z + W \\
X & = \begin{cases} 0.6 & \text{for the LAD,} \\ 0.2 & \text{for the LCx,} \\ 0.4 & \text{for the RCA,} \end{cases} \\
Y & = \begin{cases} 0.3 & \text{if age } < 65[y], \\ 0.1 & \text{otherwise,} \end{cases} \\
Z & = -0.1 \times \text{DM} - 0.1 \times \text{HAS,} \\
W & = -0.1 \times \text{LVEF} + 0.2 \times \text{LVMI} + 0.1 \times \text{CD.}
\end{cases}
\tag{9.3.1}
$$

A base value of CFR= 2.3 is modified by a series of terms accounting for: (X) myocardial territory, the LAD usually irrigates a larger portion of the myocardial muscle[3] than the LCx and the RCA; (Y) age of the patient, elders have reduced CFR; (Z) clinical condition, boolean variables (with value $0, 1$) for patient testing positive for diabetes (DM) and hypertension (HAS) decrease the CFR; (W) heart related status, boolean variables

---

[2]Which is the case of patients subjected to IVUS but not to CCTA studies.
[3]This term does not include information of the circulation dominance of the patient, this could be an improvement for future versions of the CFR estimation function.

for cardiopathies may increase the CFR, i.e. left ventricular hypertrophy (LVMI> 70%) and if the artery under examination provides collateral circulation to any other territory (CD), or decrease it, i.e. presence of left ventricular dysfunction (LVEF< 40%).

However, it may be very complicated and also empirical to consider CFR values based on clinical conditions, age or coronary territory. Despite this, we believe it is interesting to individualize according to the clinical characteristics.

(a)   (b)
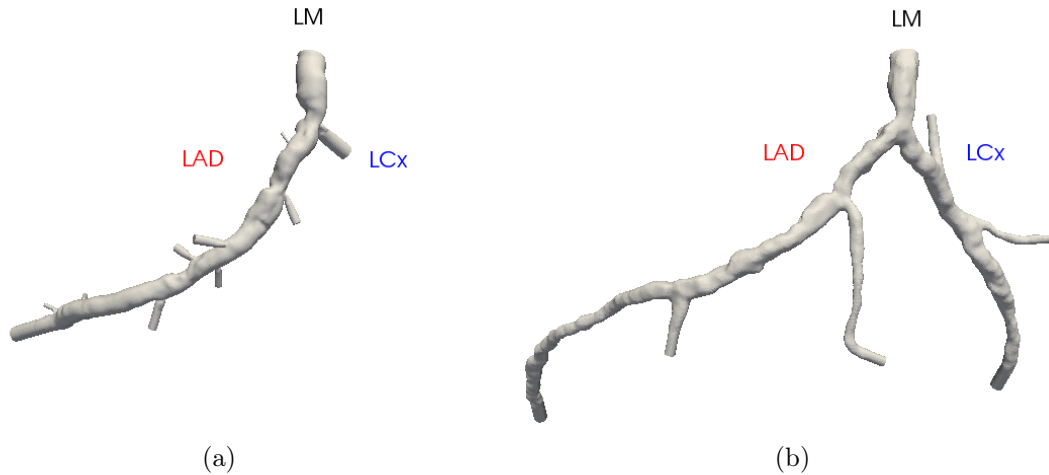
Figure 9.4: Illustration of IVUS (a) and CCTA models (b) for patient ID 25. The LM, LAD and LCx branches are indicated in each model.

9.4 Simulations post-processing

In the case of 3D models, after the simulation is performed, solutions for the velocity ($\mathbf{v}$) and pressure (p) fields are available for each time step (in the case of transient simulations) or at a single time (steady-state simulations). Estimation of FFR field needs a proximal pressure P_a, which is calculated as the spatial average at the inlet region of approximately 2 mm length. Such region is manually defined using points of the centerline, which are used to clip the tetrahedral mesh. Then, the time dependent FFR is calculated as

$$\text{FFR}(t, \mathbf{x}) = \frac{p(t, \mathbf{x}) - p_v(t)}{P_a(t) - p_v(t)}, \tag{9.4.1}$$

where p_v is the venous pressure, which is equal to zero in this work, as it is assumed in general clinical practice. The field of time-averaged $\text{FFR}(\mathbf{x})$, is estimated by computing the average of $\text{FFR}(t, \mathbf{x})$ over the last cardiac cycle. Then, the final FFR value is estimated as the average of the $\text{FFR}(\mathbf{x})$ at a distal region of approximately 2 mm length, manually defined (analogously to the proximal region used in the estimation of P_a). Such region is identified as Ω_{FFR}, and its definition is guided by AX images showing the location of the invasive pressure wire during the clinical FFR procedure. We define such a value as Computational Estimation of the Fractional Flow Reserve (FFR_{CE}).

Two other hemodynamic quantities of interest need post-processing, i.e. wall shear stress (WSS) and the oscillatory shear index (OSI). Both are defined over the boundary that corresponds to the lateral lumen boundary, and are computed from the so called wall shear rate vector ($\tau(t, \mathbf{x})$), defined as the derivative of the tangential flow velocity ($\mathbf{v}_t$) in

the normal direction (n) at each surface point $\mathbf{x}$,

$$
\begin{cases}
\tau(t, \mathbf{x}) & = \dfrac{\partial \mathbf{v}_t}{\partial n}, \\[2em]
\text{WSS}(t, \mathbf{x}) & = -2\mu\tau(t, \mathbf{x}), \\[2em]
\text{AWSS}(\mathbf{x}) & = \dfrac{1}{T} \displaystyle\int_0^T \|\text{WSS}(t, \mathbf{x})\| \, dt, \\[2em]
\text{OSI}(\mathbf{x}) & = \dfrac{1}{2} \left(1 - \dfrac{\left\| \displaystyle\int_0^T \text{WSS}(t, \mathbf{x}) \, dt \right\|}{\displaystyle\int_0^T \|\text{WSS}(t, \mathbf{x})\| \, dt} \right).
\end{cases}
\tag{9.4.2}
$$

Note that AWSS and OSI are time-averaged indexes, typically over a cardiac cycle. For steady simulations just WSS is computed. In this work, the $\tau(t, \mathbf{x})$ field is calculated using the vmtk [11].

   In the case of 1D models, solutions provide fields of flow (Q), pressure (P) and area (A) over time. The only field that is post-processed is the FFR, which is estimated using the same method as for 3D models. The only difference is that the spatial regions for average calculation are now 1D centerline segments.

Chapter 10

Simulations results

"You may never know what results come of your actions, but if you do nothing, there will be no results."

Mahatma Gandhi.

This chapter presents the results of the second Part of the Thesis, and its layout as follows: Section 10.1 presents demographics and individual information of the patient population. Section 10.2 briefly details the computational infrastructure used to perform the simulations. Section 10.3 presents mesh independence tests for the quantities of interest. Comparisons of steady state and transient simulations are presented in Section 10.4. The impact of image modality on several hemodynamic variables is shown in Section 10.5. In Section 10.6, a comparison between 3D and 1D models is presented, focusing the estimation of FFR. Finally, Section 10.7 compares the FFR_{CE} to the invasive measure, distinguishing between different methods to estimate the flow distribution in models constructed from CCTA and IVUS.

10.1 Patient population

Through this chapter, several studies are presented involving computational simulations targeting the estimation of FFR. The characteristics of such studies involved different patient samples from the same population. The complete set of patients is presented in this section, and a unique patient identification number (ID) is assigned for future reference. Patients with clinical suspicion of atherosclerotic coronary disease, who underwent multimodal evaluation with CCTA and IVUS at least, but also FFR, at the Radiology Department at the Heart Institute (InCor) and Hospital Sirio-Libanês, were selected. Image data were acquired using standardized acquisition protocols. Data processing and analysis were performed retrospectively following methodologies explained in Chapter 9. The study protocol was approved by the local ethics committees of the medical centers.

Table 10.1 presents demographic information relevant for the definition of hemodynamic simulations parameters. A total of 3 female and 21 male, all adults aging $61 \pm 10[43, 84]$ years. Circulation dominance distribution is closed to reported percentage in the literature [108], with 92% right-, 4% left- and 4% co-dominant circulation. When performing the invasive measurement of FFR, adenosine was administrated intra-coronary in all but one patient. Although a CCTA study is present for each patient, at the moment of writing this document, patients with IDs $\{36 - 39\}$ have not been processed yet, and computational models were only available for patients with IDs $\{6 - 25\}$, totaling 11 CCTA computational models. Regarding the IVUS studies, some patients were subjected to 2 or even 3 IVUS studies in major arteries, therefore a total of 33 computational models are

available. Estimated hemodynamics parameters are in the range of physiological values reported in the literature, e.g., the myocardial mass averaging $218 \pm 56[114, 326]$ matches data reported in [203] and the resting CBF averaging $251 \pm 40[173, 331]$ agrees with values reported in [136, 353, 286].

10.2 Computational resources

All CFD simulations were performed in heterogeneous clusters available at the *Laboratório Nacional de Computação Científica* (LNCC, Petrópolis, Brazil):

- The INCT-MACC[1] cluster consisting of 100 nodes with `2 x Intel Xeon X5670 2.93GHz (6 cores), 36GB of RAM` and 54 nodes with `2 x Intel Xeon E5-2660 2.20GHz (8 cores), 64GB of RAM` interconnected through `Infiniband QDR`.

- The Santos Dumont[2] cluster consisting of 504 nodes with `2 x CPU Intel Xeon E5-2695v2 2.4GHZ (12 cores), 64GB of RAM` interconnected through `Infiniband FDR`.

The number of computational tasks used to perform simulations was adapted to mesh size, in an empirical fashion, and to computational resources availability. In following sections, performance information will be provided, when relevant, in terms of: (a) the total wall clock run time (RT) from the simulation, and (b) the so-called *normalized run time* defined as

$$\text{NRT} = \frac{(\text{RT})(\#\text{Tasks})}{\overline{\#\text{Tasks}}}, \tag{10.2.1}$$

where $\overline{\#\text{Tasks}}$ is the mean number of tasks used for the specific set of simulations under consideration.

---

[1] `http://comcidis.lncc.br/tecnologias.php`
[2] `http://sdumont.lncc.br`

Patient ID	CD	G	Age [years]	W [kg]	H [cm]	SBP [mmHg]	DBP [mmHg]	MBP [mmHg]	HR [min^{-1}]	PP [mmHg]	PP* [mmHg]	SV [ml/beat]	CO [l/min]	AA	m [g]	CBF [ml/min]	IM
6	R	M	66	109	181	120	80	93	70	40	46.51	92.18	6.45	ICA	252.64	290.38	1
10	R	M	68	80	166	117	69	85	88	48	51.03	77.51	6.82	ICA	221.26	306.96	1
11	R	M	49	104	176	106	71	83	78	35	38.96	78.08	6.09	ICA	326.22	274.05	2
12	C	M	50	78	171	120	70	87	77	50	46.61	77.51	5.97	ICA	200.43	268.58	1
17	R	M	59	97	170	120	80	93	66	40	44.41	83.98	5.54	ICA	308.41	249.42	1
18	R	M	51	78	180	116	76	89	60	40	42.01	72.43	4.35	ICA	235.04	195.55	2
19	R	M	48	78	180	116	78	91	70	38	40.13	68.42	4.79	ICA	283.23	215.53	2
20	R	M	59	91	181	139	84	102	69	55	51.76	93.22	6.43	ICA	220.55	289.45	1
23	R	M	43	83	172	120	80	93	72	40	39.61	71.18	5.12	ICA	231.12	230.62	2
24	R	F	71	52	151	130	80	97	58	50	52.91	66.35	3.85	ICA	150.52	173.17	2
25	R	M	84	68	165	119	69	86	83	50	56.81	72.21	5.99	ICA	168.33	269.69	1
26	R	M	52	101	181	108	63	78	71	45	44.76	88.27	6.27	ICA	260.50	282.01	1
28	R	M	58	119	192	100	60	73	78	40	44.11	94.22	7.35	ICA	252.25	330.71	1
29	R	M	74	80	184	124	67	86	66	57	57.24	89.58	5.91	IVA	213.85	266.05	1
30	R	F	61	59	147	125	70	88	62	55	52.36	73.25	4.54	ICA	113.76	204.37	1
31	R	M	69	84	171	95	54	68	64	41	47.9	79.51	5.09	ICA	148.91	229.00	1
32	R	F	59	70	165	80	50	65	69	30	39.51	60.37	4.17	ICA	130.77	187.45	2
33	L	M	67	101	172	110	66	81	59	44	48.77	93.39	5.51	ICA	204.76	247.96	1
34	R	M	59	85	170	99	59	72	74	40	44.41	75.63	5.60	ICA	214.38	251.85	1
35	R	M	62	88	172	120	78	92	75	42	46.29	79.48	5.96	ICA	217.44	268.24	3
36	R	M	55	81	175	100	50	68	68	50	48.11	81.93	5.57	ICA		250.71	1
37	R	M	71	84	178	125	71	89	76	54	54.87	87.68	6.66	ICA		299.87	2
38	R	M	61	85	182	94	51	65	58	43	46.48	81.48	4.73	ICA		212.66	1
39	R	M	59	87	190	108	68	81	69	40	44.41	77.67	5.36	ICA		241.17	1
AVG	n_R =22	n_M =21	60.63	85.08	173.83	112.96	68.50	83.54	70.00	44.46	47.08	79.81	5.59	n_{IC} =23	217.72	251.48	n =33
STD	n_C = 1	n_F = 3	9.50	15.17	10.49	13.36	10.27	10.39	7.80	6.93	5.33	9.17	0.89	n_{IV} = 1	56.00	39.92	
MIN	n_L = 1		43.00	52.00	147.00	80.00	50.00	65.00	58.00	30.00	38.96	60.37	3.85		113.76	173.17	
MAX			84.00	119.00	192.00	139.00	84.00	102.00	88.00	57.00	57.24	94.22	7.35		326.22	330.71	

Table 10.1: Patient population demographics, statistical data of hemodynamic variables in the patient sample.

CD: Coronary circulation dominance, left (L), right (R) or co-dominant (C); G: Gender, female (F) or male (M); W: Weight; H: Height; SBP: Systemic systolic blood pressure; DBP: Systemic diastolic blood pressure; MBP: Systemic mean blood pressure; HR: Heart rate; PP: pulse pressure; PP*: corrected PP, see Chapter 7, Section 7.3.4.1; SV: Stroke volume; CO: Cardiac output; AA: Adenosine administration technique used during invasive FFR measurement, intra-coronary (IC) or intra-venous (IV); m: Myocardial mass; CBF: Resting coronary blood flow, estimated using Eq.(7.3.1); IM: Number of IVUS models associated to the patient.

10.3   Mesh independence

The goal of this section is to show that the mesh discretization level used in forthcoming sections ensures that the fluid-dynamics phenomena in the coronary arteries are accurately captured. To this purpose, a representative set of 4 CCTA models was selected, featuring different stenotic lesions, tapering and branching patterns. Such patients are identified by the IDs 10, 12, 18 and 25, see Section 10.1 for patient-specific data. Figure 10.1 illustrates the geometric domains for patients 12 and 25. Four mesh discretization levels were used for each arterial model. A radius-dependent heterogeneous discretization strategy is used to generate de CFD meshes using vmtk [11]. This means that element size is a function of the local arterial radius. In practice, vmtk offers a parameter to control the element size, called `edgelengthfactor` ($\nu \in (0,1]$), see Appendix A for a detailed description of the mesh generation pipeline. As ν value decreases, the element size decreases proportionally. Smaller elements result in meshes with more degrees of freedom[3] (dof) and (expectedly) a more accurate solution.

Hemodynamics parameters were set to simulate patient-specific hyperemic conditions following the strategy presented in Section 9.3.1. A constant pressure is imposed at the model inlet through a traction vector, resistive BC are used with a coupling equation that ensures a fixed blood inflow, see Section 9.2.1 for details on the mathematical modeling and numerical models. All simulations were ran with homogeneous initial conditions. Steady state simulations were configured with a $\Delta t = 5 \times 10^{-3}$ s for patients 12 and 18 and $\Delta t = 5 \times 10^{-4}$ s for patients 10 and 25. Constant BC during a time span of $T = 0.25$ s were used, such that the steady state was safely reached. All comparisons are performed for the final steady state.

Mesh independence is assessed for several fields, i.e. pressure (p), FFR, velocity ($\mathbf{v}$) and wall shear stress (WSS). Given two CFD simulation outcomes ($S_{\{1,2\}}$), with discretization levels $\nu_{\{1,2\}}$ for the same arterial model, comparison is performed in two steps: (i) a linear interpolation of the coarser mesh (S_2) into the refined mesh (S_1) is performed for each variable, resulting into the mesh $\hat{S}_2$; (ii) the error ($\varepsilon.$) for each variable is estimated from the difference as defined by equations (10.3.1-10.3.4),

$$\varepsilon_p = \frac{\text{mean}(|p(S_1) - p(\hat{S}_2)|)}{\Delta p(S_1)}, \tag{10.3.1}$$

where $\Delta p(\cdot)$ is a reference pressure drop defined as the average pressure difference between the inlet and all outlets of the model. Once the FFR field is computed at every node in the mesh, since it is a normalized variable, the error is defined as

$$\varepsilon_{\text{FFR}} = \text{mean}(|\text{FFR}(S_1) - \text{FFR}(\hat{S}_2)|). \tag{10.3.2}$$

For the velocity field, the difference in normalized by a reference velocity $v = Q_{in}/A_{in}$, where Q_{in} is the flow at the inlet with area A_{in}, then

$$\varepsilon_{\mathbf{v}} = \frac{\text{mean}(\|\mathbf{v}(S_1) - \mathbf{v}(\hat{S}_2)\|)}{v}. \tag{10.3.3}$$

Regarding the WSS field, the difference is normalized by the average WSS in the finner mesh, this is

$$\varepsilon_{\text{WSS}} = \frac{\text{mean}(\|\text{WSS}(S_1) - \text{WSS}(\hat{S}_2)\|)}{\text{mean}(\text{WSS}(S_1))}. \tag{10.3.4}$$

---

[3]Note that each computational node of a mesh has 4 degrees of freedom, i.e. pressure (p) and velocity ($\mathbf{v} = (v_x, v_y, v_z)$).

(a)

(b)
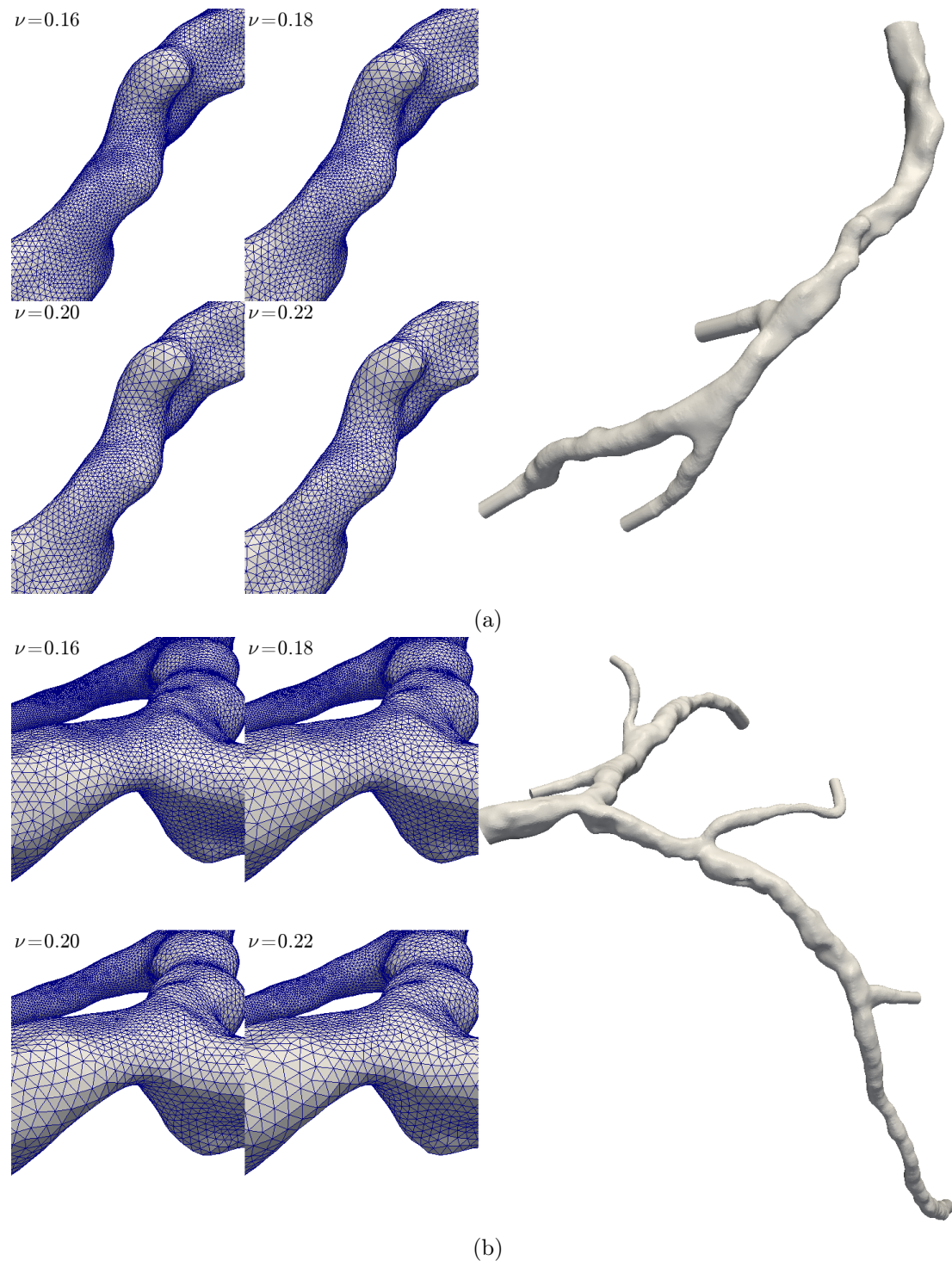
Figure 10.1: Example of mesh discretization for patients 12 (a) and 25 (b).

Table 10.2 presents details of the mesh models in terms of the number of dof and reference element size (RES)[4]. Also, the computational costs are presented in terms of the number of tasks used to solve the simulation, the wall clock run time (RT) and normalized run time (NRT). Details on the computer infrastructure used to solve the simulations are presented in Section 10.2. Note that patients 10 and 25 feature longer RT due to the

---

[4]It is computed as RES $= \sqrt{\dfrac{3}{4\pi}\bar{V}}$, where $\bar{V}$ is mean tetrahedral volume estimated from the total volume of the arterial model over the number of tetrahedral elements.

increased Δt values, which are ten times smaller than the one used for patients 12 and 18. A clear association between the ν values and the resulting mesh parameters (dof and RES) is evident for all the patient models. The number of dof almost triplicate and the RES reduces approximate a 45% between the meshes constructed with $\nu = 0.22$ and $\nu = 0.16$. Note that the #Tasks was kept constant for each patient model, and the NRT is increased by a factor of $[5.7, 7.5]$ between the extremal values of ν.

Table 10.3 presents the relative errors between different refinement meshes for each patient model. Such errors are presented in terms of sequential values of ν against a fixed reference mesh (the most refined mesh, with $\nu = 0.16$) and between subsequent ν values. Therefore, the differences can be interpreted as convergence errors. Figure 10.2 plots the error presented in Table 10.3 as a function of the number of dof. From a quantitative point of view, the differences in the pressure and FFR fields are the lowest, below 1% and 0.1%. In turn, the velocity field features differences below 5%, which are propagated to the WSS, which features the largest differences, approximately 10%. From a qualitative perspective, Figures 10.3-10.4 display the fields across the mesh refinements levels for patient 12. This allows to visualized the small differences in p, FFR and $\mathbf{v}$. Furthermore, Figure 10.4b, shows that despite the quantitative differences in the WSS, such discrepancies are not originated from different patterns in the field distribution but from local differences near regions of high gradients in the WSS field.

The main goal of these mesh independence tests is to aid in the definition of a default ν value to be used for all arterial model in future simulations. It should be reminded that the ultimate goal is to estimate the FFR field. In such scenario, the results indicate that the coarser meshes ($\nu = 0.22$) could safely be used, since the differences in the p and FFR fields are small compared to more refined meshes. Nonetheless, in order to obtain accurate solutions for the $\mathbf{v}$ and WSS without increasing the computational cost of simulations, the value of $\nu = 0.2$ was chosen as default for all future simulations of CCTA models.

Regarding simulations using IVUS models, the incorporation of small branches in the geometries forced the use of smaller ν values in some models. Taking this restriction into consideration, and the fact that the arterial volume of IVUS models is smaller than CCTA models, a different value of $\nu = 0.16$ was used for all IVUS models.

Patient ID	ν	dof	RES [cm]	#Tasks	RT [hs]	NRT [hs]
10	0.16	4648928 (2.9)	0.0039 (1.46)	168	38.8 (7.2)	56.7
	0.18	2838160 (1.8)	0.0047 (1.23)	168	9.5 (1.9)	14.2
	0.20	2211452 (1.4)	0.0051 (1.12)	168	9.0 (1.8)	13.5
	0.22	1588180 (1.0)	0.0057 (1.00)	168	4.9 (1.0)	7.8
12	0.16	1348592 (2.9)	0.0037 (1.45)	64	1.9 (6.6)	1.2
	0.18	824700 (1.8)	0.0044 (1.22)	64	0.8 (2.6)	0.5
	0.20	595044 (1.3)	0.0049 (1.09)	64	0.5 (1.7)	0.3
	0.22	463704 (1.0)	0.0054 (1.00)	64	0.3 (1.0)	0.2
18	0.16	4825872 (2.9)	0.0031 (1.46)	96	5.2 (7.5)	4.7
	0.18	2914164 (1.8)	0.0037 (1.22)	96	2.1 (3.0)	1.9
	0.20	2127224 (1.3)	0.0041 (1.10)	96	1.7 (2.5)	1.6
	0.22	1642064 (1.0)	0.0045 (1.00)	96	0.7 (1.0)	0.6
25	0.16	3448552 (2.9)	0.0037 (1.43)	96	26.9 (5.7)	24.4
	0.18	2088656 (1.8)	0.0044 (1.20)	96	11.1 (2.4)	10.1
	0.20	1522596 (1.3)	0.0049 (1.08)	96	6.7 (1.4)	6.1
	0.22	1169144 (1.0)	0.0053 (1.00)	96	4.7 (1.0)	4.3

Table 10.2: Mesh and runtime information for each refinement level (ν) of each patient model. The number of dof is presented, as well as the mean tetrahedral size (RES), the number of computational threads (#Tasks), the wall clock run time (RT) and normalized run time (NRT). When present, values enclosed in parentheses represent normalized values using the values corresponding to the coarser mesh for each patient.

Patient ID	Field	Relative error					
		$S_{0.20} - S_{0.22}$	$S_{0.18} - S_{0.20}$	$S_{0.16} - S_{0.18}$	$S_{0.16} - S_{0.22}$	$S_{0.16} - S_{0.20}$	$S_{0.16} - S_{0.18}$
10	p	0.0040±0.0052	0.0028±0.0042	0.0024±0.0038	0.0049±0.0062	0.0043±0.0041	0.0024±0.0038
	FFR	0.0009±0.0011	0.0005±0.0009	0.0004±0.0008	0.0013±0.0014	0.0006±0.0010	0.0004±0.0008
	v	0.0243±0.0310	0.0197±0.0265	0.0223±0.0293	0.0357±0.0484	0.0278±0.0451	0.0223±0.0293
	WSS	0.0817±0.1397	0.0660±0.0916	0.0785±0.1096	0.1123±0.1600	0.0920±0.1298	0.0785±0.1096
12	p	0.0016±0.0028	0.0032±0.0025	0.0039±0.0024	0.0074±0.0038	0.0066±0.0034	0.0039±0.0024
	FFR	0.0002±0.0003	0.0003±0.0002	0.0004±0.0003	0.0008±0.0005	0.0007±0.0004	0.0004±0.0003
	v	0.0313±0.0333	0.0274±0.0296	0.0257±0.0280	0.0471±0.0505	0.0349±0.0373	0.0257±0.0280
	WSS	0.0910±0.0912	0.0860±0.0846	0.0844±0.0855	0.1226±0.1221	0.1022±0.1011	0.0844±0.0855
18	p	0.0026±0.0023	0.0017±0.0018	0.0027±0.0022	0.0055±0.0049	0.0033±0.0034	0.0027±0.0022
	FFR	0.0001±0.0001	0.0001±0.0001	0.0001±0.0001	0.0002±0.0002	0.0001±0.0001	0.0001±0.0001
	v	0.0112±0.0116	0.0097±0.0102	0.0079±0.0088	0.0128±0.0139	0.0102±0.0112	0.0079±0.0088
	WSS	0.0569±0.0649	0.0540±0.0591	0.0526±0.0609	0.0641±0.0908	0.0581±0.0656	0.0526±0.0609
25	p	0.0071±0.0037	0.0089±0.0030	0.0051±0.0026	0.0206±0.0072	0.0137±0.0043	0.0051±0.0026
	FFR	0.0012±0.0006	0.0014±0.0005	0.0008±0.0004	0.0039±0.0016	0.0022±0.0007	0.0008±0.0004
	v	0.0423±0.0440	0.0363±0.0400	0.0363±0.0413	0.0642±0.0667	0.0480±0.0519	0.0363±0.0413
	WSS	0.0902±0.0840	0.0862±0.0835	0.0868±0.0867	0.1182±0.1165	0.1001±0.0991	0.0868±0.0867

Table 10.3: Mean and SD of relative errors (ε.) for the pressure, FFR, velocity and WSS fields for each patient. The first three error columns feature differences between meshes constructed with subsequent values of the ν parameter ($S_{\nu_{i-1}} - S_{\nu_i}$). The last three error columns present the difference of each mesh against the corresponding finer model ($S_{\nu=0.16} - S_{\nu_i}$).
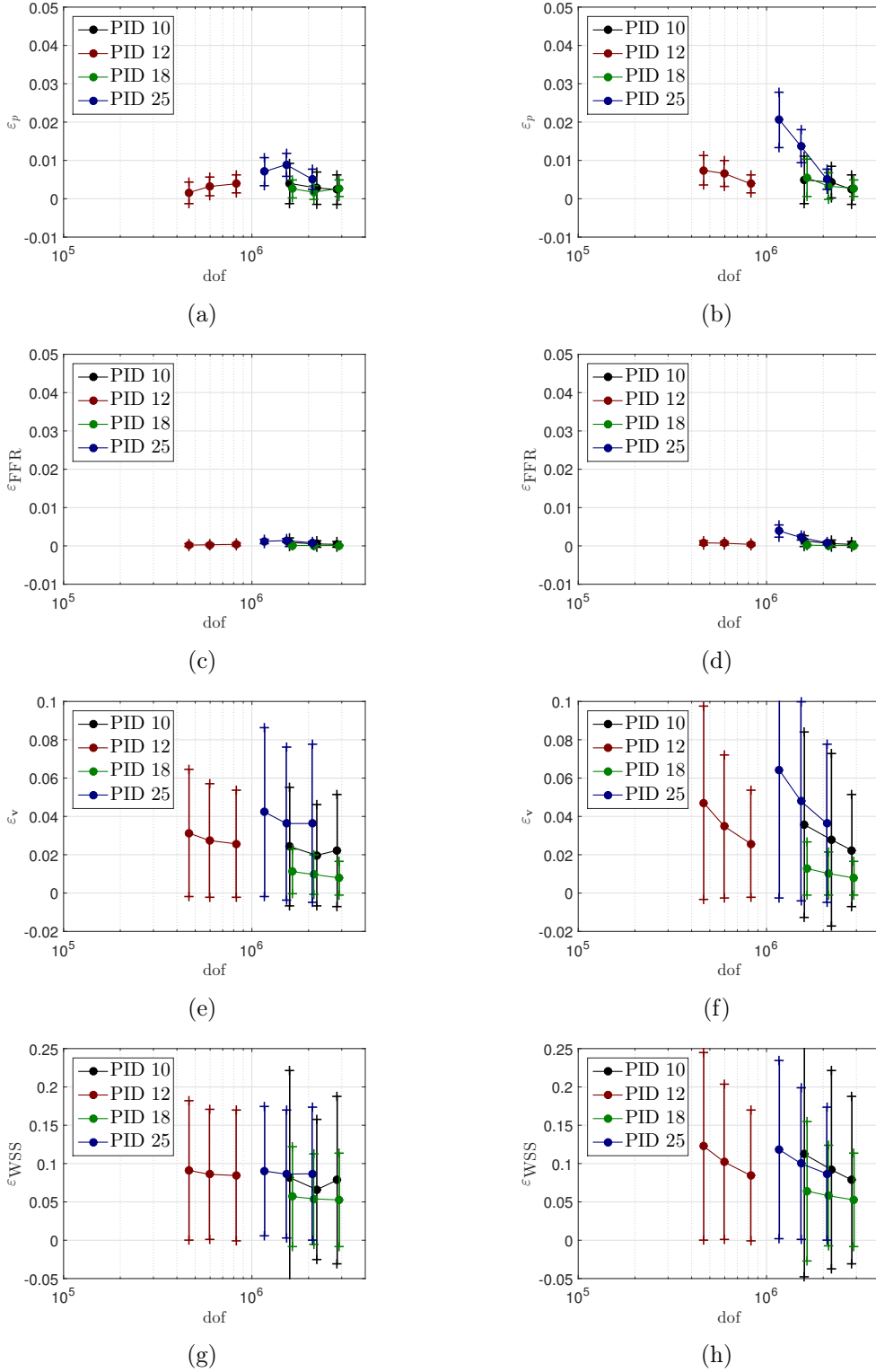
Figure 10.2: Convergence plots for all quantities of interest in each patient model. Panels (a,b) display errors in the pressure field (ε_p); panels (c,d) presents errors in the FFR field (ε_{FFR}); panels (e-f) shows the errors in the velocity field ($\varepsilon_{\mathbf{v}}$); and panels (g-h) display the error for the wall shear stress field (ε_{WSS}). Left column groups the relative errors between meshes created with subsequent refinement parameter ν, i.e. $\varepsilon(S_{\nu_i}, S_{\nu_{i-1}})$. In turn, right column groups the relative errors between meshes created with each ν against a reference mesh constructed with $\nu = 0.16$.

(a)

(b)
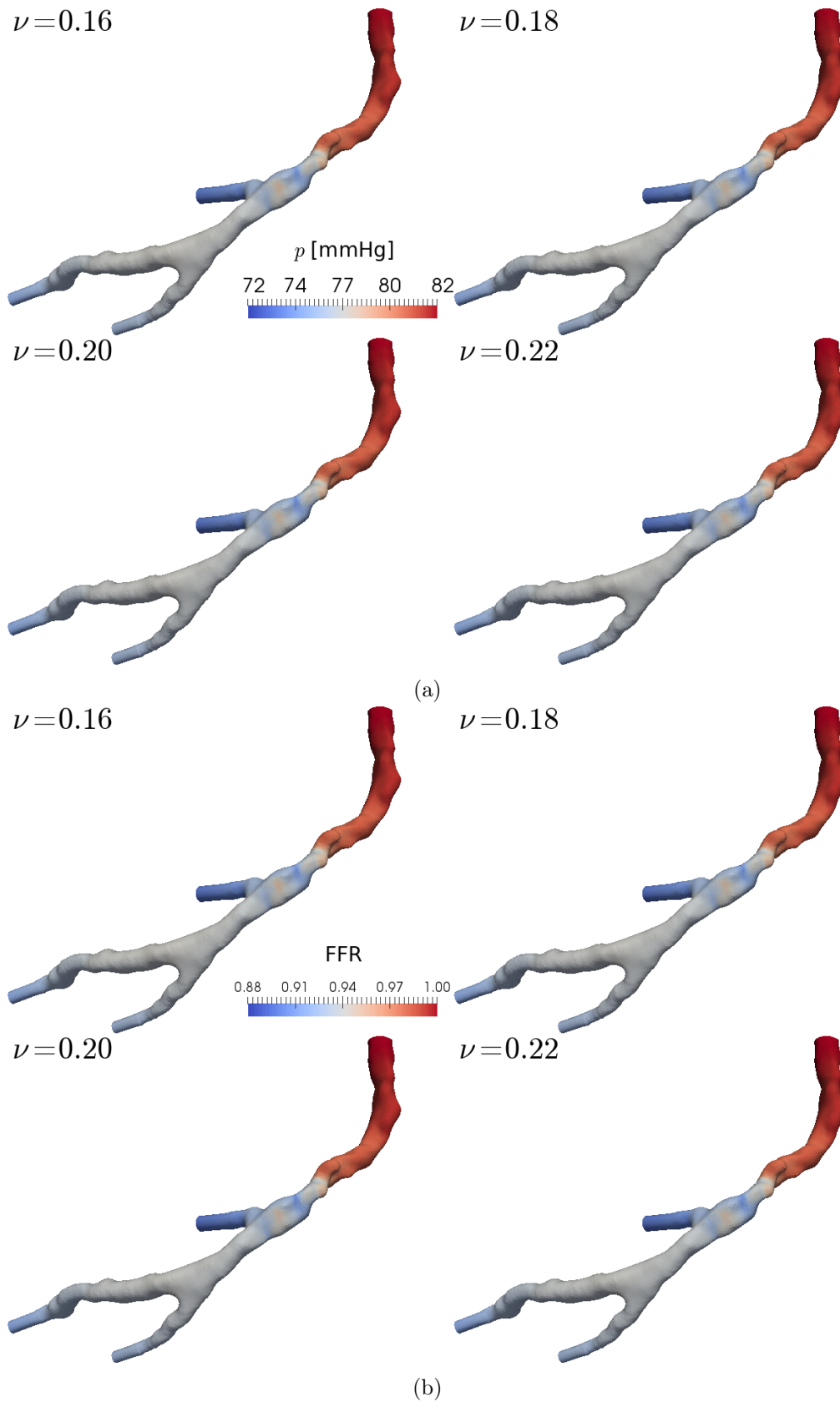
Figure 10.3: Qualitative assessment of all quantities in the arterial model of patient 12, for different values parameter ν. Panel (a) displays the pressure (p) and fractional flow reserve (FFR) is presented in panel (b).

$\nu=0.16$ $\nu=0.18$

$||v||$ [cm^2/s]

0   30   60   90   120

$\nu=0.20$ $\nu=0.22$

(a)

$\nu=0.16$ $\nu=0.18$

WSS [dyn/cm^2]

0   75   150   225   300

$\nu=0.20$ $\nu=0.22$

(b)
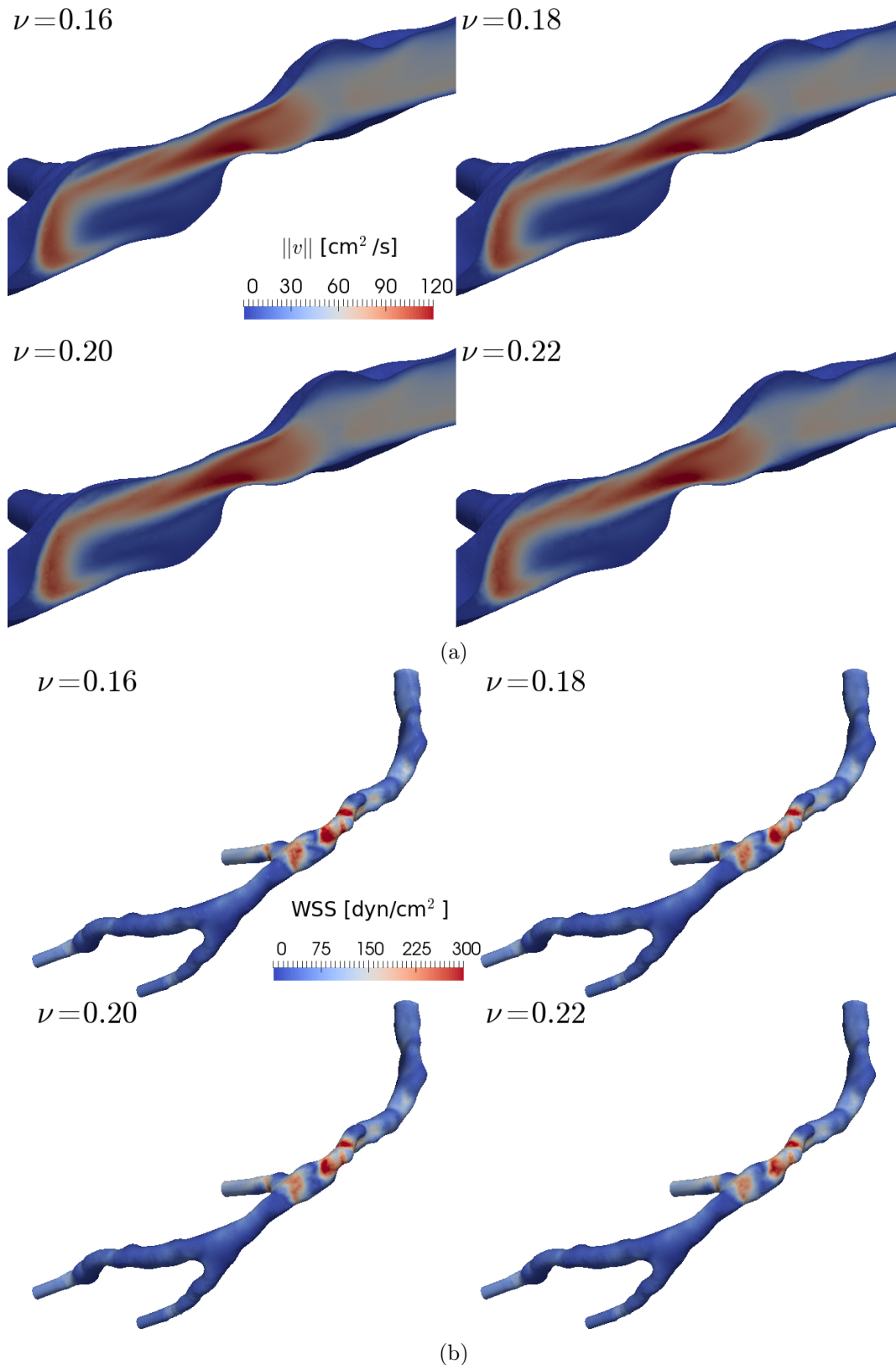
Figure 10.4: Qualitative assessment of all quantities in the arterial model of patient 12, for different values parameter ν. Panel (a) displays a clip of the volume mesh through the stenosis region to show the internal state of the blood velocity magnitude ($||\mathbf{v}||$). Panel (b) features the wall shear stress (WSS) in the arterial surface.

10.4   Transient versus steady simulations

This section focuses on the comparison between steady state and transient[5] simulations. Comparisons are performed using the same set of indexes $\varepsilon_p, \varepsilon_{\text{FFR}}, \varepsilon_{\mathbf{v}}$ and ε_{WSS} introduced in Section 10.3.

A total of 60, 11 CCTA and 49 IVUS, simulations where compared. Such simulations were performed in the context of the studies presented in Sections 10.5 and 10.6. Simulations are grouped into three sets: (A) 11 CCTA simulations which are used in Sections 10.5 and 10.6; (B) 16 IVUS simulations, which are used in Section 10.5; and (C) 33 IVUS simulations used in Section 10.6. Hemodynamics parameters were set to simulate patient-specific hyperemic conditions, see Sections 10.5 and 10.6. A constant pressure is imposed at the model inlet through a traction vector, resistive BC are used with a coupling equation that ensures a fixed mean inflow, see Section 9.2.1 for details on the mathematical and numerical models. All simulations were ran with homogeneous initial conditions.

Steady state simulations were configured with $\Delta t = 5 \times 10^{-3}$ s or $\Delta t = 5 \times 10^{-4}$ s. Constant BC during a time span of $T = 0.25$ s were used to safely reach the steady state. In turn, transient simulations were ran with $\Delta t = 5 \cdot 10^{-4}$ s, and time dependent BC at the outlets. Three cardiac cycles were simulated, which yielded a mean total time of $T = 2.635 \pm 0.319$ s. The same mesh was used for both simulation, i.e. the dof remained constant between runs.

Table 10.4 presents a quantitative comparison between the steady and transient simulations in terms of the errors between the hemodynamics variables and wall clock run times. The difference in RT and NRT is greater in set A than in the other two sets, which is explained by the larger meshes of set A. Regarding the errors in each field, there was not statistical significant differences[6] between the mean values of the three sets. It was found that, in mean, the differences in $p, \mathbf{v}$ and WSS are less than 4%, and the FFR field features smallest differences ($< 0.5\%$).

Considering that the RT for all steady state simulations averages 3 ± 4 hs, against 71 ± 57 hs for transient simulations, and the small differences in the hemodynamics variables, the results presented here support the decision of using steady state simulations to estimate the FFR. Furthermore, the average wall shear stress over a cardiac cycle can also be estimated with good accuracy from the steady state simulation, which results in the same gross distribution of WSS over the arterial wall.

Index	Simulation set			All ($n = 60$)
	A ($n = 11$)	**B** ($n = 16$)	**C** ($n = 33$)	
ε_p	0.030 ± 0.015	0.039 ± 0.017	0.037 ± 0.015	0.036 ± 0.016
ε_{FFR}	0.006 ± 0.007	0.003 ± 0.003	0.003 ± 0.005	0.004 ± 0.005
$\varepsilon_{\mathbf{v}}$	0.031 ± 0.026	0.036 ± 0.046	0.022 ± 0.012	0.027 ± 0.029
ε_{WSS}	0.032 ± 0.014	0.035 ± 0.011	0.034 ± 0.012	0.034 ± 0.012
Δ RT [hs]	106 ± 80	65 ± 37	58 ± 46	69 ± 54
Δ NRT [hs]	87 ± 85	55 ± 24	58 ± 36	62 ± 47
dof [Million]	2.05 ± 1.18	1.51 ± 0.41	1.58 ± 0.51	1.65 ± 0.68

Table 10.4: Quantitative comparison between steady state and transient simulations for all groups. For the computation of the NRT, the total mean of computational tasks was used ($\#$Tasks $= 137$). Since the meshes are the same for steady state and transient simulations, the dof values do not represent a difference.

---

[5]The time-average quantities over the third cardiac cycle of the transient simulation are used for comparison.
[6]According to a two-tailed U-Test with 95% confidence interval.

10.5   Impact of image modality on hemodynamic variables

Coronary blood flow simulations have played a major role in the understanding of hemodynamic mechanisms involved in the onset and progression of atherosclerotic disease [69, 70, 79, 187, 320], characterization of plaque location [278], plaque erosion [59] and plaque rupture [73]. Moreover, as presented in Chapter 8, there is an increasing interest from the medical community in the use of such computational tools to aid decision making process due to feasible estimation of FFR without invasive pressure measurements.

Patient-specific vascular geometries are obtained using a variety of imaging methods: coronary computed tomography angiography (CCTA) [73, 278, 328] or angiograms (AX), which can be utilized alone [59, 236], or in combination with either intra vascular ultrasound (IVUS) [70, 187, 320] or optical coherence tomography (OCT) [103].

Among them, CCTA and IVUS are the most common[7]. Although there have been studies addressing the consistency between these two image modalities concerning the overall decision-making process [105], it has been largely acknowledged that these modalities feature several differences ranging from the economic cost and patient risk to the resulting anatomical definition [188, 195].

Previous works merged IVUS data into CCTA models [124, 283], and recently, the differences of FFR estimated by CCTA and by quantitative coronary angiography were studied in [201]. A comparison between CCTA and IVUS in terms of hemodynamic variables predicted by computational fluid dynamic models could help to better understand the implications of modeling choices, and gain insight about the sensitivity to imaging modality. Therefore, the goal of the study presented in this section is to compare the hemodynamic variables in coronary vessels when the geometric models are constructed from CCTA and from IVUS image modalities.

10.5.1   Materials and methods

The study sample consisted of patients with ID= $[6, 25]$ from Section 10.1, a total 11 patients and 16 arteries, all of them are left coronary networks. The time span between both medical studies was 3.4±4.9 days, and the CCTA was always performed first. Patients demographics are presented in Table 10.5.

Men, n(%)	10 (91%)
Age (years)	59±12
Weight (kg)	83±16
Resting mean systemic pressure (mmHg)	91±6
Resting heart rate (bpm)	72±9
Arteries, n(%)	
Left anterior descending (LAD)	10 (62%)
Left circumflex (LCx)	5 (31%)
Ramus intermedius (RI)	1 (7%)
Circulation dominance, n(%)	
Right	10 (91%)
Co	1 (9%)

Table 10.5: Baseline characteristics of the study sample (11 patients and 16 arteries). Data are represented as mean±SD, or as number and percentages of patients.

Geometric models constructed from CCTA and IVUS are shown in Figure 10.5. Image and mesh processing were performed as detailed in Chapter 9, Section 9.1. Finite

---

[7]Although computational models constructed from OCT are gaining popularity.

element meshes for models of CCTA and IVUS contained, respectively, 2.05 ± 1.18 M and 1.52 ± 0.43 M degrees of freedom. Fully 3D fluid dynamics simulations were performed following the methodology explained in Chapter 9, Section 9.2.1. Steady state and transient (over three patient-specific cardiac cycles) simulations were performed. Patient-specific hemodynamics parameters were defined following the methodology detailed in Chapter 9, Section 9.3. For the study sample, the estimated resting CBF is 251 ± 42 ml/min, which agrees with physiological ranges (270 ± 82 ml/min) reported in [286]. Regarding flow distributions, see Chapter 9, Section 9.3.1, the resistance parameter in the CCTA models were estimated using the DMD approach. For the present sample, the average resting flow at the inlet of the LM coronary, resulted 142 ± 38 ml/min, in agreement with values reported elsewhere (156 ± 40 ml/min) [286], furthermore, the CFR was set to 2.6, which is a mean value for nonischemic human coronary arteries [165]. For the IVUS models, flow distributions was performed using the CSRD approach.

Post-processing and data analysis of the simulations results for comparisons was performed as following. For each geometric model, the centerline (resolution of 0.5 mm between points) was computed and was used to clip the model at the ostium of the artery of interest. From the CCTA model, a region of the centerline was chosen such that it matches the length of the IVUS centerline (see solid surfaces in Figure 10.5). Side branches were removed for comparison purposes. Cross-sectional slices, denoted Γ_s, with contour $\partial \Gamma_s$, were extracted at each point over the centerline (see Figure 10.6).

Quantities defined in the bulk of the domain were averaged at each section Γ_s, while quantities defined over the surface of the domain were averaged over $\partial \Gamma_s$. We simply refer to these as Γ_s-averaged quantities, and are denoted by $\overline{(\cdot)}$.

Comparisons along the region of interest focused on the magnitude of velocity $\bar{v} = \overline{\|\mathbf{v}\|}$ and pressure $\bar{p}$, lumen area A (D the diameter), Reynolds number $\text{Re} = \frac{\rho \bar{v} D}{\mu}$, time average wall shear stress $\overline{\text{AWSS}}$, oscillatory shear index $\overline{\text{OSI}}$, flow rate $\bar{Q}$ and fractional flow reserve ($\overline{\text{FFR}} = \bar{p}/P_p^H$). Time-dependent quantities were averaged over the last cardiac cycle. Also, the branch count in the regions of interest, and the fraction of flow at the outlet relative to the total flow rate coming into the coronary tree, denoted FFOI, were compared.

Point-wise comparison between Γ_s-averaged quantities was performed. Paired non-parametric Mann-Whitney U-Test (two tailed) and Bland-Altman (BA) analysis of differences were used to show statistical discrepancies between variables from CCTA and IVUS simulations. All centerlines were scaled down to a normalized centerline with parametric arc-length coordinate $s \in [0, 1]$, and re-sampled to 200 points for each centerline for comparison purposes.

Invasive measurements of FFR were available for each vessel of the set, see Section 10.7 for comparison results.

10.5.2 Results

The absolute relative error of the FFR field (in the complete domain) between pulsatile and steady simulations was $0.9\% \pm 1.2\%$ (CCTA) and $0.3\% \pm 0.4\%$ (IVUS). Moreover, the absolute relative error in the AWSS was $3.7\% \pm 1.6\%$ (CCTA) and $4.0\% \pm 1.3\%$ (IVUS). Such errors are computed using relative error at each point in the mesh. The mean absolute relative difference across all outlet flows between pulsatile and steady simulations was $1.5\% \pm 1.6\%$ (CCTA) and $0.5\% \pm 0.7\%$ (IVUS). More comparisons between steady and transient simulations are presented in Section 10.4.

Regarding the α variable, see Chapter 9, Section 9.2.1, which adjusts the terminal resistances to satisfy myocardial demand, steady-state simulations lead to $\alpha = 0.78 \pm 0.16$ for CCTA and $\alpha = 0.89 \pm 0.16$ for IVUS. In turn, pulsatile simulations result in time-dependent α as shown in Figure 10.7 (cardiac period normalized to 1 s). Such time-
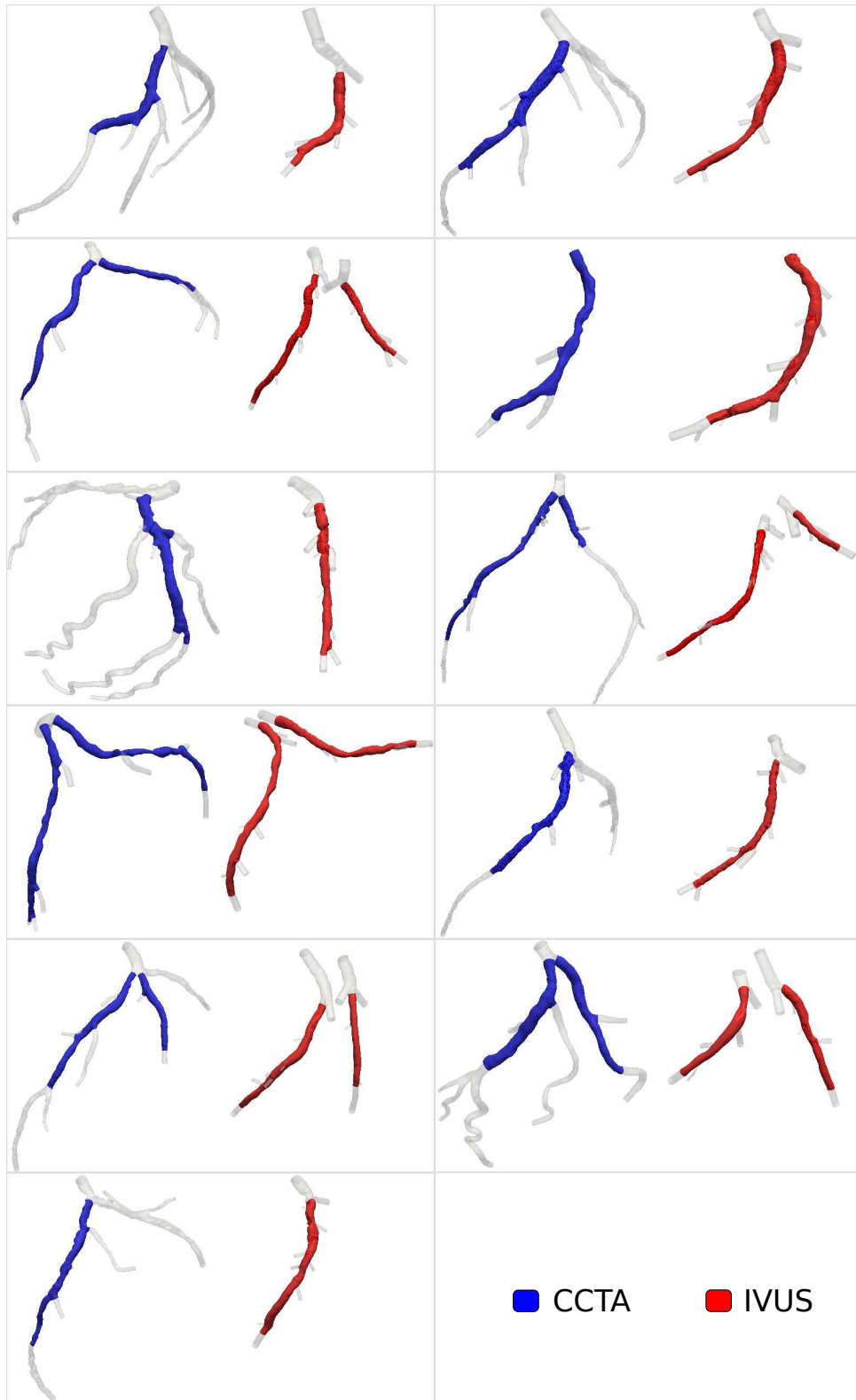
Figure 10.5: Geometric models of the 11 patients (16 arteries) included in the study sample. Blood flow domains for computational simulations are shown with transparency. Regions for comparison are highlighted with solid colors, blue for CCTA and red for IVUS.
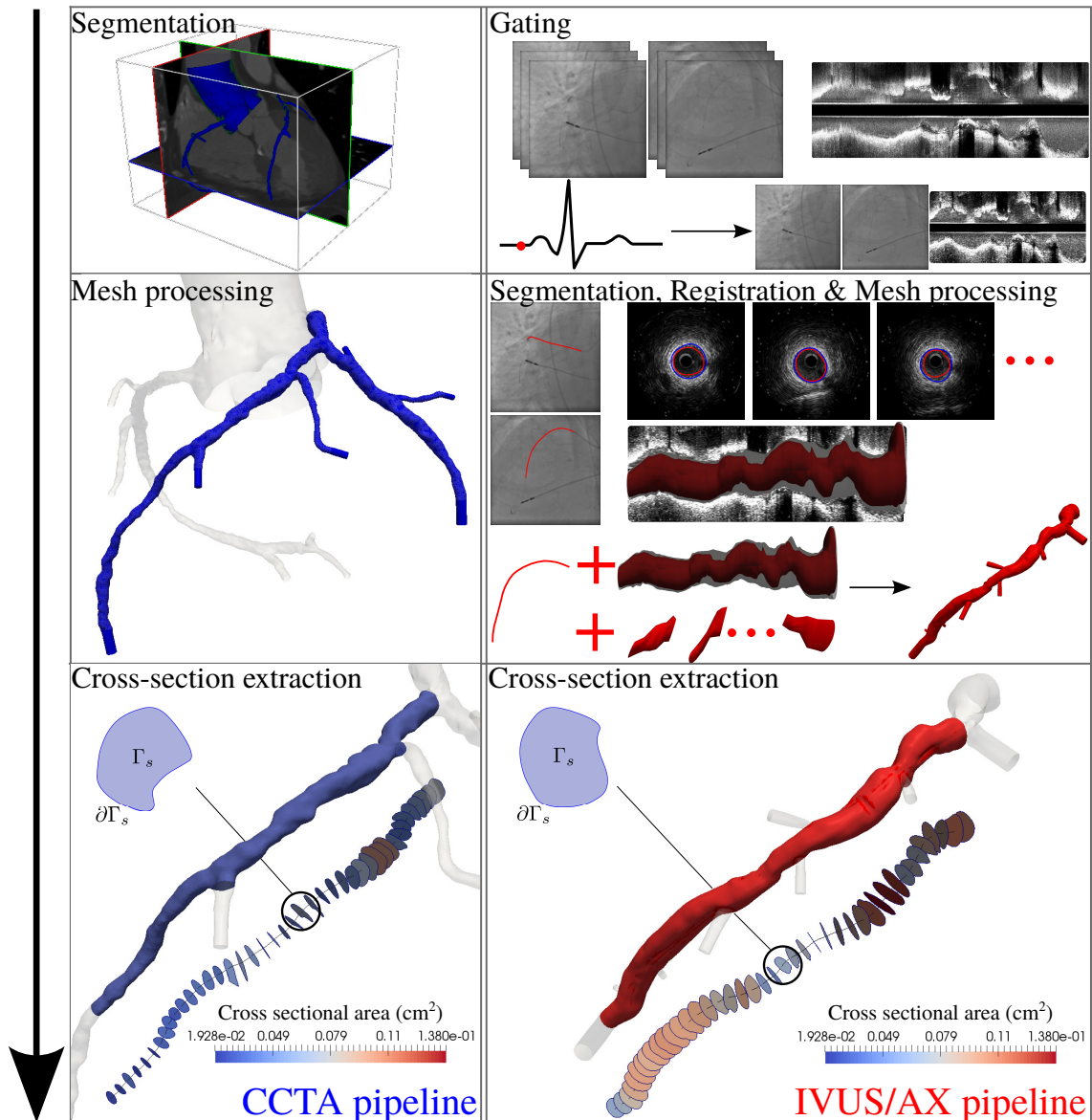
Figure 10.6: Complete processing pipeline from medical images to geometric models. The CCTA procedure is presented in the left column and the IVUS procedure is shown in the right column.

dependent α has mean value 0.89 ± 0.22 for CCTA and 1.06 ± 0.12 for IVUS. Furthermore, the absolute difference between the steady-state α and the pulsatile values for each model was 0.13 ± 0.09 for CCTA and 0.17 ± 0.08 for IVUS.

The remainder of the results presented here are based on the transient simulations, averaged over the last cardiac cycle.

Because a novel strategy to set up boundary conditions was developed in this work, see Chapter 9, Section 9.2.1, it is important to analyze the discrepancies in the flow distribution with respect to the distribution dictated by Murray's law. Particularly, for our patient sample, the absolute relative difference across all outlets between Murray's outflow and the actual outflow in the simulations is, in average over all the outlets of all patients, $12.4\% \pm 14.4\%$ for CCTA and $6.1\% \pm 15.2\%$ for IVUS, recalling that these values correspond to hyperemic conditions. These differences characterize the coronary steal phenomenon taking place in the coronary tree because of the non-negligible resistance of major coronary vessels.
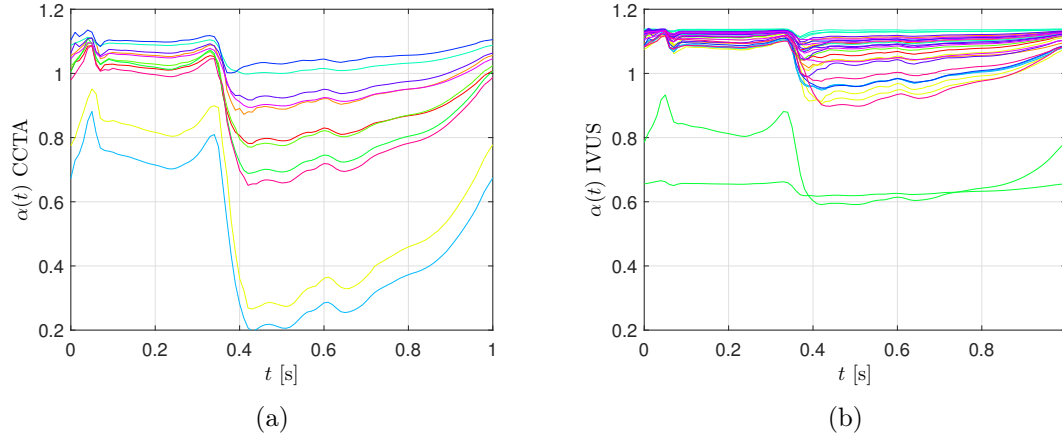
Figure 10.7: Time dependent $\alpha(t)$ for all pulsatile simulations. Panel (a) shows α for CCTA models and panel (b) shows α for IVUS models. Line color matches patient between CCTA and IVUS models.

The statistical analysis for the entire sample is presented in Table 10.6. It was found that A, $\bar{p}$ and $\overline{\text{OSI}}$ are larger in IVUS than CCTA, while $\bar{v}$, Re and $\overline{\text{AWSS}}$ are smaller. Such results are confirmed through the U-test with statistical significance of p-value $\ll 0.01$. The BA analysis (CCTA $-$ IVUS) shows that all variables have significant (p-value $\ll 0.01$) correlation with moderate to high values of the Spearman's correlation coefficient (ρ). The bias and limits of agreement (LA) of BA analysis were normalized by the average between CCTA and IVUS means. Figure 10.8 displays the sample mean $\pm$ SD of the quantities over the normalized centerline.

	CCTA	IVUS	ρ	Rel. Bias	Rel. LA
A [mm^2]	6.07$\pm$2.92	7.55$\pm$2.77	0.51	-0.22$\pm$0.39	[-0.98, 0.55]
$\bar{p}$ [mmHg]	79$\pm$13	84$\pm$5	0.92	-0.05$\pm$0.12	[-0.29, 0.18]
Re	257$\pm$125	238$\pm$184	0.74	0.08$\pm$0.34	[-0.60, 0.75]
$\bar{v}$ [cm^2/s]	38$\pm$23	31$\pm$14	0.54	0.23$\pm$0.58	[-0.91, 1.37]
$\overline{\text{AWSS}}$ [dyn/cm^2]	79$\pm$92	49$\pm$38	0.41	0.47$\pm$1.39	[-2.25, 3.19]
$\overline{\text{OSI}}$	0.009$\pm$0.017	0.010$\pm$0.015	0.38	-0.15$\pm$2.15	[-4.36, 4.05]
$\overline{\text{FFR}}$	0.93$\pm$0.12	0.97$\pm$0.03	0.60	-0.04$\pm$0.11	[-0.27, 0.18]
Q [ml/s]	1.99$\pm$1.06	2.15$\pm$1.00	0.80	-0.08$\pm$0.30	[-0.66, 0.51]
Branch count	2.5$\pm$1.21	5.69$\pm$2.33	0.61	-0.75$\pm$0.44	[-1.19,-0.31]
FFOI	0.17$\pm$0.09*	0.21$\pm$0.08*	0.20*	-0.11$\pm$0.37	[-0.48, 0.26]

Table 10.6: Statistical analysis of all Γ_s-averaged quantities. Mean $\pm$ standard deviation are shown for each model and for the relative bias. The bias (CCTA-IVUS) and the limits of agreements (mean$\pm$SD) for the Bland-Altman analysis were normalized by the average between CCTA and IVUS means. Only for the fraction of flow between outlet and total inflow (FFOI), the U-test and ρ were not statistically significant (p-value > 0.05), which is indicated by the marker *. For all other variables, the Spearman's correlation coefficient ρ and the U-Test are significant (p-value $\ll 0.01$).

The smallest relative biases were featured by the $\overline{\text{FFR}}$ (-4%), $\bar{p}$ (-5%), Q (-8%) and Re (+8%). Large biases are seen in $\overline{\text{AWSS}}$ (47%) and $\overline{\text{OSI}}$ (-15%). However, $\overline{\text{OSI}}$ is relatively small in all cases. The SD of the bias analysis indicates that $\bar{p}$ and $\overline{\text{FFR}}$ are the less affected by imaging modality (SD 12%), in contrast to $\overline{\text{AWSS}}$ and $\overline{\text{OSI}}$, with SD reaching 140% and 215% respectively. As expected, the area A was larger in IVUS, whereas $\bar{v}$ was larger in CCTA models. However, this is not a direct consequence. Main artery flow rate Q at distal locations can vary because IVUS models feature, in average, 3 more side branches than
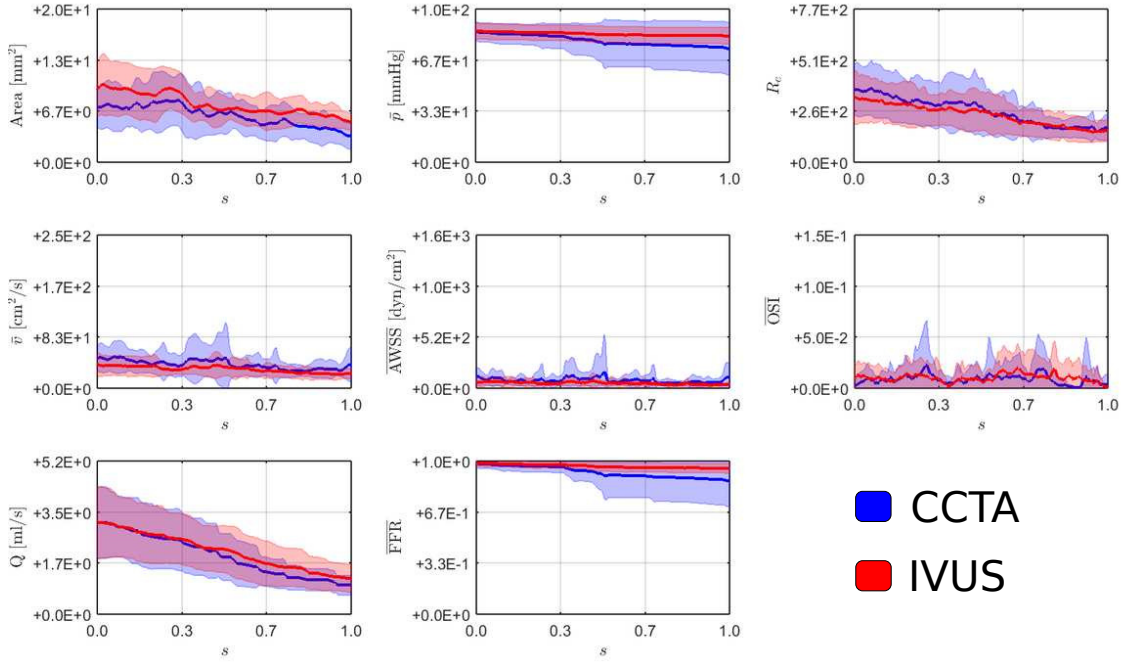
Figure 10.8: Mean (solid lines) and standard deviation (light areas) along the normalized arc length of the centerline for each quantity of interest. Blue represents CCTA and red stands for IVUS.

CCTA models, promoting the deviation of blood through proximal branches. Despite this, Q continues to be larger in IVUS, which implies that the flow deviation is actually more pronounced in the CCTA model. This can also be appreciated in the lack of correlation for FFOI.

Visual inspection of Figure 10.8 shows how the different variables differ in the proximal, mid and distal thirds of the arterial models. Particularly, focusing on the $\overline{\text{FFR}}$ and $\overline{\text{AWSS}}$, differences in the three portions of the arterial segments are reported in Table 10.7. For both variables, correlation decreases towards the distal section. While the $\overline{\text{FFR}}$ relative bias and dispersion increases from proximal to distal thirds, the $\overline{\text{AWSS}}$ results in larger bias in the last two-thirds. Furthermore, arterial tapering is far from linear, and differences in the area between models impact directly in the discrepancies of hemodynamic variables between models. To illustrate such behavior, Figure 10.9 presents scatter plots of discrepancies (CCTA minus IVUS) in $\overline{\text{FFR}}$ and $\overline{\text{AWSS}}$ as a function of the discrepancy in the lumen area (CCTA minus IVUS). As expected, larger differences in the area result in larger deviation in the $\overline{\text{AWSS}}$. In turn, deviations in the $\overline{\text{FFR}}$ depend not only of local difference in lumen area, but also on the cumulative pressure drop caused by discrepancies in the lumen area at proximal locations. For instance, discrepancies in the second third of the vessels are caused by lumen area differences at the first third of the vessel.

The analysis is now focused on three specific vessels (12_{LAD}, 24_{LAD} and 25_{LAD}), which were chosen to discuss typical differences observed between CCTA and IVUS models. The behavior of Γ_s-averaged quantities and the 3D spatial distribution of AWSS and FFR are shown, respectively, in Figures 10.10, 10.11 and 10.12.

For vessel 12_{LAD}, the lumen area obtained from both geometric models is affected by a focal constriction at mid point of the vessel, more pronounced in the CCTA model. Also, the IVUS model features much more branches. Regarding Γ_s-averaged quantities, and as a consequence of the focal constriction, the velocity increases and then the pressure drops. Therefore, $\overline{\text{AWSS}}$ features a peak at that location, with an overall bias of 50% (larger in

	CCTA	**IVUS**	ρ	**Rel. Bias**	**Rel. LA**
$\overline{\text{FFR}}$					
Proximal	0.97±0.03	0.98±0.02	0.69	-0.01±0.03	[-0.07, 0.05]
Mid	0.92±0.11	0.96±0.03	0.51	-0.04±0.11	[-0.27, 0.18]
Distal	0.89±0.16	0.96±0.03	0.39	-0.07±0.16	[-0.38, 0.24]
$\overline{\text{AWSS}}$ [dyn/cm^2]					
Proximal	81± 68	55±40	0.54	0.38±0.98	[-1.54, 2.29]
Mid	93±126	54±43	0.43	0.53±1.63	[-2.67, 3.73]
Distal	63± 66	37±24	0.17	0.51±1.33	[-2.01, 3.11]

Table 10.7: Statistical analysis of Γ_s-averaged quantities in the proximal, mid and distal thirds of geometric models. Mean ± standard deviation are shown for each model and for the relative bias. The bias (CCTA-IVUS) and the limits of agreements (mean±SD) for the Bland-Altman analysis were normalized by the average between CCTA and IVUS means. All statistical tests, including correlations were statistically significant (p-value $\ll 0.01$).
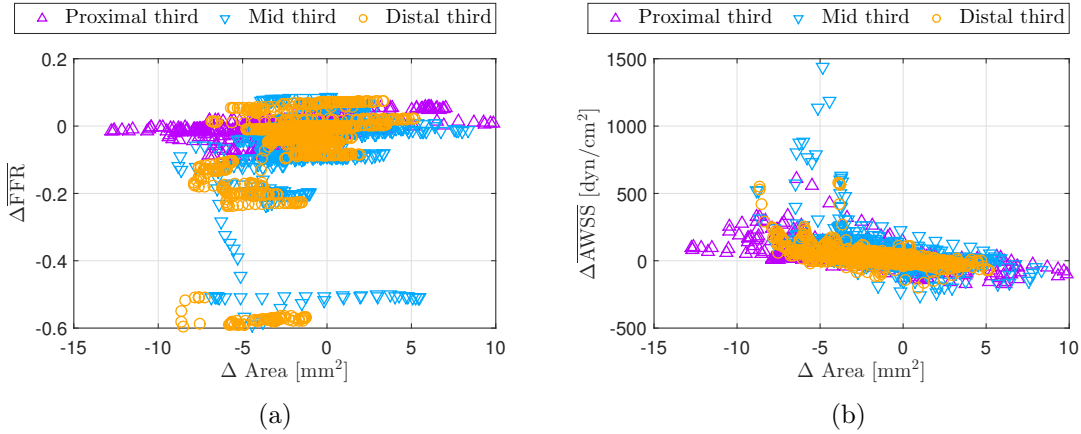
Figure 10.9: Scatter plots featuring differences between CCTA and IVUS models in (a) $\overline{\text{FFR}}$ and (b) $\overline{\text{AWSS}}$, against differences in area, in the entire sample. The position, i.e. proximal, mid and distal third, are identified.

CCTA), and $\overline{\text{FFR}}$ drops abruptly, resulting in a mean bias of 6% (smaller in CCTA). It is also observed that Q is progressively dimininshed in the IVUS model, while it drops markedly at the first branching point in the CCTA model.

The geometric models for vessel 24_{LAD} present good agreement for all Γ_s-averaged quantities. As in most of the vessels, the CCTA model features a highly oscillating lumen area A, which impacts the behavior of $\bar{v}$ and $\overline{\text{AWSS}}$. However, the behavior of these quantities is roughly the same from both models, rendering a low sensitivity to imaging modality. As well, $\bar{p}$ and $\overline{\text{FFR}}$ are not sensitive to imaging modality. Finally, the coronary anatomy for the vessel of interest is almost identical, except for a small branch appearing in the IVUS model at the distal-most region. As a consequence, the flow rate Q is quite similar for both models, and a relatively similar $\overline{\text{AWSS}}$ is therefore obtained, with a bias of 10% larger in the IVUS model, in contrast to the trend of the entire sample.

On the other hand, models for patient 25_{LAD} exemplify the typical case in which cross sectional area A is smaller in the CCTA model and greatly impacts the rest of the quantities. In fact, BA analysis yields that $\overline{\text{AWSS}}$ is 80% larger in the CCTA model. Also, pressure drop in the IVUS model is smaller than in the CCTA model, which is exclusively caused by the progressive vessel tapering seen in the CCTA geometry (note that the flow rate is similar in both models). Moreover, in the CCTA model $\overline{\text{FFR}}$ is 12% smaller, resulting from an overestimation of a calcified stenosis at the LAD-LCx branching

point, proximal to the region of interest (see 3D distribution at different scales for CCTA and IVUS). The behavior of $\overline{\mathrm{FFR}}$ along the centerline also shows a different pattern from both models, closely following the one of $\bar{p}$.
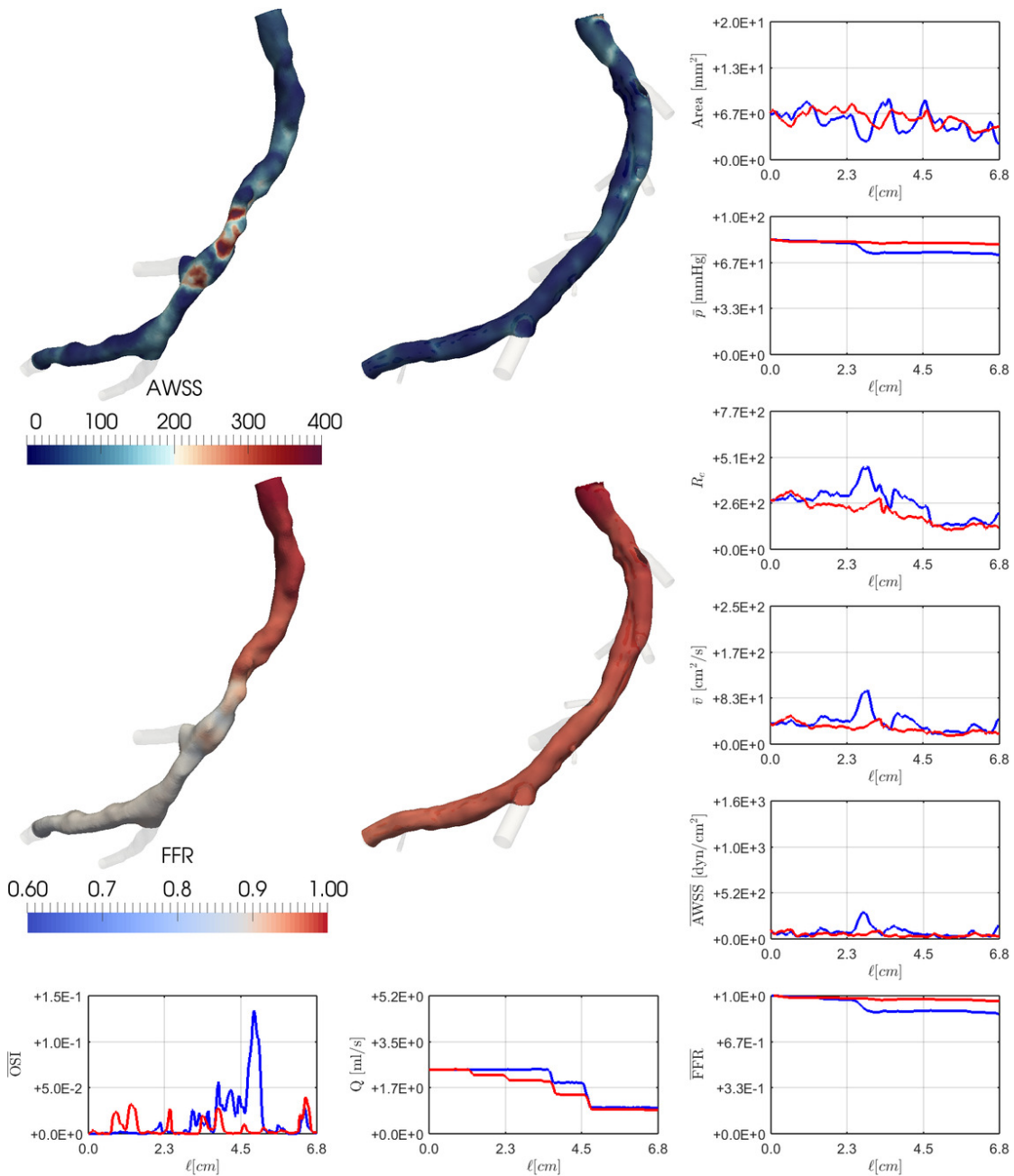
Figure 10.10: Distribution of the variables along the normalized centerline of 12_{LAD}. Blue represents CCTA and red stands for IVUS. Particularly, 3D distribution of FFR and AWSS through the associated arterial region are shown for both geometric models.

10.5.3 Discussion

Before going into the specific discussions, it is worthwhile to remark that the results presented in this section can be strongly dependent on the magnitude assigned to the total coronary blood flow in hyperemia. We have employed a value of CFR as reported in the literature [165]. However, the CFR can be up to 4, or even 6, in some patients [165].
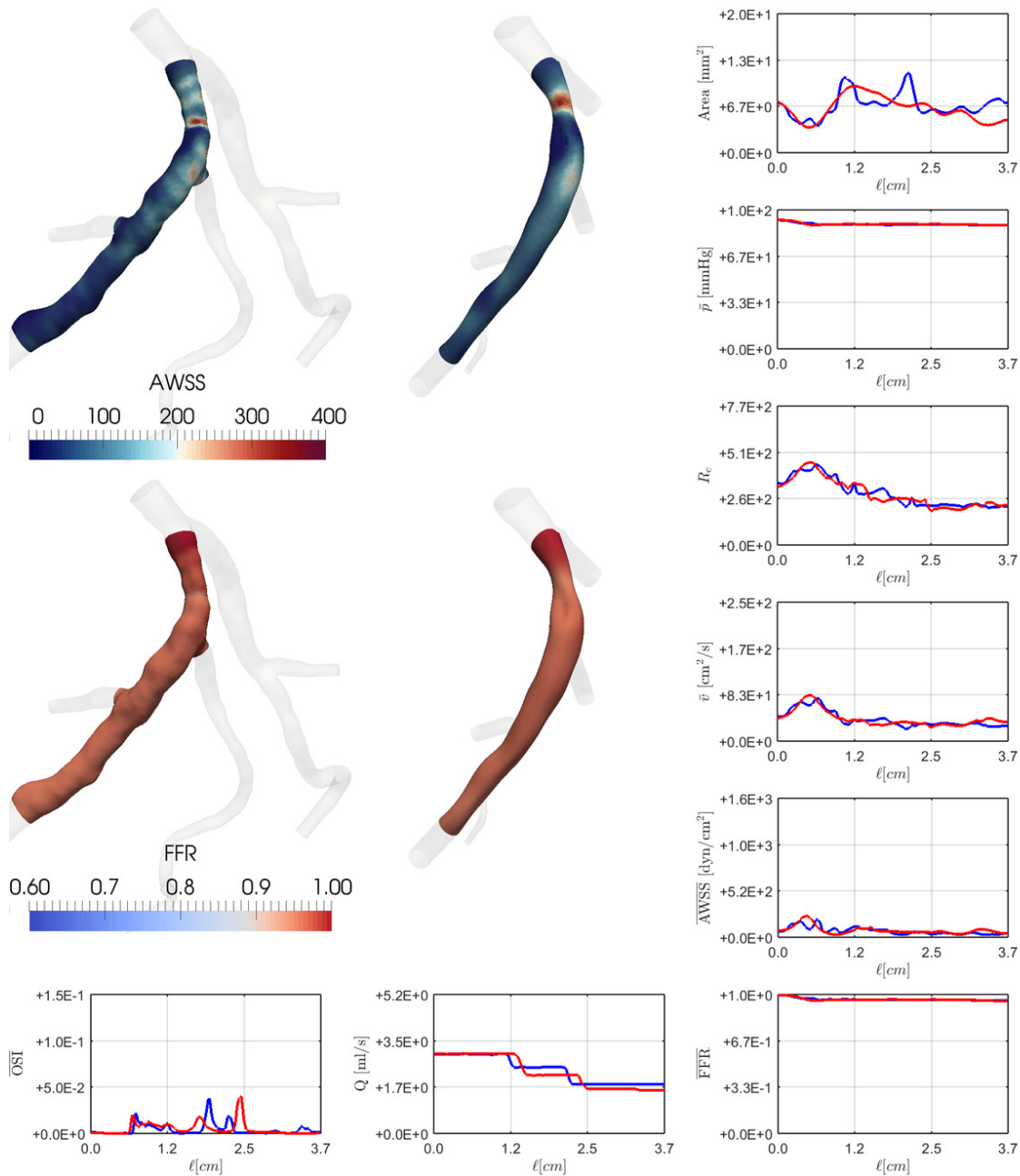
Figure 10.11: Distribution of the variables along the normalized centerline of 24_{LAD}. Blue represents CCTA and red stands for IVUS. Particularly, 3D distribution of FFR and AWSS through the associated arterial region are shown for both geometric models.

Discrepancies in the prediction of hemodynamics variables delivered by CCTA and IVUS models under such more extreme flow regimes are expected to be significantly larger.

10.5.3.1 Sample-wide analysis

Patient-specific hemodynamic simulations for coronary arteries have, for long, received much attention because of the potentialities to understand onset and progress of coronary disease as well as to develop simulation-based diagnostic tools to assess risk of myocardial ischemia. However, head-to-head comparisons of predictions made by models of the same arterial vessels obtained with different modalities was, until recently, completely overlooked. This work reported a quantitative analysis of several hemodynamic variables
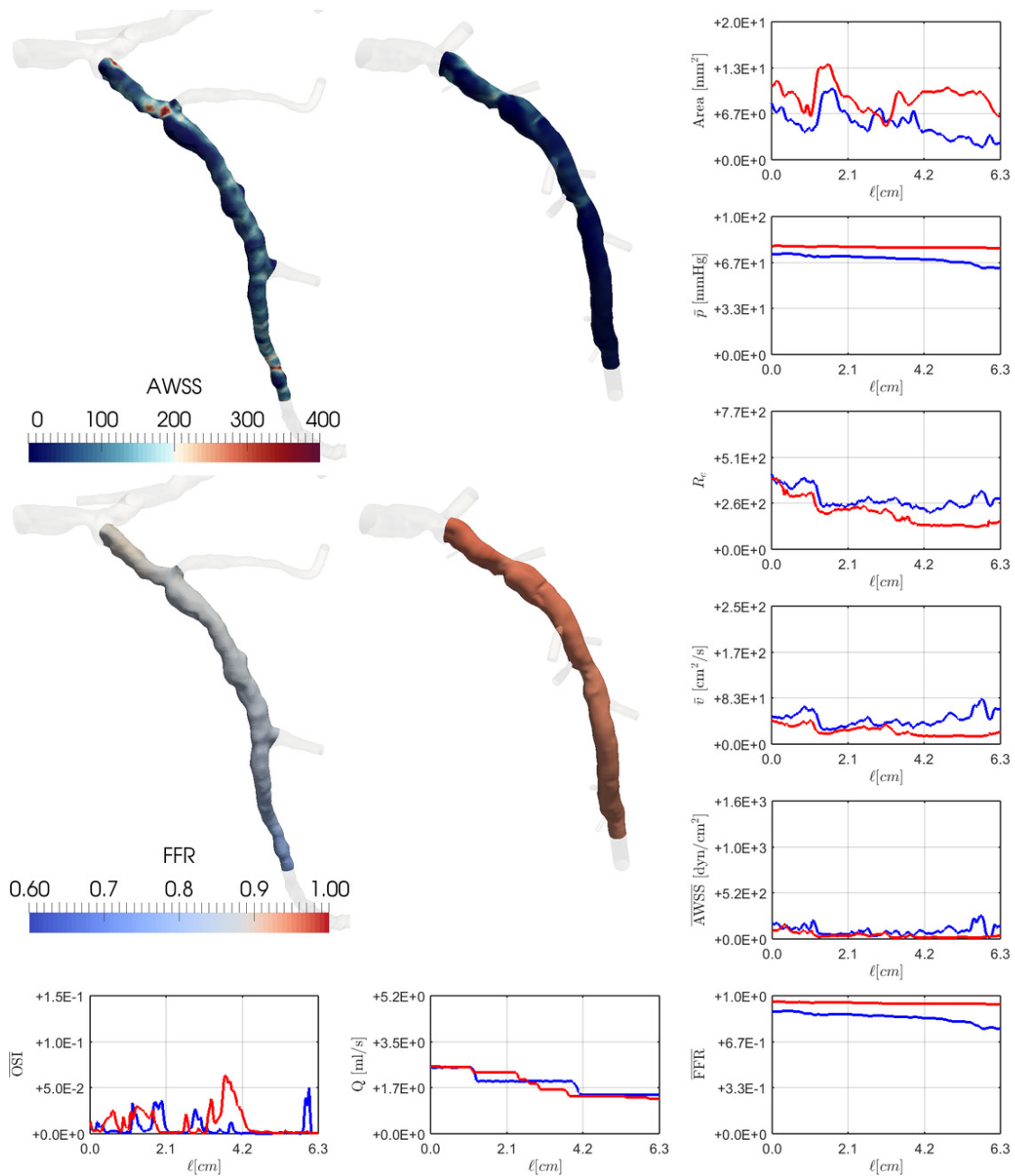
Figure 10.12: Distribution of the variables along the normalized centerline of 25_{LAD}. Blue represents CCTA and red stands for IVUS. Particularly, 3D distribution of FFR and AWSS through the associated arterial region are shown for both geometric models.

for 16 vessels (11 patients) facing CCTA and IVUS blood flow models under myocardial hyperemia.

Results reported in this section indicate that IVUS models are able to retrieve a more refined anatomical vasculature in terms of lumen area and branch count. However, IVUS clinical procedure focuses on one (or two) arterial vessels, and inclusion of branches in the geometric models is an arduous task. Hence, from a practical point of view, CCTA modality is the easiest alternative. Furthermore, due to the presence of the catheter in the AX images used to reconstruct the vessel in 3D, IVUS models smay undergo vessel straightening, see Section 9.1.2.1. Such distortion of arterial topology does not occur in CCTA models.

The definition of coronary anatomy is crucial to define boundary conditions. According to the criteria developed in this work, the number of outlet boundaries, as well as the relative size of branching vessels are key to establish blood flow distribution. It was found that, despite the fact that IVUS models feature more branches, and the size of side branches is different in IVUS and CCTA models (not quantified in this work), for the same inflow, the relative flow at the outlet of the main vessel is larger in IVUS models. This is explained by the phenomenon known as coronary steal, through which side branches become a preferred pathway for the blood when the main vessel presents a relatively larger resistance to flow. This is the particular case of some exaggeratedly tapered vessels in CCTA models.

Overall, a smaller lumen area consistently yields larger blood velocity, forcing the pressure to drop more markedly in CCTA than in IVUS models. Focusing on the pressure and FFR, the sensitivity to the imaging modality increases as we move distally. This can be explained as the result of three major factors: (i) low image resolution of CCTA compared to IVUS; (ii) different lumen definition in regions with calcified lesions, which are better captured by IVUS models (see Figure 10.13); and (iii) in CCTA, the natural tapering of vessels may be distorted due to attenuation of lumen pixel intensity in distal regions [74].

Following the same rationale, the smaller lumen area of the CCTA models results in larger $\overline{\mathrm{AWSS}}$, for roughly the same flow rate. Differently from the pressure and FFR, the bias and limits of agreement of the wall shear stress are extremely large, which indicate that wall shear stress estimation from CCTA is to be carefully regarded when correlating this to coronary disease, at least under hyperemic conditions. In turn, the oscillatory shear index featured small values in both imaging modalities, which is consistent with the fact that no retrograde flow is occurring along the cardiac cycle.
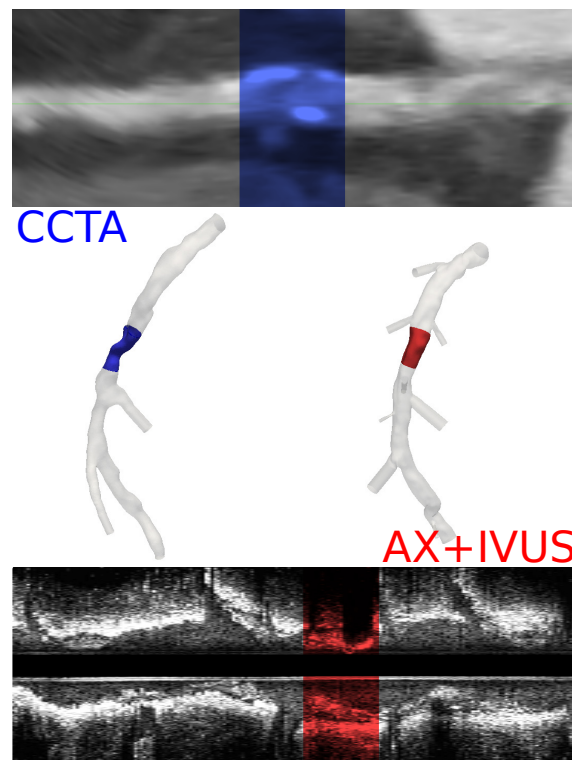
Figure 10.13: Comparison of rectified vessel lumen for calcified regions in model 12_{LAD}. Top: CCTA image, bottom: IVUS image, and corresponding models.

10.5.3.2 Specific vessel analysis

In addition, qualitative assessment of per vessel area, allows classification into three cases:

(i) focal constriction in the CCTA model, that is a localized underestimation of lumen area, which therefore causes focal deviations in the hemodynamic quantities (vessel 12_{LAD});

(ii) excellent agreement between both geometric models along the vessel, which results in consistent predictions from both models (patient 24_{LAD}); and

(iii) distributed (and also possibly focal) underestimation of lumen area, which provokes progressive (and possibly focal) alteration of all hemodynamic quantities (patient 25_{LAD}).

According to this classification, the entire sample presents: 3 vessels for case (i), 6 for case (ii) and 7 for case (iii). This analysis helps us to discern those cases that, a priori, could result in distorted predictions. For example, characterization of lesion components such as fatty component, calcifications and fibrotic components turns out to be crucial for geometry improvement in CCTA models (see approaches in [124, 283]).

In any case, the ultimate challenge is whether to identify that the lumen area in CCTA models is in fact being underestimated, and in such cases how to correct such situation. The present quantitative analysis indicates that this may be a sensitive issue that must be addressed in CCTA models.

10.5.3.3 Validity and limitations

In the present study the consistency between CCTA and IVUS boundary conditions was achieved using a hierarchical strategy which implied setting boundary conditions for the CCTA models and just then adapting these to the IVUS models. Nevertheless, working only with IVUS implies that one has to somehow define these boundary conditions, which would result in different boundary conditions than those derived here. This is a major concern in the community and still remains as an open and foundational problem. In Chapter 9, Section 9.3, flow distribution criteria for IVUS models were proposed. Such criteria do not make use of the complete coronary tree to estimate flow per-outlet. See Section 10.7, for preliminary results using such criteria.

In turn, segmentation procedures usually involve propagation of uncertainties, and recent efforts started to address this problem [293]. Results reported here are consistent with literature specialized in comparing CCTA and IVUS imaging procedures [105].

An additional limitation of the present study is the relatively small number of vessels considered. Nevertheless, collecting the amount of data for each patient is an extremely complex task, and the results reported here have helped to elucidate some of the main drawbacks when trying to simulate coronary blood flow under hyperemic conditions.

10.6 Comparison of 3D and 1D models

As presented in Chapter 8, Section 8.4, in the context of computational calculation of FFR, the use of 3D models has been the most natural approach to try to estimate pressure losses in coronary vessels using image modalities such as CCTA [328, 368], AX [236, 336, 256], OCT [137] and some pilot studies using IVUS [313]. Nonetheless, there is an increasing interest in the use of simplified mathematical models, either based on the 1D Navier-Stokes equations in compliant vessels (in CCTA [76, 184] and AX [334]) or based on compartmental (0D) representations using CCTA data [368]. Since these models neglect fundamental aspects of the 3D physics regarding flow across geometric singularities, specific models to account for focal pressure losses, i.e. lesions and junctions, are usually employed [362, 363, 152, 242], as presented in Chapter 9, Section 9.2.2.

Validation of 1D models against 3D simulations has been reported in other arterial districts such as the cerebral vessels, aorta and major vessels [16, 131, 166, 359]. To the best of our knowledge, comparison of 1D and 3D simulations in a large sample of patient specific coronary arterial domains has not been reported in the past. Such study is key for the interpretation of computational evaluation of FFR using 1D models.

The goal of this section is to demonstrate, for the first time, that 1D models are capable of predicting FFR (denoted FFR_{1D}) with the same degree of accuracy as 3D models (denoted FFR_{3D}). Importantly, and because of our interest in the estimation of FFR, the focus of this section is exclusively given to the comparison of FFR in the vessel domain. The sensitivity of the FFR_{1D} to the modeling of arterial stenoses and arterial bifurcations is assessed in detail.

10.6.1 Material and methods

The study sample consisted of all patients from Section 10.1, a total of 11 CCTA models and 33 IVUS models.

Image and mesh processing for the generation of 3D and 1D models were performed as detailed in Chapter 9, Section 9.1. Fully 3D fluid dynamic simulations were performed following the methodology explained in Chapter 9, Section 9.2.1. Transient 3D simulations, spanning three patient-specific cardiac cycles were performed. In turn, 1D simulations were performed following the methodology explained in Chapter 9, Section 9.2.2. Transient 1D simulations, spanning six patient-specific cardiac cycles were performed. For each patient, a total of 6 simulations were performed using different approaches to model junctions and stenoses, namely:

- Junctions are treated with a standard model in which continuity of total pressure is enforced.

  - **SJ:fwd**: No stenosis model is used.
  - **SJ:S:fwd**: The Young model [363] is used at each stenosis. Default parameters are used at each stenosis model.
  - **SJ:S:fwd:kv**: The Young model [363] is used at each stenosis. The K_v parameter, for each stenosis model, is estimated using the Kalman filter, such that pressure drop across the stenosis matches the one given buy the 3D simulation at each time step.

- Analogously, three setups are defined when the Mynard model [242] for junctions is used, in which pressure losses at the junctions are considered.

  - **MJ:fwd**
  - **MJ:S:fwd**

– **MJ:S:fwd:kv**

Regarding boundary conditions, the same pressure was imposed at the inlet of both models, and the resulting flow rate curve retrieved from 3D simulations was imposed in the corresponding outlets of the 1D models. Patient-specific hemodynamics parameters were defined following the methodology detailed in Chapter 9, Section 9.3. For the study sample, the estimated resting CBF is 251 ± 40 ml/min, which agrees with physiological ranges (270 ± 82 ml/min) reported in [286].

Regarding flow distributions, see Chapter 9, Section 9.3, the resistance parameter in the CCTA models were estimated using the DMD approach, and for the IVUS models the PDC was employed. All the 11 CCTA models consisted of left coronary arteries, while the IVUS models are divided in 29 left and 4 right coronaries. From the literature [286], average resting flow at the inlet of the LM and RCA are 156 ± 40 ml/min and 113 ± 49 ml/min, respectively. For the present sample, the average resting flow at the inlet of the LM coronary resulted in 142 ± 38 ml/min and 154 ± 27 ml/min for CCTA and IVUS, and for the RCA in 100 ± 19 ml/min for IVUS, which agrees with reported values.

All simulations were performed under hyperemic conditions with the same CFR= 2.6, which is a mean value for nonischemic human coronary arteries [165]. Then, the 11 CCTA simulations are the same as the ones used in Section 10.5.

Post-processing and data analysis of the simulations results involved in the comparison, was performed as following. Direct comparison is performed over the main coronary arteries, i.e. LAD, LCX and RCA, since they are of most clinical relevance for the FFR index. For a given patient, each of these arteries (when present) is sampled at four points, proximal ($L \times 0.25$), middle ($L \times 0.5$), distal ($L \times 0.75$) and end (L), here L is the length of the artery The value of FFR is linearly interpolated in points associated to stenoses, for simulations using the Young model (recall that in such case the Young model replaces the 1D portion of the vessel with the stenosis). The solution of 3D simulations is lumped to the centerline points as follows: (i) cross-sectional slices of the tetrahedral mesh are computed at each centerline point; (ii) pressure and FFR are averaged in such slices; (iii) flow is computed using the velocity field interpolated in the slice and the slice area. This study focuses on comparing the resulting FFR field in the centerlines.

Point-wise comparison between FFR_{3D} and FFR_{1D} was performed. Statistical analysis to show agreement between FFR values comprised: Spearman's correlation coefficient (ρ); slope (a) and intercept (b) of linear regression equation; and paired nonparametric Mann-Whitney U-Test (two tailed) and Bland-Altman (BA) analysis of differences (mean m_{BA} with standard deviation SD_{BA}).

The diagnostic capability of the 1D model, taking the 3D result as gold standard, was assessed using a cut-off value of FFR≥ 0.8. The location for the comparison, Ω_{FFR} was determined as explained in Chapter 9, Section 9.4. Invasive measurements of FFR were available for each vessel of the set, see Section 10.7 for results.

10.6.2 Results

Regarding the construction of 1D models, the automatic stenosis detection method consistently detected more lesions (percentage area reduction $\geq 40\%$) in the 11 CCTA models (73 lesions) than in the 33 IVUS models (8 lesions). Such difference can be explained, in part by: (i) CCTA models comprise larger vessels, while IVUS has shorter branches; (ii) as shown in Section 10.5, CCTA models tendto underestimate lumen cross-sectional area.

Models for 3D simulations of CCTA and IVUS contained, respectively, 2.05 ± 1.18 M and 1.58 ± 0.51 M degrees of freedom. In turn, 1D models contained 348 ± 189 and 162 ± 40 degrees of freedom for CCTA and IVUS respectively. The average wall clock run-time (RT) of all the 44 3D simulations was 79.9 ± 65.3 hs, using 137 ± 59 computational tasks.

Regarding the IVUS 1D simulations, 7 geometries where excluded from the sample due to problems in the 1D solution. In such cases, the intrinsic limitations of the setting of boundary conditions, i.e. a prescribed flow curve generated from the 3D simulations output, rendered numerical instabilities in the 1D simulations. Therefore, a total of 26 IVUS models were used in the forthcoming analysis. As for the CCTA 1D simulations, no problems were encountered with the exception of one simulation resulting in negative pressure due to an excessive pressure drop on the Young model with default parameters (**SJ:S:fwd** and **MJ:S:fwd**). Both simulations were excluded in the forthcoming analysis, since the results are not physiologically valid. For the final set of 134 1D simulations, average wall clock run-time (RT) was 0.6 ± 0.6 hs, using 12 computational tasks. Note that to perform the same amount of cardiac cycles than the 3D simulations, the RT of 1D simulations was 0.3 ± 0.3. Noteworthy, for the 26 IVUS models, only 4 were found to present stenosis as detected by the automatic method, and therefore a total of 68 IVUS 1D simulations plus the 66 CCTA 1D simulations were performed taking into account all the scenarios.

10.6.2.1 Comparison along major arteries

Table 10.8 presents the statistical results for the comparison between FFR_{3D} and each simulation setup for the FFR_{1D}. Values of FFR were taken at four location the LAD, LCx or RCA arteries whenever present, which produce similar sample size fpr CCTA and IVUS models. Figure 10.14 plots the same information in the form of scatter and Bland-Altman plots. Regarding the CCTA simulations, it can be observed that:

 i large correlation coefficients ($0.87 < \rho < 0.94$) result in all six cases, with slightly better correlation when the stenosis parameter K_v is estimated;

 ii the linear regression consistently improves with the use of the Young model and with the estimation of K_v;

 iii the analysis of difference shows that the m_{BA} is smaller when the Young model is used directly ($<\cdot>$:**S:fwd**), the estimation of K_v doubles the bias and slightly reduces the dispersion, which implies that modeling errors are being compensated. Both mean and SD of the difference are larger when no stenosis model is used ($<\cdot>$:**fwd**);

 iv in all cases, m_{BA} indicates an error below the 2%;

 v notably, simulation **MJ:S:fwd:kv**, although presented good agreement for all statistical indexes, was the only case in which the null hypothesis was rejected (95% confidence interval) using the U-Test.

Regarding IVUS simulations, note that statistics for the cases in which the Young model was used ($<\cdot>$:**S:**$<\cdot>$) are presented for the sake of completeness, but are not discussed due to the small number of simulations (4) in which stenosis model were employed. Compared to CCTA, the IVUS simulations featured:

 i similar correlation coefficients, $\rho \sim 0.87$;

 ii better linear approximation, $FFR_{1D} = 0.85FFR_{3D} + 0.14$ compared to $FFR_{1D} = 0.65FFR_{3D} + 0.32$;

 iii approximately 5 times smaller biases, m_{BA}, and three times smaller dispersion, SD_{BA};

 iv furthermore, the U-Test rejected the null hypothesis of zero mean at 95% confident interval in all cases.

Overall, in our data sample, the use of the Mynard model for junctions resulted in: (a) slightly better linear approximation (only for CCTA) and Spearmans's correlation coefficients; (b) slightly smaller dispersion SD_{BA} values, with better bias, m_{BA}, only when no stenosis model is used. In turn, the use of the Young model for stenosis resulted in: (d) considerable improvements in the linear approximations; (e) the Spearmans's correlation coefficient is improved only if the K_v parameter is estimated; (f) smaller mean difference (m_{BA}) and dispersion (SD_{BA}) values.

	1D Model	n	Linear approx. a	b	Corr. ρ^*	Difference $m_{BA} \pm SD_{BA}$
CCTA	**MJ:fwd**	92	0.661	0.311	0.939	$0.010 \pm 0.063^{\dagger}$
	MJ:S:fwd	84	0.920	0.068	0.928	$-0.004 \pm 0.037^{\dagger}$
	MJ:S:fwd:kv	92	1.002	-0.010	0.941	-0.008 ± 0.033
	SJ:fwd	92	0.645	0.331	0.899	$0.016 \pm 0.065^{\dagger}$
	SJ:S:fwd	84	0.907	0.085	0.878	$0.001 \pm 0.042^{\dagger}$
	SJ:S:fwd:kv	92	0.988	0.009	0.901	$-0.002 \pm 0.038^{\dagger}$
IVUS	**MJ:fwd**	104	0.850	0.145	0.886	$0.002 \pm 0.019^{\dagger}$
	MJ:S:fwd	16	0.820	0.179	0.941	$0.011 \pm 0.020^{\dagger}$
	MJ:S:fwd:kv	16	1.110	-0.103	0.973	$0.000 \pm 0.011^{\dagger}$
	SJ:fwd	104	0.854	0.141	0.863	$0.003 \pm 0.020^{\dagger}$
	SJ:S:fwd	16	0.883	0.116	0.956	$0.007 \pm 0.020^{\dagger}$
	SJ:S:fwd:kv	104	1.177	-0.169	0.994	$-0.004 \pm 0.015^{\dagger}$

Table 10.8: Comparison between FFR_{3D} and each simulation setup for the FFR_{1D}. Values of FFR were taken at four location along arterial segments belonging to the LAD, LCx or RCA arteries. The linear approximation coefficients represents the equation $FFR_{1D} = aFFR_{3D} + b$. Spearman's correlation coefficient ρ was statistically significant ($p < 0.05$) in all cases. Marker † in the Bland-Altman analysis of difference ($FFR_{1D} - FFR_{3D}$) indicates $p > 0.05$, i.e. the U-Test can not detect significant differences between the values being compared.

10.6.2.2 Comparison at clinically relevant locations

Analogous to Table 10.8, in Table 10.9 the comparisons are presented for values of FFR taken at the so called Ω_{FFR}, the location where clinical measurements were performed. Figure 10.15 plots the same information in the form of scatter and Bland-Altman plots. Additionally, Table 10.9, also presents the diagnostic capabilities of FFR_{1D} taking as gold standard FFR_{3D}. Note that the number of comparison points is significantly reduced in all cases. Regarding CCTA simulations, remarks follows:

i the linear approximation behaves similar than in the case of more sample points (Table 10.8), improving when the use of Young model and the estimation of K_v. Although, the values of a and b are not as good as in Table 10.8.

ii correlation coefficients are also large, $0.89 < \rho < 0.92$;

iii contrary to the m_{BA} from Table 10.8, the bias is larger with the use of the Young model, although the dispersion is reduced;

iv for a prevalence ($FFR_{3D} < 0.8$) around 25%, the predictive capabilities of the FFR_{1D} are remarkable, with large values of area under the receiver operator curve (AUC> 93%), accuracy (Acc> 81%), specificity (Spe> 91%) and negative predictive value (PPV> 84%);

v in turn, the ability of correctly identifying positive cases (true positives $FFR_{1D} < 0.8$) features less impressive results, although the sensitivity (Sen) and positive predictive
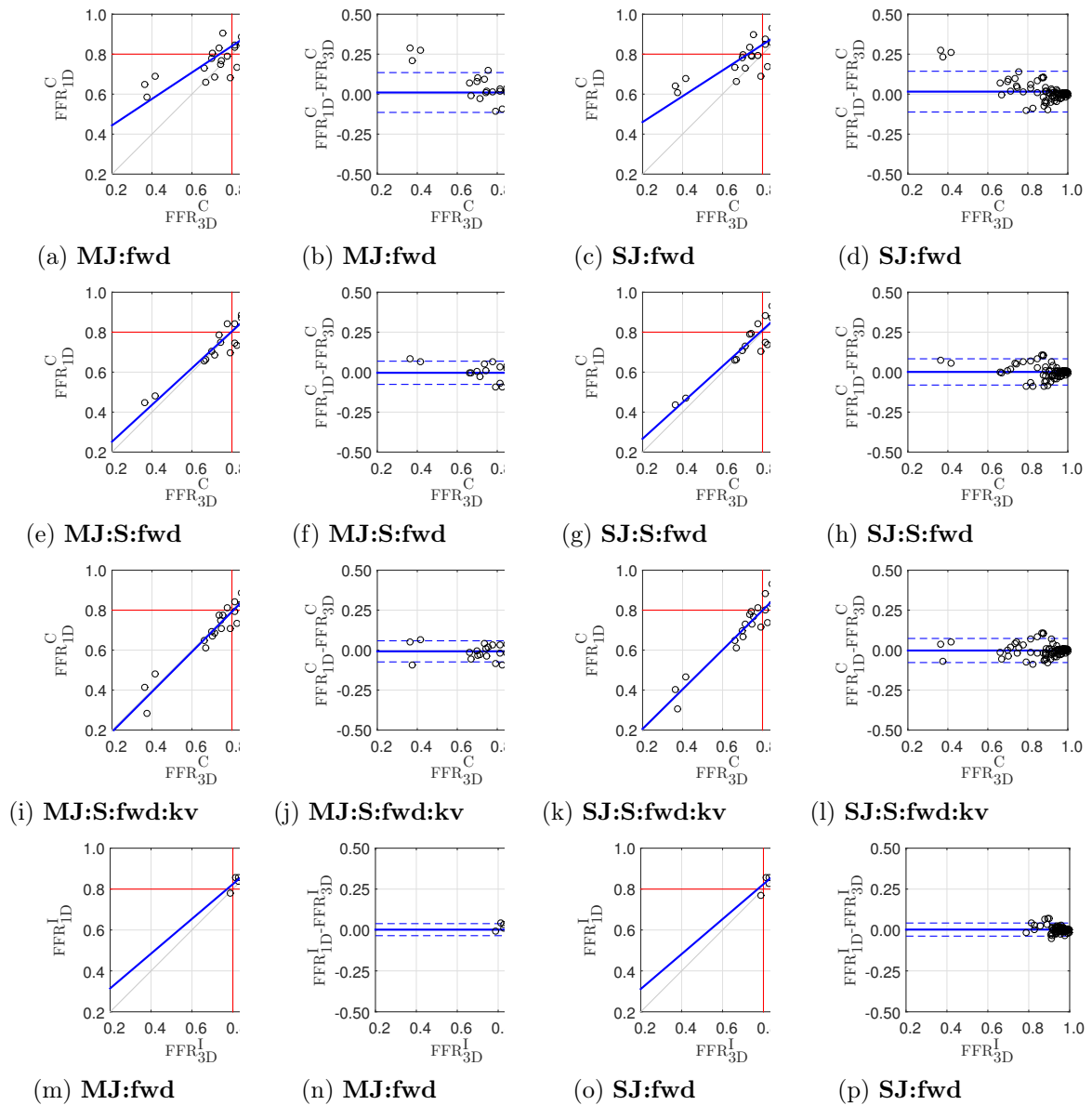
Figure 10.14: Scatter and Bland-Altman plots featuring comparison between FFR_{3D} and FFR_{1D} simulations, superscripts C and I stands for CCTA and IVUS models. Values of FFR were taken at four location along arterial segments belonging to the LAD, LCx or RCA arteries. Rows one-to-three show results for CCTA models for $<\cdot>$:**fwd**, $<\cdot>$:**S:fwd** and $<\cdot>$:**S:fwd:kv** respectively. Row four, presents results for the IVUS model when no stenosis model is used, i.e. $<\cdot>$:**fwd**. Columns one and two feature results when the Mynard model for junctions is used. In turn, columns three and four present results when the standard junction model is used.

value (PPV) improve with the use of the Young model, and were higher for the Mynard junction model.

Regarding the IVUS simulations, and again focusing on **MJ:fwd** and **SJ:fwd**, results indicated:

i small underestimation of FFR value, with good agreement in terms of linear approximation, ρ, m_{BA} and SD_{BA};

ii predictive capabilities are biased due to the low prevalence (Prev= 4%, only one

simulation presented $FFR_{3D} < 0.8$), nonetheless, only using the standard junction model resulting in a perfect classification;

Overall, regarding the evaluation of FFR at clinically relevant locations, the use of the Mynard model for junctions resulted in: (a) slightly better linear approximation (only for CCTA) and Spearmans's correlation coefficients; (b) larger mean difference m_{BA}, at similar dispersion SD_{BA} values; (c) better predictive capabilities in terms of the classification indexes. In turn, the use of the Young model for stenosis resulted in: (d) considerable improvements in the linear approximations; (e) the Spearmans's correlation coefficient is improved only if the K_v parameter is estimated; (f) larger mean difference m_{BA}, with smaller dispersion SD_{BA} values, such tendency accentuates with the estimation of K_v; (g) better predictive capabilities in terms of the classification indexes.

	1D Model	n	Linear approx. a	Linear approx. b	Corr. ρ	Difference $m_{\mathrm{BA}} \pm \mathrm{SD}_{\mathrm{BA}}$	Prev	AUC	Acc	Sen	Spe	PPV	NPV
CCTA	MJ:fwd	16	0.479	0.452	0.892*	$0.007\pm0.093^{\dagger}$	0.250	0.938	0.875	0.750	0.917	0.750	0.917
	MJ:S:fwd	14	0.813	0.143	0.914*	$-0.018\pm0.052^{\dagger}$	0.214	0.970	0.929	1.000	0.909	0.750	1.000
	MJ:S:fwd:kv	16	0.863	0.093	0.922*	-0.024 ± 0.044	0.250	0.979	0.938	1.000	0.917	0.800	1.000
	SJ:fwd	16	0.476	0.460	0.907*	$0.011\pm0.092^{\dagger}$	0.250	0.958	0.813	0.500	0.917	0.667	0.846
	SJ:S:fwd	14	0.805	0.155	0.893*	$-0.013\pm0.054^{\dagger}$	0.214	0.970	0.857	0.667	0.909	0.667	0.909
	SJ:S:fwd:kv	16	0.861	0.100	0.912*	$-0.019\pm0.046^{\dagger}$	0.250	0.979	0.875	0.750	0.917	0.750	0.917
IVUS	MJ:fwd	26	0.811	0.174	0.869*	$-0.003\pm0.022^{\dagger}$	0.038	1.000	0.962	0.000	1.000	-	0.962
	MJ:S:fwd	4	0.832	0.158	0.800	$0.006\pm0.022^{\dagger}$	0.250	1.000	0.750	0.000	1.000	-	0.750
	MJ:S:fwd:kv	4	1.116	-0.114	1.000*	$-0.010\pm0.010^{\dagger}$	0.250	1.000	1.000	1.000	1.000	1.000	1.000
	SJ:fwd	26	0.833	0.154	0.859*	$-0.002\pm0.023^{\dagger}$	0.038	1.000	1.000	1.000	1.000	1.000	1.000
	SJ:S:fwd	4	0.894	0.095	0.800	$0.000\pm0.025^{\dagger}$	0.250	1.000	0.750	0.000	1.000	-	0.750
	SJ:S:fwd:kv	4	1.182	-0.180	1.000*	$-0.016\pm0.016^{\dagger}$	0.250	1.000	1.000	1.000	1.000	1.000	1.000

Table 10.9: Comparison between FFR_{3D} and each simulation setup for the FFR_{1D}. Values of FFR were taken at clinically relevant location for diagnosis, Ω_{FFR}. The linear approximation coefficients are for the equation $\mathrm{FFR}_{1D} = a\mathrm{FFR}_{3D}+b$. Marker * indicates that the Spearman's correlation coefficient (ρ) was statistically significant ($p < 0.05$). Marker † in the Bland-Altman analysis of difference ($\mathrm{FFR}_{1D} - \mathrm{FFR}_{3D}$) indicates $p > 0.05$. Predicted values are computed using FFR_{3D} as gold standard and a cut-off value of $\mathrm{FFR} \geq 0.8$. The prevalence of functional stenoses according to FFR_{3D} are also displayed.
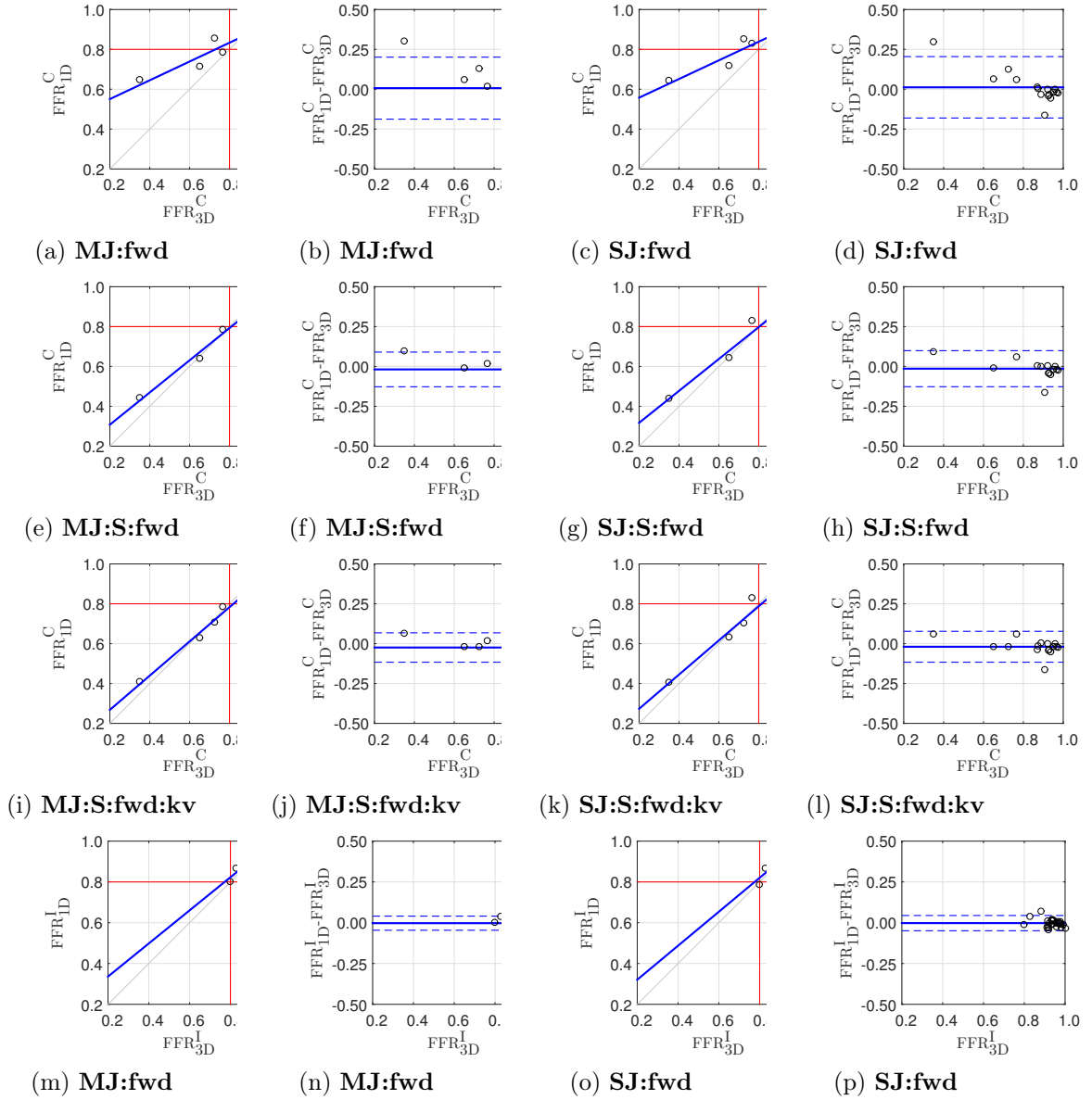
Figure 10.15: Scatter and Bland-Altman plots featuring comparison between FFR_{3D} and FFR_{1D} simulations, superscripts C and I stands for CCTA and IVUS models. Values of FFR were taken at clinically relevant location for diagnosis, Ω_{FFR}. Rows one-to-three show results for CCTA models for $<\cdot>$:**fwd**, $<\cdot>$:**S:fwd** and $<\cdot>$:**S:fwd:kv** respectively. Row four, presents results for the IVUS model when no stenosis model is used, i.e. $<\cdot>$:**fwd**. Columns one and two feature results when the Mynard model for junctions is used. In turn, columns three and four present results when the standard junction model is used.

10.6.2.3 Stenoses analysis

The analysis is now focused on the stenotic regions. Table 10.10 presents the mean±SD for several stenosis related quantities, i.e. degree and length of stenosis, a multiplicative factor for the K_v parameter estimated by the Kalman filter, the pressure drop (ΔP) across the stenosis for each simulation type and the Reynolds number averaged between the inlet and outlet of the stenosis region.

As in previous tables, statistical results for IVUS are presented for the sake of completeness, but since only 4 stenoses were detected results should be carefully interpreted.

Then, for the CCTA models, the following remarks can be made:

i notably, the comparison between ΔP^{3D} and ΔP^{1D} for each 1D simulation shows small discrepancies.

ii moreover, no statistically significant difference was found in such comparisons, i.e. $p > 0.05$ in the U-Tests.

iii note that $\Delta P^{3D} = 4.66 \pm 5.9$ mmHg is relatively low, which is related to the low prevalence of functional estenoses FFR < 0.8 and to the relative low values for the Reynolds number Re $= 199 \pm 94$.

iv furthermore, it is important to mention that approximately 73 stenoses were automatically detected in the 11 CCTA models, several of which are in branches with no clinical relevance and low blood flow rates.

Overall, note that pressure drops and estimation of K_v are insensitive to the use of the Mynard or standard model for the junctions. As expected, the use of the Young model improves the ΔP estimation and calibration of K_v using the Kalman filter results in an excellent agreement between pressure drops. Remarkably, the correction factor $K_v^f = 0.97 \pm 0.57$, indicates that default values of the K_v parameter results in accurate results, in mean, for most of automatically detected stenoses.

Regarding the IVUS models, for the 4 models containing stenoses, note that pressure drops are smaller, the Re is larger and significant corrections K_v^f are needed to match pressure drops. Also the prescence of more branches in the main artery indicates that the use of the Mynard model favorably impacts the results.

	Junc. Model	K_v^f	Steno. Degree	L [cm]	Re	ΔP^{3D}	Pressure drop † [mmHg] $<\cdot>$:fwd	$<\cdot>$:S:fwd	$<\cdot>$:S:fwd:kv
CCTA	MJ	0.97±0.56	0.56±0.15	0.52±0.31	199± 94	4.66±5.90	4.32±3.62	4.42±5.19	4.66±5.86
	SJ	0.97±0.57					4.32±3.62	4.42±5.19	4.66±5.88
IVUS	MJ	1.85±1.68	0.64±0.13	0.41±0.35	287±166	2.52±2.43	1.79±1.92	1.39±0.79	2.52±2.36
	SJ	1.86±1.69					1.79±1.92	1.39±0.79	2.58±2.38

Table 10.10: Comparison of the pressure drop, in [mmHg], across all stenoses between all 1D simulations and the 3D simulations. Marker † indicates that all 1D simulations render $p > 0.05$ in the U-Test, meaning that no significant differences between the pressure drops of each 1D simulation and the 3D outcome was found. The Reynolds number for each stenosis was defined as the average between the inlet and outlet of the stenotic region of length L, in [cm] defined by the automatic algorithm explained in Chapter 9, Section 9.1.3. The stenosis degree represents the ratio $\frac{A_s}{A}$ of the Young model, where A is the area at the stenosis inlet and A_s is the minimum area of stenosis Finally, the value K_v^f represents a factor estimated by the Kalman filter, for which the actual K_v parameter is multiplied.

10.6.3 Discussions

The results presented in this section indicate that 1D simulations can reproduce FFR$_{CE}$ values of 3D simulations with bias smaller than -0.024 ± 0.044. The overall agreement between the different 1D model configurations and the 3D simulations is remarkable, as well as the predictive capabilities in terms of diagnosis, for FFR < 0.8. It was found that, in general, using the Young model for stenosis in combination with the Mynard model for junctions leads to better linear approximation, correlations and predictive values, with

smaller dispersions (SD_{BA}), in detriment of the bias (m_{BA}). Such tendency accentuates when the Kalman filter is used to estimate the stenosis parameter K_v.

Note that the methodology employed for the imposition of the boundary conditions in the 1D models ensures a fair comparison in terms of flow rate per arterial segment. The results presented here must be interpreted in such context, i.e. for prescribed inlet pressure and outflows, 1D simulations are equivalent to 3D simulations in the calculation of FFR_{CE}.

Since the use of flow rate BC may produce problems in some networks, a more robust methodology for the computation of FFR using 1D models could use a different type of BC. For example, the method employed in 3D simulations that enforces a total inflow with resistive terminals, could be implemented in the 1D model directly, or by means of the Kalman filter. In such scenario, the flow distribution along the outlets may differ from the one predicted by the resistance parameters, as in the 3D simulations, which would certainly impact in the prediction of FFR_{1D} compared to FFR_{3D}. Moreover, such methodology could be useful in real-life scenarios, i.e. estimating invasive FFR in a blinded fashion using 1D models.

Note that the small discrepancies between simulations performed with the standard and Mynard model for junctions may be explained for the fact that such junction model was originally developed for planar branches and tested for $350 < \text{Re} < 2400$ [242]. Regarding the Young model, although the calibration of K_v results in an overall improvement in comparison statistics, the use of default values are useful to predict FFR accurately.

10.7   Comparison to invasive FFR

The goal of this section is to present the diagnostic capabilities of the FFR_{CE}, when compared to the invasive measurements of FFR. A total of 33 invasive measurements of FFR are available, one for each IVUS model in Table 10.1. For a subset of 16 invasive measurements, CCTA models are available. As explained in Chapter 9, Section 9.4, the location of the pressure wire in the arterial models is manually determined by an expert from the associated angiographic image. A region Ω_{FFR} of approximately 2 mm of length is used to average the FFR field which is used as FFR_{CE}. Due to poor image quality, only 1 (of 11) CCTA model did not reach the measurement domain Ω_{FFR}. In turn, 15 IVUS models did not reach the Ω_{FFR}, because IVUS pullbacks started more proximally than the location of the pressure wire at the moment of the FFR test, for all other IVUS models, Ω_{FFR} coincides with the distal part of the computational model. Despite this mismatch between the location of invasive measurement and Ω_{FFR} in some models, the region comprised between Ω_{FFR} and the actual location of the pressure sensor was free of elements that could produce modification in flow or pressure, i.e. lesions or large branches. Therefore they were considered safe to be used. In all cases, the cut-off value of $FFR < 0.8$ and $FFR_{CE} < 0.8$ were employed to detect functional lesions, or positive measurements.

Simulations performed for the study presented in Sections 10.5 and 10.6, as well as tests for different flow distribution strategies, see Chapter 9, Section 9.3, will be compared to invasive measurements of FFR. Therefore, for the sake of clarity, a set of study cases are defined, see Table 10.11, and agreement to invasive FFR is performed for each set.

Study case ID	Patient sample	Image modality	Flow dis.	CFR	Description
SC1	[6,25]	CCTA	DMD	2.6	Associated to the tests presented in Section 10.5, 3D models and transient simulations.
SC2	[6,25]	IVUS	CSRD	2.6	Associated to the tests presented in Section 10.5, 3D models and transient simulations.
SC3	[6,39]	IVUS	PDC	2.6	Associated to the tests presented in Section 10.6, 3D models and transient simulations.
SC4	[6,25]	CCTA	DMD	2.6	Associated to the tests presented in Section 10.6, **MJ:fwd** simulations.
SC5	[6,25]-{11}	CCTA	DMD	2.6	Associated to the tests presented in Section 10.6, **MJ:S:fwd** simulations.
SC6	[6,25]	CCTA	DMD	2.6	Associated to the tests presented in Section 10.6, **MJ:S:fwd:kv** simulations.
SC7	[6,25]	CCTA	DMD	2.6	Associated to the tests presented in Section 10.6, **SJ:fwd** simulations.
SC8	[6,25]-{11}	CCTA	DMD	2.6	Associated to the tests presented in Section 10.6, **SJ:S:fwd** simulations.
SC9	[6,25]	CCTA	DMD	2.6	Associated to the tests presented in Section 10.6, **SJ:S:fwd:kv** simulations.
SC10	$S_{1D.I}$	IVUS	PDC	2.6	Associated to the tests presented in Section 10.6, **MJ:fwd** simulations.
SC11	$S_{1D.II}$	IVUS	PDC	2.6	Associated to the tests presented in Section 10.6, **MJ:S:fwd** simulations.
SC12	$S_{1D.II}$	IVUS	PDC	2.6	Associated to the tests presented in Section 10.6, **MJ:S:fwd:kv** simulations.
SC13	$S_{1D.I}$	IVUS	PDC	2.6	Associated to the tests presented in Section 10.6, **SJ:fwd** simulations.
SC14	$S_{1D.II}$	IVUS	PDC	2.6	Associated to the tests presented in Section 10.6, **SJ:S:fwd** simulations.
SC15	$S_{1D.II}$	IVUS	PDC	2.6	Associated to the tests presented in Section 10.6, **SJ:S:fwd:kv** simulations.
SC16	[6,25]	CCTA	DMD	2.0	
SC17	[6,25]	CCTA	DMD	2.6	Sensitivity to variations in the CFR, 3D models and steady state simulations.
SC18	[6,25]	CCTA	DMD	3.0	
SC19	[6,25]	CCTA	DMD	4.0	
SC20	[6,25]	CCTA	PMD	2.0	
SC21	[6,25]	CCTA	PMD	2.6	Sensitivity to variations in the CFR, 3D models and steady state simulations.
SC22	[6,25]	CCTA	PMD	3.0	
SC23	[6,25]	CCTA	PMD	4.0	
SC24	[6,39]	IVUS	PDC	PS	Testing patient-specific CFR and sensitivity to the flow distribution strategy, 3D models
SC25	[6,39]	IVUS	PDP	PS	and steady state simulations.

Table 10.11: Definition of all study cases used in this section. Set definition for simulation cases [4-15] are as follows. $S_{1D.I} = [10,39] - \{11_{LCx}, 18_{LCx}, 20_{LAD}, 34_{LAD}, 35_{LCx}, 35_{RCA}\}$, and $S_{1D.II} = \{19_{LCx}, 26, 28, 36\}$.

Table 10.12, summarizes the statistical results for all study cases defined in Table 10.11. Discussion is focused in groups of related study cases.

Simulations used in Section 10.5, study cases SC1 and SC2, comprise CCTA and IVUS 3D models using DMD and CSRD flow distribution strategies, respectively. All simulations were performed using a CFR= 2.6 for modeling hyperemia, and transient-state flow conditions were used. A total of 16 invasive measures were used, with a prevalence of 12.5% (2 positive measurements). Note that, under the associated setting for SC2 (IVUS), all FFR_{CE} were found to be negative, i.e. Sen=0, Spe=1. The linear regression and correlation coefficients show poor agreement. A moderate bias and dispersion were obtained, 0.07 ± 0.07. In turn, for SC1 (CCTA), more positive values of FFR_{CE} were detected, improving the sensitivity, and decreasing the specificity. Linear regression and correlation show poor agreement, and the analysis of difference indicated large dispersion -0.03 ± 0.18.

Simulations used in Section 10.6 are divided in several study cases, SC{3-15}. All simulations were performed with CFR= 2.6, flow distribution for CCTA models SC{4-9} was defined by the DMD strategy and for all other cases (IVUS), the PDC strategy was employed to determine flow distribution. Note that cases SC{4-9} are 1D transient simulations associated to the 3D transient simulations of SC1. For such cases, the sensitivity was consistently 0.5, and the specificity range was $0.71 < \text{Spe} < 0.86$. Pearson's correlation was poor and non significant ($r < 0.29$), and the linear approximation coefficients presented low slope ($0.21 < a < 0.36$) and large intercepts ($0.52 < b < 0.64$). Overall, the best results were obtained by SC7, corresponding to 1D simulations without stenosis model and standard junction model, **SJ:fwd**, for which the analysis of difference featured small bias with moderate dispersion -0.02 ± 0.1.

Regarding cases SC{10-15}, corresponding to 1D simulations for IVUS models, only cases SC{10,13} are considered, since the others comprise a small sample. It was found that the use of the standard model for junctions (SC13) results in better agreement to the invasive measurement. Although the low sensitivity (0.17) for a prevalence of 0.23 (six positive measurements), the rest of the classification index are above 0.8. The Pearson correlation was moderate (0.7) and significant, although the linear approximation was poor ($a = 0.35, b = 0.62$). The analysis of difference featured low bias and moderate bias of 0.06 ± 0.07.

Note that case SC3, corresponds to the 3D simulations of the IVUS models which 1D simulations were compared to. In such case, with a few more measurements, the agreement is very similar to the one of SC13.

Simulations grouped in cases SC{16-23}, comprise tests for variations in CFR and flow distribution strategy in the 11 CCTA models, 16 invasive FFR measurements with prevalence 12.5% (2 positive measurements). Full 3D simulation in steady-state flow conditions were performed. Results indicates that for DMD flow distribution strategy, the CFR= 3 scores better results, i.e. SC18. In turn, for the PMD flow distribution strategy, the CFR=2.6 improves the overall statistics, i.e. SC21. Although the same level of sensitivity (0.5) is obtained in SC18 and SC21, the predictive capability of SC18 is slightly better than SC21. In turn, linear approximation, Person's correlation and the analysis of difference favor SC21. Despite the poor correlation ($r = 0.28$) and linear approximation ($a = 0.32, b = 0.57$), SC21 featured the lowest bias in all study cases and a moderate dispersion (-0.002 ± 0.1).

Simulations grouped in cases SC24 and SC25, comprise tests for variations in the flow distribution strategy for fixed CFR estimation using the PS criterion in the 33 IVUS models, 33 invasive FFR measurements with prevalence 21.2% (7 positive measurements). Full 3D simulation in steady-state flow conditions were performed. Results consistently indicate that the use of the PDP flow distribution, i.e. SC25, outper-

formed the PDC criterion. Overall, the SC25 case obtained the best linear approximation ($a = 0.76, b = 0.24$), largest significant Pearson correlation ($r = 0.77$), the smallest dispersion and low bias (0.028 ± 0.056). Regarding the predictive capabilities of case SC25, all classification indexes rate remarkable values (> 0.84) with the exception of sensitivity (0.29). Which indicates that 70% of positive measurements are misclassified by the corresponding FFR_{CE}.

Overall, the results from classification indexes should be interpreted carefully, since the sample is small and with low prevalence of positive FFR measurements. In fact, the patient sample was purposely set up in order to have borderline patients. As a general tendency, all FFR_{CE} presented here featured small values for sensitivity and PPV, indicating an underestimation of pressure drop in patients with postive FFR measurements. In turn, for most of the cases, the specificity and NPV resulted in large values. Note that, as expected, when CFR is increased the sensitivity increases and the specificity decreases, since simulations yield larger pressure drops and lower FFR_{CE} values. Moreover, the linear approximations and Pearson's correlation were generally weak and non-significant. Finally, smaller bias are neither related to better linear approximation nor to stronger correlations, since the dispersion may be large. Figure 10.16 presents scatter and Bland-Altman plots for the best cases of each group from the above discussion.

As expected, the CFR and flow distribution criterion were found to be key for a better agreement of the FFR_{CE} and invasive FFR. Which is explained by the direct relation to the blood flow and consequently pressure drop in the hemodynamic simulations.

Table 10.13 is an expanded version of Table 8.2, in which the most relevant cases from Table 10.12 were included for comparison purposes. When comparing to reported data, note that the reported prevalence ranged 20 to 54%, while cases using CCTA models, i.e. SC7 and SC21, have a low prevalence (12.5%), cases using IVUS models, i.e. SC3, SC13 and SC25, feature prevalence of 21.2%. Also, the number of measurements in this study is smaller than most of those reported in the literature, with exception of [236, 368]. Focusing on the predictive capabilities, all study cases are comparable to those reported in the literature with the distinction of the sensitivity which is considerably lower in all the SC, and the PPV which is low in the cases with low specificity. As for the linear correlation, r, it is weak and non significant for cases SC7 and SC21. In turn, for SC3, SC13 and SC25, r values are in the range of reported data $[0.50, 0.93]$. Regarding the analysis of difference, the bias and dispersion in all the SC are comparable to data reported in the literature.

Finally, despite the small sample and relatively low prevalence in the data used in this work, it was found that: (a) predictive value of FFR_{CE} are comparable to the state of the art, although a considerably low sensitivity was obtained; (b) agreement in terms of correlation r was in the range of reported values for cases based on IVUS, and was not good for cases based on CCTA, which also comprised smallest sample of all study cases; (c) the bias and dispersion obtained in all cases are comparable to the state of the art methods.

Study case	#Patients/ #Arteries	Prev	Measured FFR prediction value						Corr.	Difference	Linear approx.	
			AUC	Acc	Sen	Spe	PPV	NPV	r	$m_{\mathrm{BA}} \pm \mathrm{SD}_{\mathrm{BA}}$	a	b
SC1	11/16	0.125	0.679	0.750	**0.500**	0.786	0.250	**0.917**	0.016	-0.031±0.179[†]	0.034	0.820
SC2	11/16	0.125	**0.929**	**0.875**	0.000	**1.000**	-	0.875	0.456	0.070±0.069	0.186	0.788
SC3	24/33	0.212	0.827	0.818	0.143	**1.000**	**1.000**	0.813	0.645*	0.063±0.064	0.339	0.641
SC4	11/16	0.125	0.732	0.750	**0.500**	0.786	0.250	**0.917**	0.288	-0.025±0.101[†]	0.336	0.560
SC5	10/14	0.143	0.792	0.714	**0.500**	0.750	0.250	0.900	0.195	-0.045±0.151[†]	0.358	0.522
SC6	11/16	0.125	0.750	0.688	**0.500**	0.714	0.200	0.909	0.129	-0.056±0.156[†]	0.240	0.614
SC7	11/16	0.125	0.679	0.813	**0.500**	0.857	0.333	0.923	0.270	-0.020±0.101[†]	0.308	0.590
SC8	10/14	0.143	0.792	0.786	**0.500**	0.833	0.333	0.909	0.192	-0.040±0.151[†]	0.352	0.532
SC9	11/16	0.125	0.750	0.750	**0.500**	0.786	0.250	**0.917**	0.113	-0.051±0.158[†]	0.212	0.644
SC10	21/26	0.231	0.888	0.769	0.000	**1.000**	-	0.769	0.701*	0.063±0.066	0.338	0.639
SC11	4/ 4	0.500	1.000	0.500	0.000	1.000	-	0.500	0.934	0.045±0.058[†]	0.528	0.453
SC12	4/ 4	0.500	1.000	0.750	0.500	1.000	1.000	0.667	0.838	0.030±0.063[†]	0.599	0.376
SC13	21/26	0.231	0.904	0.808	0.167	**1.000**	**1.000**	0.800	0.704*	0.064±0.065	0.355	0.625
SC14	4/ 4	0.500	1.000	0.500	0.000	1.000	-	0.500	0.947	0.039±0.052[†]	0.584	0.398
SC15	4/ 4	0.500	1.000	0.750	0.500	1.000	1.000	0.667	0.864	0.023±0.058[†]	0.657	0.318
SC16	11/16	0.125	0.696	0.813	0.000	0.929	0.000	0.867	-0.075	0.013±0.161[†]	-0.129	1.008
SC17	11/16	0.125	0.679	0.750	**0.500**	0.786	0.250	**0.917**	-0.015	-0.028±0.184[†]	-0.032	0.882
SC18	11/16	0.125	0.679	0.750	**0.500**	0.786	0.250	**0.917**	0.028	-0.057±0.200[†]	0.066	0.766
SC19	11/16	0.125	0.679	0.625	**0.500**	0.643	0.167	0.900	0.133	-0.136±0.247[†]	0.417	0.378
SC20	11/16	0.125	0.750	**0.875**	0.000	**1.000**	-	0.875	0.334	0.036±0.079[†]	0.240	0.705
SC21	11/16	0.125	0.750	0.688	**0.500**	0.714	0.200	0.909	0.282	**-0.002**±0.100[†]	0.321	0.596
SC22	11/16	0.125	0.679	0.688	**0.500**	0.714	0.200	0.909	0.259	-0.031±0.119[†]	0.374	0.520
SC23	11/16	0.125	0.643	0.563	**0.500**	0.571	0.143	0.889	0.227	-0.111±0.181[†]	0.532	0.301
SC24	24/33	0.212	0.876	0.818	0.143	**1.000**	**1.000**	0.813	0.703*	0.051±0.059	0.446	0.536
SC25	24/33	0.212	0.909	0.848	0.286	**1.000**	**1.000**	0.839	**0.768***	0.028±**0.056**	**0.757**	**0.241**

Table 10.12: Summary of statistical results for each study case. All statistics are performed at a per-artery level. Values of FFR were taken at clinically relevant location for diagnosis, Ω_{FFR}. The linear approximation coefficients represents the equation $\mathrm{FFR}_{\mathrm{CE}} = a\mathrm{FFR}+b$. Marker * indicates if the Pearson's correlation coefficient (r) was statistically significant ($p < 0.05$). Marker [†] in the Bland-Altman analysis of difference ($\mathrm{FFR}_{\mathrm{CE}} - \mathrm{FFR}$) indicates $p > 0.05$. Predicted values are computed using FFR as gold standard and a cut-off value of FFR ≥ 0.8. The prevalence (Prev) of functional stenoses according to FFR is also display.

Research group	Study (year)	#Patients/#Arteries	Prev	AUC	Acc	Sen	Spe	PPV	NPV	Corr. r	Difference $m_{BA} \pm SD_{BA}$
HeartFlow	DISCOVER-FLOW [186] (2011)	103 / 159	36.5	90.0	84.0	87.9	82.2	73.9	92.2	0.68	0.022 ± 0.116
	Yoon et al. [360] (2012)	65 / 82	39.0	94.0	89.0	81.3	94.0	89.7	88.7	0.70	-
	DeFACTO [226] (2012)	**252** / 406	54.4	81.0	73.0	**90.0**	54.0	67.0	84.0	0.63	0.058± -
	Nakazato et al. [247] (2013)	82 / 150	23.3	79.0	69.0	74.0	67.0	41.0	90.0	0.50	0.050 ± 0.200
	NXT [251] (2014)	235 / **484**	20.7	90.0	81.0	86.0	79.0	65.0	93.0	**0.93**	0.020 ± 0.074
Siemens	Renker et al. [275] (2014)	53 / 67	29.8	92.0	-	85.0	85.0	71.0	93.0	0.66	-
	Coenen et al. [76] (2014)	106 / 189	42.3	83.0	74.6	87.5	65.1	64.8	87.7	0.59	-0.040 ± 0.130
	Tröbs et al. [334] (2016)	73 / 100	29.0	93.0	90.0	79.0	94.0	85.0	92.0	0.85	0.008 ± 0.063
Toshiba	Ko et al. [184] (2016)	30 / 56	33.9	83.9	88.0	77.8	86.8	73.7	89.2	0.57	0.065 ± 0.137
Univ. of Sheffield, UK	VIRTU-1 [236] (2013)	19 / 35	20.0	-	**97.0**	86.0	**100.**	**100.**	**97.0**	0.84	0.020 ± 0.080
Lediden, Netherlands	Tu et al. [336] (2014)	68 / 77	29.9	93.0	88.0	78.0	93.0	82.0	91.0	0.81	**0.000** ± 0.060
Univ. from Greece and UK	Papafaklis et al. [256] (2014)	120 / 139	37.4	92.0	86.0	79.0	90.0	82.0	88.0	0.78	-0.004 ± 0.085
Univ. of Yonsei, Korea	Ha et al. [137] (2016)	92 / 92	26.1	93.0	88.0	68.7	95.6	84.2	89.0	0.72	-0.030 ± 0.080
Univ. from Singapore, USA, China	Zhang et al. [368] (2016)	21 / 32	31.2	**95.5**	90.6	80.0	95.5	88.9	91.3	0.84	0.026 ± **0.050**
This work	SC3	24 / 33	21.2	82.7	81.8	14.3	**100.**	**100.**	81.3	0.64	0.063 ± 0.064
	SC7	11 / 16	12.5	67.9	81.3	50.0	85.7	33.3	92.3	0.27	-0.020 ± 0.101
	SC13	21 / 26	23.1	90.4	80.8	16.7	**100.**	**100.**	80.0	0.70	0.064 ± 0.065
	SC21	11 / 16	12.5	75.0	68.8	50.0	71.4	20.0	90.9	0.28	-0.002 ± 0.100
	SC25	24 / 33	21.2	90.9	84.8	28.6	**100.**	**100.**	83.9	0.77	0.028 ± 0.056

Table 10.13: Summary of results available in the literature comparing invasive FFR and computational estimations. All listed publications used a threshold value of 0.8 to diagnose risk of ischemia in both invasive and computational FFR indexes. Correlation, prediction and differences indexes computed in a per-artery basis. The most relevant study cases performed in this work are presented for comparison.
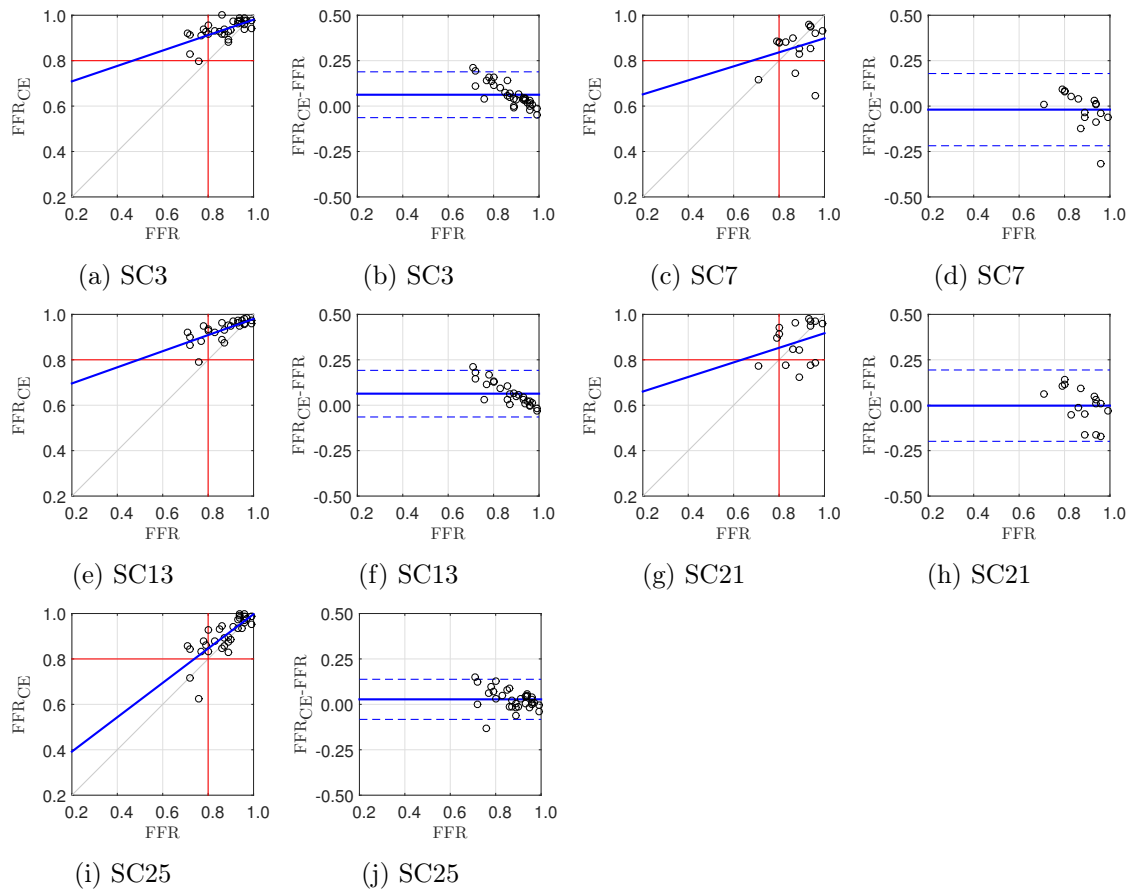
Figure 10.16: Scatter and Bland-Altman plots featuring comparison between FFR_{CE} and invasive FFR for most relevant study cases. Scatter plots indicate in red the threshold FFR=0.8 and in blue the linear regression approximation. Bland-Altman plots feature the bias in blue line and the limits of agreement ($m_{BA} \pm 1.96SD_{BA}$) in dashed blue lines. Study cases are presented as follows: SC3 in panels (a) and (b), SC7 in panels (c) and (d), SC13 in panels (e) and (f), SC21 in panels (g) and (h) and SC25 in panels (i) and (j).

Chapter 11

Computational estimation of FFR: Final comments

"Would it save you a lot of time if I just gave up and went mad now?"

Douglas Adams, *The Hitchhiker's Guide to the Galaxy.*

Through Chapter 10, a comprehensive set of studies designed to test the capability of different numerical methodologies to perform hemodynamics simulations in patient-specific coronary arterial trees was presented. The ultimate goal was to estimate the invasive measurement of FFR. Nonetheless, studies comprised the impact of image modality in hemodynamic variables, as well as comparisons between 3D and 1D CFD models. This chapter addresses such results to provide a global perspective of the second Part of this Thesis.

11.1   On 3D simulations

Full 3D simulations can demand computational power exceeding the capabilities of a personal computer. The second part of this Thesis would have been impossible to perform in a feasible time span without the use of the high performance computing hardware described in Chapter 10, Section 10.2. The results of 274 computer simulations (214 steady state and 60 transient) were presented in this work. A total of 36720 computational tasks were allocated in two clusters (Santos Dumont and MACC-HPC) and the total wall clock runtime was 5124 hs (213 days).

To ensure that all relevant hemodynamics quantities are accurately computed, mesh independence tests were performed. Results presented in Chapter 10, Section 10.3, allowed the determination of the parameters used to construct computational meshes with sufficient refinement to ensure convergence for all relevant hemodynamic variables. Such results also suggested that coarser meshes could be used and still compute the pressure and FFR fields with small errors. This could be useful to reduce computational costs in the context of an application specifically focusing the estimation of FFR.

In such scenario, the results of the comparison between steady and transient simulations, see Chapter 10, Section 10.4, pose relevant practical implications. With the level of mesh refinement and numerical methods employed in this work, a good agreement in all hemodynamics variables is obtained between steady state and transient simulations. Specifically, average discrepancies are bellow 4% disregarding the image modality used to construct the computational models, and, particularly, differences in the FFR field are below 1%. In turn, steady state simulations are performed $57 \pm 37\times$ faster than transient ones, in terms of normalized runtime (NRT). Regarding the computational estimation of

FFR, our results indicate that steady state simulations can be safely used, making 3D FFR$_{\text{CE}}$ affordable in terms of computational cost.

11.2   On the impact of image modality

In Chapter 10, Section 10.5, a comparison between blood flow simulations in coronary arteries performed on top of geometric models constructed from two imaging modalities, CCTA and IVUS, was presented.

The boundary conditions developed in Chapter 9, Section 9.2.1, were used with appropriate flow distributions (DMD and CSRD, for CCTA and IVUS models respectively), such that comparisons were well defined and simulation scenarios emulate hyperemic conditions typically encountered in FFR procedures.

In such context, it was observed that the major factor affecting hemodynamics was arterial geometry, more specifically, lumen cross-sectional area. Wall shear stress and blood velocity were largely sensitive to the lumen radius. In turn, pressure and FFR were not that sensitive, although pressure drop was systematically larger in CCTA models. However, and also as a consequence of the smaller lumen area rendered by CCTA, and even featuring less proximal side branches, these models are more affected by coronary steal phenomena than IVUS ones. This fact implies that the IVUS model carries more flow rate than the CCTA model, which, in terms of the prediction of FFR, counterbalances the effect of IVUS having a larger lumen area.

Results indicate that much care should be taken when drawing conclusions from computational simulations of coronary flow using CCTA models under hyperemic conditions. Although in certain cases the agreement of hemodynamics as predicted by CCTA models and by IVUS models was excellent, there are fundamental situations in which such agreement is lost. This is the case of vessels with large calcified lesions, for which strong underestimation of lumen area (focally or distributedly) leads to overestimation of blood velocity, wall shear stresses, pressure drop and, finally, underestimation of FFR. In these cases, hemodynamics is largely sensitive to imaging modality.

11.3   On 1D simulations

In Chapter 10, Section 10.6, the capabilities of several 1D model configurations, i.e. 6 variants combining the use of junction and stenosis models, were compared to 3D simulations. The imposition of BC in the 1D model was chosen such that the flow rate at each outlet is the same in both 3D and 1D simulations. A total of 11 CCTA and 26 IVUS models were employed.

Results indicate that 1D simulations can reproduce the FFR field computed from 3D simulations with remarkable agreement when dedicated junction and stenoses models are used (Mynard and Young models). Furthermore, 1D transient simulations can be performed in minutes, compared to the average of 80 hs or 3 hs for transient and steady 3D simulations, which require much more computational resources. In terms of RT, the 1D simulations are 298 ± 326 times faster than 3D pulsatile simulations and 16 ± 30 times faster than steady 3D simulations, the amount of computational tasks are 11 ± 5 times less in the 1D model.

All considering, the use of 1D models for the computational assessment of FFR is a cheaper and safe alternative to 3D simulations, under the hypothesis tested in this work. The use of other BC in the 1D models, e.g. the one developed for 3D simulations in this work, will not drastically increment the computational time, although it is difficult to predict the impact in the discrepancies against the corresponding 3D simulations, since flow distribution may be affected. This is matter of current research.

11.4   On the estimation of invasive FFR

In Chapter 10, Section 10.7, several computational methodologies for the calculation of FFR_{CE} were compared to invasive FFR measurements using a comprehensive set of statistical indexes. A total of 25 study cases were used, comprising all simulations performed in Sections 10.5 and 10.6 from Chapter 10, plus tests changing the CFR and flow distribution criterion.

When using computational models derived from CCTA images, it was found that the combination of CFR= 2.6, a standard value reported in the literature, and the PMD flow distribution criterion developed in this work, improved the overall agreement of 3D (steady-state) simulations. Although 1D tests were only performed for CFR=2.6 and DMD flow distribution criterion, it was found that using the setting **SJ:fwd**, i.e. standard junction model and no stenosis model, results in an overall better agreement to the invasive FFR, even better than the associated 3D simulation. This opens room for the discussion about the compensation of modeling errors in 1D and 3D simulations.

When IVUS images are employed to construct computational models, it was found that the combination of a patient-specific criterion (PS) for the determination of CFR and the flow distribution criterion PDP produced the best overall agreement to invasive FFR. Since such configuration was not tested using 1D simulations, we highlight that the model using standard junctions slightly outperformed the one using the Mynard model. For IVUS models, the small number of geometries in which stenoses were detected restricts their inclusion in the analysis and discussions.

When comparing FFR_{CE} to the state of the art methods reported in the literature, it should be taken into account that the sample used in this work is relatively small and with relatively low prevalence of positive measurements (FFR < 0.8). Nonetheless, the following remarks are worth mentioning: (a) predictive value of FFR_{CE} are comparable to the state of the art, although a considerably low sensitivity was obtained; (b) agreement in terms of correlation r was in the range of reported values for cases based on IVUS, and was not good for cases based on CCTA, which also comprised a smaller sample; (c) the bias and dispersion obtained in all cases are comparable to the state of the art methods.

Furthermore, to the best of the author's knowledge, the computational assessment of FFR using IVUS data with a patient sample as large as the one presented here had never been reported before.

11.5   Limitations

The main limitation of the present study is the relatively small sample. Nevertheless, the construction of computational models for each patient is a complex task, and the results reported here have helped to elucidate some of the main drawbacks when trying to simulate coronary blood flow under hyperemic conditions. Particularly, the determination of patient-specific boundary condition, e.g. CBF, flow distribution criterion and CFR, are key points to accurately simulate coronary blood flow. When studying the diagnostics capabilities of FFR_{CE}, the relatively low prevalence of positive FFR measurements in the sample must be taken into consideration to interpret statistics.

An intrinsic limitation of all applications aiming to simulate patient-specific computational hemodynamics, lies on the uncertainties propagated from the image processing procedures. Although such topic was not directly analyzed in this work, the study presented in Chapter 10, Section 10.5, clearly shows that models construed from CCTA and IVUS medical image modalities produce different results in several relevant hemodynamics quantities, e.g. WSS, OSI and FFR. Results reported here are consistent with literature specialized in comparing CCTA and IVUS imaging procedures [105]. In the context of the

computational assessment of FFR, recent efforts started to address sensitivity to arterial geometry, see [293].

Although 3D models capture the complex fluid dynamic phenomena, carrying out transient simulations is computationally expensive, which poses a practical limitation. Although it was shown that to calculate the FFR_{CE}, simulations runtime can be reduced by performing steady state simulations, high performance hardware is still required to obtain results in a few hours of runtime.

In turn, 1D models certainly eliminate the need for high performance computing hardware, and it was shown that 3D FFR_{CE} can be predicted with 1D models with good agreement. Nevertheless, it should be noted that discrepancies are originated by the intrinsic limitations of 1D models. Specifically, in this work, the special cases in which a junction features a stenosis, cannot be accurately modeled by either the standard not the Mynard junction models. Furthermore, the automatic stenoses detection algorithm was set to detect stenoses percentage area $> 40\%$, which may identify lesions that do not require the use of a Young model, which could overestimate the pressure drop.

11.6 Concluding remarks for Part II

A comprehensive analysis of the different aspects related to the computational assessment of FFR was presented. Particularly, this work focused on

- Relevant topics related to the determination of patient-specific parameters for simulation of coronary blood flow, i.e. estimation of total coronary blood flow, criteria for distribution of flow among outlets and estimation of coronary flow reserve, which is key to simulate hyperemic scenarios.

- Computational tests were performed to ensure appropriate mesh refinement for simulations.

- Comparisons between steady and transient state simulations showed that the former setting can be safely used to calculate the FFR_{CE}, considerably saving time.

- Impact on hemodynamic variables produced by the use of CCTA- and IVUS-derived computational models was quantified.

- The capability of 1D models to predict the FFR_{CE} obtained with 3D models was demonstrated.

- Several simulation settings were compared to invasive measurements, it was shown that results are comparable to the state of the art. The results presented here should be interpreted as preliminary results, due to the small nature of the patient sample.

- This work presented results of computational assessment of FFR using IVUS image data in a moderate-sized sample for the first time.

It is important to remark that this work could not have been possible without the synergistic collaboration between the HeMoLab and the InCor research groups. Although this Thesis ends here, several future works ramify from it, for which the continuity of such collaboration is fundamental. Particularly, it is of utmost importance to enlarge the patient sample, but several other studies embracing diverse related topics can be done, for example

- Develop automatic image segmentation algorithms would be key to deal with large patient samples.

- Performance and scaling analysis would be important to optimize computational resources in a production scenario using 3D simulations.

- Explore new 3D meshing algorithms that can reduce the number of degrees of freedom taking into account the tubular nature of the arterial domain, see [211].

- Test the patient-specific CFR estimation (PS) in CCTA models. It was shown that this could improve the agreement in IVUS models, it could also improve the results in CCTA models.

- Perform systematic sensitivity analysis to quantify the impact on FFR_{CE} of several parameters, e.g. arterial and lesion geometry, CBF, CFR, flow distribution criteria, blood viscosity, velocity profile (exclusively for 1D models). Note that such studies are more viable on 1D models due to their computational efficiency.

- Develop stenotic-junction models for the 1D model. This will improve the agreement between 3D and 1D simulations in certain cases.

- Implement algorithms for CBF estimation from angiographic images. This could eliminate the uncertainty in the total inflow parameter. However, this approach could only be used in combination with an invasive procedure.

- Develop models of collateral circulation for both, 3D and 1D models. The importance of collateral circulation was highlighted in the seminal work of FFR [266], and it is intrinsically taken into account in the invasive measurement of FFR. Moreover, current publications regarding computational approaches to estimate FFR (summarized in Chapter 8, Section 8.4.2) do not model collaterals and rarely mention the existence of the collateral circulation, which probably is a source of modeling error between the computational estimation and the actual measure of FFR.

Final thoughts

"Only a few things are cheaper than dying."

Pedro Lemos

For those who have reached this final chapter, I salute you!. This final chapter was written after presenting the Thesis, motivated by a suggestion from Prof. Rodrigo to give a unified ending to the manuscript. In order to not fall into repetition of technical and theoretical aspects of the Thesis, this chapter sums-up some discussions and comments that took place during the Thesis presentation.

The extension of this document was initially conditioned by its two main goals: (i) to propose methods for the geometrical characterization and comparison of coronary arterial trees; and (ii) to develop a methodology for the computational estimation of FFR (FFR$_{CE}$). The amount of work carried out to reach both goals naturally shaped this document in two parts, and the desire to make it self-complete sealed its destiny as a long manuscript. As Prof. Buscaglia pointed out, *The more complete a work is, the more incomplete it gets.* But that is a good thing to be, since the very foundation of knowledge and progress are rooted in the everlasting human curiosity.

Through Part I, a comprehensive analysis of the geometric characteristics of the coronary arterial tree was presented. Such studies comprised morphometric analysis of the coronary arteries, similarity metrics based on geometry, heritability of arterial geometric characteristics and exploration of geometric risk factors for CAD. A summary of contributions is presented in Chapter 6.

Through Part II, a comprehensive set of studies designed to test the capability of different numerical methodologies to perform hemodynamics simulations in patient-specific coronary arterial trees was presented. The ultimate goal was to estimate the invasive measurement of FFR. Furthermore, studies comprised the impact of image modality in hemodynamic variables, as well as comparisons between 3D and 1D CFD models. A summary of contributions is presented in Chapter 11.

Although in this document both Parts were only related by the type of input data and methodological procedure, e.g. image processing and centerline models, the combination of both topics is feasible. For example, hemodynamic risk factors can be explored and combined with the geometric characteristics; the true effect of arterial geometry over hemodynamics can be studied; geometric characteristic of arteries can be incorporated in the 1D model, through geometric-dependent additional pressure losses or by including an adaptive velocity profile coefficient.

Prof. Pedro, who closely accompanied this work pointed out limitations and questions on how to improve the very invasive FFR index, and how these improvements could be incorporated in the computational models, e.g. measuring pressure during diastolic flow. He also pointed out that typically, clinical research focuses on the diseased and the risk factors, and proposed a paradigm shift, in which we could focus in the healthy and protective factors. This kind of fundamental questioning is, without doubt, the kind of questions that motivate high impact research. For me, it was a great experience working

with Prof. Pedro and his research group, and I hope to continue such collaboration in the future.

As discussed with Prof. Abimael, multidisciplinary research contain in this work, is key to forge bridges between different areas, in this case, mathematical and computational models with cardiology. In the context of medicine assisted by scientific computing, and in particular in the topics studied in this work, it is possible to speculate future academic careers and specializations training professionals that would be able to extract and interpret computational models and simulations, giving more information to physicians and helping in the clinical decision process.

Finally, Prof. Gilson accompanied my progress since the masters dissertation, and his comments addressed more specific and technical issues related to data mining, which also helped to improved the manuscript.

When I was starting this Thesis, Profs. Pablo and Raúl indicated several papers and books to introduce me into the area. Those initial references rapidly multiplied to a long list of bibliography covering a broad spectrum of complexity, from basic definitions to detailed methods and information in areas such as anatomy, physiology, image processing, geometric analysis, statistics and computational fluid dynamics. I hope that this document can be used by new students and collaborators as a reference and as a starting point to begin research in topics related to patient specific modeling and simulation of the coronary arterial physiology and pathophysiology.

Appendix A

Mesh quality improvement operations

This appendix describes the default mesh quality improvement pipeline used to generate three-dimensional meshes for hemodynamic simulations. Each processing step is described by: application (HeMoLab [4] or vmtk [11]), filter name, typical parameters and a description.

Application	Filter name	Parameters	Description
HeMoLab	Clip	**Clip type**: Box	This operation is used to open the aortic root at its start (aortic valves location).
HeMoLab	Connectivity + Threshold	**RegionID**: The id of the region corresponding to the entire mesh	This operations eliminate any spurious (disconnected) surface that may be created after the surcafe opening or be present in the original surface.
HeMoLab	HM3DPolyDatatoUnstructuredGridConverter + HM3DUnstructuredGridtoHMMeshDataConverter	**Fix deformed edge triangles**: true	This filters convert surface to a convenient the data structure representation to used in the following filter. It also correct mesh elements to ensure that all elements be triangles.
HeMoLab	HMD3DSurfaceMesher (Insert Nodes)	**Value**: 0.31	This operation insert nodes over the surface in order to reach semi homogeneous node density. It also ensure connectivity of new and old nodes.
HeMoLab	HMD3DSurfaceMesher (Smooth)	**Rlaxation Factor**: 0.63; **Group**: -1; **No shrink**: true; **Number of Interactions**: 30; **Remove Needles**: false	The entire surface is smoothed, using a non-shrink restriction to avoid collapse. This is an iterative process that uses a default relaxation factor. Although the overall mesh quality is improved, degenerate (needle) triangles may remain. These elements will be corrected in forthcoming filter operations.
HeMoLab	HMD3DSurfaceMesher (Swap diagonals)	**Angle**: 10	This filter correct some degenerate triangles by changing connectivity of nodes, but maintains nodes positions.

Application	Filter name	Parameters	Description
HeMoLab	HM3DCenterLineFilter	**Resampling**: 0.5; **Tolerance**: 0.001; **Absolute Tolerance**: 0; **Convert Lines to Points**: true; **Convert Polys to Lines**: true; **Convert Strips to Polys**: true; **Point Merging**: true	An auxiliary centerline is computed using all arterial terminals.
HeMoLab	HM3DClipByCenterLineFilter		The previously computed centerline is used to perform opening of arterial end-points on the associated surface. The output of this filter is an opened surface triangulation. Although this mesh has not the necessary quality to be used in 3D hemodynamics simulations, it can be used to extract centerlines for reduced models.
HeMoLab	HM3DCenterLineFilter	**Resampling**: 0.5; **Tolerance**: 0.001; **Absolute Tolerance**: 0; **Convert Lines to Points**: true; **Convert Polys to Lines**: true; **Convert Strips to Polys**: true; **Point Merging**: true	A centerline of the complete coronary tree is extracted, this model is used for geometric characterization and as based geometry for $1D^+$, 1D or 0D simulations.
HeMoLab	Clip	**Clip type**: Box	The clip filter is used to separete the subtree of interest, i.e. the left tree from the aorta. If hemodynamics will be perform in the entire tree this, and the following filter are not used.
HeMoLab	Connectivity + Threshold + ExtractSurface + Triangulate	**Clip type**: Box	This operations ensure correct extraction of a triangulated surface of the target arterial tree.

vmtk	Flow extension		Flow extension of short arteries or arteries ending in curve segments. This improves simulation results by better impositions of boundary conditions.
			Command:
			
			`vmtksurfacereader -ifile temp_001.vtk --pipe`
			`vmtkcenterlines -seedselector openprofiles --pipe`
			`vmtkflowextensions -adaptivelength 1 -extensionratio 5`
			`-normalestimationratio 1 -extensionmode boundarynormal --pipe`
			`vmtksurfacewriter -ofile temp_002.vtk`

Application	Filter name	Parameters	Description
vmtk	MeshGenerator		This filter perform remeshing of the input surface, nodes and connectivity are modified. The output are a volumetric mesh (tetrahedrons) suitable for hemodynamics simulations and an associated surface (triangles) mesh. **Command**:

```
vmtksurfacereader -ifile temp_002.vtk --pipe
vmtkcenterlines -endpoints 1 -seedselector openprofiles --pipe
vmtkdistancetocenterlines -useradius 1 --pipe
vmtkmeshgenerator -elementsizemode edgelengtharray -edgelengtharray
 DistanceToCenterlines -edgelengthfactor 0.18 -ofile volume.vtk
 -remeshedsurfacefile surface.vtk
```

Table A.1: Mesh improvement pipeline.

Appendix B

Arterial labeling considerations

Centerlines tracks representing arterial segments are labeled by cardiologist using a fixed set of labels (see Table B.1). The large quantity of labels is due to the high variability of the coronary anatomy and multiple bifurcation levels that may be model from the medical images. The complexity of the heart vasculature may produce uncertainty or ambiguity during the labeling procedure. In order to tackle this problem, the following guidelines and considerations were defined:

- An artery can change its label only after a bifurcation point. This restriction eliminates physician's subjectivity at the time of defining when an artery ends and another starts.

- An artery is considered to be *bifurcated* when it separates itself in two branches with approximately the same length/radius (meaning that one does not double in length/radius the other), and both branches follow a similar path, which would be the one of the original artery if not bifurcated. Otherwise, the smaller artery is considered as a branch of the bigger one.

- Branches are enumerated from proximal to distal in a consecutive manner. Only segmented arteries are considered, this means that if the cardiologist sees a branch that is no segmented, that branch should not be considered in the counter. Arteries such as diagonals and marginals are enumerated (see Table B.1 for a list of arteries with enumeration).

- The posterolateral segment artery (PLSA) is labeled as RPLSA/LPLSA depending on its parent, right coronary or left circumflex artery. All the PLSA branches towards the posterolateral face of the left ventricle are labeled as posterolateral branches and enumerated from proximal to distal appearance. The same applies to the atrioventricular node artery.

- The posterior descendant artery (PDA) is labeled as RPDA/LPDA depending on its parent, right coronary or left posterolateral artery. All arteries that reach the posterior interventricular sulcus are considered PDA, and therefore listed in proximal to distal order.

- All arteries reaching the interface between the right ventricle and the pulmonary artery root are considered conus arteries and listed from proximal to distal appearance.

Label	Description		Label	Description
Ao	Aorta		RCA	Right Coronary Artery
LM	Left Main artery			
			ConusA1	First Conus Artery, also known as Third coronary
LAD	Left Anterior Descendant, also known as Anterior Interventricular Artery		ConusA1_B1	First Branch of the ConusA1
LAD_bif1	First bifurcation of the LAD		ConusA1_B2	Second Branch of the ConusA1
LAD_bif2	Second bifurcation of the LAD		ConusA1_B3	Third Branch of the ConusA1
			ConusA2	Second Conus Artery
D1	Diagonal 1 of the LAD		ConusA2_B1	First Branch of the ConusA2
D1_B1	First Branch of the Diagonal 1 of the LAD		ConusA2_B2	Second Branch of the ConusA2
D1_B2	Second Branch of the Diagonal 1 of the LAD		ConusA2_B3	Third Branch of the ConusA2
D1_B3	Third Branch of the Diagonal 1 of the LAD		ConusA3	Third Conus Artery
D1_bif1	First Bifurcation of the D1 segment		ConusA3_B1	First Branch of the ConusA3
D1_bif1_B1	First Branch of the D1_bif1		ConusA3_B2	Second Branch of the ConusA3
D1_bif1_B2	Second Branch of the D1_bif1		ConusA3_B3	Third Branch of the ConusA3
D1_bif2	Second Bifurcation of the D1 segment			
D1_bif2_B1	First Branch of the D1_bif2		RCA_AB1	First Atrial Branch of the RCA
D1_bif2_B2	Second Branch of the D1_bif2		RCA_AB1_B1	First Branch of the First Atrial Branch of the RCA
			RCA_AB1_B2	Second Branch of the First Atrial Branch of the RCA
D2	Diagonal 2 of the LAD		RCA_AB2	Second Atrial Branch of the RCA
D2_B1	First Branch of the D2 of the LAD		RCA_AB2_B1	First Branch of the Second Atrial Branch of the RCA
D2_B2	Second Branch of the D2 of the LAD		RCA_AB2_B2	Second Branch of the Second Atrial Branch of the RCA
D2_B3	Third Branch of the D2 of the LAD		RCA_AB3	Third Atrial Branch of the RCA
D2_bif1	First Bifurcation of the D2 segment		RCA_AB3_B1	First Branch of the Third Atrial Branch of the RCA
D2_bif1_B1	First Branch of the D2_bif1		RCA_AB3_B2	Second Branch of the Third Atrial Branch of the RCA
D2_bif1_B2	Second Branch of the D2_bif1			
D2_bif2	Second Bifurcation of the D2 segment		RM1	First right marginal of the RCA
D2_bif2_B1	First Branch of the D2_bif2		RM1_B1	First Branch of the RM1
D2_bif2_B2	Second Branch of the D2_bif2		RM1_B2	Second Branch of the RM1
			RM1_bif1	First bifurcation of the RM1
D3	Diagonal 3 of the LAD		RM1_bif1_B1	First Branch of the RM1_bif1
D3_B1	First Branch of the D3 of the LAD		RM1_bif1_B2	Second Branch of the RM1_bif1
D3_B2	Second Branch of the D3 of the LAD		RM1_bif2	Second bifurcation of the RM1
D3_B3	Third Branch of the D3 of the LAD		RM1_bif2_B1	First Branch of the RM1_bif2
D3_bif1	First Bifurcation of the D3 segment		RM1_bif2_B2	Second Branch of the RM1_bif2
D3_bif1_B1	First Branch of the D3_bif1			
D3_bif1_B2	Second Branch of the D3_bif1		RM2	Second right marginal of the RCA
D3_bif2	Second Bifurcation of the D3 segment		RM2_B1	First Branch of the RM2
D3_bif2_B1	First Branch of the D3_bif2		RM2_B2	Second Branch of the RM2
D3_bif2_B2	Second Branch of the D3_bif2		RM2_bif1	First bifurcation of the RM2
			RM2_bif1_B1	First Branch of the RM2_bif1
D4	Diagonal 4 of the LAD		RM2_bif1_B2	Second Branch of the RM2_bif1
D4_B1	First Branch of the D4 of the LAD		RM2_bif2	Second bifurcation of the RM2
D4_B2	Second Branch of the D4 of the LAD		RM2_bif2_B1	First Branch of the RM2_bif2
D4_B3	Third Branch of the D4 of the LAD		RM2_bif2_B2	Second Branch of the RM2_bif2
D4_bif1	First Bifurcation of the D4 segment			
D4_bif1_B1	First Branch of the D4_bif1		RM3	Third right marginal of the RCA
D4_bif1_B2	Second Branch of the D4_bif1		RM3_B1	First Branch of the RM3
D4_bif2	Second Bifurcation of the D4 segment		RM3_B2	Second Branch of the RM3
D4_bif2_B1	First Branch of the D4_bif2		RM3_bif1	First bifurcation of the RM3
D4_bif2_B2	Second Branch of the D4_bif2		RM3_bif1_B1	First Branch of the RM3_bif1
			RM3_bif1_B2	Second Branch of the RM3_bif1
D5	Diagonal 5 of the LAD		RM3_bif2	Second bifurcation of the RM3
D5_B1	First Branch of the D5 of the LAD		RM3_bif2_B1	First Branch of the RM3_bif2
D5_B2	Second Branch of the D5 of the LAD		RM3_bif2_B2	Second Branch of the RM3_bif2
D5_B3	Third Branch of the D5 of the LAD			
D5_bif1	First Bifurcation of the D5 segment		RM4	Fourth right marginal of the RCA
D5_bif1_B1	First Branch of the D5_bif1		RM4_B1	First Branch of the RM4

Label	Description	Label	Description
D5_bif1_B2	Second Branch of the D5_bif1	RM4_B2	Second Branch of the RM4
D5_bif2	Second Bifurcation of the D5 segment	RM4_bif1	First bifurcation of the RM4
D5_bif2_B1	First Branch of the D5_bif2	RM4_bif1_B1	First Branch of the RM4_bif1
D5_bif2_B2	Second Branch of the D5_bif2	RM4_bif1_B2	Second Branch of the RM4_bif1
		RM4_bif2	Second bifurcation of the RM4
D6	Diagonal 6 of the LAD	RM4_bif2_B1	First Branch of the RM4_bif2
		RM4_bif2_B2	Second Branch of the RM4_bif2
S1	Septal 1 of the LAD		
S1_B1	First Branch of the Septal 1 of the LAD	RM5	Fifth right marginal of the RCA
S1_B2	Second Branch of the Septal 1 of the LAD	RM5_B1	First Branch of the RM5
S1_B3	Third Branch of the Septal 1 of the LAD	RM5_B2	Second Branch of the RM5
S2	Septal 2 of the LAD	RM5_bif1	First bifurcation of the RM5
S2_B1	First Branch of the Septal 2 of the LAD	RM5_bif1_B1	First Branch of the RM5_bif1
S2_B2	Second Branch of the Septal 2 of the LAD	RM5_bif1_B2	Second Branch of the RM5_bif1
S2_B3	Third Branch of the Septal 2 of the LAD	RM5_bif2	Second bifurcation of the RM5
S3	Septal 3 of the LAD	RM5_bif2_B1	First Branch of the RM5_bif2
S3_B1	First Branch of the Septal 3 of the LAD	RM5_bif2_B2	Second Branch of the RM5_bif2
S3_B2	Second Branch of the Septal 3 of the LAD		
S3_B3	Third Branch of the Septal 3 of the LAD	RM6	Sixth right marginal of the RCA
S4	Septal 4 of the LAD	RM6_B1	First Branch of the RM6
S4_B1	First Branch of the Septal 4 of the LAD	RM6_B2	Second Branch of the RM6
S4_B2	Second Branch of the Septal 4 of the LAD	RM6_bif1	First bifurcation of the RM6
S4_B3	Third Branch of the Septal 4 of the LAD	RM6_bif1_B1	First Branch of the RM6_bif1
S5	Septal 5 of the LAD	RM6_bif1_B2	Second Branch of the RM6_bif1
S5_B1	First Branch of the Septal 5 of the LAD	RM6_bif2	Second bifurcation of the RM6
S5_B2	Second Branch of the Septal 5 of the LAD	RM6_bif2_B1	First Branch of the RM6_bif2
S5_B3	Third Branch of the Septal 5 of the LAD	RM6_bif2_B2	Second Branch of the RM6_bif2
LAD_ConusA	Conus artery of the LAD	R_AVNA	Atrioventricular nodal Artery of the Right subtree
		L_AVNA	Atrioventricular nodal Artery of the Left subtree
LCx	Left Circumflex		
LCx_AB1	First Atrial Branch of the LCx	LPD1	Left Posterior Descendent Artery (First)
LCx_AB1_B1	First Branch of the First Atrial Branch of the LCx	LPD1_B1	First branch of the LPDA1
LCx_AB1_B2	Second Branch of the First Atrial Branch of the LCx	LPD1_B2	Second branch of the LPDA1
LCx_AB1_B3	Third Branch of the First Atrial Branch of the LCx	LPD1_B3	Third branch of the LPDA1
LCx_AB2	Second Atrial Branch of the LCx	LPD1_bif1	First bifurcation of the LPD1
LCx_AB2_B1	First Branch of the Second Atrial Branch of the LCx	LPD1_bif1_B1	First branch of the LPDA1_bif1
LCx_AB2_B2	Second Branch of the Second Atrial Branch of the LCx	LPD1_bif1_B2	Second branch of the LPDA1_bif1
LCx_AB3	Third Atrial Branch of the LCx	LPD1_bif1_B3	Third branch of the LPDA1_bif1
LCx_AB3_B1	First Branch of the Third Atrial Branch of the LCx	LPD1_bif2	Second bifurcation of the LPD1
LCx_AB3_B2	Second Branch of the Third Atrial Branch of the LCx	LPD1_bif2_B1	First branch of the LPDA1_bif2
		LPD1_bif2_B2	Second branch of the LPDA1_bif2
LCx_bif1	First bifurcation of the LCx	LPD1_bif2_B3	Third branch of the LPDA1_bif2
LCx_bif1_AB1	First Atrial Branch of the LCx_bif1	LPD2	Left Posterior Descendent Artery (Second)
LCx_bif1_AB1_B1	First Branch of the LCx_bif1_AB1	LPD2_B1	First branch of the LPDA2
LCx_bif1_AB1_B2	Second Branch of the LCx_bif1_AB1	LPD2_B2	Second branch of the LPDA2
LCx_bif1_AB1_B3	Third Branch of the LCx_bif1_AB1	LPD2_B3	Third branch of the LPDA2
LCx_bif1_AB2	Second Atrial Branch of the LCx_bif1	LPD2_bif1	First bifurcation of the LPD2
LCx_bif1_AB2_B1	First Branch of the LCx_bif1_AB2	LPD2_bif1_B1	First branch of the LPDA2_bif1
LCx_bif1_AB2_B2	Second Branch of the LCx_bif1_AB2	LPD2_bif1_B2	Second branch of the LPDA2_bif1
LCx_bif1_AB3	Third Atrial Branch of the LCx_bif1	LPD2_bif1_B3	Third branch of the LPDA2_bif1
LCx_bif1_AB3_B1	First Branch of the LCx_bif1_AB3	LPD2_bif2	Second bifurcation of the LPD2
LCx_bif1_AB3_B2	Second Branch of the LCx_bif1_AB3	LPD2_bif2_B1	First branch of the LPDA2_bif2
		LPD2_bif2_B2	Second branch of the LPDA2_bif2
LCx_bif2	Second bifurcation of the LCx	LPD2_bif2_B3	Third branch of the LPDA2_bif2
LCx_bif2_AB1	First Atrial Branch of the LCx_bif2	LPD3	Left Posterior Descendent Artery (Third)
LCx_bif2_AB1_B1	First Branch of the LCx_bif2_AB1	LPD3_B1	First branch of the LPDA3
LCx_bif2_AB1_B2	Second Branch of the LCx_bif2_AB1	LPD3_B2	Second branch of the LPDA3

Label	Description	Label	Description
LCx_bif2_AB1_B3	Third Branch of the LCx_bif2_AB1	LPD3_B3	Third branch of the LPDA3
LCx_bif2_AB2	Second Atrial Branch of the LCx_bif2	LPD3_bif1	First bifurcation of the LPD3
LCx_bif2_AB2_B1	First Branch of the LCx_bif2_AB2	LPD3_bif1_B1	First branch of the LPDA3_bif1
LCx_bif2_AB2_B2	Second Branch of the LCx_bif2_AB2	LPD3_bif1_B2	Second branch of the LPDA3_bif1
LCx_bif2_AB3	Third Atrial Branch of the LCx_bif2	LPD3_bif1_B3	Third branch of the LPDA3_bif1
LCx_bif2_AB3_B1	First Branch of the LCx_bif2_AB3	LPD3_bif2	Second bifurcation of the LPD3
LCx_bif2_AB3_B2	Second Branch of the LCx_bif2_AB3	LPD3_bif2_B1	First branch of the LPDA3_bif2
		LPD3_bif2_B2	Second branch of the LPDA3_bif2
OM1	Obtuse Marginal 1 of the LCx	LPD3_bif2_B3	Third branch of the LPDA3_bif2
OM1_B1	First Branch of the OM1		
OM1_B2	Second Branch of the OM1	RPD1	Right Posterior Descendent Artery (First)
OM1_B3	Third Branch of the OM1	RPD1_B1	First branch of the RPDA1
OM1_bif1	First bifurcation of the OM1	RPD1_B2	Second branch of the RPDA1
OM1_bif1_B1	First Branch of the OM1_bif1	RPD1_B3	Third branch of the RPDA1
OM1_bif1_B2	Second Branch of the OM1_bif1	RPD1_B4	Fourth branch of the RPDA1
OM1_bif1_B3	Third Branch of the OM1_bif1	RPD1_bif1	First bifurcation of the RPD1
OM1_bif2	Second bifurcation of the OM1	RPD1_bif1_B1	First branch of the RPDA1_bif1
OM1_bif2_B1	First Branch of the OM1_bif2	RPD1_bif1_B2	Second branch of the RPDA1_bif1
OM1_bif2_B2	Second Branch of the OM1_bif2	RPD1_bif1_B3	Third branch of the RPDA1_bif1
OM1_bif2_B3	Third Branch of the OM1_bif2	RPD1_bif2	Second bifurcation of the RPD1
		RPD1_bif2_B1	First branch of the RPDA1_bif2
OM2	Obtuse Marginal 2 of the LCx	RPD1_bif2_B2	Second branch of the RPDA1_bif2
OM2_B1	First Branch of the OM2	RPD1_bif2_B3	Third branch of the RPDA1_bif2
OM2_B2	Second Branch of the OM2	RPD2	Right Posterior Descendent Artery (Second)
OM2_B3	Third Branch of the OM2	RPD2_B1	First branch of the RPDA2
OM2_bif1	First bifurcation of the OM2	RPD2_B2	Second branch of the RPDA2
OM2_bif1_B1	First Branch of the OM2_bif1	RPD2_B3	Third branch of the RPDA2
OM2_bif1_B2	Second Branch of the OM2_bif1	RPD2_bif1	First bifurcation of the RPD2
OM2_bif1_B3	Third Branch of the OM2_bif1	RPD2_bif1_B1	First branch of the RPDA2_bif1
OM2_bif2	Second bifurcation of the OM2	RPD2_bif1_B2	Second branch of the RPDA2_bif1
OM2_bif2_B1	First Branch of the OM2_bif2	RPD2_bif1_B3	Third branch of the RPDA2_bif1
OM2_bif2_B2	Second Branch of the OM2_bif2	RPD2_bif2	Second bifurcation of the RPD2
OM2_bif2_B3	Third Branch of the OM2_bif2	RPD2_bif2_B1	First branch of the RPDA2_bif2
		RPD2_bif2_B2	Second branch of the RPDA2_bif2
OM3	Obtuse Marginal 3 of the LCx	RPD2_bif2_B3	Third branch of the RPDA2_bif2
OM3_B1	First Branch of the OM3	RPD3	Right Posterior Descendent Artery (Third)
OM3_B2	Second Branch of the OM3	RPD3_B1	First branch of the RPDA3
OM3_B3	Third Branch of the OM3	RPD3_B2	Second branch of the RPDA3
OM3_bif1	First bifurcation of the OM3	RPD3_B3	Third branch of the RPDA3
OM3_bif1_B1	First Branch of the OM3_bif1	RPD3_bif1	First bifurcation of the RPD3
OM3_bif1_B2	Second Branch of the OM3_bif1	RPD3_bif1_B1	First branch of the RPDA3_bif1
OM3_bif1_B3	Third Branch of the OM3_bif1	RPD3_bif1_B2	Second branch of the RPDA3_bif1
OM3_bif2	Second bifurcation of the OM3	RPD3_bif1_B3	Third branch of the RPDA3_bif1
OM3_bif2_B1	First Branch of the OM3_bif2	RPD3_bif2	Second bifurcation of the RPD3
OM3_bif2_B2	Second Branch of the OM3_bif2	RPD3_bif2_B1	First branch of the RPDA3_bif2
OM3_bif2_B3	Third Branch of the OM3_bif2	RPD3_bif2_B2	Second branch of the RPDA3_bif2
		RPD3_bif2_B3	Third branch of the RPDA3_bif2
OM4	Obtuse Marginal 4 of the LCx		
OM4_B1	First Branch of the OM4	RPLSA	Right Posterolateral Segment Artery
OM4_B2	Second Branch of the OM4	RPLSA_PLB1	First posterolateral brach of the RPLSA
OM4_B3	Third Branch of the OM4	RPLSA_PLB1_B1	First branch of the RPLSA_PLB1
OM4_bif1	First bifurcation of the OM4	RPLSA_PLB2	Second posterolateral brach of the RPLSA
OM4_bif1_B1	First Branch of the OM4_bif1	RPLSA_PLB2_B1	First branch of the RPLSA_PLB2
OM4_bif1_B2	Second Branch of the OM4_bif1	RPLSA_PLB3	Third posterolateral brach of the RPLSA
OM4_bif1_B3	Third Branch of the OM4_bif1	RPLSA_PLB3_B1	First branch of the RPLSA_PLB3
OM4_bif2	Second bifurcation of the OM4	RPLSA_PLB4	Fourth posterolateral brach of the RPLSA
OM4_bif2_B1	First Branch of the OM4_bif2	RPLSA_PLB4_B1	First branch of the RPLSA_PLB4
OM4_bif2_B2	Second Branch of the OM4_bif2	RPLSA_AB1	First atrial brach of the RPLSA

Label	Description		Label	Description
OM4_bif2_B3	Third Branch of the OM4_bif2		RPLSA_AB2	Second atrial brach of the RPLSA
			RPLSA_AB3	Third atrial brach of the RPLSA
OM5	Obtuse Marginal 5 of the LCx			
OM5_B1	First Branch of the OM5		LPLSA	Left Posterolateral Segment Artery
OM5_B2	Second Branch of the OM5		LPLSA_PLB1	First posterolateral brach of the LPLSA
OM5_B3	Third Branch of the OM5		LPLSA_PLB1_B1	First Branch of the LPLSA_PLB1
OM5_bif1	First bifurcation of the OM5		LPLSA_PLB1_B2	Second Branch of the LPLSA_PLB1
OM5_bif1_B1	First Branch of the OM5_bif1		LPLSA_PLB2	Second posterolateral brach of the LPLSA
OM5_bif1_B2	Second Branch of the OM5_bif1		LPLSA_PLB3	Third posterolateral brach of the LPLSA
OM5_bif1_B3	Third Branch of the OM5_bif1		LPLSA_PLB4	Fourth posterolateral brach of the LPLSA
OM5_bif2	Second bifurcation of the OM5		LPLSA_AB1	First atrial brach of the LPLSA
OM5_bif2_B1	First Branch of the OM5_bif2		LPLSA_AB2	Second atrial brach of the LPLSA
OM5_bif2_B2	Second Branch of the OM5_bif2		LPLSA_AB3	Third atrial brach of the LPLSA
OM5_bif2_B3	Third Branch of the OM5_bif2			
RI				
RI_B1	First Branch of the RI			
RI_B2	Second Branch of the RI			
RI_B3	Third Branch of the RI			
RI_bif1	First bifurcation of the RI			
RI_bif1_B1	First Branch of the RI_bif1			
RI_bif1_B2	Second Branch of the RI_bif1			
RI_bif1_B3	Third Branch of the RI_bif1			
RI_bif2	Second bifurcation of the RI			
RI_bif2_B1	First Branch of the RI_bif2			
RI_bif2_B2	Second Branch of the RI_bif2			
RI_bif2_B3	Third Branch of the RI_bif2			

Table B.1: Complete list of arterial labels and the corresponding description.

Appendix C

Coronary anatomy

As any other tissue, the heart needs to be perfused. The arterial network responsible for the blood to the heart is the *coronary arterial tree*. A gross anatomical description of coronary arteries is presented, with the primary objective of: (i) serving as quick reference guide for medical image interpretation through the segmentation process, (ii) understanding of morphometric information through arterial modeling and analysis, (iii) being useful through hemodynamic simulation parametrization and interpretation. This appendix resumes the work of [108].

The clinical importance of which artery perfuses each myocardial territory, had led to the concept of dominance, which resumes to the identification of the artery that gives rice to the *posterior descendant artery* (PDA), the *posterolateral artery* (PLA), and the atrioventricular (AV) nodal artery. Therefore, if these arteries originate from the *right coronary artery* (RCA), the circulation can be classified as "right-dominant". Alternatively, if supplied by the left *circumflex artery* (LCx), the circulation can be classified as "left dominant". Furthermore, a third classification is used, the "co-dominant" circulation, when the right coronary artery supplies the PDA and terminates.

Approximately 85% of the general population is right-dominant, 8% are left-dominant, and 7% are co-dominant. Therefore, there are many variations of "normal" anatomy that are not considered "abnormal". Figure C.1 presents the schematic structure of heart vessels for different circulation dominance.

The left ventricle connects to the aorta through the aortic valve, the *bulbar aortic sinus* and the *proximal ascending aorta* comprise the *aortic root*. The bulbous sinus and the three *aortic cusps* merge to form the *sinuses of Valsalva*. The coronary *ostia*[1] are usually located below the *sinotubular ridge*[2], within the sinus of Valsalva, centrally located between the commissural attachments of the aortic cusps. These structures are illustrated in Figure C.2. The heart tissue irrigation originates at the *right and left coronary arteries*, which (in principle) provide blood to the right and left heart structures respectively.

C.1 Right coronary artery (RCA)

The RCA, lies deep in the epicardial fat between the *pulmonary conus*[3]. It continues to course downward around the *acute margin of the heart*[4] and then posteriorly, remaining

---

[1] The ostia is the rising point, the beginning of an artery.

[2] A slight circumferential thickening, also known as *sinotubular junction*, that marks the separation of the ascending aorta and the sinuses of Valsalva.

[3] A conical extension of the right ventricle, from which the pulmonary artery originates.

[4] Left border of the heart associated to the right ventricle.
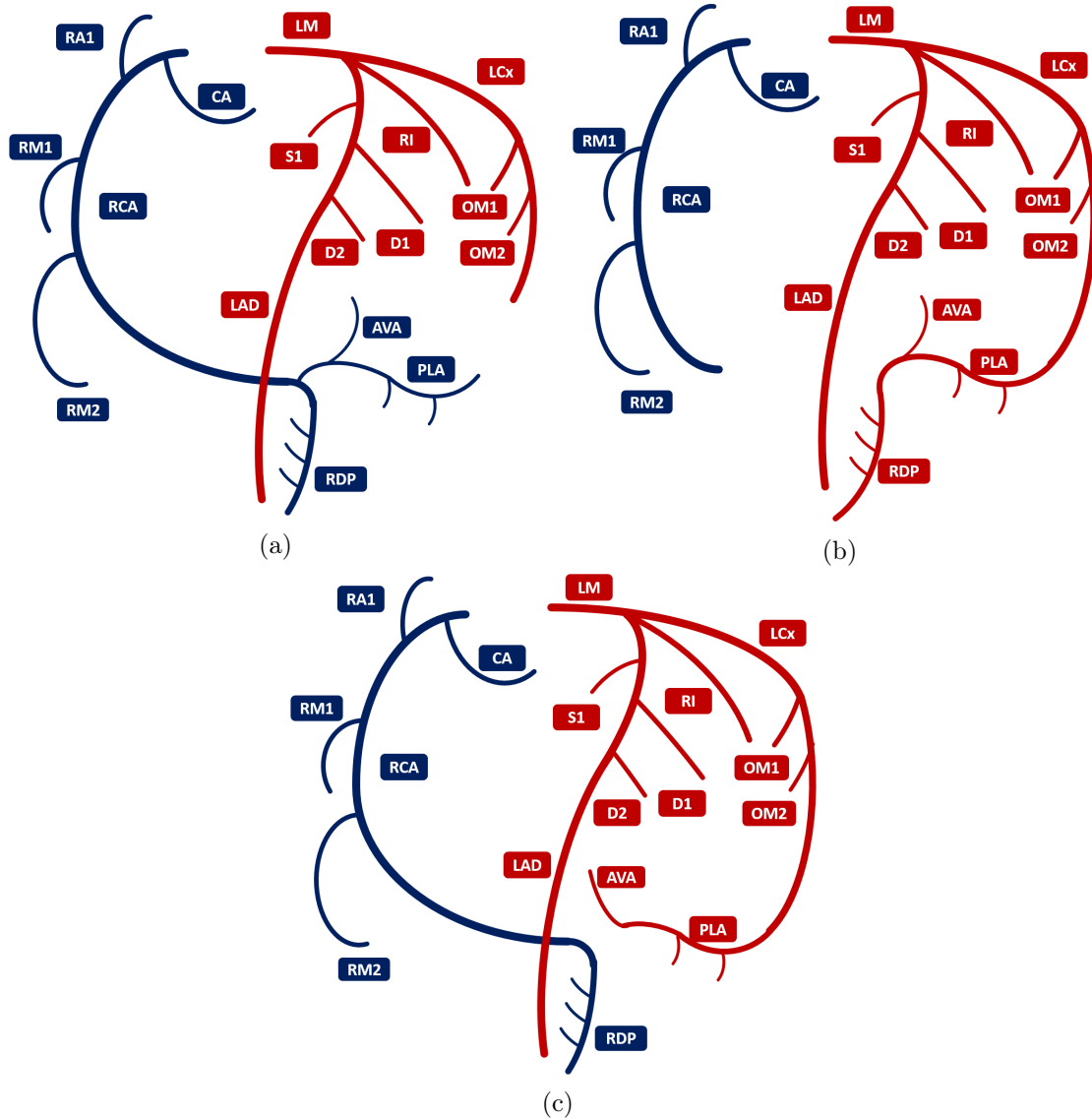
Figure C.1: Right-dominant (a), left-dominant (b) and co-dominant circulation. LM = left main artery; LAD = left anterior descending artery; Cx = circumflex; RCA = right coronary artery; S = septal; D = diagonal; OM = obtuse marginal; RM = right marginal; RPDA = right posterior descending artery; RPL = right posterolateral; RI = ramus intermediate.

in the *atrioventricular sulcus*[5] until it reaches the *interventricular sulcus*[6] at the *crux*[7].

The branches of the RCA, from proximal to distal are: The *conus artery*, right atrial branches, right ventricular branches, interventricular septal branches, atrioventricular nodal branches, and left ventricular branches (posterolateral branches of the posterolateral segment artery). Both, atrial and ventricle right branches are named by the point of rise: anterior (proximal), marginal (intermediate) or posterior (distal).

The conus artery[8] when present, takes a semicircular course away from the RCA on the epicardial anterior surface of the right ventricle at the level of the pulmonary valve.

---

[5] Area of separation of the right atrium and right ventricle, at the heart surface.

[6] Area of separation of the right and left ventricles, at the heart surface.

[7] The point where the *interatrial sulcus* (which separates the right and left atrium) crosses the interventricular sulcus

[8] Also known as *infundibular artery*, *adipose artery*, *third coronary artery*, *arteria of Vieussens*.

(a)

(b)
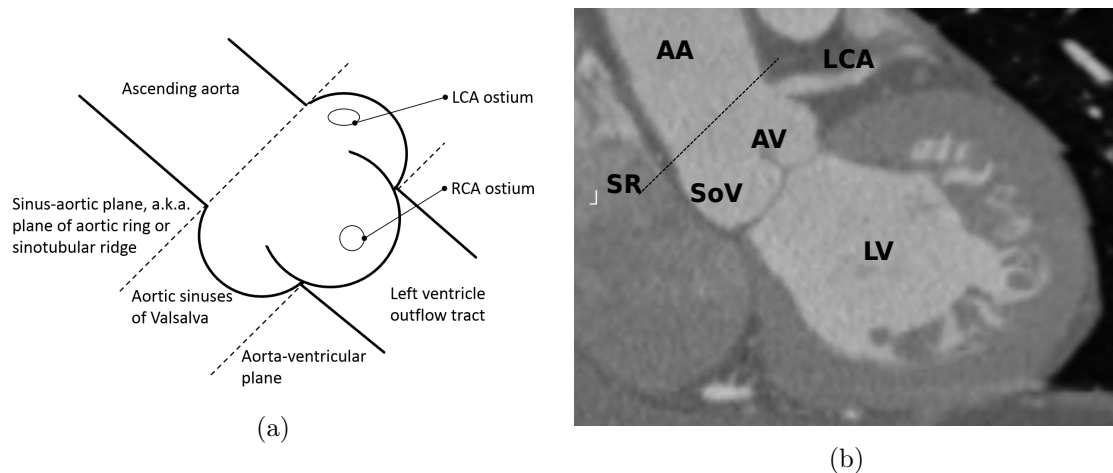
Figure C.2: Aortic root structure illustrations (a), and a visualization in a CTA image (b). AA - Ascending Aorta; AV - Aortic valve; LV - Left ventricle; LCA - Left coronary artery; SR - Sinotubular ridge; SoV - Sinus of Valsalva.

It terminates near the superior aspect of the anterior interventricular sulcus. A separate ostium, at the right sinuses, gives rise to the conus artery in 23% to 51% of patients. The conus artery often forms a *vascular anastomotic bridge*[9] with a corresponding branch from either the *left main* (LM) or proximal *left anterior descending artery*[10] (LAD) forming the *circle of Vieussens*[11].

The atrial branches of the RCA are very variable in number, location and size (usually small in caliber, ≤ 1 mm). The main atrial artery is usually the atrial branch that terminates in the *sinoatrial node*. The artery to the sinoatrial node arises from the RCA in 60% of subjects and from the left *circumflex artery* (LCx) in the remaining 40%. During its course, it gives off branches to both atria and penetrates into the *interatrial septum*[12]

The right ventricular branches originates from the RCA when it passes the atrioventricular sulcus at nearly right angles from the RCA and course over the anterior, marginal, and posterior surface of the right ventricle. In approximately 65% to 85% of subjects, 1 or 2 right ventricular branches arise from the anterior segment of the RCA.

The posterior descending artery[13] (PDA) usually arises as a branch or continuation of the RCA at the crux, and courses along the posterior aspect of the interventricular sulcus a variable distance toward the *apex*[14]. The interventricular septum branches arises from the PDA and supply the inferior aspect of the interventricular septum.

The atrioventricular nodal arteries usually arises from the RCA and less frequently from the left circumflex artery, depending on which artery crosses the crux.

The left ventricular branches of the RCA are known as the *posterolateral arteries*. Angiographically, they represent a continuation of the RCA beyond the PDA. These branches traverse the interventricular septum and supply the inferior wall of the left ventricle.

---

[9]Connection of two arterial branches, resulting in a blood flow junction, not a separation as occur in branches.

[10]Also known as intervetricular anterior artery.

[11]This bridge may play a role as a collateral pathway to the LAD.

[12]The wall of tissue that separates the right and left atria.

[13]Also known as intervetricular posterior artery.

[14]The lowest superficial part of the heart.

C.2 Left coronary

The left coronary or left main artery[15] (LMA) arises from the left sinus of Valsalva and courses laterally between the base of the pulmonary trunk and left atrium. The LMA usually has two major branches, the LAD and LCx. Occasionally, the left main "trifurcates" into the LAD, LCx, and the ramus intermediate artery (RIA)[16].

In practice, the LAD is the continuation of the LMA. It passes to the left of the pulmonary trunk (forming a 90° angle), travels into the upper portion of the interventricular sulcus, and continues toward the apex of the heart[17]. How far the LAD extends is variable, but it usually at least continues to the apex. Occasionally, the LAD bifurcates into two parallel vessels.

The diagonal branches of the LAD, irrigates the left ventricle. They run parallel to one another and are variable in number (2 to 9)[18]. Right ventricular branches of the LAD, when present, are usually short and extend over the adjacent right ventricular surface, usually meeting right ventricular branches of the RCA.

Interventricular branches, or *septal perforating* branches[19], descend from the LAD and travel down through the interventricular septum toward the smaller branches traveling upward from the posterior descending artery. This branches also has a mechanical function, which is immobilize the LAD, fixing it to the heart, limiting its motion, and preventing buckling of the artery during systole.

The LCx arises from the LMA at almost a right angle[20], and follows a course that nearly mirrors the RCA. The degree of variability of the left circumflex artery and its branches is comparable to that of the RCA. At the crux, the left circumflex artery may extend to become the posterior descending artery and supply the AV node or may terminate, depending on dominance, as described above.

The ventricular branches of the LCx branch at acute angles. In 80% of subjects, 1 to 3 anterior left ventricular branches are present. Clinicians usually name them as *obtuse marginals* (OM1, OM2, OM3).

---

[15]The length of the LMA, in general, varies from 2 to 12 mm but may be up to 30 mm. Its diameter, ranging from 5 to 10 mm, is generally inversely related to its length.

[16]This third branch originates between the angle formed by the LAD and the left circumflex arteries and has various names, including *median artery*, *left diagonal artery*, and *straight left ventricular artery*.

[17]During its course, the LAD is often covered by superficial muscle fibers, which run at right angles to the vessel, creating what is known as a "myocardial bridge".

[18]If a RI artery is present, the diagonal vessels are less prominent and arise more distally.

[19]Which range in diameter from 0.5 to 1.2 mm and penetrate two-thirds into the anterior septum. The length of these vessels ranges from 40 to 80 mm and tends to become shorter as they reach the apex.

[20]At its origin, the LCx has a diameter ranging between 1.5 and 5 mm.

Appendix D

Diagnostic of coronary artery disease

Over the years, several clinical tests were developed to detect the presence of CAD, with increase interest in quantifying the functional significance of stenosis. Such procedures can be roughly divided in three categories: (i) exercise test with monitoring of CAD symptoms or direct observation of coronary flow; (ii) invasive and noninvasive medical images; (iii) functional assessment of lesion through physiologic response, i.e. absolute/relative coronary flow reserve (CFR) and fractional flow reserve (FFR). Details on FFR are presented in Chapter 8 and Appendix E.

D.1 Tests based on exercise

D.1.1 Stress test

The patient is hooked up to equipment to monitor the heart. Walks slowly in place on a treadmill. Then the speed is increased for a faster pace and the treadmill is tilted to produce the effect of going up a small hill. Afterward, the patient will sit or lie down to have their heart and blood pressure checked.

Heart rate, breathing, blood pressure, electrocardiogram, and how tired the patient feel are monitored during the test.

It is a noninvasive, safe and inexpensive test that can be used to obtain information on functional capacity and the symptomatic, hemodynamic, and ECG responses to exercise. Although it provides valuable prognostic and diagnostic information, inconclusive test results are common and can lead to uncertainty about the likelihood of flow-limiting coronary artery disease [47].

D.1.2 Stress echocardiography

It utilizes ultrasound imaging of the heart. First, images are taken "at rest" to acquire a baseline of the patient's wall motion. Then, the patient heart rate is increased by a controlled exercise modality. Finally, images of the heart are taken "at stress" to assess wall motion at the peak heart rate. Ischemia of one or more coronary arteries could cause a wall motion abnormality which could indicate CAD.

It is a noninvasive test, that assesses wall motion of the heart, it does not, however, image the coronary arteries directly. Patients with poor acoustic windows (e.g., obesity, obstructive lung disease) may have reduced image quality, which can lower the diagnostic accuracy of the examination [47]. The lack of radiation exposure makes this a compelling option for young patients.

D.1.3 Exercise test and thallium scanning

Measures the amount of blood in the heart muscle at rest and during exercise. A radioactive tracer (thallium) is injected into the vein in the arm, as the tracer moves through the heart muscle, areas that have good blood flow absorb the tracer. Areas that do not absorb tracer may not be getting enough blood or may have been damaged. This test is also known by other names including myocardial perfusion scan, myocardial perfusion imaging, thallium scan, cardiac perfusion scan, sestamibi cardiac scan, and nuclear stress test.

Images may be taken by a rotating gamma scintillation camera, or a single photon emission computed tomography (SPECT) scan.

It is a noninvasive test, that can provide data for (A/R)-CFR index calculus. In general, nuclear techniques tend to underestimate the extent of CAD, and are sensitive to attenuation artifacts, common in obese patients and women with extensive breast tissue [47].

D.2 Medical imaging

D.2.1 Coronary angiography (CA)

It is a procedure based on x-ray imaging to see the coronary arteries. During the procedure, a catheterization is performed in order to reach the coronary tree. An x-ray contrast agent is injected into the arteries of interest, while the x-ray images (angiograms) are taken. Due to the spatial and temporal resolution, CA is considered the gold standard for CAD detection and diagnosis.

D.2.2 Quantitative coronary angiography (QCA)

Using biplane coronary angiography, perpendicular images of the heart vasculature are acquired and used to measure the percentage of stenosis, area of stenosis, stenosis length, reference diameter of the adjacent normal segments and minimal luminal diameter. Then the measure of both planes is averaged to get the final values of each geometric variable. Despite previous works, [274] was the first to propose an automatic methodology with small variability for the segmentation process.

It is an invasive test that needs catheterization in order to achieve biplane angiogrpahic images. It strongly depends on image quality and segmentation algorithm for the correct determination of different geometric characteristics of the stenotic arteries.

D.2.3 Multi Slice Computed Tomography Angiography (MSCTA)

MSCTA, or coronary computer tomography angiography (CCTA), is a conventional computed tomography angiography study, conducted with a multi slice scanner. This type of scanner can acquire multiple CT slice at a time, decreasing the study length. The acquisition process is synchronized with an electrocardiogram in order to sample the heart at the same moment over the cardiac cycle. The injection of contrast agent is performed through veins at the arm.

With MSCTA it si possible to evaluate the coronary luminal changes, visualize the coronary artery wall morphology, identify and characterize coronary plaques, especially the non-stenotic plaques that may be undetected by conventional coronary angiography. Furthermore, MSCTA is a noninvasive technique that can provide prognostic information in patients suspected of having CAD. According to [323], despite promising results reported in the literature, MSCTA has the disadvantage of having a high radiation dose. Nevertheless,

MSCTA can be used as a reliable technique for excluding patients suspected of CAD, thereby reducing the need for invasive coronary angiography.

D.3   Functional assessment of lesions

D.3.1   Absolute coronary flow reserve (A-CFR)

Introduced by [130], A-CFR, also known as coronary vasodilatory reserve, is defined as the maximal flow (reaching myocardium) under vasodilation, divided (normalized) by control flow at rest. The A-CFR is defined as

$$\text{A-CFR} = \frac{Q_{\text{s}}^{\text{max}}}{Q_{\text{s}}^{\text{res}}} \tag{D.3.1}$$

where sub-index s indicates that an stenosis is present, and supra-indexes max and res stand for maximal vasodilation and rest conditions. Q is the flow reaching the myocardium.

The different flow values can be measured by invasive catheterization (flow-meters) or by noninvasive exercise test and thallium scans. As explained by [129], changes in aortic pressure and heart rate are known to alter cardiac workload and, therefore, baseline coronary blood flow, as well as altering maximal coronary flow under conditions of maximal vasodilation.

This index reflects the flow capacity of the entire coronary vascular bed under whatever conditions of pressure, work load, hypertrophy, vasomotor tone or stenosis are present.

There is controversy on the normal ranges. Kern et al. [179] studied A-CFR in 214 patients using average peak velocities for estimation of flow in a per vessel fashion (416 arteries). They established normal reference ranges for assessing the coronary circulation and post-stenotic A-CFR in patients with and without coronary artery disease. They also present reference values of peak velocities in the coronary arteries.

McGinn et al. [218] studied the long-term variability of serial CFR measurements in humans. Differences in CFR between studies were related to changes in heart rate but not to changes in mean arterial pressure. They concluded that serial CFR measurements in humans are highly reproducible in the absence of conditions known to affect resting or hyperemic coronary blood flow. Increases in heart rate reduced CFR because (resting) CBFV was increased while (hyperemic) CBFV was unchanged. In contrast, changes in mean arterial pressure did not alter CFR. Proper interpretation of CFR measurements should take into account the hemodynamic conditions at which they are obtained.

D.3.2   Relative coronary flow reserve (R-CFR)

In an effort to complement the A-CFR index, [129] presented the R-CFR, defined as maximal flow in a stenotic artery divided (normalized) by the normal maximal flow in the absence of stenosis. The R-CFR is defined as

$$\text{R-CFR} = \frac{Q_{s}^{\text{max}}}{Q_{n}^{\text{max}}} \tag{D.3.2}$$

where sub-index s and n indicate stenotic and normal artery, and supra-indexes max stands for maximal vasodilation and rest conditions.

[129] concluded that R-CFR reflects more specifically the effects of the stenosis independent of and not affected by the other physiologic variables if normal maximal flow is high enough. And the index can complement A-CFR information. R-CFR is computed directly from flow measurements acquired by invasive catheterization or noninvasive nuclear scanning. The normal flow is measured on a healthy contra-lateral artery, therefore in cases of three vessel diseases it could not be measured properly.

D.3.3 Absolute/Relative Stenosis flow reserve (A/R-SFR)

In an effort to estimate CFR from pressure drops over a stenotic artery, [128, 127, 129] developed an alternative procedure to indirectly measure CFR from QCA. The geometrical parameters (together with estimated normals fluxes) are used to predict pressure drops using a (hemodynamic based) stenosis model, proposed in [362].

Although the index allows comparison of complex lesions without misleading effects due to differences in physiologic conditions among the patients (separate from stenosis geometry). As the model strongly depends on stenosis geometry, the image segmentation process is crucial to achieve good results. At the time this index was proposed, limitations on automatic segmentation were too high for clinical usage. Due to the angiography imaging process, this is an invasive test.

D.3.4 dp$_{v50}$

The combination of the diastolic flow velocity and pressure gradient (v-dp) gives a comprehensive description of the coronary stenosis severity [212]. It was shown that the v-dp relation in humans is associated to normal arteries versus intermediate and severe coronary stenoses. The dp$_{v50}$ is the instantaneous pressure gradient at a middiastolic coronary flow velocity of 50 cm/s. In essence, this measurement provides an index of stenosis resistance and could potentially be able to differentiate the contribution of epicardial disease to abnormal CFR. The main drop-back of this method is the special doppler catheter that needs to be used for velocity measurements.

D.3.5 Transluminal attenuation gradient

Opacification of coronary artery lumen and luminal contrast density with CTA is dependent upon contrast bolus geometry (contrast iodine concentration, contrast infusion rate, and volume), timing of image acquisition, cardiac output, and coronary flow. Using sufficiently new CT scanner technology, the heart region can be imaged in a single heartbeat, reducing the effects of such factors. Furthermore, measurement of coronary contrast opacification might be used to estimate, indirectly, coronary blood flow [74, 191]. It might be useful for estimating flow across unevaluable coronary segments, such as stents or calcified regions, which might improve diagnostic accuracy. Using such measurements on hyperemic states could allow identification of hemodynamically significant stenoses [357, 322].

Transluminal attenuation gradient (TAG), is defined as the gradient of intraluminal radiological attenuation. It is computed as the slope of the linear regression of pixel intensity through a region of interest of an artery containing a lesion. Several studies have correlated it with percentage stenosis and even with FFR [356].

D.3.6 Instantaneous wave-free ratio (iFR)

Sometimes referred to as instant flow reserve, it is an invasive technique to assess ischemia risk of a stenosis. iFR is performed using invasive coronary pressure wires placed proximal and distal to the stenosis that is to be assessed. Pressure is recorded in an specific period in diastole called the wave-free period. It is defined as the ratio iFR $= P_a/P_d$, between distal (P_d) and proximal (P_a) pressures, over such period. The rationale behind the definition of iFR is that during this wave-free period, the microvascular resistance is approximatly constant, and therefore there is a linear relation between pressure and flow.

Note that the definitions of iFR and FFR are the same. Both indexes exploit the linear relationship between flow and pressure in a constant microvascular resistance period. The difference is that iFR uses the wave-free period under normal (resting) condition, while FFR is defined during drug-induced hyperemic conditions. Therefore, the iFR can

be computed using available equipment without the need for pharmacological vasodilators. Usually, the iFR is averaged through several wave-free periods, and iFR values below 0.90 suggest flow limitation.

Since its introduction in 2012 [303], there have been several studies testing and comparing iFR to FFR [279, 36, 164, 302, 261, 261, 159, 248]. Furthermore, three large randomized trials are in progress (DEFINE-FLAIR, iFR-SWEDEHEART and SYTNAX II), which aim to consolidate the iFR technique in clinical practice.

Appendix E

FFR formulae Derivation

This appendix explains how the FFR formulae are derived from the hypothesis that coronary circulation can be modeled with purely resistive electrical components under maximum hyperemia, see Figure E.1.

(a)   (b)
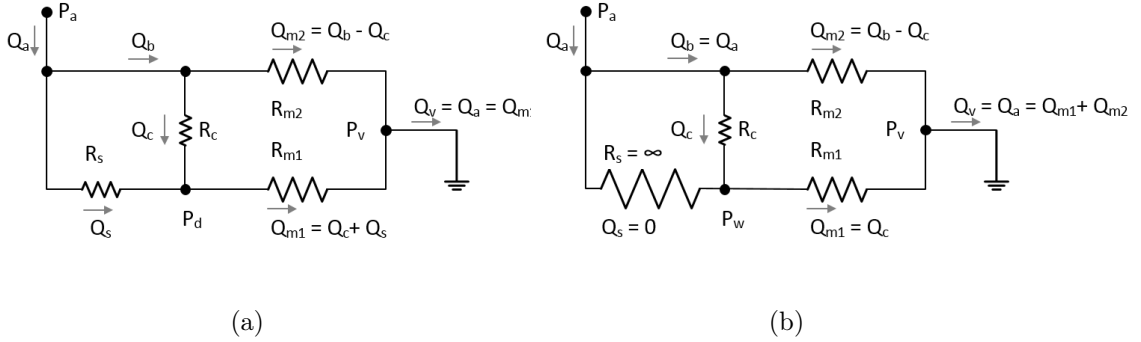
Figure E.1: Schematic representation of coronary circulation with a purely resistive electrical model. Panel (a) represents a stenotic condition, while panel (b) stands for a total occlusion condition.

Before starting with the derivation, some useful relationships (valid in maximum vasodilation) are presented. All of them are easily obtained from Figure E.1, considering total occlusion of the stenosis ($R_s = \infty$).

$$Q_{m1} = Q_c \tag{E.0.1a}$$

$$P_a - P_v = Q_{m1}(R_{m1} + R_c) \tag{E.0.1b}$$

$$P_w - P_v = Q_{m1}R_{m1} \tag{E.0.1c}$$

$$P_a - P_w = Q_c R_c = Q_{m1}R_c \tag{E.0.1d}$$

Then, the following ratios between pressure drops are constant,

$$\frac{P_a - P_v}{P_w - P_v} = \frac{Q_{m1}(R_{m1} + R_c)}{Q_{m1}R_{m1}} = 1 + \frac{R_c}{R_{m1}} = C_1 \tag{E.0.2a}$$

$$\frac{P_w - P_v}{P_a - P_w} = \frac{Q_{m1}R_{m1}}{Q_{m1}R_c} = \frac{R_{m1}}{R_c} = C_2 \tag{E.0.2b}$$

$$\frac{P_a - P_v}{P_a - P_w} = \frac{Q_{m1}(R_{m1} + R_c)}{Q_{m1}R_c} = \frac{R_{m1}}{R_c} + 1 = C_3 \tag{E.0.2c}$$

Hereafter, the supra-index N stands for normal conditions, which means that there is no stenosis nor collateral flux ($Q_c^N = 0$). In normal conditions, the other resistances, as well as P_a and P_v do not change.

Now, consider the definition of coronary fractional flow reserve (FFR$_{\text{cor}}$), and let expand the expression,

$$\text{FFR}_{\text{cor}} = \frac{Q_s}{Q_s^N} = \frac{Q_{m1} - Q_c}{Q_{m1}^N - Q_c^N}$$

Using the fact that $Q_c^N = 0$ and substituting the fluxes,

$$= \frac{\dfrac{P_d - P_v}{R_{m1}} - \dfrac{P_a - P_d}{R_c}}{\dfrac{P_a - P_v}{R_{m1}}} = \frac{P_d - P_v - (P_a - P_d)\dfrac{R_{m1}}{R_c}}{P_a - P_v} \tag{E.0.3}$$

Substituting by (E.0.2b) and by simple algebra,

$$= \frac{P_d - P_w}{P_a - P_w} = 1 - \frac{\Delta P_s}{P_a - P_w}$$

Here, $\Delta P_s = P_a - P_d$ is the pressure drop across the stenosis. Then, the myocardium fractional flow reserve (FFR$_{\text{myo}}$) can be calculated from its definition as follows,

$$\text{FFR}_{\text{myo}} = \frac{Q_{m1}}{Q_{m1}^N} = \frac{\dfrac{P_d - P_v}{R_{m1}}}{\dfrac{P_a - P_v}{R_{m1}}} = \frac{P_d - P_v}{P_a - P_v} = 1 - \frac{\Delta P_s}{P_a - P_v} \tag{E.0.4}$$

Note that it is possible to calculate the contribution of collateral flow to the myocardial flow in presence of stenosis relative to the normal myocardium flow, as

$$\frac{Q_c}{Q_{m1}^N} = \frac{Q_{m1} - Q_s}{Q_{m1}^N} = \frac{Q_{m1}}{Q_{m1}^N} - \frac{Q_s}{Q_{m1}^N}$$

Due that $Q_{m1}^N = Q_s^N$ without stenosis $\tag{E.0.5}$

$$= \frac{Q_{m1}}{Q_{m1}^N} - \frac{Q_s}{Q_s^N} = \text{FFR}_{\text{myo}} - \text{FFR}_{\text{cor}}$$

Finally, the ratio between these indexes associated to two clinical scenarios, before (*bi*) and after (*ai*) intervention, can be derived using simple algebra and the constant relationships from equation (E.0.2). Therefore, the ratio between stenotic flow before and after intervention is

$$\frac{Q_s^{(ai)}}{Q_s^{(bi)}} = \frac{Q_s^{(ai)}}{Q_s^{(bi)}} \frac{Q_s^{(bi)^N}}{Q_s^{(bi)^N}} \frac{Q_s^{(ai)^N}}{Q_s^{(ai)^N}} = \frac{\text{FFR}_{\text{cor}}^{(ai)}}{\text{FFR}_{\text{cor}}^{(bi)}} \frac{Q_s^{(ai)^N}}{Q_s^{(bi)^N}}$$

In normal condition $Q_s^{(x)^N} = Q_{m1}^{(x)^N} = (P_a^{(x)} - P_v^{(x)})/R_{m1}$, then

$$= \frac{\text{FFR}_{\text{cor}}^{(ai)}}{\text{FFR}_{\text{cor}}^{(bi)}} \frac{P_a^{(ai)} - P_v^{(ai)}}{P_a^{(bi)} - P_v^{(bi)}} \tag{E.0.6}$$

Expressing the FFR in terms of pressure drops

$$= \frac{P_d^{(ai)} - P_w^{(ai)}}{P_a^{(ai)} - P_w^{(ai)}} \frac{P_a^{(bi)} - P_w^{(bi)}}{P_d^{(bi)} - P_w^{(bi)}} \frac{P_a^{(ai)} - P_v^{(ai)}}{P_a^{(bi)} - P_v^{(bi)}} = \frac{P_d^{(ai)} - P_w^{(ai)}}{P_d^{(bi)} - P_w^{(bi)}}$$

Note that $Q_s^{(ai)}/Q_s^{(bi)}$ does not depend on arterial pressure P_a. Another way to test the functional improvement of a stenotic artery after an angioplasty accounting the arterial pressure, or as [266] stated: "correcting by arterial pressure changes"

$$\frac{\text{FFR}_{\text{cor}}^{(ai)}}{\text{FFR}_{\text{cor}}^{(bi)}} = \frac{P_d^{(ai)} - P_w^{(ai)}}{P_a^{(ai)} - P_w^{(ai)}} \frac{P_a^{(bi)} - P_w^{(bi)}}{P_d^{(bi)} - P_w^{(bi)}} \tag{E.0.7}$$

Note that, if arterial (and wedge) pressure is maintained before and after intervention, equations (E.0.6) and (E.0.7) are the same. An equivalent reasoning can be followed to measure the relative improvement on the myocardial perfusion flow, therefore

$$\frac{Q_{m1}^{(ai)}}{Q_{m1}^{(bi)}} = \frac{P_d^{(ai)} - P_v^{(ai)}}{R_{m1}} \frac{R_{m1}}{P_d^{(bi)} - P_v^{(bi)}} = \frac{P_d^{(ai)} - P_v^{(ai)}}{P_d^{(bi)} - P_v^{(bi)}} \tag{E.0.8}$$

As before, in order to correct by accounting possible arterial pressure changes,

$$\frac{\text{FFR}_{\text{myo}}^{(ai)}}{\text{FFR}_{\text{myo}}^{(bi)}} = \frac{P_d^{(ai)} - P_v^{(ai)}}{P_a^{(ai)} - P_v^{(ai)}} \frac{P_a^{(bi)} - P_v^{(bi)}}{P_d^{(bi)} - P_v^{(bi)}} \tag{E.0.9}$$

Note that, if arterial (and venous) pressure is maintained before and after intervention, equations (E.0.8) and (E.0.9) are equivalent.

Finally, calculating the relative contribution of collateral flow before and after the intervention is another indicator of improved functionality of the stenosed artery. Contrary to equations (E.0.6) and (E.0.8) where incremental values indicates better angioplasty outcomes, (E.0.10) must decrease in order to indicate that collateral flow is no longer needed (or at least, less needed),

$$\frac{Q_c^{(ai)}}{Q_c^{(bi)}} = \frac{P_a^{(ai)} - P_d^{(ai)}}{R_c} \frac{R_c}{P_a^{(bi)} - P_d^{(bi)}} = \frac{P_a^{(ai)} - P_d^{(ai)}}{P_a^{(bi)} - P_d^{(bi)}} = \frac{\Delta P_s^{(ai)}}{\Delta P_s^{(bi)}}$$

Or corrected by arterial - venous pressure changes $\tag{E.0.10}$

$$= \frac{\Delta P_s^{(ai)}}{\Delta P_s^{(bi)}} \frac{P_a^{(bi)} - P_v^{(bi)}}{P_a^{(ai)} - P_v^{(ai)}}$$

Appendix F

Proximal Murray Distribution criterion

This appendix details the Proximal Murray Distribution (PMD) criterion to determine the terminal resistance parameters of a given network: a centerline with point-wise radius information, a total inlet flow Q_{in}, a characteristic ΔP between the inlet and the outlets and a Murray exponent γ. The criterion consists in the recurrent usage of Murray's law at each branch point, while traversing the network from the inlet to all the outlets in a pre-order fashion.

The algorithm pseudo-code is presented in Alg. 1, where it is assumed that the coronary arterial tree model is represented by a tree-like computational structure. Note that at each junction (node), the algorithms checks for an existing physiological restriction, and if it exists, the restriction is ensured by modifying the Murray's flow estimated at the junction.

The so-called physiological restrictions are rules of flow distribution per outlet of specifics junctions, that depend on the circulation dominant of the complete tree, and are based on medical observations reported in the literature [286]. Table F.1 presents the mean and STD used in our implementation for the Ao-RCA-LM and LM-LAD-LCx junctions, the only restrictions that were enforced. If the given flow distribution does not satisfy the criterion in Table F.1, it is slightly modified until the flow percentage is in the range specified by the restriction.

| Circ. Dominance | Inlet: Ao | | Inlet: LM | |
	RCA	LM	LAD	LCx
Right	42±8	58±14	54±19	46±4
Left or Co	25±15	75±15	45±5	55±15

Table F.1: Physiological restrictions enforced in this work. Flow values are percentages of the inlet flow.

Algorithm 1 Pseudo-code of the PMD algorithm for estimation of terminal resistances. Some generic functions are used:

ISTERMINAL: Returns true if the node of the arterial tree represents a terminal segment.

EMPTYLIST: Creates an empty list object.

APPEND: Appends a value or a list to a given list (first argument).

GETLISTOFRADIUSOUTLETS: Returns a list with the radius value at each arterial outlet of the given node.

GETNUMOUTLETS: Returns the number of arterial segment outlets of the given node.

GETOUTLETNODE: Returns the arterial segment outlet i of the given node.

HASPHYSIOLOGICRESTRICTION: Returns true if the given node has an associated physiological restriction based on the label of the outlet segments.

ENSURESPHYSIOLOGICRESTRICTION: Returns a list of flows that satisfy the physiological restriction associated to the given node.

1: **function** PMD(Q_{in}, ΔP, γ, node)
2:     **if** ISTERMINAL(node) **then**
3:         **return** $R = \Delta P / Q_{\text{in}}$;
4:     **end if**
5:     listR = EMPTYLIST();
6:     r = GETLISTOFRADIUSOUTLETS(node);
7:     $\beta = Q_{\text{in}} / \sum_j r_j$;
8:     **for** $i = 0$ **to** GETNUMOUTLETS(node) **do**
9:         $Q_i = \beta r_i^{\gamma}$;
10:     **end for**
11:     **if** HASPHYSIOLOGICRESTRICTION(node) **then**
12:         Q = ENSURESPHYSIOLOGICRESTRICTION(node, Q)
13:     **end if**
14:     **for** $i = 0$ **to** GETNUMOUTLETS(node) **do**
15:         append(listR, PMD(Q, ΔP, γ, GETOUTLETNODE(node, i)))
16:     **end for**
17:     **return** listR;
18: **end function**

Bibliography

[1] Computational Hemodynamics Lab website, 2015.

[2] euHeart project website, 2015.

[3] HeartFlow Inc. website, 2015.

[4] Hemodynamics Modeling Laboratory (HeMoLab), 2015.

[5] The AneurRisk Project website, 2015.

[6] The ARCH project website, 2015.

[7] The Brain Vasculature (BraVa) website, 2015.

[8] The Cardiac Atlas Project website, 2015.

[9] The Graphical Interface for Medical Image Analysis and Simulation (GIMIAS) website, 2015.

[10] The Insight Segmentation and Registration Toolkit, 2015.

[11] The Vascular Modeling Toolkit website, 2015.

[12] The Virtual Physiological Human (VPH) initiative website, 2015.

[13] ADINA, 2016.

[14] ANSYS CFX, 2016.

[15] ANSYS FLUENT, 2016.

[16] Jordi Alastruey, Nan Xiao, Henry Fok, Tobias Schaeffter, e C. Alberto Figueroa. On the impact of modelling assumptions in multi-scale, subject-specific models of aortic haemodynamics. Journal of The Royal Society Interface, 13(119):20160073, 2016.

[17] Jean-Paul Allouche e Laurence Maillard-Teyssier. Inconstancy of finite and infinite sequences. Theoretical Computer Science, 412(22):2268–2281, 2011.

[18] H. Vernon Anderson, Michael J. Stokes, Miltiadis Leon, Subhi A. Abu-Halawa, Yvonne Stuart, e Richard L. Kirkeeide. Coronary artery flow velocity is related to lumen area and regional left ventricular mass. Circulation, 102(1):48–54, 2000.

[19] D. F. Andrews. Plots of high-dimensional data. Biometrics, 28(1):125, 1972.

[20] L. Antiga, B. Ene-Iordache, e A. Remuzzi. Computational geometry for patient-specific reconstruction and meshing of blood vessels from MR and CT angiography. IEEE Transactions on Medical Imaging, 22(5):674–684, May 2003.

[21] Luca Antiga, Marina Piccinelli, Lorenzo Botti, Bogdan Ene-Iordache, Andrea Remuzzi, e David A. Steinman. An image-based modeling framework for patient-specific computational hemodynamics. Medical & Biological Engineering & Computing, 46(11):1097–1112, November 2008.

[22] A. Arbab-Zadeh. Fractional Flow Reserve-Guided Percutaneous Coronary Intervention Is Not a Valid Concept. Circulation, 129(18):1871–1878, May 2014.

[23] Yaron Arbel, Danny Dvir, Micha S. Feinberg, Roy Beigel, e Michael Shechter. The association between right coronary artery morphology and endothelial function. International Journal of Cardiology, 115(1):19–23, January 2007.

[24] Gonzalo Damian Ares. Integrative computational modeling and invivo characterization of residual deformations in hemodynamics, Mar 2016.

[25] Antonio Auriti, Vincenzo Loiaconi, Christian Pristipino, Francesco Saverio Leonardi Cattolica, Roberto Cini, Vincenzo Guido, Cinzia Cianfrocca, Salvatore Greco, Filomena Agostini, Mario Staibano, e others. Recovery of distal coronary flow reserve in LAD and LCx after Y-Graft intervention assessed by transthoracic echocardiography. Cardiovascular ultrasound, 8(1):34, 2010.

[26] Antonio Auriti, Christian Pristipino, Cinzia Cianfrocca, Antonino Granatelli, Vincenzo Guido, Francesco Pelliccia, Salvatore Greco, Giuseppe Richichi, e Massimo Santini. Distal left circumflex coronary artery flow reserve recorded by transthoracic Doppler echocardiography: a comparison with Doppler-wire. Cardiovascular Ultrasound, 5(1), December 2007.

[27] Authors/Task Force members, Stephan Windecker, Philippe Kolh, Fernando Alfonso, Jean-Philippe Collet, Jochen Cremer, Volkmar Falk, Gerasimos Filippatos, Christian Hamm, Stuart J. Head, Peter Jüni, A. Pieter Kappetein, Adnan Kastrati, Juhani Knuuti, Ulf Landmesser, Günther Laufer, Franz-Josef Neumann, Dimitrios J. Richter, Patrick Schauerte, Miguel Sousa Uva, Giulio G. Stefanini, David Paul Taggart, Lucia Torracca, Marco Valgimigli, William Wijns, e Adam Witkowski. 2014 ESC/EACTS Guidelines on myocardial revascularization: The Task Force on Myocardial Revascularization of the European Society of Cardiology (ESC) and the European Association for Cardio-Thoracic Surgery (EACTS)Developed with the special contribution of the European Association of Percutaneous Cardiovascular Interventions (EAPCI). European Heart Journal, 35(37):2541–2619, October 2014.

[28] A. P. Avolio. Multi-branched model of the human arterial system. Medical and Biological Engineering and Computing, 18(6):709–718, 1980.

[29] Aldo Balestrino, Andrea Caiti, e Emanuele Crisostomi. A classification of nonlinear systems: an entropy based approach. Chemical Engineering transactions, 11:119–124, 2007.

[30] Aldo Balestrino, Andrea Caiti, e Emanuele Crisostomi. Generalised entropy of curves for the analysis and classification of dynamical systems. Entropy, 11(2):249–270, 2009.

[31] L E Ballesteros e L M Ramirez. Morphological expression of the left coronary artery: a direct anatomical study. Folia morphologica, 67(2):135–142, may 2008. PMID: 18521813.

[32] G. Baroldi, O. Mantero, e G. Scomazzoni. The Collaterals of the Coronary Arteries in Normal and Pathologic Hearts. Circulation Research, 4(2):223–229, March 1956.

[33] J.B. Bassingthwaighte e J.H.G.M. Van Beek. Lightning and the heart: fractal behavior in cardiac function. Proceedings of the IEEE, 76(6):693–699, June 1988.

[34] Daniel A. Beard e James B. Bassingthwaighte. The fractal nature of myocardial blood flow emerges from a whole-organ model of arterial network. Journal of vascular research, 37(4):282–296, 2000.

[35] G. J. W. Bech, B. De Bruyne, N. H.J. Pijls, E. D. de Muinck, J. C.A. Hoorntje, J. Escaned, P. R. Stella, E. Boersma, J. Bartunek, J. J. Koolen, e W. Wijns. Fractional Flow Reserve to Determine the Appropriateness of Angioplasty in Moderate Coronary Stenosis : A Randomized Trial. Circulation, 103(24):2928–2934, June 2001.

[36] Colin Berry, Marcel van 't Veer, Nils Witt, Petr Kala, Otakar Bocek, Stylianos A. Pyxaras, John D. McClure, William F. Fearon, Emanuele Barbato, Pim A.L. Tonino, Bernard De Bruyne, Nico H.J. Pijls, e Keith G. Oldroyd. VERIFY (VERification of Instantaneous Wave-Free Ratio and Fractional Flow Reserve for the Assessment of Coronary Artery Stenosis Severity in EverydaY Practice). Journal of the American College of Cardiology, 61(13):1421–1427, April 2013.

[37] Cristóbal Bertoglio, Philippe Moireau, e Jean-Frederic Gerbeau. Sequential parameter estimation for fluid-structure problems: Application to hemodynamics: SEQUENTIAL ESTIMATION IN FSI. International Journal for Numerical Methods in Biomedical Engineering, 28(4):434–455, April 2012.

[38] C. G. Bezerra, B. A. Falcao, G.D. Maso Talou, C. A. Bulant, P. J. Blanco, R. A. Feijóo, Jose Mariani, e P. A. Lemos. Reconstrução Tridimensional de Artérias Coronárias à partir da Integração do Ultrassom Intra-Coronário e da Angiografia Convencional fase piloto de validação com a angiotomografia de coronárias. In Congresso da Sociedade Brasileira de Hemodinâmica e Cardiologia Intervencional, Brasilia, Brasil, 2015.

[39] Cristiano Bezerra, Carlos Bulant, Gonzalo Maso Talou, Jose Mariani, Breno Falcão, Fábio Augusto Pinton, Raúl Feijóo, Antonio Filho, e Pedro Lemos. TCT-535 Coronary computed tomography angiography (CCTA) blood flow model, how we can improve it? Insights based on comparison with intravascular ultrasound (IVUS) tridimensional model. Journal of the American College of Cardiology, 68(18):B216, November 2016.

[40] Cristiano Bezerra, Gonzalo Maso Talou, Carlos Bulant, Jose Mariani, Fábio Augusto Pinton, Breno Falcão, Antonio Filho, Raúl Feijóo, e Pedro Lemos. TCT-573 Head-to-head comparison between coronary computed tomography angiography (CCTA) and intravascular ultrasound (IVUS) tridimensional models: a geometric point of view. Journal of the American College of Cardiology, 68(18):B232, November 2016.

[41] Cristiano Guedes Bezerra, Gonzalo Daniel Maso Talou, Carlos Alberto Bulant, Breno de Alencar Araripe Falcão, José Mariani, Pablo Javier Blanco, Raúl Antonino Feijóo, e Pedro Alves Lemos Neto. Reconstrução tridimensional de artérias coronárias a partir da integração do ultrassom intracoronário e da angiografia convencional. Revista Brasileira de Cardiologia Invasiva, 23(2):134–138, April 2015.

[42] Pablo J. Blanco, Sansuke M. Watanabe, Enzo A. Dari, Marco Aurélio R. F. Passos, e Raúl A. Feijóo. Blood flow distribution in an anatomically detailed arterial network model: criteria and algorithms. Biomechanics and Modeling in Mechanobiology, 13(6):1303–1330, November 2014.

[43] Pablo J. Blanco, Sansuke M. Watanabe, Marco Aurelio R. F. Passos, Pedro A. Lemos, e Raúl A. Feijóo. An Anatomically Detailed Arterial Network Model for One-Dimensional Computational Hemodynamics. IEEE Transactions on Biomedical Engineering, 62(2):736–753, February 2015.

[44] P.J. Blanco, L.A. Mansilla Alvarez, e R.A. Feijóo. Hybrid element-based approximation for the navier–stokes equations in pipe-like domains. Computer Methods in Applied Mechanics and Engineering, 283:971 – 993, 2015.

[45] P.J. Blanco, R.A.B. Queiroz, e R.A. Feijóo. A computational approach to generate concurrent arterial networks in vascular territories. International Journal for Numerical Methods in Biomedical Engineering, 29:601–614, 2013.

[46] J. Martin Bland e DouglasG Altman. Statistical methods for assessing agreement between two methods of clinical measurement. The lancet, 327(8476):307–310, 1986.

[47] R. Blankstein e A. D. DeVore. Selecting a Noninvasive Imaging Study After an Inconclusive Exercise Test. Circulation, 122(15):1514–1518, October 2010.

[48] Hrvoje Bogunović, José María Pozo, Rubén Cárdenes, María Cruz Villa-Uriol, Raphaël Blanc, Michel Piotin, e Alejandro F. Frangi. Automated landmarking and geometric characterization of the carotid siphon. Medical Image Analysis, 16(4):889–903, May 2012.

[49] Etienne Boileau e Perumal Nithiarasu. One-Dimensional Modelling of the Coronary Circulation. Application to Noninvasive Quantification of Fractional Flow Reserve (FFR). In João Manuel R. S. Tavares e R.M. Natal Jorge, editors, Computational and Experimental Biomedical Sciences: Methods and Applications, volume 21, pages 137–155. Springer International Publishing, Cham, 2015.

[50] Anh Bui, Ilija D. Šutalo, Richard Manasseh, e Kurt Liffman. Dynamics of pulsatile flow in fractal models of vascular branching networks. Medical & Biological Engineering & Computing, 47(7):763–772, July 2009.

[51] C. A. Bulant, P. J. Blanco, A. N. Assunção, G. Liberato, T. P. Lima, J. Parga Filho, P. A. Lemos, L. F. R. Ávila, e R. A. Feijóo. Geometrical characterization of the coronary arterial tree. In XXXVI Iberian Latin-American Congress on Computational Methods in Engineering, Rio de Janeiro, Brasil, 2015.

[52] C. A. Bulant, P. J. Blanco, A. N. Assunção Jr, G. Liberato, T. P. Lima, J. R. Parga Filho, Pedro A. Lemos, L. F. R. Avila, e R. A. Feijóo. Morphological characterization and comparison of coronary arterial trees. In XXXIV Congresso da Sociedade Brasileira de Computação, Brasilia, Brasil, 2014.

[53] C. A. Bulant, P. J. Blanco, T. P. Lima, A.N. Assunção, G. Liberato, J. R. Parga, L. F. R. Ávila, A. C. Pereira, R. A. Feijóo, e P. A. Lemos. A computational framework to characterize and compare the geometry of coronary networks. International Journal for Numerical Methods in Biomedical Engineering, 33(3):e02800, March 2017.

[54] C.A. Bulant, P.J. Blanco, A. Clausse, A.N. Assunção, T.P. Lima, L.F.R. Ávila, R.A. Feijóo, e P.A. Lemos. Association between three-dimensional vessel geometry and the presence of atherosclerotic plaques in the left anterior descending coronary artery of high-risk patients. Biomedical Signal Processing and Control, 31:569–575, January 2017.

[55] C.A. Bulant, P.J. Blanco, G.D. Maso Talou, C. Guedes Bezerra, P.A. Lemos, e R.A. Feijóo. A head-to-head comparison between CT- and IVUS-derived coronary blood flow models. Journal of Biomechanics, 51:65–76, January 2017.

[56] Carlos A. Bulant, Pablo J. Blanco, Alexandre Pereira, Thais P. Lima, Antonildes N. Assunção, Gabriela Liberato, Cristiano G. Bezerra, Jose R. Parga, Luiz F. Ávila, Raúl A. Feijóo, e Pedro A. Lemos. On the search of arterial geometry heritability. International Journal of Cardiology, 221:1013–1021, July 2016.

[57] Carlos Alberto Bulant, Pablo Javier Blanco, Alejandro Clausse, Cristiano Bezerra, Thais Pinheiro Lima, L.F.R. Ávila, Pedro A. Lemos, e Raúl Antonino Feijóo. Thermodynamic analogies for the characterization of 3d human coronary arteries. Submited to: Biomedical Signal Processing and Control, 2016.

[58] A. Caiazzo, F. Caforio, G. Montecinos, L. O. Muller, P. J. Blanco, e E. F. Toro. Assessment of reduced-order unscented Kalman filter for parameter identification in one-dimensional blood flow models using experimental data. International Journal for Numerical Methods in Biomedical Engineering, 2016.

[59] I.C. Campbell, L.H. Timmins, D.P. Giddensa, R. Virmanic, A. Veneziani, S. Tanveer Rab, H. Samady, M.C. McDaniel, A.K. Finn, W.R. Taylor, e J.N. Oshinski. Computational fluid dynamics simulations of hemodynamics in plaque erosion. Cardiovascular Engineering and Technology, 4:464–473, 2013.

[60] John G. Canto e Ami E. Iskandrian. Major Risk Factors for Cardiovascular Disease: Debunking the "Only 50%" Myth. JAMA, 290(7):947, August 2003.

[61] Anna Caroli, Simone Manini, Luca Antiga, Katia Passera, Bogdan Ene-Iordache, Stefano Rota, Giuseppe Remuzzi, Aron Bode, Jaap Leermakers, Frans N. van de Vosse, e others. Validation of a patient-specific hemodynamic computational model for surgical planning of vascular access in hemodialysis patients. Kidney international, 84(6):1237–1245, 2013.

[62] Sebastián Carrizo, Xinzhou Xie, Rafael Peinado-Peinado, Angel Sánchez-Recalde, Santiago Jiménez-Valero, Guillermo Galeote-Garcia, e Raúl Moreno. Functional assessment of coronary artery disease by intravascular ultrasound and computational fluid dynamics simulation. Revista Portuguesa de Cardiologia, 33(10), October 2014.

[63] Gianni Casella, Marcus Leibig, Thomas M. Schiele, Reiner Schrepf, Victoria Seelig, Hans-Ulrich Stempfle, Petra Erdin, Johannes Rieber, Andreas König, Uwe Siebert, e Volker Klauss. Are high doses of intracoronary adenosine an alternative to standard intravenous adenosine for the assessment of fractional flow reserve? American Heart Journal, 148(4):590–595, October 2004.

[64] J. R. Cebral, F. Mut, J. Weir, e C. Putman. Quantitative characterization of the hemodynamic environment in ruptured and unruptured brain aneurysms. American Journal of Neuroradiology, 2010.

[65] J.R. Cebral, M.A. Castro, S. Appanaboyina, C.M. Putman, D. Millan, e A.F. Frangi. Efficient pipeline for image-based patient-specific analysis of cerebral aneurysm hemodynamics: technique and sensitivity. IEEE Transactions on Medical Imaging, 24(4):457–467, April 2005.

[66] Juan R. Cebral, Peter J. Yim, Rainald Löhner, Orlando Soto, e Peter L. Choyke. Blood Flow Modeling in Carotid Arteries with Computational Fluid Dynamics and MR Imaging. Academic Radiology, 9(11):1286–1299, November 2002.

[67] Su M. Chang, Sabha Bhatti, e Faisal Nabi. Coronary computed tomography angiography:. Current Opinion in Cardiology, 26(5):392–402, September 2011.

[68] Panithaya Chareonthaitawee, Philipp A. Kaufmann, Ornella Rimoldi, e Paolo G. Camici. Heterogeneity of resting and hyperemic myocardial blood flow in healthy humans. Cardiovascular research, 50(1):151–161, 2001.

[69] Yiannis S. Chatzizisis, George D. Giannoglou, George E. Parcharidis, e George E. Louridas. Is left coronary system more susceptible to atherosclerosis than right? A pathophysiological insight. International Journal of Cardiology, 116(1):7–13, March 2007.

[70] Y.S. Chatzizisis, M. Jonas, A.U. Coskun, R. Beigel, B.V. Stone, C. Maynard, R.G. Gerrity, W. Daley, C.Rogers, E.R. Edelman, C.L. Feldman, e P.H. Stone. Prediction of the localization of high-risk coronary atherosclerotic plaques on the basis of low endothelial shear stress. An intravascular ultrasound and histopathology natural history study. Circulation, 117:993–1002, 2008.

[71] B. P. Chen, Y. S. Li, Y. Zhao, K. D. Chen, S. Li, J. Lao, S. Yuan, J. Y. Shyy, e S. Chien. DNA microarray analysis of gene expression in endothelial cells in response to 24-h shear stress. Physiological Genomics, 7(1):55–63, October 2001.

[72] S Chien. Molecular and mechanical bases of focal lipid accumulation in arterial wall. Progress in Biophysics and Molecular Biology, 83(2):131–151, October 2003.

[73] G. Choi, J.M. Lee, H.-J. Kim, J.-B. Park, S. Sankaran, H. Otake, J.-H. Doh, C.-W. Nam, E.-S. Shin, C.A. Taylor, e B.-K. Koo. Coronary artery axial plaque stress and its relationship with lesion geometry. Application of computational fluid dynamics to coronary CT angiography. Journal of the American College of Cardiology: Cardiovascular Imaging, 8:1156–1166, 2015.

[74] Benjamin J.W. Chow, Malek Kass, Owen Gagné, Li Chen, Yeung Yam, Alexander Dick, e George A. Wells. Can Differences in Corrected Coronary Opacification Measured With Computed Tomography Predict Resting Coronary Artery Flow? Journal of the American College of Cardiology, 57(11):1280–1288, March 2011.

[75] J. S. Choy e G. S. Kassab. Scaling of myocardial mass to flow and morphometry of coronary arteries. Journal of Applied Physiology, 104(5):1281–1286, February 2008.

[76] Adriaan Coenen, Marisa M. Lubbers, Akira Kurata, Atsushi Kono, Admir Dedic, Raluca G. Chelu, Marcel L. Dijkshoorn, Frank J. Gijsen, Mohamed Ouhlous, Robert-Jan M. van Geuns, e others. Fractional flow reserve computed from noninvasive CT angiography data: diagnostic performance of an on-site clinician-operated computational fluid dynamics algorithm. Radiology, 274(3):674–683, 2014.

[77] Jay D. Coffman e Donald E. Gregg. Reactive hyperemia characteristics of the myocardium. American Journal of Physiology–Legacy Content, 199(6):1143–1149, 1960.

[78] J. Cornfield. A method of estimating comparative rates from clinical data; applications to cancer of the lung, breast, and cervix. Journal of the National Cancer Institute, 11(6):1269–1275, 1951.

[79] A. Umit Coskun, Caixia Chen, Peter H. Stone, e Charles L. Feldman. Computational fluid dynamics tools can be used to predict the progression of coronary artery disease. Physica A: Statistical Mechanics and its Applications, 362(1):182–190, March 2006.

[80] M. W. Crofton. On the theory of local probability, applied to straight lines drawn at random in a plane; the methods used being also extended to the proof of certain new theorems in the integral calculus. Philosophical Transactions of the Royal Society of London, 158(0):181–199, 1868.

[81] J. E. Davies. Evidence of a Dominant Backward-Propagating "Suction" Wave Responsible for Diastolic Coronary Filling in Humans, Attenuated in Left Ventricular Hypertrophy. Circulation, 113(14):1768–1778, April 2006.

[82] Peter F. Davies, Denise C. Polacek, Congzhu Shi, e Brian P. Helmke. The convergence of haemodynamics, genomics, and endothelial structure in studies of the focal origin of atherosclerosis. Biorheology, 39(3):299–306, 2002.

[83] B. De Bruyne, T. Baudhuin, J. A. Melin, N. H. Pijls, S. U. Sys, A. Bol, W. J. Paulus, G. R. Heyndrickx, e W. Wijns. Coronary flow reserve calculated from pressure measurements in humans. Validation with positron emission tomography. Circulation, 89(3):1013–1022, March 1994.

[84] Bernard De Bruyne, Ferry Hersbach, Nico HJ Pijls, Jozef Bartunek, Jan-Willem Bech, Guy R. Heyndrickx, K. Lance Gould, e William Wijns. Abnormal epicardial coronary resistance in patients with diffuse atherosclerosis but "normal" coronary angiography. Circulation, 104(20):2401–2406, 2001.

[85] Bernard De Bruyne, Walter J. Paulus, Pascal J. Vantrimpont, Stanislas U. Sys, Guy R. Heyndrickx, e Nico H.J. Pijls. Transstenotic coronary pressure gradient measurement in humans: In vitro and in vivo evaluation of a new pressure monitoring angioplasty guide wire. Journal of the American College of Cardiology, 22(1):119–126, July 1993.

[86] Stefano Fausto de Marchi, Sabina Streuli, Pascal Haefeli, Steffen Gloekler, Tobias Traupe, Cornelius Warncke, Stefano F. Rimoldi, Stefan Stortecky, Hélène Steck, e Christian Seiler. Determinants of Prognostically Relevant Intracoronary Electrocardiogram ST-Segment Shift During Coronary Balloon Occlusion. The American Journal of Cardiology, 110(9):1234–1239, November 2012.

[87] Giovanni de Simone, Mary J. Roman, Michael J. Koren, George A. Mensah, Antonello Ganau, e Richard B. Devereux. Stroke volume/pulse pressure ratio and cardiovascular risk in arterial hypertension. Hypertension, 33(3):800–805, 1999.

[88] Gregory J. Dehmer, Douglas Weaver, Matthew T. Roe, Sarah Milford-Beland, Susan Fitzgerald, Anthony Hermann, John Messenger, Issam Moussa, Kirk Garratt, John Rumsfeld, e Ralph G. Brindis. A Contemporary View of Diagnostic Cardiac Catheterization and Percutaneous Coronary Intervention in the United States. Journal of the American College of Cardiology, 60(20):2017–2031, November 2012.

[89] Recep Demirbag e Remzi Yilmaz. Effects of the shape of coronary arteries on the presence, extent, and severity of their disease. Heart and Vessels, 20(5):224–229, September 2005.

[90] Laura Dempere-Marco, Estanislao Oubel, Marcelo Castro, Christopher Putman, Alejandro Frangi, e Juan Cebral. CFD analysis incorporating the influence of wall motion: application to intracranial aneurysms. In International Conference on Medical Image Computing and Computer-Assisted Intervention, pages 438–445. Springer, 2006.

[91] A. Denis. Identification of functional relationships between atmospheric pressure and CO_2 in the cave of lascaux using the concept of entropy of curves. <u>Geophysical Research Letters</u>, 32(5), 2005.

[92] A. Denis e F. Crémoux. Using the entropy of curves to segment a time or spatial series. <u>Mathematical Geology</u>, 34(8):899–914, 2002.

[93] Developed with the special contribution of the European Association for Percutaneous Cardiovascular Interventions (EAPCI), Authors/Task Force Members, W. Wijns, P. Kolh, N. Danchin, C. Di Mario, V. Falk, T. Folliguet, S. Garg, K. Huber, S. James, J. Knuuti, J. Lopez-Sendon, J. Marco, L. Menicanti, M. Ostojic, M. F. Piepoli, C. Pirlet, J. L. Pomar, N. Reifart, F. L. Ribichini, M. J. Schalij, P. Sergeant, P. W. Serruys, S. Silber, M. Sousa Uva, D. Taggart, ESC Committee for Practice Guidelines, A. Vahanian, A. Auricchio, J. Bax, C. Ceconi, V. Dean, G. Filippatos, C. Funck-Brentano, R. Hobbs, P. Kearney, T. McDonagh, B. A. Popescu, Z. Reiner, U. Sechtem, P. A. Sirnes, M. Tendera, P. E. Vardas, P. Widimsky, EACTS Clinical Guidelines Committee, P. Kolh, O. Alfieri, J. Dunning, S. Elia, P. Kappetein, U. Lockowandt, G. Sarris, P. Vouhe, Document Reviewers, P. Kearney, L. von Segesser, S. Agewall, A. Aladashvili, D. Alexopoulos, M. J. Antunes, E. Atalar, A. Brutel de la Riviere, A. Doganov, J. Eha, J. Fajadet, R. Ferreira, J. Garot, J. Halcox, Y. Hasin, S. Janssens, K. Kervinen, G. Laufer, V. Legrand, S. A. M. Nashef, F.-J. Neumann, K. Niemela, P. Nihoyannopoulos, M. Noc, J. J. Piek, J. Pirk, Y. Rozenman, M. Sabate, R. Starc, M. Thielmann, D. J. Wheatley, S. Windecker, e M. Zembala. Guidelines on myocardial revascularization: The Task Force on Myocardial Revascularization of the European Society of Cardiology (ESC) and the European Association for Cardio-Thoracic Surgery (EACTS). <u>European Heart Journal</u>, 31(20):2501–2555, October 2010.

[94] J. T. Dodge, B. G. Brown, E. L. Bolson, e H. T. Dodge. Lumen diameter of normal human coronary arteries. influence of age, sex, anatomic variation, and left ventricular hypertrophy or dilation. <u>Circulation</u>, 86(1):232–246, jul 1992.

[95] Michael Maurice Dodson, Michel Mendes France, e Michel Mendes. On the entropy of curves. <u>Journal of Integer Sequences</u>, 16(2):3, 2013.

[96] Pamela S. Douglas, Gianluca Pontone, Mark A. Hlatky, Manesh R. Patel, Bjarne L. Norgaard, Robert A. Byrne, Nick Curzen, Ian Purcell, Matthias Gutberlet, Gilles Rioufol, Ulrich Hink, Herwig Walter Schuchlenz, Gudrun Feuchtner, Martine Gilard, Daniele Andreini, Jesper M. Jensen, Martin Hadamitzky, Karen Chiswell, Derek Cyr, Alan Wilk, Furong Wang, Campbell Rogers, e Bernard De Bruyne. Clinical outcomes of fractional flow reserve by computed tomographic angiography-guided diagnostic strategies vs. usual care in patients with suspected coronary artery disease: the prospective longitudinal trial of FFR_{ct} : outcome and resource impacts study. <u>European Heart Journal</u>, 36(47):3359–3367, December 2015.

[97] Michael Dumbser, Manuel Castro, Carlos Parés, e Eleuterio F. Toro. ADER schemes on unstructured meshes for nonconservative hyperbolic systems: Applications to geophysical flows. <u>Computers & Fluids</u>, 38(9):1731–1748, October 2009.

[98] Yves Dupain, Teturo Kamae, e Michel Mendés. Can one measure the temperature of a curve? <u>Archive for Rational Mechanics and Analysis</u>, 94(2):155–163, 1986.

[99] C. S. Duvernoy, C. Meyer, V. Seifert-Klauss, F. Dayanikli, I. Matsunari, J. Rattenhuber, C. Höss, H. Graeff, e M. Schwaiger. Gender differences in myocardial blood flow

dynamics: lipid profile and hemodynamic effects. Journal of the American College of Cardiology, 33(2):463–470, February 1999.

[100] Danny Dvir, Ran Kornowski, Tuvia Ben-Gal, Marius Berman, Bernardo Vidne, e Dan Aravot. Relation of amounts of narrowing to the length of the right coronary artery. The American journal of cardiology, 90(1):46–48, 2002.

[101] Danny Dvir, Ran Kornowski, Jacob Gurevich, Boris Orlov, e Dan Aravot. Degrees of severe stenoses in sigma-shaped versus C-shaped right coronary arteries. The American Journal of Cardiology, 92(3):294–298, August 2003.

[102] Mauro Echavarria-Pinto, Javier Escaned, Enrico Macías, Miguel Medina, Nieves Gonzalo, Ricardo Petraco, Sayan Sen, Pilar Jimenez-Quevedo, Rosana Hernandez, Rafael Mila, e others. Disturbed Coronary Hemodynamics in Vessels With Intermediate Stenoses Evaluated With Fractional Flow Reserve A Combined Analysis of Epicardial and Microcirculatory Involvement in Ischemic Heart Disease. Circulation, 128(24):2557–2566, 2013.

[103] L.M. Ellwein, H. Otake, T.J. Gundert, B.-K. Koo, T. Shinke, Y. Honda, J. Shite, e J.F. LaDisa Jr. Optical coherence tomography for patient-specific 3D artery reconstruction and evaluation of wall shear stress in a left circumflex coronary artery. Cardiovascular Engineering and Technology, 2:212–227, 2011.

[104] Martin Farrall, Fiona R. Green, John F. Peden, Per G. Olsson, Robert Clarke, Mai-Lis Hellenius, Stephan Rust, Jacob Lagercrantz, Maria Grazia Franzosi, Helmut Schulte, Alisoun Carey, Gunnar Olsson, Gerd Assmann, Gianni Tognoni, Rory Collins, Anders Hamsten, e Hugh Watkins. Genome-Wide Mapping of Susceptibility to Coronary Artery Disease Identifies a Novel Replicated Locus on Chromosome 17. PLoS Genetics, 2(5):e72, 2006.

[105] Collin Fischer, Edward Hulten, Pallavi Belur, Ryan Smith, Szilard Voros, e Todd C. Villines. Coronary CT angiography versus intravascular ultrasound for estimation of coronary stenosis and atherosclerotic plaque burden: A meta-analysis. Journal of Cardiovascular Computed Tomography, 7(4):256–266, July 2013.

[106] M. Fischer. Distinct Heritable Patterns of Angiographic Coronary Artery Disease in Families With Myocardial Infarction. Circulation, 111(7):855–862, February 2005.

[107] M. Fischer, B. Mayer, A. Baessler, G. Riegger, J. Erdmann, C. Hengstenberg, e H. Schunkert. Familial aggregation of left main coronary artery disease and future risk of coronary events in asymptomatic siblings of affected patients. European Heart Journal, 28(20):2432–2437, September 2007.

[108] D.M. Fiss. Normal coronary anatomy and anatomic variations. Applied Radiology, 36(1 SUPPL.):14–26, jan 2007.

[109] C. G. Fonseca, M. Backhaus, D. A. Bluemke, R. D. Britten, J. D. Chung, B. R. Cowan, I. D. Dinov, J. P. Finn, P. J. Hunter, A. H. Kadish, D. C. Lee, J. A. C. Lima, P. Medrano-Gracia, K. Shivkumar, A. Suinesiaputra, W. Tao, e A. A. Young. The cardiac atlas project–an imaging database for computational modeling and statistical atlases of the heart. Bioinformatics, 27(16):2288–2295, 2011.

[110] Timothy FONTE, Gilwoo Choi, Leo Grady, e Michael Singer. Systems and methods for estimating ischemia and blood flow characteristics from vessel geometry and physiology, November 2016.

[111] Luca Formaggia, Alfio Quarteroni, e Alessandro Veneziani, editors. Cardiovascular Mathematics. Springer Milan, Milano, 2009.

[112] Jerome Friedman, Trevor Hastie, e Robert Tibshirani. The elements of statistical learning, volume 1. Springer series in statistics Springer, Berlin, 2001.

[113] M. H. Friedman, O. J. Deters, F. F. Mark, C. B. Bargeron, e G. M. Hutchins. Arterial geometry affects hemodynamics. a potential risk factor for athersoclerosis. Atherosclerosis, 46(2):225–231, February 1983.

[114] Morton H. Friedman, Peter B. Baker, Zhaohua Ding, e Barry D. Kuban. Relationship between the geometry and quantitative morphology of the left anterior descending coronary artery. Atherosclerosis, 125(2):183–192, 1996.

[115] W. F. Fulton. The time factor in the enlargement of anastomoses in coronary artery disease. Scottish Medical Journal, 9:18–23, January 1964.

[116] Elżbieta Gabryś, Marek Rybaczuk, e Alicja Kędzia. Blood flow simulation through fractal models of circulatory system. Chaos, Solitons & Fractals, 27(1):1–7, January 2006.

[117] Timur M. Gamilov, Philippe Yu Kopylov, Roman A. Pryamonosov, e Sergey S. Simakov. Virtual fractional flow reserve assessment in patient-specific coronary networks by 1d hemodynamic model. Russian Journal of Numerical Analysis and Mathematical Modelling, 30(5):269–276, 2015.

[118] Alan Garny, Jonathan Cooper, e Peter J. Hunter. Toward a VPH/physiome ToolKit. Wiley Interdisciplinary Reviews: Systems Biology and Medicine, 2(2):134–147, 2010.

[119] Sara Gaur, Stephan Achenbach, Jonathon Leipsic, Laura Mauri, Hiram G. Bezerra, Jesper Møller Jensen, Hans Erik Bøtker, Jens Flensted Lassen, e Bjarne Linde Nørgaard. Rationale and design of the HeartFlowNXT (HeartFlow analysis of coronary blood flow using CT angiography: NeXt sTeps) study. Journal of Cardiovascular Computed Tomography, 7(5):279–288, September 2013.

[120] Fred B. Gessner. Brief reviews: hemodynamic theories of atherogenesis. Circulation research, 33(3):259–266, 1973.

[121] J. Willard Gibbs. Elementary principles in statistical mechanics developed with especial reference to the rational foundation of thermodynamics. C. Scribner,, 1902.

[122] C. Michael Gibson, Lázaro Díaz, Krishna Kandarpa, Frank M. Sacks, Richard C. Pasternak, Tamas Sandor, Charles Feldman, e Peter H. Stone. Relation of vessel wall shear stress to atherosclerosis progression in human coronary arteries. Arteriosclerosis, Thrombosis, and Vascular Biology, 13(2):310–315, 1993.

[123] D P Giddens, C K Zarins, e S Glagov. The role of fluid mechanics in the localization and detection of atherosclerosis. Journal of biomechanical engineering, 115(4B):588–594, November 1993.

[124] F.J.H. Gijsen, J.C.H. Schuurbiers, A.G. van der Giessen, M. Schaap, A.F.W. van der Steen, e J.J. Wentzel. 3D reconstruction techniques of human coronary bifurcations for shear stress computations. Journal of Biomechanics, 47:39–43, 2014.

[125] Joan Glaunès, Anqi Qiu, Michael I. Miller, e Laurent Younes. Large deformation diffeomorphic metric curve mapping. International Journal of Computer Vision, 80(3):317–336, December 2008.

[126] Jorge A. Gonzalez, Michael J. Lipinski, Lucia Flors, Peter W. Shaw, Christopher M. Kramer, e Michael Salerno. Meta-Analysis of Diagnostic Performance of Coronary Computed Tomography Angiography, Computed Tomography Perfusion, and Computed Tomography-Fractional Flow Reserve in Functional Myocardial Ischemia Assessment Versus Invasive Fractional Flow Reserve. The American Journal of Cardiology, 116(9):1469–1478, November 2015.

[127] K L Gould. Quantification of coronary artery stenosis in vivo. Circulation research, 57(3):341–353, September 1985.

[128] K L Gould, K O Kelley, e E L Bolson. Experimental validation of quantitative coronary arteriography for determining pressure-flow characteristics of coronary stenosis. Circulation, 66(5):930–937, November 1982.

[129] K L Gould, R L Kirkeeide, e M Buchi. Coronary flow reserve as a physiologic measure of stenosis severity. Journal of the American College of Cardiology, 15(2):459–474, February 1990.

[130] K L Gould, K Lipscomb, e G W Hamilton. Physiologic basis for assessing critical coronary stenosis. Instantaneous flow response and regional distribution during coronary hyperemia as measures of coronary flow reserve. The American journal of cardiology, 33(1):87–94, January 1974.

[131] L. Grinberg, E. Cheever, T. Anor, J. R. Madsen, e G. E. Karniadakis. Modeling Blood Flow Circulation in Intracranial Arterial Networks: A Comparative 3D/1D Simulation Study. Annals of Biomedical Engineering, 39(1):297–309, 2011.

[132] BHF Family Heart Study Research Group e others. A genomewide linkage study of 1,933 families affected by premature coronary artery disease: The British Heart Foundation (BHF) Family Heart Study. The American Journal of Human Genetics, 77(6):1011–1020, 2005.

[133] Gilat L. Grunau, James K. Min, e Jonathon Leipsic. Modeling of Fractional Flow Reserve Based on Coronary CT Angiography. Current Cardiology Reports, 15(1), January 2013.

[134] Giulio Guagliumi, Vasile Sirbu, Christopher Petroff, Davide Capodanno, Giuseppe Musumeci, Hirosada Yamamoto, Amr Elbasiony, Christopher Brushett, Aleksandre Matiashvili, Nikoloz Lortkipanidze, Orazio Valsecchi, Hiram G. Bezerra, e Joseph M. Schmitt. Volumetric assessment of lesion severity with optical coherence tomography: relationship with fractional flow. EuroIntervention, 8(10):1172–1181, February 2013.

[135] Bruno Guerciotti, Christian Vergara, Sonia Ippolito, Alfio Quarteroni, Carlo Antona, e Roberto Scrofani. Computational study of the risk of restenosis in coronary bypasses. Biomechanics and Modeling in Mechanobiology, August 2016.

[136] Arthur C. Guyton e John E. Hall. Textbook of medical physiology. Elsevier Saunders, Philadelphia, 11th ed edition, 2006.

[137] Jinyong Ha, Jung-Sun Kim, Jaeyeong Lim, Gihoon Kim, Seungwan Lee, Joon Sang Lee, Dong-Ho Shin, Byeong-Keuk Kim, Young-Guk Ko, Donghoon Choi, e others. Assessing Computational Fractional Flow Reserve From Optical Coherence Tomography in Patients With Intermediate Coronary Stenosis in the Left Anterior Descending Artery. Circulation: Cardiovascular Interventions, 9(8):e003613, 2016.

[138] J. T Hack. Studies of longitudinal stream profiles in Virginia and Maryland. USGS Professional Papers 294-B, pages 46–97, 1957.

[139] Daniel G. Hackam e Sonia S. Anand. Emerging Risk Factors for Atherosclerotic Vascular Disease: A Critical Review of the Evidence. JAMA, 290(7):932, August 2003.

[140] N. Hadjiloizou, J. E. Davies, I. S. Malik, J. Aguado-Sierra, K. Willson, R. A. Foale, K. H. Parker, A. D. Hughes, D. P. Francis, e J. Mayet. Differences in cardiac microcirculatory wave patterns between the proximal left mainstem and proximal right coronary artery. AJP: Heart and Circulatory Physiology, 295(3):H1198–H1205, June 2008.

[141] D. A. Halon, D. Sapoznikov, B. S. Lewis, e M. S. Gotsman. Localization of lesions in the coronary circulation. The American Journal of Cardiology, 52(8):921–926, November 1983.

[142] David J. Hand. Assessing the Performance of Classification Methods: *Assessing the Performance of Classification Methods*. International Statistical Review, 80(3):400–414, December 2012.

[143] Charles H. Hennekens. Increasing Burden of Cardiovascular Disease Current Knowledge and Future Directions for Research on Risk Factors. Circulation, 97(11):1095–1102, 1998.

[144] K. Hirohata, A. Kano, A. Goryu, J. Ooga, T. Hongo, S. Higashi, Y. Fujisawa, S. Wakai, K. Arakita, Y. Ikeda, S. Kaminaga, B. S. Ko, e S. K. Seneviratne. A novel CT-FFR method for the coronary artery based on 4d-CT image analysis and structural and fluid analysis. page 94122O, March 2015.

[145] Mark A. Hlatky, Bernard De Bruyne, Gianluca Pontone, Manesh R. Patel, Bjarne L. Norgaard, Robert A. Byrne, Nick Curzen, Ian Purcell, Matthias Gutberlet, Gilles Rioufol, Ulrich Hink, Herwig Walter Schuchlenz, Gudrun Feuchtner, Martine Gilard, Daniele Andreini, Jesper M. Jensen, Martin Hadamitzky, Alan Wilk, Furong Wang, Campbell Rogers, e Pamela S. Douglas. Quality-of-Life and Economic Outcomes of Assessing Fractional Flow Reserve With Computed Tomography Angiography. Journal of the American College of Cardiology, 66(21):2315–2323, December 2015.

[146] Mark A. Hlatky, Akshay Saxena, Bon-Kwon Koo, Andrejs Erglis, Christopher K. Zarins, e James K. Min. Projected Costs and Consequences of Computed Tomography-Determined Fractional Flow Reserve: Consequences of CT-determined FFR. Clinical Cardiology, 36(12):743–748, December 2013.

[147] J. I. Hoffman e J. A. Spaan. Pressure-flow relations in coronary circulation. Physiological Reviews, 70(2):331–390, 1990.

[148] Benjamin D. Horne, Nicola J. Camp, Joseph B. Muhlestein, e Lisa A. Cannon-Albright. Identification of excess clustering of coronary heart diseases among extended pedigrees in a genealogical population database. American Heart Journal, 152(2):305–311, August 2006.

[149] Robert E. Horton. Drainage-basin characteristics. Eos, Transactions American Geophysical Union, 13(1):350–361, 1932.

[150] Robert E. Horton. EROSIONAL DEVELOPMENT OF STREAMS AND THEIR DRAINAGE BASINS; HYDROPHYSICAL APPROACH TO QUANTITATIVE MORPHOLOGY. Geological Society of America Bulletin, 56(3):275, 1945.

[151] Thomas J.R. Hughes e J. Lubliner. On the one-dimensional theory of blood flow in the larger vessels. Mathematical Biosciences, 18(1-2):161–170, October 1973.

[152] Yunlong Huo, Mark Svendsen, Jenny Susana Choy, Z-D Zhang, e Ghassan S Kassab. A validated predictive model of coronary fractional flow reserve. Journal of the Royal Society, Interface / the Royal Society, 9(71):1325–1338, June 2012.

[153] U. Ikeda, M. Kuroki, T. Ejiri, S. Hosoda, e T. Yaginuma. Stenotic lesions and the bifurcation angle of coronary arteries in the young. Japanese Heart Journal, 32(5):627–633, September 1991.

[154] Lucian Itu, Saikiran Rapaka, Tiziano Passerini, Bogdan Georgescu, Chris Schwemmer, Max Schoebinger, Thomas Flohr, Puneet Sharma, e Dorin Comaniciu. A machine-learning approach for computation of fractional flow reserve from coronary computed tomography. Journal of Applied Physiology, 121(1):42–52, July 2016.

[155] Lucian Itu, Puneet Sharma, Vwrel Mihalef, Ali Kamen, Constantin Suciu, e Dorm Lomaniciu. A patient-specific reduced-order model for coronary circulation. In Biomedical Imaging (ISBI), 2012 9th IEEE International Symposium on, pages 832–835. IEEE, 2012.

[156] Ananda R. Jayaweera, Kevin Wei, Matthew Coggins, Jiang Ping Bin, Craig Goodman, e Sanjiv Kaul. Role of capillaries in determining CBF reserve: new insights using myocardial contrast echocardiography. American Journal of Physiology-Heart and Circulatory Physiology, 277(6):H2363–H2372, 1999.

[157] E. T. Jaynes. Information theory and statistical mechanics. Physical Review, 106(4):620–630, 1957.

[158] E. T. Jaynes. Information theory and statistical mechanics. II. Physical Review, 108(2):171–190, 1957.

[159] Allen Jeremias, Akiko Maehara, Philippe Généreux, Kaleab N. Asrress, Colin Berry, Bernard De Bruyne, Justin E. Davies, Javier Escaned, William F. Fearon, K. Lance Gould, Nils P. Johnson, Ajay J. Kirtane, Bon-Kwon Koo, Koen M. Marques, Sukhjinder Nijjer, Keith G. Oldroyd, Ricardo Petraco, Jan J. Piek, Nico H. Pijls, Simon Redwood, Maria Siebes, Jos A. E. Spaan, Marcel van 't Veer, Gary S. Mintz, e Gregg W. Stone. Multicenter core laboratory comparison of the instantaneous wave-free ratio and resting Pd/Pa with fractional flow reserve: the RESOLVE study. Journal of the American College of Cardiology, 63(13):1253–1261, April 2014.

[160] Allen Jeremias, Robert J. Whitbourn, Steven D. Filardo, Peter J. Fitzgerald, David J. Cohen, E.Murat Tuzcu, William D. Anderson, Alexandre A. Abizaid, Gary S. Mintz, Alan C. Yeung, Morton J. Kern, e Paul G. Yock. Adequacy of intracoronary versus intravenous adenosine-induced maximal coronary hyperemia for fractional flow reserve measurements. American Heart Journal, 140(4):651–657, October 2000.

[161] N. P. Johnson, R. L. Kirkeeide, e K. L. Gould. Coronary Anatomy to Predict Physiology: Fundamental Limits. Circulation: Cardiovascular Imaging, 6(5):817–832, September 2013.

[162] Nils P. Johnson e K. Lance Gould. Integrating Noninvasive Absolute Flow, Coronary Flow Reserve, and Ischemic Thresholds Into a Comprehensive Map of Physiological Severity. JACC: Cardiovascular Imaging, 5(4):430–440, April 2012.

[163] Nils P. Johnson, Daniel T. Johnson, Richard L. Kirkeeide, Colin Berry, Bernard De Bruyne, William F. Fearon, Keith G. Oldroyd, Nico H.J. Pijls, e K. Lance Gould. Repeatability of Fractional Flow Reserve Despite Variations in Systemic and Coronary Hemodynamics. JACC: Cardiovascular Interventions, 8(8):1018–1027, July 2015.

[164] Nils P. Johnson, Richard L. Kirkeeide, Kaleab N. Asrress, William F. Fearon, Timothy Lockie, Koen M.J. Marques, Stylianos A. Pyxaras, M. Cristina Rolandi, Marcel van 't Veer, Bernard De Bruyne, Jan J. Piek, Nico H.J. Pijls, Simon Redwood, Maria Siebes, Jos A.E. Spaan, e K. Lance Gould. Does the Instantaneous Wave-Free Ratio Approximate the Fractional Flow Reserve? Journal of the American College of Cardiology, 61(13):1428–1435, April 2013.

[165] Nils P. Johnson, Richard L. Kirkeeide, e K. Lance Gould. Is Discordance of Coronary Flow Reserve and Fractional Flow Reserve Due to Methodology or Clinically Relevant Coronary Pathophysiology? JACC: Cardiovascular Imaging, 5(2):193–202, February 2012.

[166] Alena Jonášová, Ondřej Bublík, e Jan Vimmr. A comparative study of 1D and 3D hemodynamics in patient-specific hepatic portal vein networks. Applied and Computational Mechanics, 8(2), 2014.

[167] Lynn B. Jorde e Roger R. Williams. Relation between family history of coronary artery disease and coronary risk variables. The American journal of cardiology, 62(10):708–713, 1988.

[168] S.J. Julier e J.K. Uhlmann. Unscented Filtering and Nonlinear Estimation. Proceedings of the IEEE, 92(3):401–422, March 2004.

[169] Guy Jumarie. A new information theoretic approach to the entropy of non-random discrete maps relation to fractal dimension and temperature of curves. Chaos, Solitons & Fractals, 8(6):953–970, 1997.

[170] I A Kakadiaris, A Santamaría-Pang, e A Pednekar. Functional Morphology Analysis of the Left Anterior Descending Coronary Artery in EBCT Images. IEEE Transactions on Biomedical Engineering, 57(8):1886–1896, August 2010.

[171] Nikolaos Kakouros, Frank J. Rybicki, Dimitrios Mitsouras, e Julie M. Miller. Coronary pressure-derived fractional flow reserve in the assessment of coronary artery stenoses. European Radiology, 23(4):958–967, April 2013.

[172] Kentaro Kakuta, Kaoru Dohi, Tomomi Yamada, Takashi Yamanaka, Masaki Kawamura, Shiro Nakamori, Hiroshi Nakajima, Takashi Tanigawa, Katsuya Onishi, Norikazu Yamada, Mashio Nakamura, e Masaaki Ito. Detection of Coronary Artery Disease Using Coronary Flow Velocity Reserve by Transthoracic Doppler Echocardiography versus Multidetector Computed Tomography Coronary Angiography: Influence of Calcium Score. Journal of the American Society of Echocardiography, 27(7):775–785, July 2014.

[173] Rudolph E. Kalman e Richard S. Bucy. New results in linear filtering and prediction theory. Journal of basic engineering, 83(3):95–108, 1961.

[174] R. Karch. Fractal Properties of Perfusion Heterogeneity in Optimized Arterial Trees: A Model Study. The Journal of General Physiology, 122(3):307–322, August 2003.

[175] Wassef Karrowni, Ramzi N. El Accaoui, e Kanu Chatterjee. Coronary collateral circulation: Its relevance: Coronary Collateral Circulation. Catheterization and Cardiovascular Interventions, 82(6):915–928, November 2013.

[176] Ghassan S. Kassab, Dotan Algranati, e Yoram Lanir. Myocardial-vessel interaction: role of LV pressure and myocardial contractility. Medical & Biological Engineering & Computing, 51(7):729–739, July 2013.

[177] L. N. Katz e E. Lindner. Quantitative relation between reactive hyperemia and the myocardial ischemia which it follows. American Journal of Physiology–Legacy Content, 126(2):283–288, 1939.

[178] Takayuki Kawata, Masao Daimon, Rei Hasegawa, Tomohiko Toyoda, Tai Sekine, Toshiharu Himi, Daigaku Uchida, Sakiko Miyazaki, Kuniaki Hirose, Ryoko Ichikawa, Masaki Maruyama, Hiromasa Suzuki, e Hiroyuki Daida. Prognostic value of coronary flow reserve assessed by transthoracic Doppler echocardiography on long-term outcome in asymptomatic patients with type 2 diabetes without overt coronary artery disease. Cardiovascular Diabetology, 12(1):121, 2013.

[179] Morton J. Kern, Richard G. Bach, Carol J. Mechem, Eugene A. Caracciolo, Frank V. Aguirre, Leslie W. Miller, e Thomas J. Donohue. Variations in normal coronary vasodilatory reserve stratified by artery, gender, heart transplantation and coronary artery disease. Journal of the American College of Cardiology, 28(5):1154–1160, 1996.

[180] H. J. Kim, K. E. Jansen, e C. A. Taylor. Incorporating Autoregulatory Mechanisms of the Cardiovascular System in Three-Dimensional Finite Element Models of Arterial Blood Flow. Annals of Biomedical Engineering, 38(7):2314–2330, July 2010.

[181] H. J. Kim, I. E. Vignon-Clementel, J. S. Coogan, C. A. Figueroa, K. E. Jansen, e C. A. Taylor. Patient-Specific Modeling of Blood Flow and Pressure in Human Coronary Arteries. Annals of Biomedical Engineering, 38(10):3195–3209, June 2010.

[182] H. J. Kim, I. E. Vignon-Clementel, C. A. Figueroa, J. F. LaDisa, K. E. Jansen, J. A. Feinstein, e C. A. Taylor. On Coupling a Lumped Parameter Heart Model and a Three-Dimensional Finite Element Aorta Model. Annals of Biomedical Engineering, 37(11):2153–2169, November 2009.

[183] F J Klocke. Coronary blood flow in man. Progress in cardiovascular diseases, 19(2):117–166, oct 1976. PMID: 790459.

[184] Brian S. Ko, James D. Cameron, Ravi K. Munnur, Dennis T.L. Wong, Yasuko Fujisawa, Takuya Sakaguchi, Kenji Hirohata, Jacqui Hislop-Jambrich, Shinichiro Fujimoto, Kazuhisa Takamura, Marcus Crossett, Michael Leung, Ahilan Kuganesan, Yuvaraj Malaiapan, Arthur Nasis, John Troupis, Ian T. Meredith, e Sujith K. Seneviratne. Noninvasive CT-Derived FFR Based on Structural and Fluid Analysis. JACC: Cardiovascular Imaging, October 2016.

[185] J. Koerselman. Coronary Collaterals: An Important and Underexposed Aspect of Coronary Artery Disease. Circulation, 107(19):2507–2511, May 2003.

[186] B. Koo, A. Erglis, J. Doh, D.V. Daniels, S. Jegere, H. Kim, A. Dunning, T. DeFrance, A. Lansky, J. Leipsic, e J.K. Min. Diagnosis of ischemia-causing coronary stenoses by noninvasive fractional flow reserve computed from coronary computed tomographic angiograms. results from the prospective multicenter DISCOVER-FLOW (diagnosis

of ischemia-causing stenoses obtained via noninvasive fractional flow reserve) study. J Am Coll Cardiol, 58(19):1989–97, 2011.

[187] K.C. Koskinas, C.L. Feldman, Y.S. Chatzizisis, A.U. Coskun, M. Jonas, C.Maynard, A.B. Baker, E.R. Edelman M.I. Papafaklis, e P.H. Stone. Natural history of experimental coronary atherosclerosis and vascular remodeling in relation to endothelial shear stress. A serial, in vivo intravascular ultrasound study. Circulation, 121:2092–2101, 2010.

[188] Mariusz Kruk, Lukasz Wardziak, Gary S. Mintz, Stephan Achenbach, Jerzy Pregowski, Witold Ruzyllo, Zofia Dzielinska, Marcin Demkow, Adam Witkowski, e Cezary Kepka. Accuracy of coronary computed tomography angiography vs intravascular ultrasound for evaluation of vessel area. Journal of Cardiovascular Computed Tomography, 8(2):141–148, March 2014.

[189] D. N. Ku, D. P. Giddens, C. K. Zarins, e S. Glagov. Pulsatile flow and atherosclerosis in the human carotid bifurcation. Positive correlation between plaque location and low oscillating shear stress. Arteriosclerosis, Thrombosis, and Vascular Biology, 5(3):293–302, May 1985.

[190] Andrew Ladwiniec, Michael S. Cunnington, Jennifer Rossington, Adam N. Mather, Albert Alahmar, Richard M. Oliver, Sukhjinder S. Nijjer, Justin E. Davies, Simon Thackray, Farquad Alamgir, e others. Collateral donor artery physiology and the influence of a chronic total occlusion on fractional flow reserve. Circulation: Cardiovascular Interventions, 8(4):e002219, 2015.

[191] Albert C. Lardo, Amir Ali Rahsepar, Jung Hee Seo, Parastou Eslami, Frederick Korley, Satoru Kishi, Thura Abd, Rajat Mittal, e Richard T. George. Estimating coronary blood flow using CT transluminal attenuation flow encoding: Formulation, preclinical validation, and clinical feasibility. Journal of Cardiovascular Computed Tomography, 9(6):559–566.e1, November 2015.

[192] I. Larrabide, P.J. Blanco, S.A. Urquiza, E.A. Dari, M.J. Vénere, N.A. de Souza e Silva, e R.A. Feijóo. Hemolab hemodynamics modelling laboratory: An application for modelling the human cardiovascular system. Computers in Biology and Medicine, 42:993–1004, 2012.

[193] Ignacio Larrabide, Pedro Omedas, Yves Martelli, Xavier Planes, Maarten Nieber, Juan A. Moya, Constantine Butakoff, Rafael Sebastián, Oscar Camara, Mathieu De Craene, e others. GIMIAS: an open source framework for efficient development of research tools and clinical prototypes. In Functional imaging and modeling of the heart, pages 417–426. Springer, 2009.

[194] Jamie Layland, David Carrick, Matthew Lee, Keith Oldroyd, e Colin Berry. Adenosine. JACC: Cardiovascular Interventions, 7(6):581–591, June 2014.

[195] Alexander W. Leber, Andreas Knez, Franz von Ziegler, Alexander Becker, Konstantin Nikolaou, Stephan Paul, Bernd Wintersperger, Maximilian Reiser, Christoph R. Becker, Gerhard Steinbeck, e Peter Boeksteger. Quantification of obstructive and nonobstructive coronary lesions by 64-slice computed tomography. Journal of the American College of Cardiology, 46(1):147–154, 2005.

[196] Victor Legrand, John McB Hodgson, Eric R. Bates, Fred M. Aueron, GB John Mancini, Joseph S. Smith, Milton D. Gross, e Robert A. Vogel. Abnormal coronary flow reserve and abnormal radionuclide exercise test results in patients with normal

coronary angiograms. Journal of the American College of Cardiology, 6(6):1245–1253, 1985.

[197] Antonio Maria Leone, Italo Porto, Alberto Ranieri De Caterina, Eloisa Basile, Andrea Aurelio, Andrea Gardi, Dolores Russo, Domenico Laezza, Giampaolo Niccoli, Francesco Burzotta, Carlo Trani, Mario Attilio Mazzari, Rocco Mongiardo, Antonio Giuseppe Rebuzzi, e Filippo Crea. Maximal Hyperemia in the Assessment of Fractional Flow Reserve. JACC: Cardiovascular Interventions, 5(4):402–408, April 2012.

[198] David Lesage, Elsa D. Angelini, Isabelle Bloch, e Gareth Funka-Lea. A review of 3d vessel lumen segmentation techniques: Models, features and extraction schemes. Medical Image Analysis, 13(6):819–845, December 2009.

[199] David C. Levin. Pathways and functional significance of the coronary collateral circulation. Circulation, 50(4):831–837, 1974.

[200] Glenn N. Levine, Eric R. Bates, James C. Blankenship, Steven R. Bailey, John A. Bittl, Bojan Cercek, Charles E. Chambers, Stephen G. Ellis, Robert A. Guyton, Steven M. Hollenberg, Umesh N. Khot, Richard A. Lange, Laura Mauri, Roxana Mehran, Issam D. Moussa, Debabrata Mukherjee, Brahmajee K. Nallamothu, e Henry H. Ting. 2011 ACCF/AHA/SCAI Guideline for Percutaneous Coronary Intervention. Journal of the American College of Cardiology, 58(24):e44–e122, December 2011.

[201] L. Liu, W. Yang, Y. Nagahara, Y. Li, S.R. Lamooki, T. Muramatsu, P. Kitslaar, M. Sarai, Y. Ozaki, P. Barlis, F. Yan, J.H. Reiber, e S. Tu. The impact of image resolution on computation of fractional flow reserve: coronary computed tomography angiography versus 3-dimensional quantitative coronary angiography. The International Journal of Cardiovascular Imaging, 32:513–523, 2016.

[202] William E. Lorensen e Harvey E. Cline. Marching cubes: A high resolution 3d surface construction algorithm. Computer Graphics, 21(4):163–169, 1987.

[203] Christine H. Lorenz, Eloisa S. Walker, Victoria L. Morgan, Stacy S. Klein, e Thomas P. Graham. Normal human right and left ventricular mass, systolic function, and gender differences by cine magnetic resonance imaging. Journal of Cardiovascular Magnetic Resonance, 1(1):7–21, 1999.

[204] Marios Loukas, Christopher Groat, Rajkamal Khangura, Deyzi Gueorguieva Owens, e Robert H. Anderson. The normal and abnormal anatomy of the coronary arteries. Clinical Anatomy, 22(1):114–128, jan 2009.

[205] Yan-Feng Ma, Jiang-Ming Fam, e Bu-Chun Zhang. Critical analysis of the correlation between optical coherence tomography versus intravascular ultrasound and fractional flow reserve in the management of intermediate coronary artery lesion. International Journal of Clinical and Experimental Medicine, 8(5):6658–6667, 2015.

[206] Paul Magnus e Robert Beaglehole. The real contribution of the major risk factors to the coronary epidemics: time to end the only-50% myth. Archives of internal medicine, 161(22):2657–2660, 2001.

[207] Maulik D. Majmudar, Venkatesh L. Murthy, Ravi V. Shah, Swathy Kolli, Negareh Mousavi, Courtney R. Foster, Jon Hainer, Ron Blankstein, Sharmila Dorbala, Arkadiusz Sitek, Lynne W. Stevenson, Mandeep R. Mehra, e Marcelo F. Di Carli. Quan-

tification of coronary flow reserve in patients with ischaemic and non-ischaemic cardiomyopathy and its association with clinical outcomes. European Heart Journal – Cardiovascular Imaging, 16(8):900–909, August 2015.

[208] Benoit B. Mandelbrot. Fractals: form, chance, and dimension. W. H. Freeman, San Francisco, 1977.

[209] Benoit B. Mandelbrot. The fractal geometry of nature. W.H. Freeman, San Francisco, 1982.

[210] H. B. Mann e D. R. Whitney. On a test of whether one of two random variables is stochastically larger than the other. Ann. Math. Statist., 18(1):50–60, 03 1947.

[211] Luis Alvarez Mansilla, Pablo J Blanco, Carlos A Bulant, Enzo A Dari, Alessandro Veneziani, e R. A. Feijóo. Transversally Enriched Pipe Element Method (TEPEM). An effective numerical approach for blood flow modeling. International Journal for Numerical Methods in Biomedical Engineering, 2016.

[212] K. M. J. Marques, M. J. van Eenige, H. J. Spruijt, N. Westerhof, J. Twisk, C. A. Visser, e F. C. Visser. The diastolic flow velocity-pressure gradient relation and dpv50 to assess the hemodynamic significance of coronary stenoses. AJP: Heart and Circulatory Physiology, 291(6):H2630–H2635, December 2006.

[213] G.D. Maso Talou, I. Larrabide, P.J. Blanco, C. Bezerra, P.A. Lemos, e R.A. Feijóo. Improving cardiac phase extraction in ivus studies by integration of gating methods. IEEE Trans. Biomed. Eng., 2015.

[214] Gonzalo Daniel Maso Talou. Ivus images segmentation driven by active contours and spacio-temporal reconstruction of the coronary vessels aided by angiographies. Master's thesis, National Laboratory for Scientific Computing, Mar 2013.

[215] H. Matsuo. Validation of Collateral Fractional Flow Reserve by Myocardial Perfusion Imaging. Circulation, 105(9):1060–1065, February 2002.

[216] Robert A. J. Matthews. Methods for assessing the credibility of clinical trial outcomes. Drug Information Journal, 35(4):1469–1478, 2001.

[217] Jr McGill, Henry C, C Alex McMahan, e Samuel S Gidding. Preventing heart disease in the 21st century: implications of the pathobiological determinants of atherosclerosis in youth (PDAY) study. Circulation, 117(9):1216–1227, mar 2008. PMID: 18316498.

[218] A. L. McGinn, C. W. White, e R. F. Wilson. Interstudy variability of coronary flow reserve. Influence of heart rate, arterial pressure, and ventricular preload. Circulation, 81(4):1319–1330, 1990.

[219] Kenneth O. McGraw e S. P. Wong. Forming inferences about some intraclass correlation coefficients. Psychological Methods, 1(1):30–46, 1996.

[220] M. McGue. When assessing twin concordance, use the probandwise not the pairwise rate. Schizophrenia Bulletin, 18(2):171–176, 1992.

[221] R. McPherson, A. Pertsemlidis, N. Kavaslar, A. Stewart, R. Roberts, D. R. Cox, D. A. Hinds, L. A. Pennacchio, A. Tybjaerg-Hansen, A. R. Folsom, E. Boerwinkle, H. H. Hobbs, e J. C. Cohen. A Common Allele on Chromosome 9 Associated with Coronary Heart Disease. Science, 316(5830):1488–1491, June 2007.

[222] Pascal Meier, Stephan H. Schirmer, Alexandra J. Lansky, Adam Timmis, Bertram Pitt, e Christian Seiler. The collateral circulation of the heart. BMC medicine, 11(1):143, 2013.

[223] M. Mendès France. Les courbes chaotiques. Courrier du Centre National de la Recerche Scientifique, 51:5–9, 1983.

[224] Stefan Meng, Stefan H. Geyer, Matheus P. Viana, e Wolfgang J. Weninger. Objective characterization of the course of the parasellar internal carotid artery using mathematical tools. Surgical and Radiologic Anatomy, 30(6):519–526, 2008.

[225] James K. Min, Daniel S. Berman, Matthew J. Budoff, Farouc A. Jaffer, Jonathon Leipsic, Martin B. Leon, G.B. John Mancini, Laura Mauri, Robert S. Schwartz, e Leslee J. Shaw. Rationale and design of the DeFACTO (Determination of Fractional Flow Reserve by Anatomic Computed Tomographic AngiOgraphy) study. Journal of Cardiovascular Computed Tomography, 5(5):301–309, September 2011.

[226] James K. Min, Jonathon Leipsic, Michael J. Pencina, Daniel S. Berman, Bon-Kwon Koo, Carlos van Mieghem, Andrejs Erglis, Fay Y. Lin, Allison M. Dunning, Patricia Apruzzese, Matthew J. Budoff, Jason H. Cole, Farouc A. Jaffer, Martin B. Leon, Jennifer Malpeso, G. B. John Mancini, Seung-Jung Park, Robert S. Schwartz, Leslee J. Shaw, e Laura Mauri. Diagnostic Accuracy of Fractional Flow Reserve From Anatomic CT Angiography. JAMA, 308(12):1237, September 2012.

[227] James K. Min, Leslee J. Shaw, e Daniel S. Berman. The Present State of Coronary Computed Tomography Angiography. Journal of the American College of Cardiology, 55(10):957–965, March 2010.

[228] Rakesh K. Mishra, Sharmila Dorbala, Giridhar Logsetty, Alita Hassan, Therese Heinonen, Heinrich R. Schelbert, e Marcelo F. Di Carli. Quantitative relation between hemodynamic changes during intravenous adenosine infusion and the magnitude of coronary hyperemia. Journal of the American College of Cardiology, 45(4):553–558, February 2005.

[229] N. Mittal. Analysis of blood flow in the entire coronary arterial tree. AJP: Heart and Circulatory Physiology, 289(1):H439–H446, July 2005.

[230] N. Mittal, Y. Zhou, S. Ung, C. Linares, S. Molloi, e G. S. Kassab. A Computer Reconstruction of the Entire Coronary Arterial Tree Based on Detailed Morphometric Data. Annals of Biomedical Engineering, 33(8):1015–1026, August 2005.

[231] Philippe Moireau e Dominique Chapelle. Reduced-order Unscented Kalman Filtering with application to parameter identification in large-dimensional systems. ESAIM: Control, Optimisation and Calculus of Variations, 17(2):380–405, 2011.

[232] Philippe Moireau, Dominique Chapelle, e Patrick Le Tallec. Joint state and parameter estimation for distributed mechanical systems. Computer Methods in Applied Mechanics and Engineering, 197(6-8):659–677, January 2008.

[233] M.C. Molina, Guido P.M. Prause, Petia Radeva, e Milan Sonka. 3d catheter path reconstruction from biplane angiograms. In Medical Imaging'98, pages 504–512. International Society for Optics and Photonics, 1998.

[234] Gino I. Montecinos, Lucas O. Müller, e Eleuterio F. Toro. Hyperbolic reformulation of a 1d viscoelastic blood flow model and ADER finite volume schemes. Journal of Computational Physics, 266:101–123, June 2014.

[235] R. R. Moore, A. J. van der Poorten, e others. On the thermodynamics of curves and other curlicues. In <u>Miniconference on Geometry and Physics</u>, pages 82–109. Centre for Mathematics and its Applications, Mathematical Sciences Institute, The Australian National University, 1989.

[236] Paul D. Morris, Desmond Ryan, Allison C. Morton, Richard Lycett, Patricia V. Lawford, D. Rodney Hose, e Julian P. Gunn. Virtual Fractional Flow Reserve From Coronary Angiography: Modeling the Significance of Coronary Lesions: Results From the VIRTU-1 (VIRTUal Fractional Flow Reserve From Coronary Angiography) Study. <u>JACC: Cardiovascular Interventions</u>, 6(2):149 – 157, 2013.

[237] Paul D. Morris, Frans N. van de Vosse, Patricia V. Lawford, D. Rodney Hose, e Julian P. Gunn. "Virtual" (Computed) Fractional Flow Reserve. <u>JACC: Cardiovascular Interventions</u>, 8(8):1009–1017, July 2015.

[238] Paul Mosher, John Ross, Patricia Ann McFate, e Robert F. Shaw. Control of coronary blood flow by an autoregulatory mechanism. <u>Circulation research</u>, 14(3):250–259, 1964.

[239] Cecil D. Murray. The physiological principle of minimum work: I. The vascular system and the cost of blood volume. <u>Proceedings of the National Academy of Sciences of the United States of America</u>, 12(3):207, 1926.

[240] Fernando Mut, Rainald Löhner, Aichi Chien, Satoshi Tateshima, Fernando Viñuela, Christopher Putman, e Juan R. Cebral. Computational hemodynamics framework for the analysis of cerebral aneurysms. <u>International Journal for Numerical Methods in Biomedical Engineering</u>, 27:822–839, 2011.

[241] Fernando Mut, Susan Wright, Giorgio A Ascoli, e Juan R Cebral. Morphometric, geographic, and territorial characterization of brain arterial trees. <u>International journal for numerical methods in biomedical engineering</u>, January 2014.

[242] J.P. Mynard e K. Valen-SendStad. A unified method for estimating pressure losses at vascular junctions. <u>International Journal for Numerical Methods in Biomedical Engineering</u>, 31:e02717, 2015.

[243] Andriy Myronenko e Xubo Song. Point Set Registration: Coherent Point Drift. <u>IEEE Transactions on Pattern Analysis and Machine Intelligence</u>, 32(12):2262–2275, December 2010.

[244] Lucas O. Müller, Pablo J. Blanco, Sansuke M. Watanabe, e Raúl A. Feijóo. A high-order local time stepping finite volume solver for one-dimensional blood flow simulations: application to the ADAN model: LTS FOR 1d BLOOD FLOW SIMULATIONS. <u>International Journal for Numerical Methods in Biomedical Engineering</u>, 32(10):e02761, October 2016.

[245] Lucas O. Müller, Günter Leugering, e Pablo J. Blanco. Consistent treatment of viscoelastic effects at junctions in one-dimensional blood flow models. <u>Journal of Computational Physics</u>, 314:167–193, June 2016.

[246] Lucas O. Müller e Eleuterio F. Toro. Well-balanced high-order solver for blood flow in networks of vessels with variable properties: WELL-BALANCED SOLVER FOR 1d BLOOD FLOW IN NETWORKS OF ELASTIC VESSELS. <u>International Journal for Numerical Methods in Biomedical Engineering</u>, 29(12):1388–1411, December 2013.

[247] R. Nakazato, H.-B. Park, D. S. Berman, H. Gransar, B.-K. Koo, A. Erglis, F. Y. Lin, A. M. Dunning, M. J. Budoff, J. Malpeso, J. Leipsic, e J. K. Min. Noninvasive fractional flow reserve derived from computed tomography angiography for coronary lesions of intermediate stenosis severity: Results from the DeFACTO study. Circulation: Cardiovascular Imaging, 6(6):881–889, 2013.

[248] Sukhjinder S Nijjer, Sayan Sen, Ricardo Petraco, Rajesh Sachdeva, Florim Cuculi, Javier Escaned, Christopher Broyd, Nicolas Foin, Nearchos Hadjiloizou, Rodney A Foale, Iqbal Malik, Ghada W Mikhail, Amarjit S Sethi, Mahmud Al-Bustami, Raffi R Kaprielian, Masood A Khan, Christopher S Baker, Michael F Bellamy, Alun D Hughes, Jamil Mayet, Rajesh K Kharbanda, Carlo Di Mario, e Justin E Davies. Improvement in coronary haemodynamics after percutaneous coronary intervention: assessment using instantaneous wave-free ratio. Heart, 99(23):1740–1748, December 2013.

[249] Thomas J. Noto, Lewis W. Johnson, Ronald Krone, Walt F. Weaver, David A. Clark, John R. Kramer, George W. Vetrovec, e Justine J. Parker. Cardiac catheterization 1990: a report of the Registry of the Society for Cardiac Angiography and Interventions (SCA&I). Catheterization and cardiovascular diagnosis, 24(2):75–83, 1991.

[250] Bjarne L. Nørgaard, Sara Gaur, Jonathon Leipsic, Hiroshi Ito, Toru Miyoshi, Seung-Jung Park, Ligita Zvaigzne, Nikolaos Tzemos, Jesper M. Jensen, Nicolaj Hansson, Brian Ko, Hiram Bezerra, Evald H. Christiansen, Anne Kaltoft, Jens F. Lassen, Hans Erik Bøtker, e Stephan Achenbach. Influence of Coronary Calcification on the Diagnostic Performance of CT Angiography Derived FFR in Coronary Artery Disease. JACC: Cardiovascular Imaging, 8(9):1045–1055, September 2015.

[251] Bjarne L. Nørgaard, Jonathon Leipsic, Sara Gaur, Sujith Seneviratne, Brian S. Ko, Hiroshi Ito, Jesper M. Jensen, Laura Mauri, Bernard De Bruyne, Hiram Bezerra, Kazuhiro Osawa, Mohamed Marwan, Christoph Naber, Andrejs Erglis, Seung-Jung Park, Evald H. Christiansen, Anne Kaltoft, Jens F. Lassen, Hans Erik Bøtker, e Stephan Achenbach. Diagnostic performance of noninvasive fractional flow reserve derived from coronary computed tomography angiography in suspected coronary artery disease. Journal of the American College of Cardiology, 63(12):1145–1155, 2014.

[252] Padraig M. O'Flynn, Gerard O'Sullivan, e Abhay S. Pandit. Methods for three-dimensional geometric characterization of the arterial vasculature. Annals of Biomedical Engineering, 35(8):1368–1381, April 2007.

[253] Päivi Pajukanta, Michele Cargill, Laura Viitanen, Ilpo Nuotio, Anu Kareinen, Markus Perola, Joseph D. Terwilliger, Elli Kempas, Mark Daly, Heidi Lilja, e others. Two loci on chromosomes 2 and X for premature coronary heart disease identified in early-and late-settlement populations of Finland. The American Journal of Human Genetics, 67(6):1481–1493, 2000.

[254] S. Pant, B. Fabrèges, J-F. Gerbeau, e I. E. Vignon-Clementel. A methodological paradigm for patient-specific multi-scale CFD simulations: from clinical measurements to parameter estimates for individual analysis: PATIENT-SPECIFIC PARAMETER ESTIMATION FOR MULTI-SCALE CFD SIMULATIONS. International Journal for Numerical Methods in Biomedical Engineering, 30(12):1614–1648, December 2014.

[255] Y. C. Pao, J. T. Lu, e E. L. Ritman. Bending and twisting of an in vivo coronary artery at a bifurcation. Journal of Biomechanics, 25(3):287–295, March 1992.

[256] Michail I. Papafaklis, Takashi Muramatsu, Yuki Ishibashi, Lampros S. Lakkas, Shimpei Nakatani, Christos V. Bourantas, Jurgen Ligthart, Yoshinobu Onuma, Mauro Echavarria-Pinto, Georgia Tsirka, Anna Kotsia, Dimitrios N. Nikas, Owen Mogabgab, Robert-Jan van Geuns, Katerina K. Naka, Dimitrios I. Fotiadis, Emmanouil S. Brilakis, Héctor M. Garcia-Garcia, Javier Escaned, Felix Zijlstra, Lampros K. Michalis, e Patrick W. Serruys. Fast virtual functional assessment of intermediate coronary lesions using routine angiographic data and blood flow simulation in humans: comparison with pressure wire – fractional flow reserve. EuroIntervention, 10(5):574–583, September 2014.

[257] Tiziano Passerini, Laura M. Sangalli, Simone Vantini, Marina Piccinelli, Susanna Bacigaluppi, Luca Antiga, Edoardo Boccardi, Piercesare Secchi, e Alessandro Veneziani. An Integrated Statistical Investigation of Internal Carotid Arteries of Patients Affected by Cerebral Aneurysms. Cardiovascular Engineering and Technology, 3(1):26–40, March 2012.

[258] Manesh R. Patel, Gregory J. Dehmer, John W. Hirshfeld, Peter K. Smith, e John A. Spertus. ACCF/SCAI/STS/AATS/AHA/ASNC/HFSA/SCCT 2012 Appropriate Use Criteria for Coronary Revascularization Focused Update. Journal of the American College of Cardiology, 59(9):857–881, February 2012.

[259] Paris Perdikaris, Leopold Grinberg, e George Em. Karniadakis. An Effective Fractal-Tree Closure Model for Simulating Blood Flow in Large Arterial Networks. Annals of Biomedical Engineering, 43(6):1432–1442, June 2015.

[260] Karl Perktold, Michael Resch, e Reinfried O. Peter. Three-dimensional numerical analysis of pulsatile flow and wall shear stress in the carotid artery bifurcation. Journal of Biomechanics, 24(6):409–420, January 1991.

[261] Ricardo Petraco, Javier Escaned, Sayan Sen, Sukhjinder Nijjer, Kaleab N. Asrress, Mauro Echavarria-Pinto, Tim Lockie, Muhammed Z. Khawaja, Cecilia Cuevas, Nicolas Foin, Christopher Broyd, Rodney A. Foale, Nearchos Hadjiloizou, Iqbal S. Malik, Ghada W. Mikhail, Amarjit Sethi, Raffi Kaprielian, Christopher S. Baker, David Lefroy, Michael Bellamy, Mahmud Al-Bustami, Masood A. Khan, Alun D. Hughes, Darrel P. Francis, Jamil Mayet, Carlo Di Mario, Simon Redwood, e Justin E. Davies. Classification performance of instantaneous wave-free ratio (iFR) and fractional flow reserve in a clinical population of intermediate coronary stenoses: results of the ADVISE registry. EuroIntervention, 9(1):91–101, May 2013.

[262] Marina Piccinelli, David A. Steinman, Yiemeng Hoi, Frank Tong, Alessandro Veneziani, e Luca Antiga. Automatic Neck Plane Detection and 3d Geometric Characterization of Aneurysmal Sacs. Annals of Biomedical Engineering, 40(10):2188–2211, October 2012.

[263] Marina Piccinelli, Alessandro Veneziani, David A Steinman, Andrea Remuzzi, e Luca Antiga. A framework for geometric analysis of vascular structures: application to cerebral aneurysms. IEEE transactions on medical imaging, 28(8):1141–1155, August 2009.

[264] N H Pijls, G J Bech, M I el Gamal, H J Bonnier, B De Bruyne, B Van Gelder, H R Michels, e J J Koolen. Quantification of recruitable coronary collateral blood flow in conscious humans and its potential to predict future ischemic events. Journal of the American College of Cardiology, 25(7):1522–1528, June 1995.

[265] N. H. Pijls, M. J. Kern, P. G. Yock, e B. De Bruyne. Practice and potential pitfalls of coronary pressure measurement. Catheterization and Cardiovascular Interventions: Official Journal of the Society for Cardiac Angiography & Interventions, 49(1):1–16, January 2000.

[266] N. H. Pijls, J. A. van Son, R. L. Kirkeeide, B. De Bruyne, e K. L. Gould. Experimental basis of determining maximum coronary, myocardial, and collateral blood flow by pressure measurements for assessing functional stenosis severity before and after percutaneous transluminal coronary angioplasty. Circulation, 87(4):1354–1367, April 1993.

[267] N. H.J. Pijls, B. Van Gelder, P. Van der Voort, K. Peels, F. A.L.E. Bracke, H. J.R.M. Bonnier, e M. I.H. El Gamal. Fractional Flow Reserve : A Useful Index to Evaluate the Influence of an Epicardial Coronary Stenosis on Myocardial Blood Flow. Circulation, 92(11):3183–3193, December 1995.

[268] Nico H. J. Pijls e Bernard De Bruyne. Coronary Pressure, volume 195 of Developments in Cardiovascular Medicine. Springer Netherlands, Dordrecht, 2000.

[269] Nico H J Pijls, Pepijn van Schaardenburgh, Ganesh Manoharan, Eric Boersma, Jan-Willem Bech, Marcel van't Veer, Frits Bär, Jan Hoorntje, Jacques Koolen, William Wijns, e Bernard de Bruyne. Percutaneous coronary intervention of functionally non-significant stenosis: 5-year follow-up of the DEFER Study. Journal of the American College of Cardiology, 49(21):2105–2111, May 2007.

[270] Nico H.J. Pijls, Bernard de Bruyne, Kathinka Peels, Pepijn H. van der Voort, Hans J.R.M. Bonnier, Jozef Bartunek, e Jacques J. Koolen. Measurement of Fractional Flow Reserve to Assess the Functional Severity of Coronary-Artery Stenoses. New England Journal of Medicine, 334(26):1703–1708, June 1996.

[271] Olli-Pekka Pitkänen, Pirjo Nuutila, Olli T. Raitakari, Kimmo Porkka, Hidehiro Iida, Ilpo Nuotio, Tapani Rönnemaa, Jorma Viikari, Marja-Riitta Taskinen, Christian Ehnholm, e others. Coronary flow reserve in young men with familial combined hyperlipidemia. Circulation, 99(13):1678–1684, 1999.

[272] C. Quammen, C. Weigle, e R. Taylor II. Boolean operations on surfaces in vtk without external libraries. The VTK Journal, 05 2011.

[273] Gilbert L. Raff, Chair, Aiden Abidov, Stephan Achenbach, Daniel S. Berman, Lawrence M. Boxt, Matthew J. Budoff, Victor Cheng, Tony DeFrance, Jeffrey C. Hellinger, e Ronald P. Karlsberg. SCCT guidelines for the interpretation and reporting of coronary computed tomographic angiography. Journal of Cardiovascular Computed Tomography, 3(2):122–136, March 2009.

[274] J. H. Reiber, P. W. Serruys, C. J. Kooijman, W. Wijns, C. J. Slager, J. J. Gerbrands, J. C. Schuurbiers, A. den Boer, e P. G. Hugenholtz. Assessment of short-, medium-, and long-term variations in arterial dimensions from computer-assisted quantitation of coronary cineangiograms. Circulation, 71(2):280–288, February 1985.

[275] Matthias Renker, U. Joseph Schoepf, Rui Wang, Felix G. Meinel, Jeremy D. Rier, Richard R. Bayer, Helge Möllmann, Christian W. Hamm, Daniel H. Steinberg, e Stefan Baumann. Comparison of Diagnostic Value of a Novel Noninvasive Coronary Computed Tomography Angiography Method Versus Standard Coronary Angiography for Assessing Fractional Flow Reserve. The American Journal of Cardiology, 114(9):1303–1308, November 2014.

[276] K. P. Rentrop, M. Cohen, H. Blanke, e R. A. Phillips. Changes in collateral channel filling immediately after controlled coronary artery occlusion by an angioplasty balloon in human subjects. Journal of the American College of Cardiology, 5(3):587–592, March 1985.

[277] Riccardo Rigon, Ignacio Rodriguez-Iturbe, Amos Maritan, Achille Giacometti, David G. Tarboton, e Andrea Rinaldo. On Hack's Law. Water Resources Research, 32(11):3367–3374, November 1996.

[278] F. Rikhtegar, J.A. Knight, U. Olgac, S.C. Saur, D. Poulikakos, W. Marshall Jr., P.C. Cattin, H. Alkadhi, e V. Kurtcuoglu. Choosing the optimal wall shear parameter for the prediction of plaque location - A patient-specific computational study in human left coronary arteries. Atherosclerosis, 221:432–437, 2012.

[279] M. Cristina Rolandi, Froukje Nolte, Tim P. van de Hoef, Maurice Remmelink, Jan Baan Jr, Jan J. Piek, Jos A. E. Spaan, e Maria Siebes. Coronary wave intensity during the Valsalva manoeuvre in humans reflects altered intramural vessel compression responsible for extravascular resistance: Cardiac-coronary interaction during the Valsalva manoeuvre. The Journal of Physiology, 590(18):4623–4635, September 2012.

[280] Sandro Rossitti. Energetic and spatial constraints of arterial networks. ARQUIVOS DE NEUROPSIQUIATRIA, 53:333–333, 1995.

[281] Gregory A. Roth, Mohammad H. Forouzanfar, Andrew E. Moran, Ryan Barber, Grant Nguyen, Valery L. Feigin, Mohsen Naghavi, George A. Mensah, e Christopher J.L. Murray. Demographic and Epidemiologic Drivers of Global Cardiovascular Mortality. New England Journal of Medicine, 372(14):1333–1341, April 2015.

[282] Benjamin A. Rybicki e Robert C. Elston. The relationship between the sibling recurrence-risk ratio and genotype relative risk. The American Journal of Human Genetics, 66(2):593–604, 2000.

[283] H.S. Ryou, S. Kim, S.W. Kim, e S.W. Cho. Construction of healthy arteries using computed tomography and virtual histology intravascular ultrasound. Journal of Biomechanics, 45:1612–1618, 2012.

[284] ALFRPED Rèrnyi. On measures of entropy and information. In Fourth Berkeley symposium on mathematical statistics and probability, volume 1, pages 547–561, 1961.

[285] Hardeo Sahai e Anwer Khurhid. Formulae and tables for the determination of sample sizes and power in clinical trials for testing differences in proportions for the two-sample design: A review. Statistics in Medicine, 15(1):1–21, 1996.

[286] Shingo Sakamoto, Saeko Takahashi, Ahmet U. Coskun, Michail I. Papafaklis, Akihiko Takahashi, Shigeru Saito, Peter H. Stone, e Charles L. Feldman. Relation of Distribution of Coronary Blood Flow Volume to Coronary Artery Dominance. The American Journal of Cardiology, 111(10):1420–1424, May 2013.

[287] Nilesh J. Samani, Jeanette Erdmann, Alistair S. Hall, Christian Hengstenberg, Massimo Mangino, Bjoern Mayer, Richard J. Dixon, Thomas Meitinger, Peter Braund, H.-Erich Wichmann, e others. Genomewide association analysis of coronary artery disease. New England Journal of Medicine, 357(5):443–453, 2007.

[288] P.S. Sandhu, Upendra Kaul, R.K. Gupta, e Tapan Ghose. Fractional Flow Reserve: Intracoronary versus intravenous adenosine induced maximal coronary hyperemia. Indian Heart Journal, 65(2):147–151, March 2013.

[289] Laura M. Sangalli, Piercesare Secchi, e Simone Vantini. AneuRisk65: A dataset of three-dimensional cerebral vascular geometries. Electronic Journal of Statistics, 8(2):1879–1890, 2014.

[290] Laura M. Sangalli, Piercesare Secchi, Simone Vantini, e Alessandro Veneziani. A Case Study in Exploratory Functional Data Analysis: Geometrical Features of the Internal Carotid Artery. Journal of the American Statistical Association, 104(485):37–48, March 2009.

[291] Laura M. Sangalli, Piercesare Secchi, Simone Vantini, e Alessandro Veneziani. Efficient estimation of three-dimensional curves and their derivatives by free-knot regression splines, applied to the analysis of inner carotid artery centrelines. Journal of the Royal Statistical Society: Series C (Applied Statistics), 58(3):285–306, 2009.

[292] Sethuraman Sankaran, Leo Grady, e Charles A. Taylor. Fast Computation of Hemodynamic Sensitivity to Lumen Segmentation Uncertainty. IEEE Transactions on Medical Imaging, 34(12):2562–2571, December 2015.

[293] Sethuraman Sankaran, Leo Grady, e Charles A. Taylor. Impact of geometric uncertainty on hemodynamic simulations using machine learning. Computer Methods in Applied Mechanics and Engineering, 297:167–190, December 2015.

[294] Sethuraman Sankaran, Hyun Jin Kim, Gilwoo Choi, e Charles A. Taylor. Uncertainty quantification in coronary blood flow simulations: Impact of geometry, boundary conditions and blood viscosity. Journal of Biomechanics, 49(12):2540–2547, August 2016.

[295] A. Sato. Mechanism of vasodilation to adenosine in coronary arterioles from patients with heart disease. AJP: Heart and Circulatory Physiology, 288(4):H1633–H1640, December 2004.

[296] W Schaper. Quo vadis collateral blood flow? A commentary on a highly cited paper. Cardiovascular research, 45(1):220–223, January 2000.

[297] Jelle T.C. Schrauwen, Adriaan Coenen, Akira Kurata, Jolanda J. Wentzel, Antonius F.W. van der Steen, Koen Nieman, e Frank J.H. Gijsen. Functional and anatomical measures for outflow boundary conditions in atherosclerotic coronary bifurcations. Journal of Biomechanics, 49(11):2127–2134, July 2016.

[298] Will Schroeder, Ken Martin, Bill Lorensen, e Inc Kitware. The visualization toolkit: an object-oriented approach to 3D graphics. Kitware, [Clifton Park, N.Y.], 2006.

[299] Harry Schwartz, Roy H. Leiboff, George B. Bren, Alan G. Wasserman, Richard J. Katz, P. Jacob Varghese, Alexis B. Sokil, e Allan M. Ross. Temporal evolution of the human coronary collateral circulation after myocardial infarction. Journal of the American College of Cardiology, 4(6):1088–1093, 1984.

[300] B D Seeley e D F Young. Effect of geometry on pressure losses across models of arterial stenoses. Journal of biomechanics, 9(7):439–448, 1976.

[301] C. Seiler, M. Stoller, B. Pitt, e P. Meier. The human coronary collateral circulation: development and clinical importance. European Heart Journal, 34(34):2674–2682, September 2013.

[302] Sayan Sen, Kaleab N. Asrress, Sukhjinder Nijjer, Ricardo Petraco, Iqbal S. Malik, Rodney A. Foale, Ghada W. Mikhail, Nicolas Foin, Christopher Broyd, Nearchos Hadjiloizou, Amarjit Sethi, Mahmud Al-Bustami, David Hackett, Masood A. Khan, Muhammed Z. Khawaja, Christopher S. Baker, Michael Bellamy, Kim H. Parker, Alun D. Hughes, Darrel P. Francis, Jamil Mayet, Carlo Di Mario, Javier Escaned, Simon Redwood, e Justin E. Davies. Diagnostic Classification of the Instantaneous Wave-Free Ratio Is Equivalent to Fractional Flow Reserve and Is Not Improved With Adenosine Administration. Journal of the American College of Cardiology, 61(13):1409–1420, April 2013.

[303] Sayan Sen, Javier Escaned, Iqbal S. Malik, Ghada W. Mikhail, Rodney A. Foale, Rafael Mila, Jason Tarkin, Ricardo Petraco, Christopher Broyd, Richard Jabbour, Amarjit Sethi, Christopher S. Baker, Micheal Bellamy, Mahmud Al-Bustami, David Hackett, Masood Khan, David Lefroy, Kim H. Parker, Alun D. Hughes, Darrel P. Francis, Carlo Di Mario, Jamil Mayet, e Justin E. Davies. Development and Validation of a New Adenosine-Independent Index of Stenosis Severity From Coronary Wave–Intensity Analysis. Journal of the American College of Cardiology, 59(15):1392–1402, April 2012.

[304] M. J. Senneff, E. M. Geltman, e S. R. Bergmann. Noninvasive delineation of the effects of moderate aging on myocardial perfusion. Journal of Nuclear Medicine: Official Publication, Society of Nuclear Medicine, 32(11):2037–2042, November 1991.

[305] Rahil Shahzad, Hortense Kirişli, Coert Metz, Hui Tang, Michiel Schaap, Lucas van Vliet, Wiro Niessen, e Theo van Walsum. Automatic segmentation, detection and quantification of coronary artery stenoses on CTA. The International Journal of Cardiovascular Imaging, 29(8):1847–1859, December 2013.

[306] C. E. Shannon. A mathematical theory of communication. Bell system technical journal, 27, 1948.

[307] S. S. Shapiro e M. B. Wilk. An analysis of variance test for normality (complete samples). Biometrika, 52(3-4):591–611, 1965.

[308] Puneet Sharma, Lucian Itu, Xudong Zheng, Ali Kamen, Dominik Bernhardt, Constantin Suciu, e Dorin Comaniciu. A framework for personalization of coronary flow computations during rest and hyperemia. In Engineering in Medicine and Biology Society (EMBC), 2012 Annual International Conference of the IEEE, pages 6665–6668. IEEE, 2012.

[309] Puneet Sharma, Lucian Mihai Itu, Ali Kamen, Bogdan Georgescu, Xudong Zheng, Huseyin Tek, Dorin Comaniciu, Dominik BERNHARDT, Fernando Vega-Higuera, e Michael Scheuering. Method and System for Non-Invasive Functional Assessment of Coronary Artery Stenosis, September 2013. U.S. Classification 703/11; International Classification G06F19/12; Cooperative Classification A61B2576/023, A61B5/02007, A61B5/1128, G06F19/12, G06F19/3437.

[310] Puneet Sharma, Ali Kamen, Bogdan Georgescu, Frank Sauer, Dorin Comaniciu, Yefeng Zheng, Hien Nguyen, e Vivek Kumar Singh. Method and system for machine learning based assessment of fractional flow reserve, April 2015.

[311] Puneet Sharma, Ali Kamen, Bogdan Georgescu, Frank Sauer, Dorin Comaniciu, Yefeng Zheng, Hien Nguyen, e Vivek Kumar Singh. Method and System for Machine Learning Based Assessment of Fractional Flow Reserve, April 2016.

[312] Panagiotis K. Siogkas, Lambros S. Athanasiou, Antonis I. Sakellarios, Kostas A. Stefanou, Themis P. Exarchos, Michail I. Papafaklis, Katerina K. Naka, O. Parodi, Lampros K. Michalis, e Dimitrios I. Fotiadis. Validation study of a 3d-QCA coronary reconstruction method using a hybrid intravascular ultrasound and angiography reconstruction method and patient-specific Fractional Flow Reserve data. In 2015 37th Annual International Conference of the IEEE Engineering in Medicine and Biology Society (EMBC), pages 973–976. IEEE, 2015.

[313] Panagiotis K. Siogkas, Michail I. Papafaklis, Antonis I. Sakellarios, Kostas A. Stefanou, Christos V. Bourantas, Lambros M. Athanasiou, Christos V. Bellos, Themis P. Exarchos, Katerina K. Naka, Lampros K. Michalis, e others. Computational assessment of the fractional flow reserve from intravascular ultrasound and coronary angiography data: A pilot study. In Engineering in Medicine and Biology Society (EMBC), 2013 35th Annual International Conference of the IEEE, pages 3885–3888. IEEE, 2013.

[314] J. Slack e K. A. Evans. The increased risk of death from ischaemic heart disease in first degree relatives of 121 men and 96 women with ischaemic heart disease. Journal of Medical Genetics, 3(4):239–257, December 1966.

[315] N. Smith, A. de Vecchi, M. McCormick, D. Nordsletten, O. Camara, A. F. Frangi, H. Delingette, M. Sermesant, J. Relan, N. Ayache, M. W. Krueger, W. H. W. Schulze, R. Hose, I. Valverde, P. Beerbaum, C. Staicu, M. Siebes, J. Spaan, P. Hunter, J. Weese, H. Lehmann, D. Chapelle, e R. Rezavi. euHeart: personalized and integrated cardiac care using patient-specific cardiovascular modelling. Interface Focus, 1(3):349–364, 2011.

[316] Jos A. E. Spaan. Coronary Blood Flow, volume 124 of Developments in Cardiovascular Medicine. Springer Netherlands, Dordrecht, 1991.

[317] Garrison Sposito, editor. Scale dependence and scale invariance in hydrology. Cambridge University Press, Cambridge, UK ; New York, NY, USA, 1998.

[318] Brooke N Steele, Jing Wan, Joy P Ku, Thomas J R Hughes, e Charles A Taylor. In vivo validation of a one-dimensional finite-element method for predicting blood flow in cardiovascular bypass grafts. IEEE transactions on bio-medical engineering, 50(6):649–656, June 2003.

[319] N. Stergiopulos, D. F. Young, e T. R. Rogge. Computer simulation of arterial flow with applications to arterial and aortic stenoses. Journal of Biomechanics, 25(12):1477–1488, December 1992.

[320] P.H. Stone, A.U. Coskun, S. Kinlay, M.E. Clark, M. Sonka, A. Wahle, O.J. Ilegbusi, Y. Yeghiazarians, J.J. Popma, J. Orav, R.E. Kuntz, e C.L. Feldman. Effect of endothelial shear stress on the progression of coronary artery disease, vascular remodeling, and in-stent restenosis in humans. In vivo 6-month follow-up study. Circulation, 108:438–444, 2003.

[321] Student. The probable error of a mean. Biometrika, 6(1):pp. 1–25, 1908.

[322] Wynand J. Stuijfzand, Ibrahim Danad, Pieter G. Raijmakers, C. Bogdan Marcu, Martijn W. Heymans, Cornelis C. van Kuijk, Albert C. van Rossum, Koen Nieman, James K. Min, Jonathon Leipsic, Niels van Royen, e Paul Knaapen. Additional Value of Transluminal Attenuation Gradient in CT Angiography to Predict Hemodynamic Significance of Coronary Artery Stenosis. JACC: Cardiovascular Imaging, 7(4):374–386, April 2014.

[323] Zhonghua Sun. Multislice CT angiography in coronary artery disease: Technical developments, radiation dose and diagnostic value. World Journal of Cardiology, 2(10):333, 2010.

[324] Tatsuhisa Takahashi. Microcirculation in Fractal Branching Networks. Springer Japan, Tokyo, 2014.

[325] GD Maso Talou, C. A. Bulant, P. J. Blanco, I. Larrabide, C. Guedes Bezerra, P. A. Lemos, e R. A. Feijóo. Detailed 3D reconstruction and geometrical characterization of coronary arteries from IVUS+AX studies. In V Congreso de Matematica Aplicada, Computacional e Industrial, Tandil, Argentina, 2015.

[326] J. M. Tarkin, S. Nijjer, S. Sen, R. Petraco, M. Echavarria-Pinto, K. N. Asress, T. Lockie, M. Z. Khawaja, J. Mayet, A. D. Hughes, I. S. Malik, G. W. Mikhail, C. S. Baker, R. A. Foale, S. Redwood, D. P. Francis, J. Escaned, e J. E. Davies. Hemodynamic Response to Intravenous Adenosine and Its Effect on Fractional Flow Reserve Assessment: Results of the Adenosine for the Functional Evaluation of Coronary Stenosis Severity (AFFECTS) Study. Circulation: Cardiovascular Interventions, 6(6):654–661, December 2013.

[327] Charles A. Taylor e Timothy A. Fonte. Method and system for patient-specific modeling of blood flow, July 2013.

[328] Charles A. Taylor, Timothy A. Fonte, e James K. Min. Computational Fluid Dynamics Applied to Cardiac Computed Tomography for Noninvasive Quantification of Fractional Flow Reserve. Journal of the American College of Cardiology, 61(22):2233–2241, June 2013.

[329] Charles A. Taylor, Thomas J.R. Hughes, e Christopher K. Zarins. Finite element modeling of blood flow in arteries. Computer Methods in Applied Mechanics and Engineering, 158(1-2):155–196, May 1998.

[330] Charles A. Taylor, Hyun Jin Kim, Sethuraman Sankaran, Michiel Schaap, David EBERLE, Gilwoo Choi, e Leo J. GRADY. Systems and methods for modeling changes in patient-specific blood vessel geometry and boundary conditions, December 2016. International Classification G06F19/00; Cooperative Classification G06F19/3437.

[331] Mano J. Thubrikar e Francis Robicsek. Pressure-induced arterial wall stress and atherosclerosis. The Annals of Thoracic Surgery, 59(6):1594–1603, June 1995.

[332] Pim A L Tonino, Bernard De Bruyne, Nico H J Pijls, Uwe Siebert, Fumiaki Ikeno, Marcel van' t Veer, Volker Klauss, Ganesh Manoharan, Thomas Engstrøm, Keith G Oldroyd, Peter N Ver Lee, Philip A MacCarthy, William F Fearon, e FAME Study Investigators. Fractional flow reserve versus angiography for guiding percutaneous coronary intervention. The New England journal of medicine, 360(3):213–224, January 2009.

[333] Pim A.L. Tonino, William F. Fearon, Bernard De Bruyne, Keith G. Oldroyd, Massoud A. Leesar, Peter N. Ver Lee, Philip A. MacCarthy, Marcel van't Veer, e Nico H.J. Pijls. Angiographic Versus Functional Severity of Coronary Artery Stenoses in the FAME Study. Journal of the American College of Cardiology, 55(25):2816–2821, June 2010.

[334] Monique Tröbs, Stephan Achenbach, Jens Röther, Thomas Redel, Michael Scheuering, David Winneberger, Klaus Klingenbeck, Lucian Itu, Tiziano Passerini, Ali Kamen, Puneet Sharma, Dorin Comaniciu, e Christian Schlundt. Comparison of Fractional Flow Reserve Based on Computational Fluid Dynamics Modeling Using Coronary Angiographic Vessel Morphology Versus Invasively Measured Fractional Flow Reserve. The American Journal of Cardiology, 117(1):29–35, January 2016.

[335] Constantino Tsallis. Possible generalization of boltzmann-gibbs statistics. Journal of Statistical Physics, 52(1):479–487, 1988.

[336] Shengxian Tu, Emanuele Barbato, Zsolt Köszegi, Junqing Yang, Zhonghua Sun, Niels R. Holm, Balázs Tar, Yingguang Li, Dan Rusinaru, William Wijns, e Johan H.C. Reiber. Fractional Flow Reserve Calculation From 3-Dimensional Quantitative Coronary Angiography and TIMI Frame Count. JACC: Cardiovascular Interventions, 7(7):768–777, July 2014.

[337] Shengxian Tu, Christos V. Bourantas, Bjarne L. Nørgaard, Ghassan S. Kassab, Bon-Kwon Koo, e Johan H.C. Reiber. Image-based assessment of fractional flow reserve. EuroIntervention, 11(V):V50–V54, May 2015.

[338] Neal G. Uren, Jacques A. Melin, Bernard De Bruyne, William Wijns, Thierry Baudhuin, e Paolo G. Camici. Relation between Myocardial Blood Flow and the Severity of Coronary-Artery Stenosis. New England Journal of Medicine, 330(25):1782–1788, June 1994.

[339] Tim P. van de Hoef, Martijn Meuwissen, Javier Escaned, Justin E. Davies, Maria Siebes, Jos A. E. Spaan, e Jan J. Piek. Fractional flow reserve as a surrogate for inducible myocardial ischaemia. Nature Reviews Cardiology, 10(8):439–452, June 2013.

[340] Tim P. van de Hoef, Maria Siebes, Jos A. E. Spaan, e Jan J. Piek. Fundamentals in clinical coronary physiology: why coronary flow is more important than coronary pressure. European Heart Journal, 36(47):3312–3319, December 2015.

[341] Lokien X van Nunen, Frederik M Zimmermann, Pim A L Tonino, Emanuele Barbato, Andreas Baumbach, Thomas Engstrøm, Volker Klauss, Philip A MacCarthy, Ganesh Manoharan, Keith G Oldroyd, Peter N Ver Lee, Marcel van't Veer, William F Fearon, Bernard De Bruyne, e Nico H J Pijls. Fractional flow reserve versus angiography for guidance of PCI in patients with multivessel coronary artery disease (FAME): 5-year follow-up of a randomised controlled trial. The Lancet, 386(10006):1853–1860, November 2015.

[342] J. Scott VanEpps e David A. Vorp. Mechanopathobiology of Atherogenesis: A Review. Journal of Surgical Research, 142(1):202–217, September 2007.

[343] G. Vassalli e O. M. Hess. Measurement of coronary flow reserve and its role in patient care. Basic research in cardiology, 93(5):339–353, 1998.

[344] M. C. Villa-Uriol, I. Larrabide, A. J. Geers, J. Pozo, H. Bogunović, M. Mazzeo, P. Omedas, V. Barbarito, L. Carotenuto, C. Riccobene, e others. AngioLab: integrated technology for patient-specific management of intracranial aneurysms. In Engineering in Medicine and Biology Society (EMBC), 2010 Annual International Conference of the IEEE, pages 6801–6804. IEEE, 2010.

[345] M. von Lüdinghausen. The Clinical Anatomy of Coronary Arteries, volume 167 of Advances in Anatomy, Embryology and Cell Biology. Springer Berlin Heidelberg, Berlin, Heidelberg, 2003.

[346] M. von Lüdinghausen. The Clinical Anatomy of Coronary Arteries, volume 167 of Advances in Anatomy, Embryology and Cell Biology. Springer Berlin Heidelberg, Berlin, Heidelberg, 2003.

[347] Michael von Lüdinghausen. The Venous Drainage of the Human Myocardium, volume 168 of Advances in Anatomy Embryology and Cell Biology. Springer Berlin Heidelberg, Berlin, Heidelberg, 2003.

[348] Szilard Voros, Sarah Rinehart, Jesus G. Vazquez-Figueroa, Anna Kalynych, Dimitri Karmpaliotis, Zhen Qian, Parag H. Joshi, Hunt Anderson, Laura Murrieta, Charles Wilmer, Harold Carlson, William Ballard, e Charles Brown. Prospective, Head-to-Head Comparison of Quantitative Coronary Angiography, Quantitative Computed Tomography Angiography, and Intravascular Ultrasound for the Prediction of Hemodynamic Significance in Intermediate and Severe Lesions, Using Fractional Flow Reserve as Reference Standard (from the ATLANTA I and II Study). The American Journal of Cardiology, 113(1):23–29, January 2014.

[349] Bruce F. Waller, Charles M. Orr, John D. Slack, Cass A. Pinkerton, James Van Tassel, e Thomas Peters. Anatomy, histology, and pathology of coronary arteries: A review relevant to new interventional and imaging techniques—Part I. Clinical cardiology, 15(6):451–457, 1992.

[350] Jing Wan, Brooke Steele, Sean A Spicer, Sven Strohband, Gonzalo R Feijóo, Thomas J R Hughes, e Charles A Taylor. A one-dimensional finite element method for simulation-based medical planning for cardiovascular disease. Computer methods in biomechanics and biomedical engineering, 5(3):195–206, June 2002.

[351] G. B. West. A General Model for the Origin of Allometric Scaling Laws in Biology. Science, 276(5309):122–126, April 1997.

[352] Ross T. Whitaker e Xinwei Xue. Variable-conductance, level-set curvature for image denoising. In Image Processing, 2001. Proceedings. 2001 International Conference on, volume 3, pages 142–145. IEEE, 2001.

[353] H. Wieneke. Determinants of coronary blood flow in humans: quantification by intracoronary Doppler and ultrasound. Journal of Applied Physiology, 98(3):1076–1082, November 2004.

[354] D. O. Williams, E. A. Amsterdam, R. R. Miller, e D. T. Mason. Functional significance of coronary collateral vessels in patients with acute myocardial infarction: relation to pump performance, cardiogenic shock and survival. The American Journal of Cardiology, 37(3):345–351, March 1976.

[355] R. F. Wilson, K. Wyche, B. V. Christensen, S. Zimmer, e D. D. Laxson. Effects of adenosine on human coronary arterial circulation. Circulation, 82(5):1595–1606, November 1990.

[356] Dennis T.L. Wong, Brian S. Ko, James D. Cameron, Darryl P. Leong, Michael C.H. Leung, Yuvaraj Malaiapan, Nitesh Nerlekar, Marcus Crossett, John Troupis, Ian T. Meredith, e Sujith K. Seneviratne. Comparison of Diagnostic Accuracy of Combined Assessment Using Adenosine Stress Computed Tomography Perfusion + Computed

Tomography Angiography With Transluminal Attenuation Gradient + Computed Tomography Angiography Against Invasive Fractional Flow Reserve. Journal of the American College of Cardiology, 63(18):1904–1912, May 2014.

[357] Dennis T.L. Wong, Brian S. Ko, James D. Cameron, Nitesh Nerlekar, Michael C.H. Leung, Yuvaraj Malaiapan, Marcus Crossett, Darryl P. Leong, Stephen G. Worthley, John Troupis, Ian T. Meredith, e Sujith K. Seneviratne. Transluminal Attenuation Gradient in Coronary Computed Tomography Angiography Is a Novel Noninvasive Approach to the Identification of Functionally Significant Coronary Artery Stenosis. Journal of the American College of Cardiology, 61(12):1271–1279, March 2013.

[358] Susan N Wright, Peter Kochunov, Fernando Mut, Maurizio Bergamino, Kerry M Brown, John C Mazziotta, Arthur W Toga, Juan R Cebral, e Giorgio A Ascoli. Digital reconstruction and morphometric analysis of human brain arterial vasculature from magnetic resonance angiography. NeuroImage, 82:170–181, November 2013.

[359] Nan Xiao, Jordi Alastruey, e C. Alberto Figueroa. A systematic comparison between 1-D and 3-D hemodynamics in compliant arterial models. International Journal for Numerical Methods in Biomedical Engineering, 30(2):204–231, 2014.

[360] Yeonyee E. Yoon, Jin-Ho Choi, Ji-Hyun Kim, Kyung-Woo Park, Joon-Hyung Doh, Yong-Jin Kim, Bon-Kwon Koo, James K. Min, Andrejs Erglis, Hyeon-Cheol Gwon, Yeon Hyeon Choe, Dong-Ju Choi, Hyo-Soo Kim, Byung-Hee Oh, e Young-Bae Park. Noninvasive Diagnosis of Ischemia-Causing Coronary Stenosis Using CT Angiography. JACC: Cardiovascular Imaging, 5(11):1088–1096, November 2012.

[361] D. F. Young, N. R. Cholvin, e A. C. Roth. Pressure drop across artificially induced stenoses in the femoral arteries of dogs. Circulation Research, 36(6):735–743, June 1975.

[362] D F Young e F Y Tsai. Flow characteristics in models of arterial stenoses. I. Steady flow. Journal of biomechanics, 6(4):395–410, July 1973.

[363] D F Young e F Y Tsai. Flow characteristics in models of arterial stenoses. II. Unsteady flow. Journal of biomechanics, 6(5):547–559, September 1973.

[364] M. Zamir. On fractal properties of arterial trees. Journal of theoretical biology, 197(4):517–526, 1999.

[365] Christopher K. Zarins, Don P. Giddens, B. K. Bharadvaj, Vikrom S. Sottiurai, Robert F. Mabon, e Seymour Glagov. Carotid bifurcation atherosclerosis. Quantitative correlation of plaque localization with flow velocity profiles and wall shear stress. Circulation research, 53(4):502–514, 1983.

[366] Christopher K. Zarins, Charles A. Taylor, e James K. Min. Computed Fractional Flow Reserve (FFTCT) Derived from Coronary CT Angiography. Journal of Cardiovascular Translational Research, 6(5):708–714, October 2013.

[367] Jun-Mei Zhang, Tong Luo, Swee Yaw Tan, Aileen Mae Lomarda, Aaron Sung Lung Wong, Felix Yung Jih Keng, John Carson Allen, Yunlong Huo, Boyang Su, Xiaodan Zhao, Min Wan, Ghassan S. Kassab, Ru San Tan, e Liang Zhong. Hemodynamic analysis of patient-specific coronary artery tree: HEMODYNAMIC ANALYSIS OF PATIENT-SPECIFIC CORONARY ARTERY TREE. International Journal for Numerical Methods in Biomedical Engineering, 31(4):e02708, April 2015.

[368] Jun-Mei Zhang, Liang Zhong, Tong Luo, Aileen Mae Lomarda, Yunlong Huo, Jonathan Yap, Soo Teik Lim, Ru San Tan, Aaron Sung Lung Wong, Jack Wei Chieh Tan, Khung Keong Yeo, Jiang Ming Fam, Felix Yung Jih Keng, Min Wan, Boyang Su, Xiaodan Zhao, John Carson Allen, Ghassan S. Kassab, Terrance Siang Jin Chua, e Swee Yaw Tan. Simplified Models of Non-Invasive Fractional Flow Reserve Based on CT Images. PLOS ONE, 11(5):e0153070, May 2016.

[369] Jun-Mei Zhang, Liang Zhong, Boyang Su, Min Wan, Jinq Shya Yap, Jasmine P. L. Tham, Leok Poh Chua, Dhanjoo N. Ghista, e Ru San Tan. Perspective on CFD studies of coronary artery disease lesions and hemodynamics: A review. International Journal for Numerical Methods in Biomedical Engineering, 30(6):659–680, June 2014.

[370] Yifang Zhou, Ghassan S. Kassab, e Sabee Molloi. On the design of the coronary arterial tree: a generalization of Murray's law. Physics in medicine and biology, 44(12):2929, 1999.

[371] H. Zhu. Relationship Between the Dynamic Geometry and Wall Thickness of a Human Coronary Artery. Arteriosclerosis, Thrombosis, and Vascular Biology, 23(12):2260–2265, September 2003.

[372] Hui Zhu, Zhaohua Ding, Robert N. Piana, Thomas R. Gehrig, e Morton H. Friedman. Cataloguing the geometry of the human coronary arteries: A potential tool for predicting risk of coronary artery disease. International Journal of Cardiology, 135(1):43–52, June 2009.

[373] Marco Zimarino, Mariangela D'Andreamatteo, Ron Waksman, Stephen E. Epstein, e Raffaele De Caterina. The dynamics of the coronary collateral circulation. Nature Reviews Cardiology, 11(4):191–197, January 2014.

Author's biography

Carlos Alberto Bulant is software engineer, a cinephile, an otaku and also a gamer (in rehab); He is a food enthusiastic and loves chocolate; he likes to run, to hang out with his friends and being with his soul-mate, Lis.

He was born on October 18 of 1985, in Calilegua, Jujuy, Argentina. His family moved to Olavarría, a few years later, he lived there until he finished high-school in 2003. Then he moved to Tandil to study at Universidad Nacional del Centro de la Provincia de Buenos Aires (UNICEN). He graduated as software engineer in 2010, a year later he moved to Petrópolis, Rio de Janeiro, Brasil, pursuing a master degree in computational modeling at the Laboratório Nacional de Computação Científica (LNCC). In 2013 he got the master degree and started the doctorate studies. This Thesis is the result of four years of hard work and synergic interaction at HeMoLab research group, at the LNCC. A complete list of contributions published during the doctorate is presented below.

Publications in scientific journals:

- Bulant, C. A; Blanco, P. J; Clausse A; Assunção Jr, A. N; Lima, T. P; Avila, L. F. R; Feijóo, R. A; Lemos, P. A. *Association between three-dimensional vessel geometry and the presence of atherosclerotic plaques in the left anterior descending coronary artery of high-risk patients.* Biomedical Signal Processing and Control 2017; 31:569–575.

- Bulant, C. A; Blanco, P. J; Pereira, A. C; Lima, T. P; Assunção Jr, A. N; Liberato, G; Bezerra, G. G; Parga Filho, J. R; Avila, L. F. R; Feijóo, R. A; Lemos, P. A. *On the search of arterial geometry heritability.* International Journal of Cardiology 2016; 221:1013–1021.

- Bulant, C. A; Blanco, P. J; Maso Talou, G. D; Bezerra, G. G; Lemos, P. A; Feijóo, R. A. *A head-to-head comparison between CT- and IVUS-derived coronary blood flow models.* Journal of Biomechanics 2017; 51:65–76.

- Bulant, C. A; Blanco, P. J; Lima, T. P; Assunção Jr, A. N; Liberato, G; Parga Filho, J. R; Avila, L. F. R; Pereira, A. C; Feijóo, R. A; Lemos, P. A. *A computational framework to characterize and compare the geometry of coronary networks.* International Journal for Numerical Methods in Biomedical Engineering 2017. 33(3):e02800.

- Mansilla, L.A; Blanco, P. J; Bulant, C. A; Dari, E. A; Veneziani, A; Feijóo, R. A. *Transversally Enriched Pipe Element Method (TEPEM). An effective numerical approach for blood flow modeling.* International Journal for Numerical Methods in Biomedical Engineering 2016.

- Bezerra, C. G; Maso Talou, G. D; Bulant, C. A; Falcão, B. A; Mariani, J; Blanco, P. J; Feijóo, R. A. Lemos, P. A. *Reconstrução tridimensional de artérias coronárias a partir da integração do ultrassom intracoronário e da angiografia convencional.* Revista Brasileira de Cardiologia Invasiva 2015; 23(2):134–138.

Publications in proceedings:

- Bulant, C. A; Blanco, P. J; Assunção Jr, A. N; Liberato, G; Lima, T. P; Parga Filho, J. R; Lemos, P. A; Avila, L. F. R; Feijóo, R. A. *Morphological characterization and comparison of coronary arterial trees.* In proceedings: XXXIV Congresso da Sociedade Brasileira de Computação. Brasilia, Brasil, 2014.

- Bulant, C. A; Blanco, P. J; Assunção Jr, A. N; Liberato, G; Lima, T. P; Parga Filho, J. R; Lemos, P. A; Avila, L. F. R; Feijóo, R. A. *Geometrical characterization of the coronary arterial tree.* In proceedings: XXXVI Iberian Latin-American Congress on Computational Methods in Engineering, Rio de Janeiro, Brasil, 2015.

- Maso Talou, G. D; Bulant, C. A; Blanco, P. J; Larrabide, I; Bezerra, C. G; Lemos, P. A; Feijóo, R. A. *Detailed 3D reconstruction and geometrical characterization of coronary arteries from IVUs+AX studies.* In proceedings: V Congreso de Matematica Aplicada, Computacional e Industrial. Tandil, Argentina, 2015.

- Bezerra, C. G; Falcao, B. A. A; Maso Talou, G. D; Bulant, C. A; Blanco, P. J; Feijóo, R. A; Mariani Junior, J; Lemos, P. A. *Reconstrução Tridimensional de Artérias Coronárias à partir da Integração do Ultrassom Intra-Coronário e da Angiografia Convencional fase piloto de validação com a angiotomografia de coronárias.* In proceedings: Congresso da Sociedade Brasileira de Hemodinâmica e Cardiologia Intervencional. Brasilia, Brasil, 2015.

- Bezerra, C. G; Bulant, C. A; Maso Talou, G. D; Mariani, J; Falcão, B. A; Pinton, F. A; Feijóo, R. A; Filho, A; Lemos P. A. *TCT-535 Coronary computed tomography angiography (CCTA) blood flow model, how we can improve it? Insights based on comparison with intravascular ultrasound (IVUS) tridimensional model.* Journal of the American College of Cardiology 2016; 68(18):B216.

- Bezerra, C. G; Maso Talou, G. D; Bulant, C. A; Mariani, J; Pinton, F. A; Falcão, B. A; Feijóo, R. A; Filho, A; Lemos P. A. *TCT-573 Head-to-head comparison between coronary computed tomography angiography (CCTA) and intravascular ultrasound (IVUS) tridimensional models: a geometric point of view.* Journal of the American College of Cardiology 2016; 68(18):B232.